HAL
open science

Interactions effectives et dynamiques en systèmes actifs de colloïdes autopropulsés

Enrico Federico Semeraro

To cite this version:

Enrico Federico Semeraro. Interactions effectives et dynamiques en systèmes actifs de colloïdes autopropulsés. Biochimie, Biologie Moléculaire. Université Grenoble Alpes, 2017. Français. NNT : 2017GREAV017 . tel-01686239

HAL Id: tel-01686239

https://theses.hal.science/tel-01686239v1

Submitted on 17 Jan 2018

HAL is a multi-disciplinary open access archive for the deposit and dissemination of scientific research documents, whether they are published or not. The documents may come from teaching and research institutions in France or abroad, or from public or private research centers.

L'archive ouverte pluridisciplinaire **HAL**, est destinée au dépôt et à la diffusion de documents scientifiques de niveau recherche, publiés ou non, émanant des établissements d'enseignement et de recherche français ou étrangers, des laboratoires publics ou privés.

Communauté UNIVERSITÉ Grenoble Alpes

THÈSE

Pour obtenir le grade de

DOCTEUR DE LA COMMUNAUTÉ UNIVERSITÉ GRENOBLE ALPES

Spécialité : **Chimie physique moléculaire et structurale**

Arrêté ministériel : 25 mai 2016

Présentée par

Enrico Federico SEMERARO

Thèse dirigée par **Dr. Narayanan THEYENCHERI**

préparée au sein du **European Synchrotron Radiation Facility**
dans **l'École Doctorale de Chimie et Science du Vivant**

Interactions effectives et dynamiques en systèmes actifs de colloïdes autopropulsés

Thèse soutenue publiquement le **20 mars 2017**,
devant le jury composé de :

Dr. Frédéric PIGNON
Directeur de recherche, Laboratoire Rhéologie et Procédés, Université Grenoble Alpes / CNRS / Grenoble INP, Grenoble (France), Président

Dr. Thomas ZEMB
Professeur, Institut de Chimie Séparative de Marcoule, CEA / CNRS / Université de Montpellier / ENSCM, Bagnol-sur-Cèze (France), Rapporteur

Dr. Georg PABST
Professeur associé, Institute of Molecular Biosciences, Université de Graz (Autriche), Rapporteur

Dr. Christophe YBERT
Directeur de recherche, Institut Lumière Matière, Université Claude Bernard Lyon / CNRS, Lyon (France), Examinateur

Dr. Stefano MOSSA
Ingénieur chercheur, Institut Nanosciences et Cryogénie, CEA, Grenoble (France), Examinateur

Dr. Narayanan THEYENCHERI
Senior Scientist, European Synchrotron Radiation Facility, Grenoble (France), Directeur de thèse

PhD thesis

Effective Interactions and Dynamics in Active Matter Systems

Enrico Federico Semeraro

PhD Student at the
European Synchrotron Radiation Facility (ESRF) and
École Doctorale de Chimie e Science du Vivant (EDCSV)
Thesis Supervisor: Dr. Theyencheri Narayanan

Table of Contents

Abstract **7**

Abstract (Français) **9**

Acknowledgement **11**

1. Introduction **13**

1.1. Passive Colloidal Dispersions 15

1.1.1. Brownian Motion 15

1.1.2. Effective Interactions and Colloidal Stability 17

1.2. Active Colloids 19

1.2.1. Enhanced Diffusion 20

1.2.2. Collective Motions and Dynamic Clustering 21

1.2.3. Active Media 23

1.3. Aims of the Thesis 24

2. Synchrotron and Neutron Scattering Methods **27**

2.1. Small Angle Scattering 27

2.1.1. Small Angle X-ray Scattering 28

2.1.2. Scattering Form Factor 30

2.1.3. Core-Shell Models 31

2.1.4. Asymptotic limits and SLD fluctuations 33

2.1.5. Structure Factor 34

Polydispersity 37

2.1.6. Small-Angle Neutron Scattering 37

2.1.7. X-ray Photon Correlation Spectroscopy 39

2.2. Experimental Setup 41

2.2.1. Synchrotron Radiation 41

2.2.2. USAXS/SAXS Beamline Setup 43

3. Small Angle Scattering Studies of *in Vivo Escherichia Coli* Structure 47
3.1. *Escherichia Coli*: Shape and Ultrastructure . . . 47
3.2. Materials and Methods . . . 50
3.3. Modelling the Whole Cell Body . . . 51
3.3.1. USAXS Measurements . . . 51
3.3.2. Limitations of the Model . . . 53
3.3.3. Possible Applications . . . 55
3.4. X-ray and Neutron Scattering: Investigating the Internal Structure of *E. coli* . . . 58
3.4.1. USAXS/SAXS Measurements . . . 58
3.4.2. SANS Measurements: Contrast Matching Method . . . 61
3.4.3. Modelling of Gram-Negative Bacterium . . . 63
3.4.4. Data Analysis and Discussion . . . 68
3.4.5. Alternative Scattering Model . . . 80
3.5. Summary and Conclusion . . . 85

4. Passive Colloids in Active Bacterial Medium: Interactions and Dynamics 89
4.1. Materials and Methods . . . 90
4.1.1. Preliminary Data and Experimental Considerations . . . 91
Stability versus Mobility . . . 92
Swimming *E. coli*: Depletion of Energy Sources . . . 94
Bacteria in Crowded Suspensions: Physical Considerations . . . 94
4.2. Statics: Results and Discussion . . . 97
4.2.1. Investigation of Multiple-Scattering Effects . . . 97
4.2.2. Static Interactions in an Active Bacterial Medium . . . 102
E1: Hard-Sphere Interactions . . . 102
E2: Tuning the Interactions . . . 104
Summary . . . 107
4.3. Dynamics: Results and Discussion . . . 107
E1: Hard-Sphere Fluid . . . 110
E2: Weakly Attractive System . . . 112
Summary . . . 114
4.4. Summary and Conclusion . . . 115

5. Colloids in a Phase Separating Medium: Microstructure and Dynamics 119
5.1. Materials and Methods . . . 119
5.1.1. Synthesis of Silica/Nickel Janus Colloids . . . 120
Characterisation . . . 122

5.2. Silica colloids: Results and discussion 124
5.2.1. Microstructure in the Quasi-Binary Mixture 124
5.2.2. Dynamics upon Quenching 127
5.2.3. Summary 134
5.3. Janus colloids: Results and discussion 137
5.3.1. Asymmetric Static Interactions 137
Phase transition 141
Ageing 142
5.3.2. Dynamics in the Phase Separating System 144
5.3.3. Summary 152
5.4. Summary and Conclusion 153

6. Conclusion and Perspectives **155**

7. Conclusion et Perspectives (Français) **159**

Appendices **165**

A. Numerical limits in the Porod Regime **167**

B. Minimization Algorithms **169**
B.1. Levenberg-Marquardt Method 169
B.2. Monte Carlo Algorithms 172
B.2.1. Simulated Annealing Algorithm 172
B.2.2. Genetic Selection Algorithm 174

List of Symbols and Acronyms **177**

List of Figures **181**

List of Tables **193**

Bibliography **195**

Abstract

Suspensions of self-propelled particles are non-equilibrium systems that have attracted the attention of the scientific community in the last 20 years [1]. A particular interest lies on the collective behaviour that these systems display, from coordinated dynamics, reminiscent of flocks of birds, to a dynamic clustering dependent on particle velocity and concentration [2]. This thesis aims to systematically study the effective interactions, microstructure and dynamics observed in active colloidal suspensions, using (Ultra) Small-Angle X-ray Scattering (USAXS/SAXS) and multi-speckle X-ray Photon Correlation Spectroscopy (XPCS), with the focus on the interplay between interparticle interactions and phoretic dynamics.

To start, the structure and motility of active *Escherichia coli* bacteria were characterised. Combined USAXS and SAXS measurements permitted a broad range of magnitude of scattering vector q, leading to the development of a multi-scale structural model which includes colloidal (cell-body), membrane (cell-envelope) and polymer (flagella) features. Further information obtained, by contrast-variation Small Angle Neutron Scattering (SANS) measurements at three match points and the full contrast, allowed the determination of the membrane electron-density and the inter-membrane distances on a quantitative scale.

Swimming *E. coli* bacteria were then used as an active bath for suspension of sub-micron-sized passive silica colloids, whose effective interactions and dynamics were investigated by using USAXS and XPCS techniques. Both static and hydrodynamic information were obtained, suggesting active bacteria act as a fluidizing agent as they reduce attractive interactions and enhance the dynamics of passive colloids, which, at the same time, are affected by a more viscous environment due to the bacterial presence.

Connection between interparticle interactions and dynamics were analysed by studying the phoretic motions of sub-micron-sized silica colloids and half-coated silica/nickel Janus colloids suspended in a mixture of 3-methylpyridine (3MP) and water/heavy water undergoing liquid-liquid phase separation. The study was performed by means of USAXS and XPCS techniques and exploited the preferential wetting of 3MP on the silica surface [3], revealing that the colloid motion is strongly correlated to the dynamics of phase separation. Indeed, silica colloid, used as a reference systems, displayed advective motion with enhanced diffusion toward the 3MP-rich phase before the phase separation is completed, similar to self-propelled motion. In contrast, the dynamics and microstructure of Janus colloids showed peculiar features due to the influence

of asymmetric interactions with the solvent. Depending on 3MP concentration, Janus colloids exhibited different microstructure comparable with a surfactant behaviour, showing both self-organization at the 3MP/water interface and micellar structures. This microstructure directly inhibited the dynamics of Janus particles, presenting a behaviour similar to dynamic clustering in active systems.

The ability of X-ray scattering techniques to probe active dynamics and, simultaneously, their effective interparticle interactions is demonstrated. Scattering methods complement direct microscopy observations by providing ensemble averaged information in the thermodynamic limit ($N \to \infty$).

Abstract (Français)

Les suspensions de particules autopropulsées sont des systèmes hors équilibre qui ont attiré l'attention de la communauté scientifique au cours des vingt dernières années [1]. Le comportement collectif que ces systèmes adoptent est particulièrement intéressant, couvrant aussi bien la dynamique coordonnée – similaire aux vols de nuées d'oiseaux – que le "regroupement dynamique" [2]. Ce travail de thèse est une étude systématique des interactions effectives, de la microstructure et de la dynamique observées dans les suspensions colloïdales actives, en utilisant la diffusion des rayons X aux (ultra) petits angles (USAXS/SAXS) et la spectroscopie de corrélation de photons X (XPCS). L'accent est mis sur l'influence mutuelle entre les interactions inter-particules et la dynamique phorétique.

En premier lieu, la structure et la motilité de la bactérie active *Escherichia coli* ont été caractérisées. Des mesures combinées USAXS et SAXS ont permis d'obtenir une large gamme de magnitude de vecteur de diffusion q, ce qui a conduit au développement d'un modèle structurel multi-échelle combinant les caractéristiques de colloïdes (corps cellulaires), de membranes (enveloppe cellulaire) et de polymères (flagelles). Ce modèle a été affiné au moyen de mesures complémentaires de diffusion de neutrons aux petits angles (SANS) en variant le contraste externe (substitution isotopique partielle du solvant), afin d'aboutir à une détermination quantitative de la densité électronique des membranes et des distances inter-membranes.

Les bactéries mobiles *E. coli* ont ensuite été utilisées comme solution active pour la suspension de colloïdes passifs de silice de taille sub-micrométrique, dont les interactions effectives et la dynamique ont été étudiées en utilisant les techniques USAXS et XPCS. Des informations statiques et hydrodynamiques ont été obtenues, suggérant que les bactéries actives ont un effet fluidifiant. Elles réduisent les interactions attractives et accroissent la dynamique des particules de silice, qui, en même temps, sont affectées par une viscosité efficace augmentée.

La relation entre les interactions effectives inter-particules et la dynamique a été analysée en étudiant les mouvements phorétiques de colloïdes de silice et de type Janus (silice partiellement recouverte de nickel) de taille sub-micrométrique suspendus dans un mélange binarie de 3-méthylpyridine (3MP) et eau/eau lourde pendant la séparation de phase liquide-liquide. L'étude a été réalisée au moyen des techniques USAXS et XPCS en exploitant l'adsorption préférentiel de 3MP sur la surface de la silice [3], révélant que le mouvement des colloïdes est fortement corrélé à la dynamique de la séparation de phase. Les colloïdes de silice, utilisés

comme système de référence, présentent une dynamique advective avec une diffusion accrue en direction des microdomaines riches en 3MP, jusqu'à l'aboutissement de la séparation de phase, évoquant la dynamique des systèmes auto-propulsés. Par contre, la dynamique et la microstructure des colloïdes de type Janus présentent des caractéristiques particulières en raison de l'influence des interactions asymétriques avec le solvant. Selon la concentration en 3MP, ces colloïdes peuvent se comporter comme des tensioactifs, s'auto-assemblant en micelles ou aux interfaces entre 3MP et l'eau. Cette microstructuration inhibe directement la dynamique des particules de type Janus, dont le comportement s'apparente alors à celui observé dans les systèmes actifs lors du regroupement dynamique.

La capacité des techniques de diffusion de rayons X à sonder la dynamique de systèmes actifs et, simultanément, les interactions effectives inter-particules a été démontrée. Les méthodes de diffusion complètent les observations directes de microscopie et fournissent une information moyennée sur un ensemble d'un point de vue de la limite thermodynamique (nombre de particules $N \to \infty$).

Acknowledgement

I would like to extend my sincerest thanks and appreciation to my supervisor Dr. Theyencheri Narayanan, who guided me through my thesis project.

My faithful gratitude goes to the jury members who have given me the opportunity to present this work: Prof. Thomas Zemb (Institut de Chimie Séparative de Marcoule), Dr. Georg Pabst (Karl-Franzens-Universität Graz, Austria), Dr. Frédéric Pignon (Laboratoire Rhéologie et Procédés), Dr. Christophe Ybert (Université Claude Bernard de Lyon) and Dr. Stefano Mossa (CEA). Moreover, I would like to thank Dr. Frédéric Pignon and Dr. Trevor Forsyth, members of the *comité de Suivi de Thèse* of both 1st and 2nd year of the PhD, for the interest they showed on the development of the thesis.

My appreciation goes to the ESRF, which provided me with the PhD fellowship and synchrotron beamtime. The Institut Laue-Langevin (ILL) is also thanked for the provision of instrument time, and the EDCSV which have welcomed me.

I am indebted to Dr. Rajeev Dattani, with whom I collaborated to carry out the work presented in Chapter 5, giving an inestimable contribution from the synthesis and production of Silica/Nickel Janus colloids to the preparation of related manuscripts. Likewise, the assistance of Dr. Juliette Devos (ILL), who provided the *E. coli* cultures, was priceless as much as the help, support and advices I received from the ID02 beamline staff: Dr. Sylvain Prevost, Dr. Johannes Möller, Dr. Michael Sztucki, Dr. Peter Böseke, Dr. Gudrun Lotze, Oonagh Mannix and Jacques Gorini. I would like to acknowledge Dr. Yuri Chushkin for providing me with the *PYXPCS.py* routine and Dr. Lionel Porcar (ILL) for his assistance at D22 during SANS beam time.

I am grateful to a number of colleagues from the ESRF, ILL and Partnership for Soft Condensed Matter (PSCM) for access to and support at laboratories and instrumentation: Dr. Diego Pontoni and Dr. Yuri Gerelli for the access to the laboratory, Dr. Iraida Sniguirev, Dr. Oleg Konovalov, Dr. Giovanni Li Destri, Dr. Yohan Fuchs, Pierre Lloria and Andrea Tummino for the assistance during surface science characterisation. A special thanks is due to all the colleagues that I met, and who shared with me a portion of this three-year project, as they were a source of scientific interests and entertainment: Dr. Giorgio Schirò, Dr. Alessandro Longo, Alvaro Martin Ortega, Dr. Tom Dane, Dr. Nick Harker, Dr. Britta Weinhausen, Stephen Bauters, Mark Glass, Dr. Beatrice Ruta, Anastasya Shilova, Dr. Andreas Johannes and Dr. Tilman Grünewald.

Finally, my gratitude goes to my partner Marta, for her patience and support, and to my daughter Dafne, for her lovely smiles.

1. Introduction

Studies of *colloidal systems* constitutes a major segment of modern *soft matter* science [4, 5]. The term *colloid* derives from the Greek $\kappa\acute{o}\lambda\lambda\alpha$ (glue) and $\varepsilon\acute{\iota}\delta o\varsigma$ (kind) and was coined by Graham in the 1860s. Colloids have been studied for many centuries, owing to their abundance and relevance to many practical systems. Indeed, they are common in everyday life and include not only glues, but milk, coffee, paints, toothpaste and so forth. They have a number of applications in medical, pharmaceutical, chemical and food industries. Besides, they are of pivotal importance in fundamental research to the extent that they are referred to as "model atoms". As a matter of fact, colloidal systems link the molecular and macroscopic length scales and mimic atomic-scale phenomena at larger size and time scales easily accessible in a laboratory. Examples include colloidal gas, liquid, crystal and glass phases and the transition between them, which have been the subject of intense investigations in the past [6].

In the last 50 years, colloidal science has been enriched with the progress in statistical-mechanical theories, power of computer simulations together with significant advances in synthetic chemistry, which allows designing model colloidal systems. The combination of analytical theories and computer simulations can now predicts the structure and dynamics of such systems.

A unique feature of colloids is that they can mimic purely hard-sphere interparticle interactions (only involving volume exclusion), which does not have atomic analogue. Indeed other types of more realistic interactions, such as screened Coulomb, Lennard-Jones, etc., can also be realised in colloidal systems.

Colloids comprise not only hard particles but also soft self-assemblies, including micelles, vesicles, emulsions and so forth. This also brings them in close similarity with biological assemblies, such as globular proteins, cellular organelles and eventually whole cells. As an example, interactions and dynamics of dispersions of globular proteins, improperly named as "solutions", are satisfactorily described by models of interacting colloids. The investigation of such systems also leads to the realisation of the so-called "patchy-particles" with inhomogeneous interactions.

An important feature of colloids is their dynamics. Common solid/liquid colloidal suspensions undergo Brownian motion, which has been the subject of a large number of investigation, most notably the work of eminent scientists, such as Einstein, Perin, Smoluchowski and so on. Such systems exhibiting Brownian motion are nowadays called "passive" colloids. In con-

strat, *active colloids* define a novel class of particles displaying self-propulsion phenomena, in addition to Brownian motion, as they posses a *chemical engine* [7]. Active systems usually exhibit an enhanced diffusion characterised by a ballistic component in contrast to the pure random-walk of their passive equivalents. Moreover, such systems can present very fascinating collective behaviour reminiscent of a flock of birds, schools of fish, a swarm of insects and so forth [8–13]. Practical instances of active systems are commonly found in nature. Many living microorganisms make use of self-propulsion mechanisms to effectively achieve their fundamental needs, such as food harvesting and survival. Among them there is the bacterium *Escherichia coli*, which, for example, move by chemotaxis following a chemical gradient [14].

As the nature is currently a source of inspiration for scientific development, artificial swimmers have been synthesised, named *Janus*, which can exhibit active motion in appropriate conditions and mimic the motility of active cells. The name Janus was used for the first time by de Gennes during his Nobel lecture. He used this term to describe a colloid whose surface is characterised by two distinct areas with different physico-chemical properties [15]. The name comes from Roman mythology, where Janus (*Ianus* in Latin) was the god of the transitions and was often represented with two, opposed faces. Although de Gennes was referring to amphiphilic colloids in that speech, the asymmetric composition of Janus particles is the key to achieve self-propulsion when they are dispersed in a suitable suspension medium.

The focus of this thesis is on the interplay between interparticle interactions and dynamics, in particular on how specific effective interactions and microstructure may affect colloid motions in active systems. Effective interactions are pivotal in passive systems while they are not deeply probed in active dispersions as the dynamics of Janus colloids are based on the asymmetry of the interactions with the suspension medium. Experiments were primarily performed using synchrotron techniques such as (Ultra) Small-Angle X-ray Scattering (USAXS/SAXS) and multi-speckle X-ray Photon Correlation Spectroscopy (XPCS) at the Time-Resolved Ultra-Small-Angle X-ray Scattering (TRUSAXS) beamline ID02, at the ESRF – The European Synchrotron. A recent upgrade (2014) [16] made possible to perform USAXS measurements reaching a magnitude of scattering vector $q_{min} \sim 10^{-3}\ nm^{-1}$ and, accordingly, to probe micron-scale sizes. In addition, multi-speckle XPCS, done on this USAXS-range, permits the measurements of the dynamics of sub-micron colloids in suspensions of media with water-like viscosity. USAXS and XPCS measurements allow one to simultaneously obtain information about static interactions and dynamics and, then, to analyse a possible connection between them.

1.1. Passive Colloidal Dispersions

According to the definition of the International Union of Pure and Applied Chemistry, colloids consist of mesoscopic entities of sizes from 1 nm to 1 μm (dispersed phase) distributed throughout a dispersion medium that could be a liquid, solid or gas [17].

Table 1.1.: Technical names of colloidal systems in various combinations of dispersed phase and medium [17].

Dispersed phase	Dispersion medium	Definition	Example
Solid	Gas	Aerosol	Smoke
Liquid	Gas	Aerosol	Fog
Solid	Liquid	Sol / Dispersion	Coffee, Paints
Liquid	Liquid	Emulsion	Mayonnaise
Gas	Liquid	Foam	Whipped cream
Solid	Solid	Solid dispersion	Stained glasses
Liquid	Solid	Solid emulsion	Ice cream
Gas	Solid	Solid foam	Pumice

Colloidal systems of interest in this work are model solid/liquid dispersions, or suspensions, involving particles of uniform size, either in the micron or sub-micron scale, dispersed in water-based solvents. Whether colloids are active or not, the physical bases that govern their interactions and dynamics are the same, therefore knowledge of "passive" colloids is a prerequisite for understanding active colloidal systems.

1.1.1. Brownian Motion

Particles dispersed in a liquid solvent are subjected to fluctuation in position due to collisions with molecules of the dispersion medium. This is the basis of *Brownian motion*, which links together phenomena occurring in the macroscopic and microscopic scales, respectively due to the viscosity and the discrete nature of the fluid.

If interparticle interactions are negligible, equations of motion in one dimension are expressed as the following (Langevin equations) [18]:

$$m\frac{dv(t)}{dt} = -\gamma_f v(t) + \Lambda(t) \tag{1.1}$$

$$\frac{dr(t)}{dt} = v(t) \tag{1.2}$$

where m, $r(t)$ and $v(t)$ are particle mass, position and velocity, γ_f is the friction coefficient related to the viscosity of the medium in laminar flow and $\Lambda(t)$ is a stochastic force (Langevin force) which accounts for random collisions with solvent molecules [19]. It can be assumed that the stochastic variable $\Lambda(t)$ is a Gaussian white noise, therefore its mean value, among all

the random realisations, is $\langle \Lambda(t) \rangle_\Lambda = 0$ and the correlation between two instantaneous events is $\langle \Lambda(t_1)\Lambda(t_2) \rangle_\Lambda = a\delta(t_1 - t_2)$, where a is the amplitude of the noise and $\delta(t)$ is the Dirac delta-function.

By solving the Langevin equations, imposing that these "Brownian" particles are in thermal equilibrium with the medium and that the motion is a stationary process, the mean square displacement (MSD), $\langle \Delta r(t)^2 \rangle$, becomes:

$$\langle \Delta r(t)^2 \rangle = \langle [r(t) - r(0)]^2 \rangle_{\Lambda,T} = \frac{(2d_s)k_B T}{\gamma_f} \left[t - \frac{m}{\gamma_f} \left(1 - e^{-(\gamma_f/m)t} \right) \right] \quad , \quad a = (2d_s)\gamma_f k_B T \tag{1.3}$$

where the mean $\langle \cdots \rangle_{\Lambda,T}$ involves both white noise and thermal ensemble averages, the starting condition $\langle r(0) \rangle_T = 0$ was used, k_B is the Boltzmann constant and T is the absolute temperature. d_s is the number of spatial dimensions which originates from the equipartition theorem as, without loss of generality, this solution can be also applied to two and three dimensions ($d_s = 2$ and 3). The MSD also represents the variance of a Gaussian distribution describing the magnitude of the displacement vectors, whose mean value is $\langle r(t) \rangle_{\Lambda,T} = 0$. When viscous forces dominate over inertial ones, $\gamma_f \gg m$, or for long times, $t \to +\infty$, the MSD has a linear dependence on time:

$$\langle \Delta r(t)^2 \rangle = (2d_s)Dt \tag{1.4}$$

where the proportionality term, D, is the *diffusion coefficient* [19, 20], which is linked to the thermal energy and friction coefficient by the Einstein-Smoluchowski relation:

$$D = \frac{k_B T}{\gamma_f} \tag{1.5}$$

The friction coefficient, γ_f, can be determined by the conditions of the fluid and by the geometry of the Brownian particle. A spherical object moving in a viscous fluid in laminar flow is conditioned by a Stokes friction coefficient, $\gamma_f = 6\pi\eta R_H$, where η is the (shear) viscosity of the medium and R_H is the hydrodynamic radius of the particle, which takes into account fluid deformations induced by the diffusing object. Finally the diffusion coefficient of spherical colloids undergoing Brownian motion is described by the Stokes-Einstein equation [21]:

$$D = \frac{k_B T}{6\pi\eta R_H} \tag{1.6}$$

The diffusion coefficient, D, refers to translational motion and, as a macromolecule possesses rotational degrees of freedom, in analogy, a similar procedure can be applied to fluctuations of a particle orientation. In the case of a sphere, it leads to the rotational diffusion coefficient, D_r:

$$D_r = \tau_r^{-1} = \frac{k_B T}{8\pi\eta R^3} \tag{1.7}$$

where τ_r is the characteristic time scale of rotation fluctuations.

1.1.2. Effective Interactions and Colloidal Stability

Brownian colloids, in the long time range, can probe the entire available space and go in close contact among them. If attractive interparticle interactions are present, colloids may form aggregate and, possibly, flocculate. Unfortunately, attractive forces between colloids are always present because of the van der Waals potential U_{vdW} (dispersion forces). This latter decays as $U_{vdW}(r) \propto -r^{-6}$ for molecular dipoles, but becomes long-ranged for macroscopic objects, as it scales as $U_{vdW}(r) \propto -A_H(r-\sigma)^{-1}$, where σ is the colloid diameter (for spheres) and A_H is the Hamaker constant which depends of the material of the colloid and on the dispersion medium [17, 22].

A colloidal suspension is called *stable* when aggregation is prevented and single colloids are dispersed as individual objects. The stability of a colloidal system depends on interparticle and solvent/colloid interactions, which can be tuned by knowing their physical or chemical origins.

Commonly used stabilisation is achieved by electrostatic repulsion of colloids having sufficient surface charge. Such an object can be considered as a macroion generating an electric field that attracts available counterions present in the dispersion medium (for example, in a water-based solvent). These counterions form a cloud that surrounds the colloid and screens its actual charge, bringing about a reduction of the intensity and of the range of the interparticle Coulomb repulsion U_C, which, according to the Derjaguin-Landau-Verwey-Overbeek (DLVO) expression, is proportional to $U_C(r) \propto \exp[\kappa(r-\sigma)]r^{-1}$, where κ is the inverse Debye screening length (accordingly to the Poisson-Boltzmann equation of the electrostatic potential for a system in thermodynamic equilibrium [17]) that is a measures of the extension of the diffuse layer of counterions.

When an electric field is applied, a charged colloid, along with its counterion cloud, moves accordingly to the external potential. This motion causes a deformation of the external region of the diffuse layer whilst the counterions closer to the colloid surface remain in their positions. The separation between these two areas is called "slipping plane". This behaviour (electrophoresis) permits to measure the ζ-potential, which is the Coulomb screened potential calculated from $r \to \infty$ to the slipping plane. Note that it is not equivalent to $U_C(\sigma)$, which represents the potential from infinite to the colloid surface. $U_C(\sigma)$ and ζ describe the same potential but calculated at two different distances r, and their relation depends on specific properties of the system, including the extension of the slipping plane. However, ζ-potential measurements

provide a direct observation of the stability of a colloidal suspension, where the balance of the effective interaction potential $U(r) = U_{vdW}(r) + U_C(r)$ decides whether colloids are stable or unstable. An example of charge-stabilised colloids is given by either Stöber silica spheres [23], citrate-stabilised gold colloids suspended in water [24] and polyballs (polystyrene spheres suspended in water).

Another method to avoid aggregation in colloidal suspensions is by *steric stabilisation* [5,22]. Dispersion forces are delimited by an excluded volume interaction due to the presence of self-avoiding-polymers attached on colloid surfaces. Specifically, the close contact between colloids with adsorbed or chemically grafted flexible polymers on their surfaces is precluded by the presence of chains which do not overlap in a good solvent. Therefore, dispersion forces between colloids are, in fact, hindered by interactions between the chains which cover the colloids. An example of such a steric stabilisation consists on stearyl-grafted silica colloids suspended in n-dodecane. This system is stable at high temperatures (good solvent) and present short-range attractive interactions at lower temperatures (poor solvent) as the stearyl alcohol molecules collapse and interact among them [25].

A last example of interactions between colloids are *depletion forces* [22, 26]. Consider a mixture of large and small spheres, with diameter σ_1 and σ_2 respectively, that interact via a hard-sphere potential, i.e. an approximation in which rigid, non-penetrable spheres only interact via a repulsive interaction at the contact $r \leq \sigma_i$. In the equivalent case of non-interacting point-like particles, the highest entropy is reached by maximising the free volume available for each colloid, corresponding to a homogeneous dispersion. The same principle is valid in the case of spheres, however, when two large particles are close, with a distance $(r - \sigma_1) < \sigma_2$, small colloids cannot occupy the volume between large spheres. This simple consideration brings to the definition of a depletion layer of thickness $\sigma_2/2$ around large colloids, which defines the effective unavailable volume for small particles. When large colloids are close to each other and depletion layers are overlapping, the sum of depletion volumes is lower and, consequently, the free volume available for small spheres is higher with respect to situations with homogeneously dispersed large colloids. This situation is entropically favoured, therefore, in order to reduce the unavailable volume for smaller particles, the large ones come together resulting in an effective attraction [27].

Interactions in passive, traditional colloidal systems are pivotal to understand the physics of active systems. In real many-component systems, interparticle interactions may result from various contributions and they define the microstructure, i.e. the structural arrangement or the specific spatial-distribution of colloids. The concept of *effective* interaction accounts for the balance of all contributions, it helps to simplify observed phenomena and provides a direct link with experiments.

1.2. Active Colloids

The motility of natural swimmers, from the bacterium *E. coli* to spermatozoa, has been studied in the last 50 years [14, 28, 29]. Nevertheless, the interest on active systems began later with the simulation reported by Vicsek et al. [1]. They reported collective motions of self-driven particles which, for the first time, were associated to non-equilibrium dynamics. This simulation consisted on self-propelled particles able to re-orient each time-step following the average orientation of the first neighbours. By tuning the particle density and a noise-parameter, that represented the possibility of making "mistakes" in the re-orientation process (temperature-like effect), Vicsek and co-workers found that such a system was able to exhibit different behaviour, from a gas-like phase with independent motions to collective dynamics of groups of particles, evocative of flocks of birds. Vicsek's model is simple and leads to as much intuitive results, real systems, instead, are much more complex and may bring to unexpected results.

There are several mechanisms of self-propulsion in active colloidal suspensions. For example, a conceptual division exists between living and artificial swimmers. The movement of motile cells is called taxis, they are sensitive to specific external conditions and possess a metabolism that permits to move either towards adequate locations or away from a dangerous environment. *E. coli* taxes include chemotaxis [30] and thermotaxis [31], which respectively make them sensitive to chemical and temperature gradients, practically they are able to "sense" the environment and direct towards food-rich and warm areas. Other examples are aerotaxis (toward oxygen), phototaxis (toward light), magnetotaxis (according to a magnetic field) and so forth.

In the case of artificial active colloids, primarily of type Janus, the propulsion is achieved by a self-generated phoretic process. A more ordinary motion of colloids, the phoresis, is obtained by applying an external field (electrophoresis), a concentration (diffusiophoresis) or a temperature (thermophoresis) gradient. The key to achieve self-propulsion is to find the right combination of Janus-colloid configuration and suspension medium. When a colloid is able to locally generate its own gradient (or field) by catalytic reactions [32–36], it moves according to phoretic mechanisms, as, in its frame of reference, local gradients are perceived as external ones. An example of such active behaviour, reported by Howse and co-workers [35], consists in the use of micron-sized polystyrene beads coated by a thin layer of platinum only on one hemisphere, dispersed in a solution of hydrogen peroxide: H_2O_2 decomposition is catalysed by the platinum face of the colloids whereas the polystyrene face is inert with respect to this reaction. As the decomposition occurs only on a specific side, the colloid itself is able to create a gradient of molecular oxygen that trigger *self*-diffusiophoretic motions. Indeed, as an alternative, Buttinoni et al. [37–39] reported a method to induce self-diffusiophoresis by exploiting the unbalanced interactions in a binary mixture of 2,6-lutidine/H_2O near to the Lower Critical Solution Temper-

ature (LCST), above which it separates into a lutidine-rich and a water-rich phase [3, 40]. The idea consisted of using green laser light to selectively heat the gold hemisphere of a silica/gold Janus colloid via its plasmonic absorption band. When the increased temperature, diffused from the colloid to the medium, reaches above the separation temperature, a phase separation occurs locally on the gold side of the colloid and trigger the self-diffusiophoretic motion. In that case, colloids moved away from the lutidine-rich phase but, depending on the functionalisation of gold caps with either hydrophilic or hydrophobic groups, the gold side was oriented inside or outside the lutidine-rich phase.

Janus colloids are a subset of a broader class of "patchy" particles, i.e. objects with loci specifically modified in term of shape or surface chemistry, which are a subject of interest in the field of nanotechnology due to their peculiar properties of self-assembly and the aim to obtain programmable, tailored self-organisation in the nanometre scale. The attention is then focused on the synthesis of such particles, including Janus colloids, and a number of procedure, from bulk to surface chemistry, have been reported [41–43].

1.2.1. Enhanced Diffusion

Active colloids, such as Janus particles in catalytic or phase-separating media, display a self-propulsion characterised by enhanced MSD values [35, 37]. Such systems, consisting of dilute micron-sized spherical colloids, have been primarily studied by microscopic observations in 2D geometries and can be modelled including a ballistic contribution, via an average constant velocity, $\langle v \rangle$, coupled to the common Brownian translational, D, and rotational, τ_r, diffusion of particles in passive conditions [35]. As opposed to dilute passive systems, where the short- and long-time diffusion terms are the same, the active behaviour is characterised by two regimes shown in Figure 1.1. For short-time, within a range defined by the rotational diffusion $t \ll \tau_r$, the propulsive mechanism results in a MSD proportional to time squared, $\langle \Delta r^2(t) \rangle \propto t^2$. For $t \gg \tau_r$, instead, MSDs are function of both passive diffusion, D, and ballistic velocity, $\langle v \rangle$, and are linear with time, $\langle \Delta r^2(t) \rangle \propto t$. Therefore, in the long-time range, active colloids exhibit a Brownian-like diffusive behaviour, represented by an enhanced, *effective* diffusion coefficient D_{eff}.

Time dependencies of MSDs in systems displaying anomalous diffusion have also been analytically investigated [44] as well as their probability distribution functions (PDF) [45], which displayed a non-Gaussian description as compared to the classic Brownian diffusion.

Although the behaviour of the MSD in the case of self-propulsion is systematically observed in the experiments, the precise physico-chemical mechanisms is still under debate. The initial model of a neutral self-diffusiophoresis [35, 46], for the propulsion of metal half-coated Janus colloids in H_2O_2 solutions, is not longer a sufficient description of the system, as new

observations shown how self-induced electrophoresis must be taken into account [34, 47, 48].

Differences in the short- and long-time dynamics are also attributed to hydrodynamics effects. Thorneywork and co-workers [49] reported a comparison between experiments and simulations of self-propelled particles in a quasi-2D configuration, showing that in the long-time range hydrodynamic interactions can be considered absent, whereas they have a strong influence in the short-time self-diffusion coefficient which varies with the colloidal concentration.

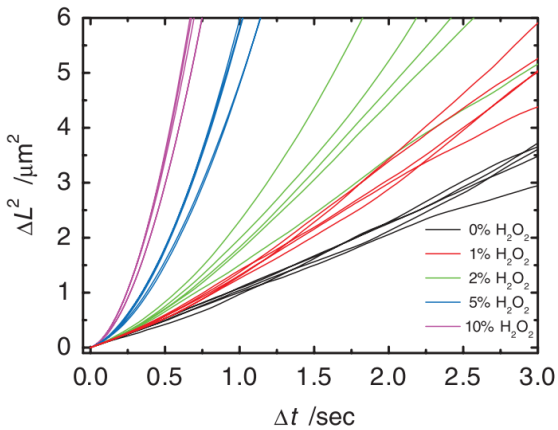

Figure 1.1.: MSDs as a function of time at different H_2O_2 concentrations. Reproduced from Ref. [35] (DOI: 10.1103/PhysRevLett.99.048102) with permission from The American Physical Society.

1.2.2. Collective Motions and Dynamic Clustering

The enhanced diffusion and ballistic motion are features of the individual active particle and are observable in dilute dispersions. For more concentrated systems, where interparticle or hydrodynamic interactions are no longer negligible, colloid dynamics are responsible for collective behaviour characteristic of active systems.

Coordinate motions have been observed in motile *Bacillus Subtilis* [50–52] and gliding *Myxococcus xanthus* systems [53], forming jets and whirls generated by long-range hydrodynamic interactions and short-range collisions.

The collective behaviour found in suspensions of elongated bacterial is not visible in systems consisting of spherical Janus colloids. The propulsion parallel to the body-axis could be a cause of coordination, whilst colloids that lack orientation do not shows collective, ordered dynamics. However, living bacteria and synthetic Janus systems exhibit a common behaviour, the *dynamic clustering*, as it was reported by Theurkauff et al. [2]. They presented an investigation on half-coated gold/platinum Janus colloids suspended in a H_2O_2 solutions that, depending on particle velocity and concentration, displayed a cluster formation characterised by a dynamic change of shape and size (see Fig. 1.2).

This behaviour has been further investigated and simulated velocity/concentration phase diagrams have been presented [54]. Active systems [2] show a phase transition from a gas-like state with self-propelled particles to a cluster phase (see Fig. 1.3) with high concentration fluctuation due to the dynamic variation of the particle numbers forming clusters.

Theurkauff and co-workers suggested that the clustering is induced by an effective interparticle interactions resulting from concentration monopoles generated aside colloids which, in turn,

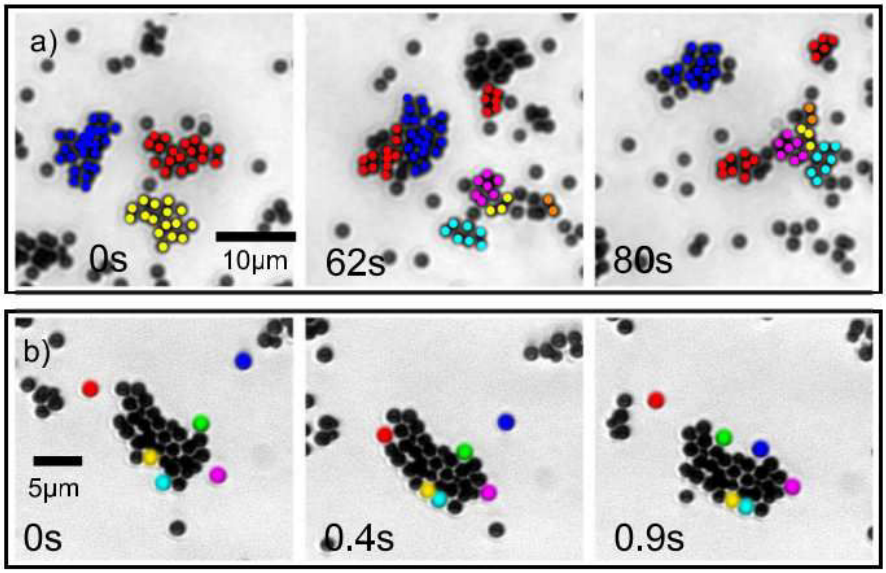

Figure 1.2.: Dynamic clustering evolution monitored at different times. The colour map is maintained in both raw (a) and (b) in order to show the current colloid dynamics. Reproduced from Ref. [2] (DOI: 10.1103/PhysRevLett.108.268303) with permission from The American Physical Society.

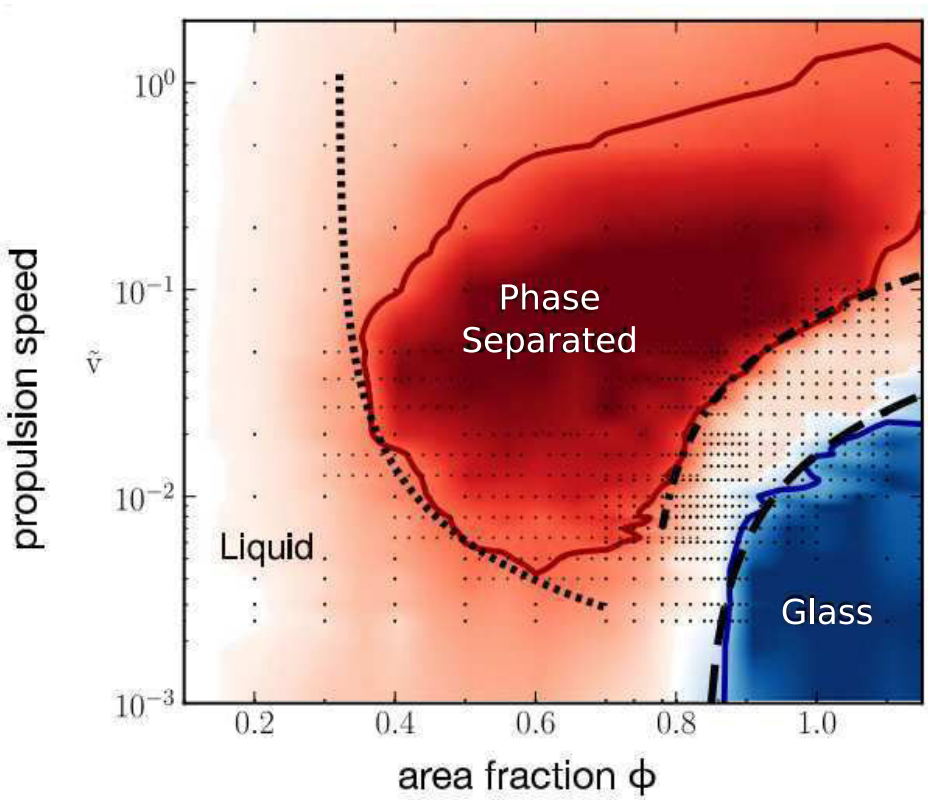

Figure 1.3.: Numerical velocity/concentration phase diagram of active particles. Dashed lines represent boundaries of the clustering phase and the red scale indicates the concentration fluctuation due to dynamics. Reproduced from Ref. [54] (DOI: 10.1016/j.jnoncrysol.2014.08.011) with permission from Elsevier.

create concentration gradients [2]. This hypothesis was also deepened by Pohl and Stark [55], who associated the concentration monopole to the secretion of bacteria moving by chemotaxis. They modelled the dynamic clustering in terms of effective *phoretic* interactions related to active translation and rotation and included the "chemotactic" collapse (the formation of a single non-dynamic cluster) observed in bacterial colonies [53, 55].

Another analogy between Janus particles and living microorganisms was introduced by Cates and Tailleur [56]. They reported how the motility-induced phase-separation in both active Brownian (fixed velocity and slow rotational diffusion) and "run and tumble" particles (fixed velocity and sudden re-orientation) can be described by the same formalism in the long-time regime. However, the model only accounts for the case of a motility independent from the particle body-axis, instance which is instead observed elongated object.

The existence of phase separation and dynamical clustering as a function of propulsion speed and particle density is a feature in model active systems and seems to be caused by motility-induced, effective, interparticle interactions in both two- and three-dimensional configuration [57, 58]. An example of such interactions was shown by Soto and Golestanian [59], who reported a theoretical study of the self-assembly in a system involving two kind of symmetric active particles, where the interparticle interactions are induced by concentration gradient. In such a system, where a hetero-dimer represents a Janus-particle model, each self-assembled oligomer was either inert or motile depending on its geometry and particle distribution.

Effective interparticle interactions — either motility-induced or due to the concentration gradient — seem to rule over the intrinsic interaction potential between active particles, such as Coulomb and dispersion forces. Phase separation phenomena were observed in different simulations, including particles having a base short-range repulsion [54], attraction [60] or even accounting for hydrodynamic interactions [61]. Although the dynamical clustering appears to be a general behaviour in these systems, the specific features of phase diagrams in these works varied accordingly to the respective "passive" interparticle interactions.

1.2.3. Active Media

Suspensions of passive colloids in active bath are of great interest to the investigation of effective interactions induced by the activity. An example of such a system which mimics natural behaviour, is a simulation of the chasing dynamics of a group of predators (active) and prey (passive) carried out by Angelani [62], in which relative concentrations and interactions have a great impact on hunt and escape strategies.

Experiments and simulations involving *E. coli* bacteria have been performed with the aim of study the dynamics of passive, micron-sized tracers suspended in such a motile active bath [63–66]. In this cases, passive colloids displayed enhanced diffusion coefficients with a time

dependence of MSD similar to active particles, with a quadratic trend in the short-time range turning to a linear behaviour in later stages. In these reports the long-time enhanced diffusion of passive colloids linearly depends with the bacterial concentration and seems generated by far-field hydrodynamic interactions. An *E. coli* swimmer creates a hydrodynamic flow-field which has a dipole pattern that decay in the long-range proportional to $\propto r^{-2}$ [64, 67, 68]. Passive tracers are "pushed" by the dipole field as they are more and more involved and the bacterial concentration increase due the higher influenced volume. However, when dipole fields start interacting and coordinate bacterial motions arise, tracer dynamics change accordingly to the collective behaviour [64]. Such deformations of hydrodynamic flow-field cause also swimmers moving along a surface [64, 67], but, in the case of high volume fractions interested by bacteria and collective motion, this behaviour is lost.

The use of passive tracers was applied to measure the *effective temperature* in active systems [69, 70]. As the temperature is defined by the average kinetic energy on the atomic scale, in the macroscopic length scale an active colloidal suspension displays dynamics which can be related to an increased temperature effect. Such concept was investigated by Palacci and co-workers [71] and Ginot and co-workers [72] who reported sedimentation density-profiles of active Janus colloids as a function of their swimming activity and showed that such profiles could be associated to the sedimentation behaviour of passive particles at higher temperatures. Ni and co-workers [73] simulated glassy systems of hard spheres doped with active colloids which promoted crystallisation as a function of the activity, similar to an enhanced temperature effect in probing the free energy landscape.

1.3. Aims of the Thesis

As a first active system, the structure and motility of *E. coli* bacteria were investigated. *E. coli* is a model gram-negative bacterium whose morphology has been studied over the last 60 years [74] using different techniques including optical microscopy, light scattering [75] and atomic force microscopy [76]. All the structural features in the nanometre scale, that are not visible by optical microscopy, define the *ultrastructure* which so far has been investigated by means of Transmission Electron Microscopy (TEM) [77–80]. By exploiting the wide (almost four orders of magnitude) scattering vector q-range available by combining USAXS and SAXS measurements, in **Chapter 3** the derivation of a multi-scale structural model of these bacteria is presented. The cell description spans from the overall geometry of *E. coli* down to nanometric sizes, providing a micron-sized scattering model that can be used for USAXS experiments with active systems and, at the same time, an alternative tool for the investigation of the ultrastructure. The arrangement of the cell-envelope, was modelled combining SAXS and contrast-variation

Small-Angle Neutron Scattering (SANS) at three match points and the full contrast that, finally, allowed the determination of the membrane electron-density and the inter-membrane distances on a quantitative scale.

These bacteria were then used as active component in a mixture with sub-micron-sized passive silica colloids. Such passive/active mixtures, including *E. coli* suspensions, are of particular interest in the context of statistical physics of active systems, as they offer the possibility of probing the influence of the anomalous dynamics on passive colloids. Angelani and co-workers [81] reported both simulations and experiments on passive colloidal systems in an active bath of *E. coli*, where passive colloids experience a mobility-induced attractive interaction reminiscent of depletion forces. Besides changes in the effective interactions, variations in dynamics have been found independently by Wu et al. [63] and Jepson et al. [65], who reported an enhanced diffusion coefficient of passive micron-sized colloids due to the *E. coli* swimming. In **Chapter 4**, an investigation by USAXS and XPCS of the effective interactions and dynamics of such an active/passive system are presented. As opposed to those previous reports, the aim here is to study how the motility of active bacteria affects the interactions and the dynamics of *crowded* passive colloids of sub-micron sizes, varying the colloidal and bacterial concentrations and tuning the interparticles interactions. The objective is to investigate the physics of active/passive concentrated dispersions which are closer to physiological, crowded conditions.

In **Chapter 5**, systems of sub-micron sized silica colloids (used as a reference) and half-coated silica/nickel Janus colloids suspended in a mixture of 3-methylpyridine (3MP) and water/heavy water undergoing liquid-liquid phase separation were investigated using USAXS and XPCS. Due to the preferential wetting of 3MP on the silica surface [40], colloids displayed phoretic motion, which is strongly correlated to the dynamics of phase separation, mimicking active dynamics which last for a few minutes. In particular, silica colloids exhibited advective motion with enhanced diffusion toward the 3MP-rich phase, reminiscent of self-propelled dynamics, until the phase separation was completed. Suspensions of Janus colloids, instead, showed a much richer picture. As opposed to the partitioning into the 3MP-rich phase in the case of silica colloids, Janus particles behave like surfactants at the 3MP/water interface. These dynamics are strongly affected by the asymmetric interactions with the solvent as they were either enhanced or suppressed depending on the 3MP concentration, which, concurrently, affected the microstructure of the system, exhibiting dynamic clustering.

2. Synchrotron and Neutron Scattering Methods

Small angle scattering (SAS) techniques are well-established for probing soft matter systems including colloids, polymers, glasses and biological macromolecules. SAS is a non-invasive technique which permits to gather precise structural information over a wide range of space-scale, from the radius of gyration of micron-sized particles down to their nanostructures.

In particular, SAXS instruments available at modern synchrotron facilities, providing high photon flux and degree of coherence, are powerful tools for the structural investigation of soft matter systems, allowing high space and time resolutions, the use of small sample volumes and the possibility to perform experiments down to the millisecond range even with weak-scattering samples [82, 83].

2.1. Small Angle Scattering

Basic principles are common to X-ray, neutron and light scattering and rather independent from the incident beam wavelength, λ, whose order of magnitude should be comparable to the smallest length scale to probe. In the following, the attention is focused on synchrotron SAXS and a small introduction to the main differences with respect to SANS will be provided [84–86].

A coherent, monochromatic, planar electromagnetic wave of wave vector $\mathbf{k}_i$, with $|\mathbf{k}_i| = \frac{2\pi}{\lambda}$ which interacts with the electrons of in the sample medium, generates a secondary, spherical wave — in the far-filed approximation — with wave vector $|\mathbf{k}_s| = |\mathbf{k}_i|$ as the scattering event is completely elastic due to the high energy of the X-ray beam compared to typical excitations in the sample. The scattering vector definition is $\mathbf{q} = \mathbf{k}_s - \mathbf{k}_i$ and is magnitude is expressed as:

$$|\mathbf{q}| = q = \frac{4\pi}{\lambda} \sin\left(\frac{\theta}{2}\right) \tag{2.1}$$

where λ is the wavelength of the incident and scattered photons and θ is the scattering angle, as illustrated in Figure 2.1. The scattering vector $\mathbf{q}$ is a quantity defined in the reciprocal space and, as an approximation, is related to the real space by the relation $l \sim \frac{2\pi}{q}$. Therefore, a q-range

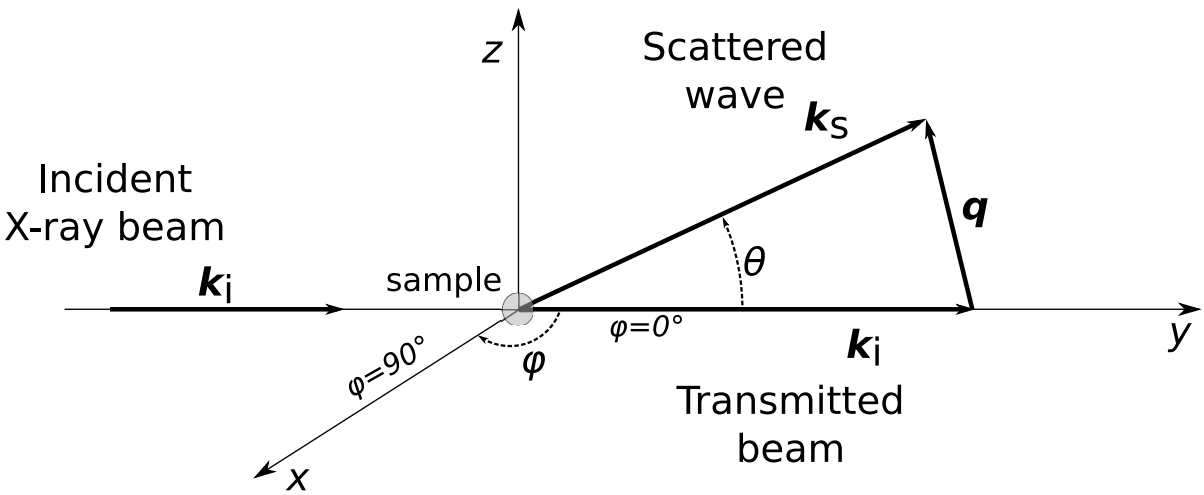

Figure 2.1.: Schematic illustration of SAS. The incident beam (wave vector $\mathbf{k}_i$), arriving on the sample, generates a scattered wave (wave vector $\mathbf{k}_s$) with $|\mathbf{k}_i| = |\mathbf{k}_s|$ at a scattering angle θ.

of 0.001 to 10 nm^{-1} can provide structural information over a broad length-scale from around 0.6 to 6000 nm.

2.1.1. Small Angle X-ray Scattering

When a coherent and monochromatic (λ) electromagnetic wave (**E** and **H**) interacts with a free electron, this is accelerated and, oscillating accordingly with the electric field, generate a dipole electric field at the same frequency $\nu = c/\lambda$ of the incident photons which do not lose energy (*elastic scattering*). This is possible if the photon energy is much lower compared to the rest energy of the electron of mass m_e, $h\nu \ll m_e c^2$, and the interaction is known as Thomson scattering [87].

The secondary, generated dipole electric field is approximated to a spherical wave in the far-field limit and, in the case of non-polarised incident beam, the scattering intensity from a single electron, I_e, is given by:

$$I_e = I_i r_e^2 \frac{1+\cos^2(\theta)}{2} \tag{2.2}$$

where I_i is the intensity of the incident beam and r_e is the classic electron radius ($r_e = 2.818 \times 10^{-15}\ m$). Synchrotron radiation is linearly polarised in the horizontal direction (x-axis) and elliptically polarised in the other directions [83]. The scattered intensity for the linear polarisation is then expressed as:

$$I_e = I_i r_e^2 [1 - \sin^2(\theta)\cos^2(\varphi)] \tag{2.3}$$

but for small angles θ there are little differences in the final scattered intensity between polarised

and non-polarised electromagnetic wave.

In the case of interaction with the electron cloud of an atom, the Thomson scattering limits are still fulfilled and the coherent scattered intensity is given by:

$$I_{tot} = f^2 I_e \tag{2.4}$$

where f is the scattering factor which for X-ray scattering is equivalent to the number of electrons Z, except for energies close to the absorption edge of a specific element. The product $f r_e$ is the scattering density, b.

The scattering cross-section, σ, which results from the ratio of the scattered to incident energy of the electromagnetic wave obtained via the Poynting's theorem. The differential scattering cross-section per unit of solid angle Ω, $\mathrm{d}\sigma/\mathrm{d}\Omega$, contains all the information about the interaction with the scattering objects. The quantity $\mathrm{d}\sigma/\mathrm{d}\Omega$ is proportional to the scattering intensity, I_S, acquired by a two-dimensional detector, normal to the incident beam direction:

$$I_S = I_0 T_r \varepsilon_d W A_b \Delta\Omega \frac{\mathrm{d}\Sigma}{\mathrm{d}\Omega} \tag{2.5}$$

where I_0 is the incident photon intensity per unit time per unit area, T_r is the transmission coefficient due to the sample absorption, ε_d is the detector efficiency, W is the sample path length, A_b is the cross section of the beam and $\mathrm{d}\Sigma/\mathrm{d}\Omega$ is the total differential scattering cross-section per unite volume.

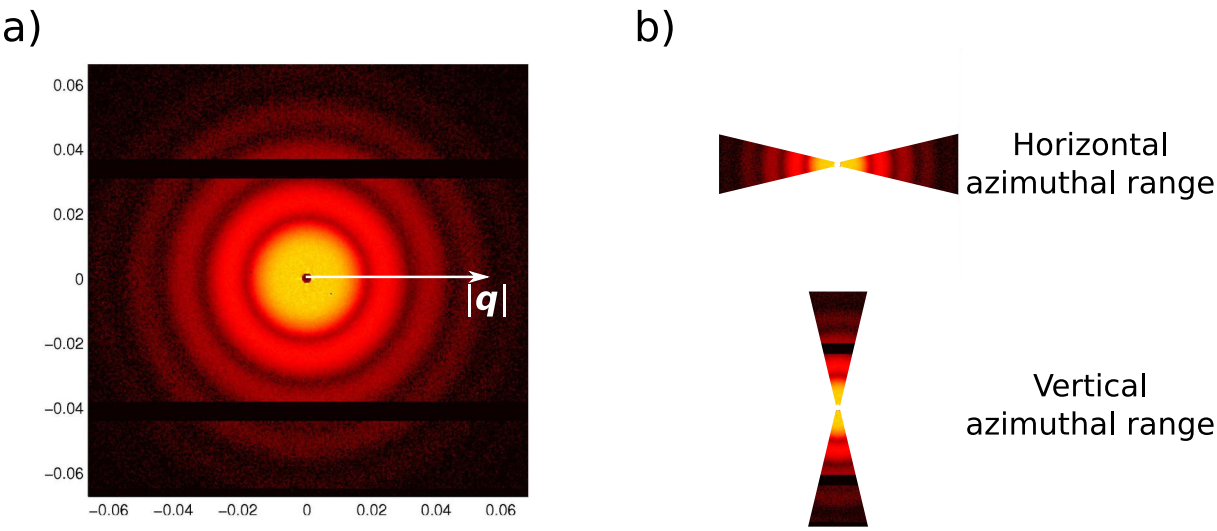

Figure 2.2.: a) 2D scattering pattern acquired on a Pilatus 300k detector from a suspension of concentrated spherical silica colloids. Tics represent the magnitude of the scattering vector $|q|$ from the centre of the image in nm^{-1}. The colour scale displays the scattering intensity. b) Examples of partial azimuthal integration, only accounting for partial azimuthal sections of the 2D scattering pattern.

In the case of isotropic scattering, $I_S(q)$ is calculated from an azimuthal averaging over the

two-dimensional scattering pattern recorded on the detector, as shown in Figure 2.2(a), and the 1D scattering curve is obtained as a function of $|\mathbf{q}|$. A correct normalisation of the the detected signal permit to obtain the real $\mathrm{d}\Sigma/\mathrm{d}\Omega$ which, hereafter, will be denoted as $I(q)$.

For anisotropic scattering, the intensity distribution for a given q along the azimuthal angle, φ, becomes asymmetric. In this case, the integration range will be limited to the azimuthal range $\Delta\varphi$ covering the appropriate orientation distribution. In Figure 2.2(b), an example of angular sections of a scattering pattern are shown, displaying partial vertical and horizontal region of the detector area.

2.1.2. Scattering Form Factor

Consider a dilute system consisting of N objects where each electron is subjected to a single scattering event per photon (*single scattering approximation*). In this case, interparticle interactions can be neglected and scattering intensity $I(q)$ is formulated as:

$$I(q) = \frac{N}{V_S}|A(q)|^2 \tag{2.6}$$

where $V_S = WA_b$ is the scattering volume, i.e. the portion of sample illuminated by the incident beam, and $A(q)$ is the scattering amplitude, which accounts for the coherent sum from all the scattering events occurring within a single object:

$$A(q) = \sum_{i=1}^{M} b_i e^{i\mathbf{q}\cdot\mathbf{r_i}} \quad \rightarrow \quad A(q) = \int_V \rho(\mathbf{r}) e^{i\mathbf{q}\cdot\mathbf{r}}\,\mathrm{d}V \tag{2.7}$$

where M is number of atoms i constituting the single particle and b_i and r_i respectively are their scattering length and relative position. In SAXS, the discrete sum can be approximated to a integral assuming a continuous distribution of the scattering length density (SLD), $\rho(\mathbf{r})$, which takes into account the relative distribution of b_i per unit volume. The single scattering approximation is fundamental for the definition of Equation 2.7, as *multiple scattering* events require a more complex dissertation [88]. The scattering amplitude is sensitive to variations in SLD within the scattering volume, the relevant quantity is then the contrast length density $\Delta\rho(\mathbf{r}) = \rho(\mathbf{r}) - \rho_M$, where ρ_M is the average, homogeneous SLD of the dispersion medium of the object of interest. Finally, assuming that the particle is isotropic, the integral in Eq. 2.7 can be transformed in spherical coordinates and reduced to a one dimensional expression [84]:

$$A(q) = 4\pi \int_0^{+\infty} \Delta\rho(\mathbf{r}) \frac{\sin(qr)}{qr}\,\mathrm{d}r \tag{2.8}$$

In the case of a monodisperse suspension of spherical particles of homogeneous SLD, the scattering amplitude is easily solved [85, 86]:

$$A_{sphere}(q,R) = \Delta\rho 4\pi R^3 \frac{\sin(qR) - qR\cos(qR)}{(qR)^3} = \Delta\rho V_{sphere} 3 \frac{\sin(qR) - qR\cos(qR)}{(qR)^3} \tag{2.9}$$

where limit for $q \to 0$ brings about $A(0) \propto \Delta\rho V_{sphere}$. This expression leads to the definition of the *scattering form factor*, $P(q) = |A(q)|^2$, which is directly linked to the differential cross-section via Equation 2.6:

$$I(q) = nP(q) \tag{2.10}$$

where $n = N/V_S$ is the number density of the suspended particles.

One of the drawback of colloids is that they have a finite size distribution, unlike their molecular analogue that are monodisperse. In this case the polydispersity can be modelled by intervening on the form factor. The model requires the knowledge of the specific particle-size distribution $D(R)$, a normalised PDF ($\int_V D(R)\,\mathrm{d}V = 1$), which leads to the expression:

$$I(q,R) = n\langle P(q)\rangle = n\Delta\rho^2 \int_0^{+\infty} P(q,R)D(R)\,\mathrm{d}R \tag{2.11}$$

2.1.3. Core-Shell Models

Scattering form factors from monodisperse suspensions of homogeneous objects can be calculated starting from Equation 2.7 and using appropriate integration volumes and coordinates. For example, the simplest case of isotropic particle beside the sphere is a spherical core-shell configuration consisting of a inner sphere of SLD ρ_c and radius R_c enclosed by an shell with ρ_s and thickness $\Delta R = R_s - R_c$ (see Fig. 2.3).

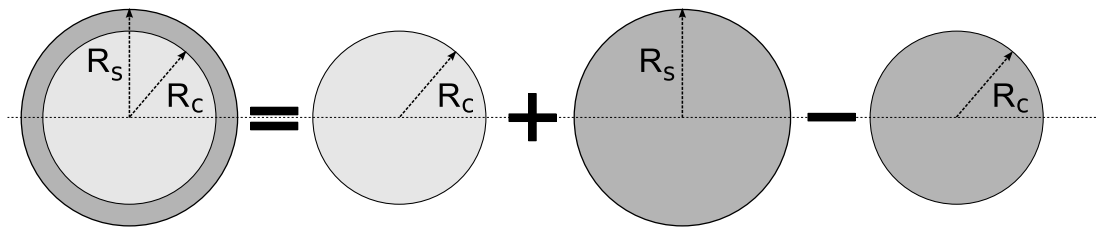

Figure 2.3.: Schematic illustration of the building-up of the core-shell scattering amplitude by summing, separately, the core and shell terms, where the latter is obtained by removing from a sphere ρ_s, R_s the equivalent volume of the core. Different SLDs are represented by light and dark grey, for ρ_c and ρ_s respectively.

The scattering form factor, P_{cs} is expressed by:

$$P_{cs}(q,R) = \left|\Delta\rho_c A(q,R_c) + \Delta\rho_s \left[A(q,R_s) - A(q,R_c)\right]\right|^2 \tag{2.12}$$

where $\Delta\rho_c$ and $\Delta\rho_s$ are the contrast SLD with respect to the dispersion solvent.

Core-shell geometries including one ore more outer layers are often used to model amphiphilic assemblies forming micelles or double-layer vesicles. The latter, moreover, are of particular interest as model systems for cellular membranes and SAXS technique has been a great tool for the structural investigation of model lipid membranes [89–94].

According to the Fluid Mosaic Model for the description of the biological membranes [95], cell membranes, either prokaryotic or eukaryotic, are composed by a phospholipid bilayer including membrane and peripheral proteins. The scientific attention on proteins, which carry out specific biological functions, has been followed by the investigation of the cell membranes, whose function goes beyond being just a scaffold, or an envelope, and actually is very important in inter- and intra-cell dynamics. The *Revised* Fluid Mosaic Model [96] accounts for new discoveries about biological membranes, including, as an example, the presence of lipid and protein rafts, which are domains of the membranes rich in a specific type of lipids, or proteins, that play specific roles as much as functional proteins.

Biological membranes are very complex and dynamic systems. Simple core-shell SAS models, even accounting for more than one layer, are rough approximations of a model lipid systems and hold only for coarse-grained studies. SAXS technique is sensitive for a finer structure of the bilayer matrix, hence more refined and dedicated models are required for the description of SLD profiles in such systems [97–100], as depicted in the sketches in Figure 2.4.

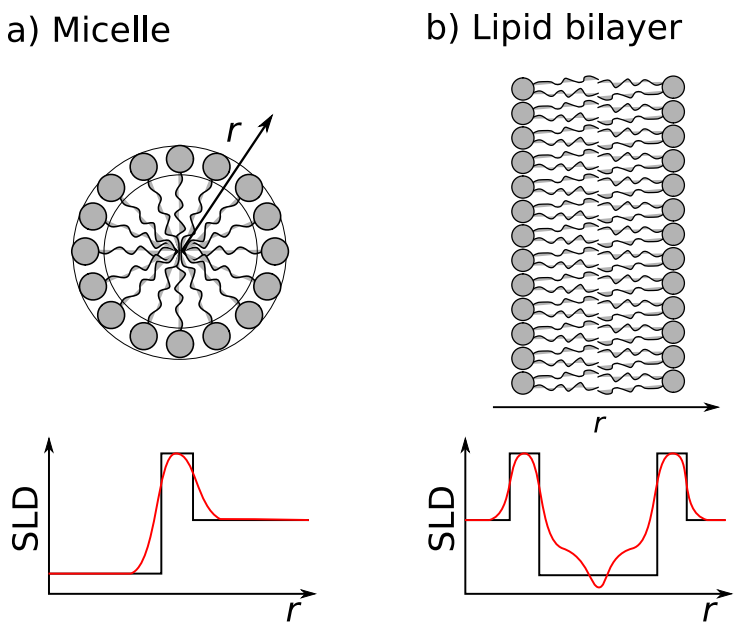

Figure 2.4.: Sketches of SLD profiles for two examples of lipid systems, a) a micelle and b) a lipid bilayer. In the plots, black lines represent the rectangular profiles of the simple core-shell approximation, whereas red lines depict more realistic gaussian SLD profiles $\Delta\rho(r)$.

2.1.4. Asymptotic limits and SLD fluctuations

The scattering amplitude of non interactic objects with a homogeneous SLD in Equation 2.8, can be expanded at low-q values in terms of the radius of gyration, R_g, leading to an expression of the scattering intensity named **Guinier** law [101]:

$$I(q) = n\Delta\rho^2 V^2 e^{-\frac{1}{3}(qR_g)^2} \tag{2.13}$$

which is valid for $qR_g \ll 1$. For example, the radius of a perfect sphere, R, is related to the Guinier radius via $R_g^2 = \frac{3}{5}R^2$. The q-range from 0 to $q < R_g^{-1}$ is called "Guinier plateau", and it is largely used to extract information about the average size of irregular objects, such as proteins.

The opposite asymptotic limit $q \to \infty$, again for homogeneous particles, conducts to the **Porod** law, which is an expression of the scattering intensity that is sensitive to the object interface:

$$I(q) = 2\pi n\Delta\rho^2 S q^{-4} \tag{2.14}$$

where S is the average surface of particles. The power law q^{-4} in the asymptotic limit describes a smooth surface with a sharp separation between the object and medium. In the case of rough surfaces or a more complex surface organisation of the scatterer geometry, the actual fractal dimension d_f is taken into account by a different scaling of the power law $I(q) \propto q^{-p}$ [82, 102], where the relation between the exponent p and d_f is given by:

$$p = \begin{cases} 6 - d_f^s, & p \geq 3 \quad (surface\ fractal) \\ d_f^m, & p < 3 \quad (mass\ fractal) \end{cases} \tag{2.15}$$

where d_f^s and d_f^m refer to surface and mass fractal, respectively. From this relation it follows that for $p = 4$, the dimension $d_f^s = 2 \equiv d_s$, where d_s is the spatial dimension.

Equation 2.8 can be formulated using the SLD fluctuation $\gamma(r)$ in disordered binary systems, described as the self-convolution of the SLD distribution $\gamma(r) = (\rho * \rho)(r)$ in the scattering volume. The scattering intensity is then expressed by:

$$I(q) = 4\pi \int_0^{+\infty} \gamma(\mathbf{r}) \frac{\sin(qr)}{qr} \mathrm{d}r = \frac{8\pi\xi^3 \langle \Delta\rho^2 \rangle}{[1 + (q\xi)^2]^2} \tag{2.16}$$

which is called Debye-Büche (DB) scattering function [103], where $\langle \Delta\rho^2 \rangle$ is the mean squared SLD fluctuation and ξ is the correlation length of such fluctuations that exponentially decay as $\gamma(r) \propto e^{-r/\xi}$. The DB function can be used to investigate a number of disordered binary

systems, such as spinodal decompositions and cluster formations. The correlation length also expresses the average size of the scattering domains via the gyration radius:

$$\xi^2 = \frac{R_g^2}{6} \tag{2.17}$$

In analogy, exploiting the fractal theory used along with the Porod law, aggregates of fractal dimensions can be modelled with an extension of the DB function that lead to:

$$I(q) = \frac{I(0)}{[1+(q\xi)^2]^{p/2}} \tag{2.18}$$

which is the Ornstein-Zernike (OZ) scattering function, where the relation between the correlation distance ξ and the radius of Guinier R_g is:

$$\xi^2 = R_g^2 \frac{2}{3p} \tag{2.19}$$

The OZ function, for $qR_g \gg 1$, has an asymptotic behaviour directly linked with a Porod law, as $I(q \to \infty) \propto q^{-p}$. The slope in such q-range is a powerful tool to investigate the particle/media interface in complex systems. Values of $p = 2$, or lower, can be associated to Gaussian polymer chains, but can also describe the scattering asymptotic behaviour of flat objects. Another example which does not include fractal dimension occurs for for values $p > 4$. This trend is displayed by objects surrounded by a diffused layer of solvent with a different SLD as compared to the bulk, such as the hydration shells of protein suspensions.

2.1.5. Structure Factor

In a systems where interparticle interactions are not longer negligible, the differential cross-section is also a function of the *static structure factor*, $S(q)$. In the case of monodisperse spheres $S(q)$ can be factorised and the total intensity is given by:

$$I(q) = n\langle|A(q)|^2 S(q) \tag{2.20}$$

which reproduces Equation 2.6 as $S(q) \simeq 1$ for dilute systems. The static structure factor is related to the microstructure of the system by the Fourier transform of the pair correlation function, $g(r)$ via the expression [82]:

$$S(q) = 1 + 4\pi n \int_0^\infty [g(r) - 1] \frac{\sin(qr)}{qr} r^2 \, \mathrm{d}r \tag{2.21}$$

The expression of $g(r)$ describes the probability of finding two particles at a certain distance r and depends on the *direct* correlation between two objects plus many contributions involving

many-body correlations. Such a problem leads to the Ornstein-Zernike equation, expressed as:

$$g(r) - 1 = h(r) = c(r) + n \int c(|\mathbf{r} - \mathbf{r}'|) h(\mathbf{r}') \, \mathrm{d}\mathbf{r}' \tag{2.22}$$

where $h(r)$ is the total correlation function and $c(r)$ is the direct correlation function which is *unknown* a priori [104]. In order to solve such an equation and calculate $S(q)$ it is necessary to introduce approximations, called *closure relations*, by introducing an *ad hoc* expression of $c(r)$. The most common closure relations are the Mean-Spherical-Approximation (MSA), $c(r) = -U(r)/k_B T$, and the Percus-Yevick (PY) approximation, $c(r) = g(r)\left(1 - e^{-U(r)/k_B T}\right)$. The structure factor $S(q)$ is linked to the direct correlation function by taking the Fourier transform of the OZ equation (Eq. 2.22):

$$S(q) = \frac{1}{1 - n\tilde{c}(q)} \tag{2.23}$$

where $\tilde{c}(q)$ is the Fourier transform of $c(r)$. MSA and PY closure relations are often convenient because result in analytical functions of $S(q)$ for some interaction potentials. In the case of Hard-Sphere (HS) potential, described by:

$$\frac{U(r)}{k_B T} = \begin{cases} +\infty, & 0 < r \leq \sigma_{HS} \\ 0, & r > \sigma_{HS} \end{cases} \tag{2.24}$$

where σ_{HS} is the HS diameter, the $S(q)$ is obtained by using PY closure relation and is given by [105–107]:

$$f_1 = \frac{(1+2\phi_{HS})^2}{(1-\phi_{HS})^4}, \qquad f_2 = -6\phi_{HS}\frac{(1+\frac{\phi_{HS}}{2})^2}{(1-\phi_{HS})^4}, \qquad f_3 = \alpha\frac{\phi_{HS}}{2}$$

$$p_1(q) = \frac{f_1}{q\sigma_{HS}}\left(\frac{cos(q\sigma_{HS})}{q\sigma_{HS}} - \frac{sin(q\sigma_{HS})}{(q\sigma_{HS})^2}\right)$$

$$p_2(q) = \frac{f_2}{q\sigma_{HS}}\left(\frac{cos(q\sigma_{HS})}{q\sigma_{HS}} - 2\frac{sin(q\sigma_{HS})}{(q\sigma_{HS})^2} - 2\frac{cos(q\sigma_{HS})}{(q\sigma_{HS})^3} + \frac{2}{(q\sigma_{HS})^3}\right)$$

$$p_3(q) = \frac{f_3}{q\sigma_{HS}}\left(\frac{cos(q\sigma_{HS})}{q\sigma_{HS}} - 4\frac{sin(q\sigma_{HS})}{(q\sigma_{HS})^2} - 12\frac{cos(q\sigma_{HS})}{(q\sigma_{HS})^3} + 24\frac{sin(q\sigma_{HS})}{(q\sigma_{HS})^4} + 24\frac{cos(q\sigma_{HS})}{(q\sigma_{HS})^5} - \frac{24}{(q\sigma_{HS})^5}\right)$$

$$S(q) = \frac{1}{1 - 24\phi_{HS}\left[p_1(q) + p_2(q) + p_3(q)\right]} \tag{2.25}$$

Besides the HS potential, representing a pure exclusion-volume interaction, other models have been calculated, such as short-ranged attractive interactions that can be modelled with the Square-Well (SW) potential:

$$\frac{U(r)}{k_B T} = \begin{cases} +\infty, & 0 < r \leq \sigma_{HS} \\ -\varepsilon, & \sigma_{HS} < r \leq \sigma \\ 0, & r > \sigma \end{cases} \tag{2.26}$$

where σ_{HS} is the HS diameter of the repulsive core and σ represents the actual diameter that include a potential well of width $\Delta\sigma = \sigma - \sigma_{HS}$ and depth ε. Analytical expressions of $S(q)$ for such a potential was calculated in PY closure relation [108, 109]. As an approximation of the SW potential, the so called "Sticky" potential for $\Delta\sigma \to 0$ and $\varepsilon \to \infty$ also leads to the analytical solution of the $S(q)$ in PY closure [110].

However, the SW potential is accurate for $\Delta\sigma/\sigma < 5\%$ but, in colloidal physics, Coulomb and dispersion forces, for example, have a longer interaction range. In these cases, the Yukawa potential is a widely used model for the description of interaction potentials with a significant range with respect to the particle sizes. A 2-term Yukawa potential is expressed as:

$$\frac{U(r)}{k_B T} = \begin{cases} +\infty, & 0 < r \leq \sigma_{HS} \\ \frac{K_1}{r} e^{-Z_1(r-\sigma_{HS})} - \frac{K_2}{r} e^{-Z_2(r-\sigma_{HS})}, & r > \sigma_{HS} \end{cases} \tag{2.27}$$

where K_i are the amplitudes of two interactions opposite in sign, representing attraction and repulsion forces, and $1/Z_i$ are the correspondent characteristic interaction-lengths. When a repulsive Yukawa term is used to describe the screened Coulomb potential, Z corresponds to the inverse screening Debye length κ. The analytical form of the $S(q)$ for the 2-term Yukawa potential was calculated in MSA closure relation for the monodisperse case [111]. Moreover, the MSA only holds for highly-screened Coulomb potentials, whereas it is not a good approximation in the weakly-screened case, such as for charged particles in free-salt water suspensions. In such a case, the issue can be overcome by using the rescaled MSA (RMSA), which successfully fits data even if underestimating $g(r)$ as compared to numerical simulations [112].

However, more approximations exist and are more or less appropriate depending on the specific physical system. In general, one of the most accurate closure relations is the HyperNetted-Chain (HNC) approximation, but it requires numerical methods to solve the scattering structure factor. The HNC and PY approximations are usually complementary, as for highly-correlated, repulsive systems both deviate from numerical simulations of $g(r)$. In this cases the Rogers-Young (RY) approximation can be used, whose closure relation consists in a mixing of the HNC and PY functions [113].

Polydispersity

In the case of polydispersity — or in the more generic case of a multi-component system — the factorisation in Equation 2.20 is not accurate. The rigorous expression in this case is:

$$I(q) = n\langle|A(q)|^2\rangle \left[\frac{1}{\langle|A(q)|\rangle^2}\sum_{a,b} A_a(q)A_b(q)S_{ab}(q)\right] \tag{2.28}$$

where the couple a,b represents every possible combination between spheres of size a and size b and S_{ab} the static structure factor between particle of sizes a and b. However, notice that the term within the squared brackets can be expressed as single observable $S_M(q)$, which is the measurable structure factor. Irrespective to the rigorous formula, $I(q)$ can be expressed as a factorised product of $S_M(q)$ and the polydisperse form factor $\langle|A(q)|^2\rangle$, giving a direct comparison with the experiments. Such consideration leads to the *monodisperse approximation*:

$$I(q) = n\langle|A(q)|^2\rangle S_M(q) \tag{2.29}$$

In truly monodisperse conditions, the microstructure is linked with thermodynamic properties of the systems, as $S(0) = nk_BT\chi_T$, where χ_T is the isothermal compressibility. In the case of polydisperse systems, this identity is no longer strictly fulfilled and $S(0)$ values, using the monodisperse approximation in Equation 2.29, may underestimate the compressibility [104].

The *decoupling approximation* [82, 104], presented in the equation:

$$I(q) = n\langle|A(q)|^2\rangle S_M(q) = n\langle|A(q)|^2\rangle \left[1 + \frac{\langle|A(q)|\rangle^2}{\langle|A(q)|^2\rangle}(S(q)-1)\right] \tag{2.30}$$

offers a better description of the limit at $S(0)$, but for high particle volume fractions, $\phi = nV < 0.1$, and for high polydispersity the approximation may bring to severe overestimation of χ_T and, in such cases, the monodisperse approximation gives a better representation.

2.1.6. Small-Angle Neutron Scattering

In this section a short introduction to *Elastic* SANS is provided. The main difference between X-ray and neutron scattering involves the interaction with the matter as, opposed to photons that interacts with electrons, neutrons have no charge and directly interact with nuclei. The scattering cross-section is split in two terms. One is the *coherent* cross-section, which depends on the structural properties of the scattering elements within the sample as for the X-ray interaction. Coherent neutron scattering is comparable to SAXS and the formalism presented in the previous section is mostly unchanged. The second term is the *incoherent* cross-section, which is based on nucleus spin incoherence and random presence of isotopes. Such a term is usually

q-independent and is not visible in SAXS, unless the photon wavelength is close the absorption edge of the scattering materials. The total scattering cross-section is the sum of both coherent and incoherent terms and carries along, in principle, information about the sample structure (coherent part), composition and spin incoherence.

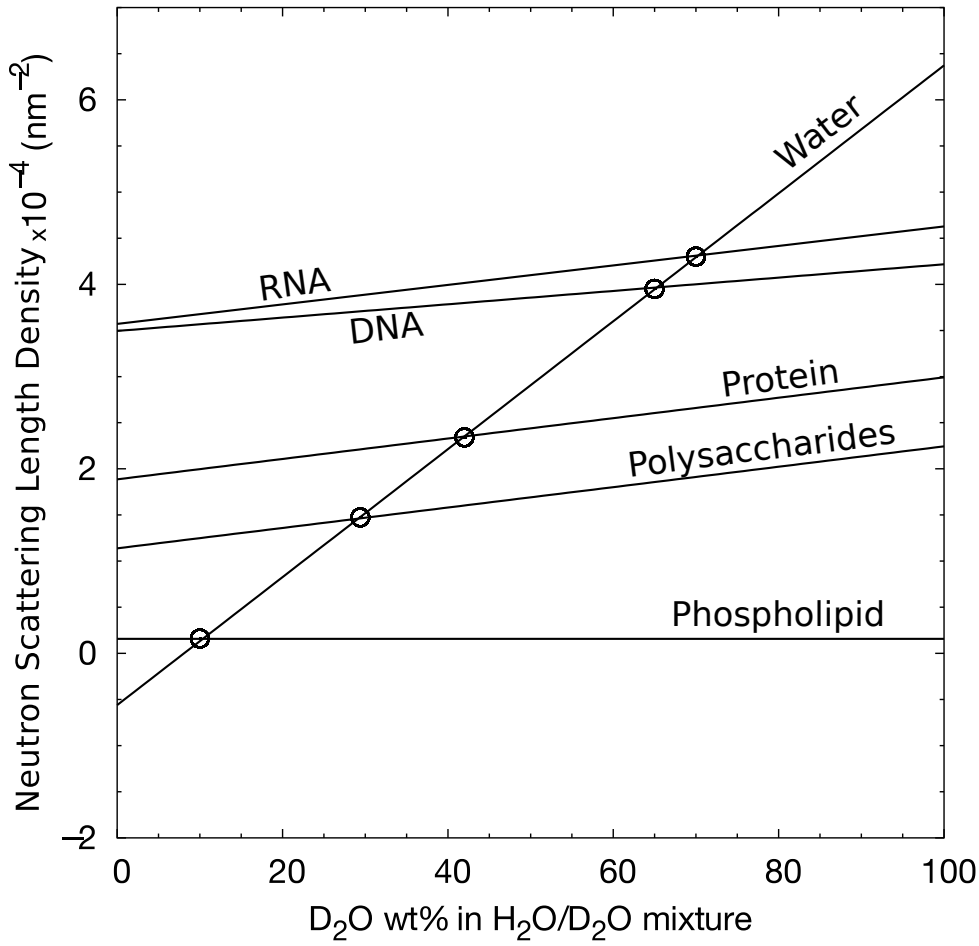

Figure 2.5.: Neutron scattering length density of biomolecules suspended in a mixture of H_2O/D_2O. Divergence from a constant trend is due to the exchange of hydrogen atoms in the solvent-accessible area of the macromolecules. Reproduced from Ref. [114] (DOI:10.1016/j.tifs.2009.07.008) with permission from Elsevier.

In SANS data shown in this work, only the coherent contribution was taken into account in the data analysis as incoherent terms were subtracted as a constant background coming from the dispersion media.

A big difference between X-ray and neutron scattering lies on the scattering length b, which, in the case of neutron, has a different value per each specific element. It results from complex, structural properties of the nucleus and there is no simple relation with the atomic number, as is shown in few examples in Table 2.1.

Fortunately, hydrogen and deuterium posses b values far apart from each other. This aspect is exploited in the *contrast variation* method, by varying the SLD of a suspension medium and

Table 2.1.: List of the scattering length b expressed in Fermi (10^{-13} cm) for common elements.

Element	H	D	C	N	O	Si
b $(Fermi)$	-3.739	6.671	6.646	9.390	5.803	4.149

eventually matching the scattering element of interest [115, 116]. Such method is feasible in SAXS too, but typical values of X-ray SLD allow small variations of $\Delta\rho$. In case of water-based suspensions, contrast variation SANS measurements are performed by varying the ratio of deuterated water D_2O in suspension media and also by substituting hydrogen with deuterium atoms of the dispersed phase prior to experiments. In Figure 2.5 matching points for common biological macromolecules are shown alongside the neutron SLD of the H_2O/D_2O mixture. Deuterated samples ares commonly used in neutron based methods but it is a good practice to always verify if the substitution is feasible, as it can affect the original microstructure and dynamics of the system.

2.1.7. X-ray Photon Correlation Spectroscopy

In the case of a high degree of coherence of the incident beam, the scattering pattern at the detector is characterised by a "speckle" pattern which originates from the exact spatial arrangement of a disordered system. Speckles randomly fluctuate over time and variations of such a pattern reflect the system's dynamics [117, 118]. Such behaviour is well-known, it is at the basis of the Dynamic Light Scattering (DLS), also known as Photon Correlation Spectroscopy (PCS), and, in analogy, find its application with multi-speckle XPCS, or Dynamic SAXS, that exploits the synchrotron radiation which is partially coherent. Compared to light scattering techniques, XPCS is particularly useful to probe dynamics in nanostructured soft matter systems and allows to explore turbid samples as wavelength-dependent multiple-scattering effects are strongly reduced.

Information about the dynamics are extracted from the temporal correlation of the scattered intensity, $I(\mathbf{q},t)$, through the intensity correlation function $G(\mathbf{q},t_1,t_2) = \langle I(\mathbf{q},t_1)I(\mathbf{q},t_2)\rangle$. When the scattered electromagnetic wave, with electric field $E_s(q,t_1)$, is coupled with a reference beam (or with an independent static component coming from the transmitted beam) the intensity correlation $G(\mathbf{q},t_1,t_2)$ is acquired in *heterodyne detection* mode and primarily depends of the normalised first-order correlation function of the intensity $g^{(1)}(\mathbf{q},t_1,t_2)$ (*field-field autocorrelation function*):

$$g^{(1)}(\mathbf{q},t_1,t_2) = \frac{\langle E_s(\mathbf{q},t_1)E_s^*(\mathbf{q},t_2)\rangle}{\langle E_s(\mathbf{q},t_1)\rangle\langle E_s^*(\mathbf{q},t_2)\rangle} \tag{2.31}$$

where $\langle\cdots\rangle$ is the time average. In the experiments conducted during this PhD project, the

XPCS setup permitted the *homodyne detection* mode, only accounting for scattered wave. In this case $G(\mathbf{q},t_1,t_2)$ is dependent on the normalised second-order correlation function of the intensity $g^{(2)}(\mathbf{q},t_1,t_2)$ (*intensity-intensity autocorrelation function*), which is defined as [20, 119]:

$$g^{(2)}(\mathbf{q},t_1,t_2) = \frac{\langle I(\mathbf{q},t_1)I(\mathbf{q},t_2)\rangle}{\langle I(\mathbf{q},t_1)\rangle\langle I(\mathbf{q},t_2)\rangle} \tag{2.32}$$

and is also called *2-time correlation function*. In the case of a stationary system, or quasi-stationary, i.e. with measurement occurring in a time scale much smaller than system evolutions, the 2-time correlation function is expressed as a function of $t = t_2 - t_1$ for each choice of $t_2 < t_1$:

$$g^{(2)}(\mathbf{q},t) = \frac{\langle I(\mathbf{q},t_0)I(\mathbf{q},t_0+t)\rangle}{\langle I(\mathbf{q})\rangle^2} \tag{2.33}$$

where $g^{(2)}(\mathbf{q},t)$ is independent from the choice of t_0 [120]. The intensity-intensity autocorrelation function is related to the field-field autocorrelation functions, $g^{(1)}(\mathbf{q},t)$, by the Siegert relation [20]:

$$g^{(2)}(\mathbf{q},t) = 1 + \beta|g^{(1)}(\mathbf{q},t)|^2 \tag{2.34}$$

where β is the contrast factor which depends on the coherence properties of the beam and is a positive value equal to 1 in the ideal case. $g^{(1)}(\mathbf{q},t)$ contains information about the time-evolution of the microstructure and, in homodyne mode, is equal to the *intermediate scattering function*, which is the Fourier transform of a generalised time-dependent pair distribution function $\tilde{G}(\mathbf{r},t)$.

For ergodic, dilute systems with particles undergoing Brownian dynamics, the intermediate scattering function is given by:

$$g^{(1)}(q,t) = e^{-\Gamma(q)t} \tag{2.35}$$

where Γ is the mean inverse relaxation time which is proportional to the diffusion coefficient D:

$$\Gamma = Dq^2 \tag{2.36}$$

In concentrated systems, or when interparticle interactions are not negligible, D becomes q-dependent and Γ is expressed as:

$$\Gamma(q) = D(q)q^2 \propto q^2 H(q)^{-1} \tag{2.37}$$

where $D(q)$ is a time and scattering vector $\mathbf{q}$-dependent diffusion coefficient and $H(q)$ is the

hydrodynamic structure factor, which, in analogy with the static structure factor $S(q)$, is linked to the time-dependent pair distribution function $\tilde{G}(\mathbf{r},t)$. The comparison between $S(q)$ and $H(q)$ gives information about indirect, solvent-mediated hydrodynamic interactions among particles [117].

For practical purposes, speckle patterns are acquired in a fast sequence, with frames spaced out by a gap Δt, Figure 2.6(a), and the intensity-intensity autocorrelation function $g^{(2)}(q,\Delta t)$ is calculated, in the case of isotropic dynamics, from the two-dimensional multi-speckle patterns azimuthally integrated over rings of thickness Δq, centred around each selected q value [see Fig. 2.6(b)], and enclosing all the related speckles. For anisotropic dynamics, a further selection of the speckle pattern can be achieved by considering spefic azimuthal section of the detector area, corresponding to a desired angle range $\Delta\varphi$ as shown in Figure 2.2(b).

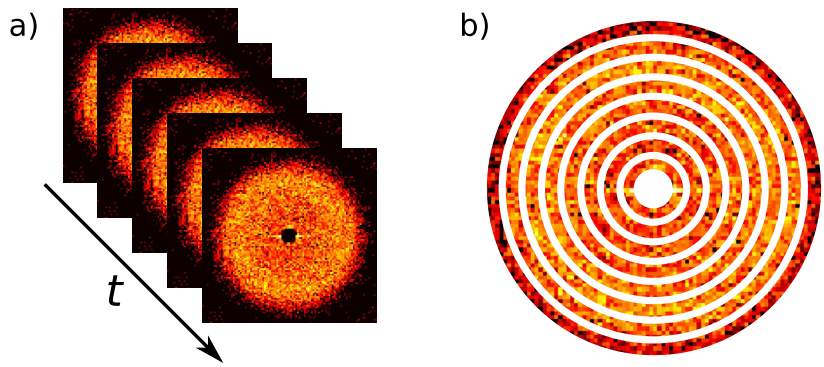

Figure 2.6.: a) Schematic illustration of the frame acquisition over time. Two-dimensional multi-speckle patterns were acquired on a Pilatus 300k detector from a suspension of concentrated spherical silica colloids. b) Example of masking of the speckle pattern to selected a series of rings of thickness Δq.

2.2. Experimental Setup

2.2.1. Synchrotron Radiation

The synchrotron radiation consists of the photon emission of high-energy electrons moving at relativistic velocities. Generally, an accelerated electron, in its frame of reference, emits photons via an electromagnetic dipole-field having an axis normal to the acceleration vector. When electrons move in a circle at a velocity close to the speed of light, c, due to a magnetic field normal to the plane defined by their motion, they are subjected to an acceleration directed towards the centre of their circular trajectory (Lorentz force). In relativistic regime, the generated dipole-field is deformed and elongated, forming a narrow emission cone in the direction of the velocity which is tangential to the circular motion [121] (see Fig. 2.7).

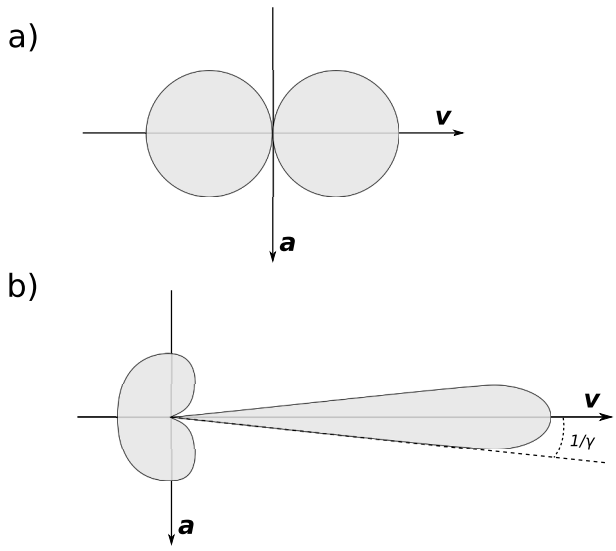

Figure 2.7.: Schematic illustration of the emission of an accelerated electron. Direction **a** and **v** describe the acceleration and velocity vectors normal and tangential to a circular trajectory, respectively, and γ is the relativistic Lorentz factor, which is a function of the electron energy. a) Dipole-field in the instantaneous reference frame of the electron. b) Deformed dipole-field in relativistic regime: photons are emitted alongside **v** with a narrow divergence with an angle equal to γ^{-1}.

In practice, such as at the European Synchrotron Facility, bunches of electrons coming from an electron gun are accelerated in a linear accelerator (Linac) and then further accelerated up to the required energy in the booster synchrotron. Such bunches of electrons at $\sim 6\ GeV$ are injected in a larger ring, called storage ring. Here, the trajectory and energy of the electrons are maintained via bending magnets (dipoles) and resonant cavities, respectively, whereas other elements such as quadrupoles and sextupoles are responsible to guarantee the electron-beam collimation [122]. Bending magnets also emit X-ray beams, but insertion devices such as *undulators* are used to produce high-brilliance X-rays which are exploited for the experiment reported in this manuscript.

Undulators consist of a periodic magnetic structure. They generate a sinusoidal magnetic field, vertically oriented, that forces electron bunches to travel along a sinusoidal path in the horizontal plane. Emitted radiation, independently generated along this path from each electron, coherently interfere and constructively sum together, resulting in an total emission whose energy spectrum is characterised by high-brilliance peaks — at energies fundamental and harmonics — which depends on the magnetic-field period of the undulator. The brilliance definition is expressed as:

$$B = \frac{N_{ph}/\Delta t}{\Delta\Omega_S \Delta S \frac{\Delta E}{E}} \tag{2.38}$$

where $\frac{N_{ph}}{\Delta t}$ is the number of photons per second, $\Delta\Omega_S$ is the source divergence ($mrad^2$), ΔS is

the source area (mm^2) and $\frac{\Delta E}{E}$ is the energy bandwidth (0.1%). Undulators generate brilliance peaks in the energy spectrum with maximum amplitude many orders of magnitude higher than the average continuous spectrum of the emission from bending magnets [82].

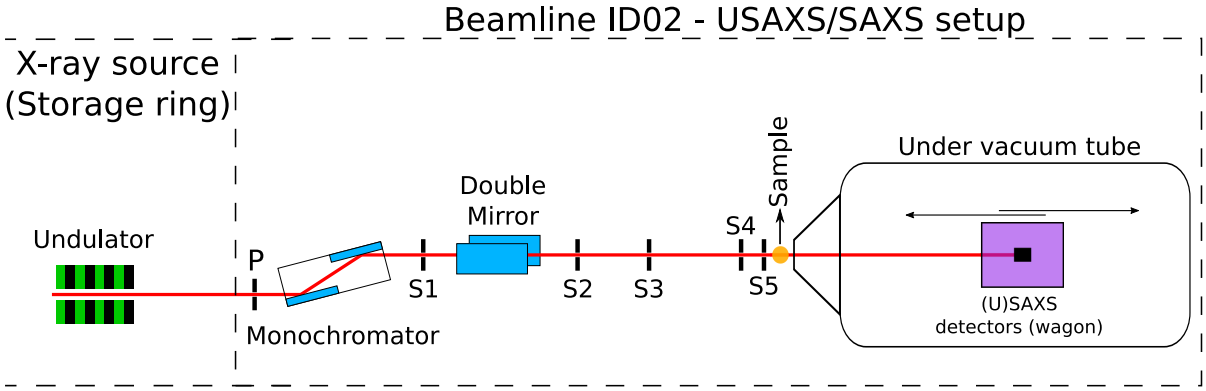

Figure 2.8.: Schematic illustration of the USAXS/SAXS setup at the TRUSAXS beamline ID02. From the left to the right, ID02 beamline exploits the undulator radiation. The beam passes through a Si 111 monochromator and is focused by a double-mirror. The pinhole collimation of the beam is performed by a series of slits, from P to S5. After the interaction with a sample, the USAXS/SAXS intensity is measured by a detector placed in a motorised wagon inside a 34 m long detector tube under vacuum. Picture adapted from [16].

2.2.2. USAXS/SAXS Beamline Setup

TRUSAXS beamline ID02 at the ESRF makes use of three different undulators (two U21 and a U35) to be used individually or in combination. Numbers in acronyms represent the period of the sinusoidal magnetic field which allows different wavelengths of the emitted X-rays, $(0.08-0.1)$ nm and $(0.05-0.15)$ nm respectively for 21.4 and 35.0 mm.

The beamline optics are optimised for the use of $\lambda = 0.0995$ nm ($E = 12.46$ keV), starting from the crystal monochromator necessary to select the wavelength from the the X-ray beam coming from the undulators. This is a Si-111 crystal cooled with liquid nitrogen [16]. It should hold the heat-load from the full power of the beam and it works in a reflection configuration (Bragg geometry). The monochromator selects the fundamental energy in the λ-range $(0.073-0.155)$ nm, with a bandwidth $\frac{\Delta\lambda}{\lambda} \sim 10^{-4}$, and simultaneously reflects all harmonics at $\lambda/2,\ \lambda/2, \ldots \lambda/n$.

Following the monochromator, a non-cooled toroidal/planar double-mirror is used to focus the beam and cut off all the harmonics and reduce the standard divergence of the beam. The standard beam size is 400×40 μm, respectively horizontal and vertical, with a diverge of 40×20 μrad. Besides the double-mirror, the beam collimation is primarily performed via a pinhole configuration by means of two primary slits, before the monochromator, and five secondary slits along the beam path, where $S1$ is placed before the double-mirror and the last, $S5$ is situated just before the sample (see Fig. 2.8).

Since synchrotron radiation is a only partially coherent, the coherent part is spatially filtered by the pinhole collimation of the X-ray beam. Multi-speckle XPCS is very sensitive on the beam coherence, whose effects are directly observable through the contrast factor β [119]. An optimal transverse coherence length of several tens of microns is obtained via tight collimation by selecting only the coherence volumes close the centre of the beam. The slit configuration of $S3$ and $S4$ define the beam size at the sample, whose FWHM can be reduced down to $20 \times 20\ \mu m$, keeping an incident photon intensity around $2 \times 10^{11}\ s^{-1}$ which permits an appropriate ensemble statistics during measurements.

After the interaction with the sample, the scattered photons enter the tube in which detectors are placed inside a motorised wagon. The tube is under vacuum as all the previous beam path, leaving at atmospheric pressure only few centimetres to place the sample. The tube is 34 m long, allowing the detector wagon to be placed in a range of sample-to-detector distances of $(0.7 - 30.8)\ m$.

The longest sample-to-detector distance permits to perform USAXS measurements in pinhole collimation, reaching q-values down to $10^{-3}\ nm^{-1}$. USAXS has been usually performed by using a Bonse-Hart instrument [82, 123]. It involves the scanning of a channel-cut crystal analyser which provides a 1D scattering profile at very low-q. The scattered intensity is superimposed to the rocking curve of the crystal, which can be subtracted after normalisation. One disadvantage is that it needs long exposure times, usually several minutes, whereas the flexible USAXS pinhole collimation gives high-quality signal-to-noise ratio using much shorter exposures of the order of $0.1\ s$, by exploiting similar beamline setup of traditional SAXS [82].

The motorised wagon contains up to three detectors: Rayonix MX170, FReLoN 4M and Pilatus 300k. Rayonix is a CCD based detector with a dynamic range of around four orders of magnitude of scattering intensity. Its active area is $17 \times 17\ cm$ with 3840 pixels per side. The pixel size of $44 \times 44\ \mu m$ gives a limit for the resolution of the scattering angle $\Delta\theta$, which is linked to the q-resolution at a fixed sample-to-detector distance and wavelength, as expressed in the following:

$$\Delta q(\theta) = \frac{2\pi}{\lambda} \cos\left(\frac{\theta}{2}\right) \Delta\theta \tag{2.39}$$

The q-resolution using CCD detectors is also limited by the point-spread function of the detector. A pixel receiving a high number of photons biases the count of the nearest pixels due to the excess of converted electrons. Such an effect can be assumed to give a Gaussian distribution of the intensity for each pixel with FWHM=120 μm for Rayonix. The point-spread function, along with the size of the beam at the sample position, cause the smearing of the scattering cross-section, which is related to the measured scattering intensity $I(q)$ via the convolution:

$$I(q) = \frac{\mathrm{d}\Sigma}{\mathrm{d}\Omega} * R(q) \tag{2.40}$$

where $R(q)$ is an effective smearing function that accounts for the detector point-spread function and beam size divergence. Assuming that both these effects are described by Gaussian functions, also the convoluted $R(q)$ expression is a Gaussian function with variance $\sigma_q^2 = \sigma_d^2 + \sigma_b^2$, where σ_q is the standard deviation of the effective smearing $R(q)$ and σ_b is the equivalent standard deviation of the beam-size profile. The low bandwidth ratio contribution, $\frac{\Delta\lambda}{\lambda}$, is negligible in this case.

FReLoN (Fast-Readout, Low-Noise) detector is smaller than the Rayonix, having a smaller active area containing 2048 pixels per side of size 23.6×24.0 μm. These characteristics allow the FReLoN detector to acquire higher resolution measurements as compared to Rayonix, as it also has a point-spread FWHM=50 μm. Moreover, it can be used for XPCS measurements in the case of systems showing slow dynamics as permits acquisitions at 5 Hz.

Pilatus is a pixel detector, where each pixel directly detects X-ray photons. Its active area consists of 487×619 pixels and the theoretical q-resolution is lower compared to CCD detectors as the pixel size (172 μm) is large. However, it does not suffer from point-spread function and only the beam size and divergence have to be accounted for the signal smearing. The main characteristic is its fast acquisition rate of 400 Hz, which allows the detection of fast dynamics with a minimum time step $\Delta t = 0.0002$ s and a read-out time of 0.0023 s.

Independent of the type of detector used, measured detector counts are converted to equivalent number of photons after normalising by the sample transmission, T_r, and detector efficiency, ε_d. Normalised 2D patterns are azimuthally averaged to obtain the intensity vs q scattering curves on absolute scale.

3. Small Angle Scattering Studies of *in Vivo Escherichia Coli* Structure

In this chapter a structural description of the motile bacterium *Escherichia coli* is presented. The interest is twofold: first, a scattering form factor of the bacterium in the sub-micron scale is necessary for the study of active suspensions and to explore if there is a measurable structure factor of interaction; then new insights about the bacterial ultrastructure can be obtained from the scattering analysis. The ultrastructure of a biological system is the nanometre scale structure that is not easily accessible by common optical microscopy techniques. So far, the cell ultrastructure has been primarily studied by electron microscopy such as cryo-TEM [77–80].

The whole geometry, the inner structure and the composition of the bacterium are firstly introduced to justify the modelling and the experimental choices. Then, USAXS measurements of *in vivo* bacterial suspensions are presented, along with a geometrical modelling of the shape of the cell by anisotropic scattering form factor models.

In the second and main part of the chapter, combination of USAXS/SAXS and SANS measurements *in vivo* are reported along with a multi-scale, structural analysis of the cell. Thanks to the extended q-range covered by the combination of USAXS and SAXS techniques, the description of the bacterium structure at various length scales has become feasible, as scattering features found in the range covered by traditional SAXS measurements became meaningful due to the information contained in the USAXS pattern. Attempts in this direction have been recently carried out [124] but such complex structures require a depeer investigation. Thus, X-ray scattering data were analysed alongside constraints imposed by using the contrast-variation SANS and this synergy permitted the development of a multi-scale model of the *E. coli*, where the sub-micron shape and the ultrastructure are integrated in a single representation.

3.1. *Escherichia Coli*: Shape and Ultrastructure

Escherichia coli is a well known bacteria, extensively studied as a model bacterial organism. It is a rod-shaped prokaryotic cell, with circular diameter of $(0.4-0.8)\ \mu m$ and total length of $(1-4)\ \mu m$. As a prokaryotic cell, the *E. coli* has neither nucleus nor organelles, as it does

not posses any internal compartment enclosed by a lipid membrane. The interior of the cell, the cytoplasm (CP), is a dense crowded dispersion of macromolecules (such as ribosomes, proteins, DNA and plasmids), diffusing inside the cell (Fig. 3.1). A nucleoid region comprises the main DNA ring (up to 1 *mm* in contour length), completely folded, and proteins. The non-nucleoid region of the cytoplasm is a concentrated solution of macromolecules, primarily consisting of proteins and ribosomes, which occupy around 30% of the available volume [125].

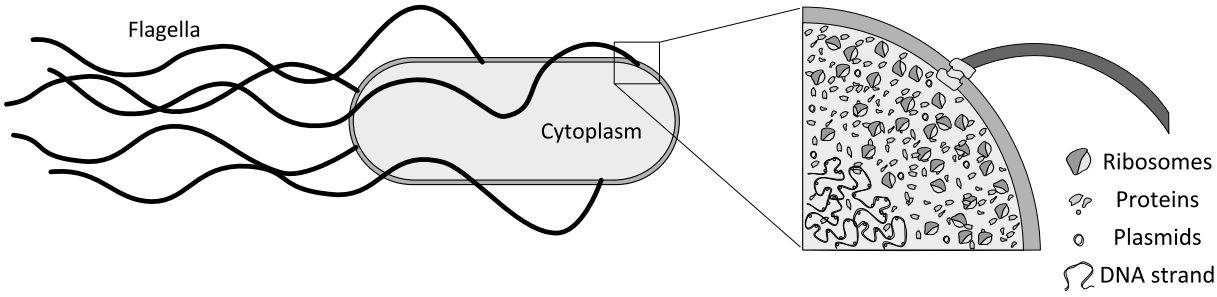

Figure 3.1.: Schematic diagram of an *E. coli* cell. The bacterium is a compact rod-like cell enclosed by the cell wall. A few flagella are anchored all around the cell body by trans-envelope machinery that cross the cell wall. The cytoplasm contains a nucleoid region mainly consisting of single folded DNA-ring and a non-nucleoid area densely packed with proteins and ribosomes.

E. coli is classified as gram-negative bacterium. Therefore, the cell envelope consists of two membranes between which there is a peptidoglycan layer (PG) (Fig. 3.2). The inner membrane (IM), or periplasmic membrane, consists of phospholipids, primarily phosphatidylethanolamine, phosphatidylglycerol and cardiolipin, and most of the aliphatic chains in the phospholipids are palmitic acids [126–129]. Due to the lack of organelles in prokaryotic cells, most of the functions occur here in the IM. For this reason, the IM is full of membrane proteins performing energy production, lipid and peptidoglycan synthesis, secretion and cross-membrane transport. On the other hand, the outer membrane (OM) acts as protective barrier. It is asymmetric, with a similar phospholipid content to the IM in the inner leaflet, but with a high concentration of lipopolysaccharides (LPS) in the outer one. LPSs are phospholipids with six to seven mostly saturated aliphatic chains, a polysaccharide core, followed by a long polysaccharide side-chain, called O-antigen. LPSs tend to tightly group in compact domains, regulating the stiffness of the OM and its permeability to hydrophobic compounds. The protein content in the OM is thought to be lower than the IM, it is only decorated by membrane proteins responsible for transport and a few enzymes such as protease and phospholipase [130].

The region in between the cell membranes is called periplasm (PP). It is a highly oxidising environment which is less dense in protein than the cytoplasm and it should serve to trap potentially dangerous enzymes. A portion of the periplasmic space is occupied by the peptidoglycan layer (PG). This is a porous and stiff net-like structure that defines the shape of the cell envelope and prevents structural damage due to osmotic pressure in hypotonic solutions. Without

it, the cell loses turgidity and acquires a spherical shape. Such cells are called "spheroplast", which can continue their function for long time but they lack the protective structure. The peptidoglycan, or murein, building block consists of a disaccharide, N-Acetylglucosamine (NAG) and N-acetylmuramic acid (NAM) linked by $\beta-(1,4)$ glycosidic bond, and of 4-unit amino-acid chain (L-alanine—D-glutamic acid—meso-diaminopimelic acid—D-alanine) bound to the NAM. The NAM-NAG subunits form chains of variable length which are covalently cross-linked by the peptide chains [131–133]. The PG is bound to the OM by the Braun's lipoproteins (Lpp). A Lpp is covalently bound to the PG at one extremity while the other is embedded in the OM [134].

Finally, *E. coli* mobility is due to its flagella. Each bacterium possesses up to 10 flagella, which in turn are anchored to the cell by a protein complex that crosses the entire cell envelope (Fig. 3.1). The single flagellum is a very long (up to 15 μm) cylindrical macromolecular assembly with flagellin subunits [135,136]. To achieve self-propulsion, the basal body functions as a rotor and delivers torque to the flagellum in order to turn it counter-clockwise. While rotating, the flagella assume an helical shape with variable waveforms and together they form a bundle that defines the back side of the bacteria during the motion ("run" phase). In order to change the orientation of the cell body, some of the rotors invert the direction of the torque and the flagella that start rotating clockwise detach from the bundle ("tumble" phase) [137, 138].

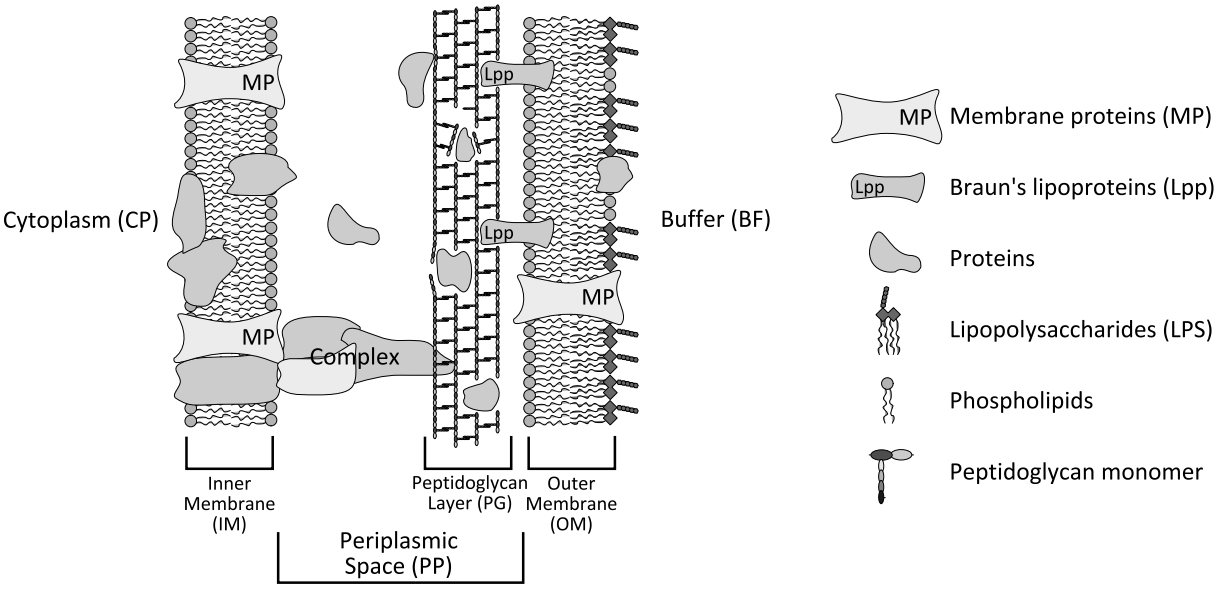

Figure 3.2.: Schematic diagram of the cell wall in gram-negative bacteria. These cells are distinguished by the presence of the periplasmic space, that is an external cellular compartment separated from the cytoplasm by the inner, or periplasmic, membrane. In turn, the periplasm is separated from the outside by a second coating, the outer membrane, that is firmly bound to the peptidoglycan layer inside.

3.2. Materials and Methods

All samples were prepared with *E. coli* chemically competent cells from Invitrogen (K-12 strain, close to DH10B^{TM} derivative). Bacteria are transformed with pUC19 DNA (Genbank Accession Number L09137) and plated on lysogeny-broth (LB) plates with ampicillin ($100\mu g/ml$). The expression of the plasmid pUC19 makes the cells ampicillin-resistant, avoiding any contamination during the cell growth. Cells were then harvested, re-suspended in LB medium containing ampicillin (100 $\mu g/ml$) and grown at 37 $^{\circ}C$ until the required concentration was attained, i.e. $OD_{600} = 0.6-2.0$ (1 $OD_{600} \simeq 8 \cdot 10^8 cells/ml$). OD_{600} stands for Optical Density at $\lambda = 600\ nm$ and it is based on turbidity measurements performed with the OD-meter GeneQuant-1300. *E. coli* cells were centrifuged using a tabletop Eppendorf centrifuge at 4 $^{\circ}C$ in sterilized 50 ml falcon tubes at 1000 g for 55 minutes and, after removing most of the supernatant, spun down for 10 minutes to obtain artificially-concentrated samples in the range $OD_{600} = 0.6-10$. Finally the cells were gently re-suspended in nutrient-free and sterile filtered Phosphate Buffer Saline solution (PBS) at $pH \simeq 7.4$ ($[KH_2PO_4] = 1.06\ mM$, $[Na_2HPO_4] = 3.00\ mM$, $[NaCl] = 154\ mM$). Contrast matching measurements were performed on bacteria re-suspended in deuterated PBS buffer (D-PBS) at $pD \simeq 7.3$ and in mixtures of PBS and D-PBS. LB medium, PBS and D-PBS tablets were purchased from Sigma Aldrich; ampicillin sodium salt was purchased from Euromedex.

USAXS/SAXS measurements were performed at the TRUSAXS beamline (ID02) at the ESRF. The set-up uses a monochromatic beam at $\lambda = 0.0995\ nm$ ($E = 12.46\ keV$), collimated in the pin-hole configuration. Measurements were performed at room temperature with sample-detector distances of 30.8, 10.0 and 1.0 m covering a q-range of nearly 4 orders of magnitude $(0.002-7)\ nm^{-1}$. Either the Rayonix MX170 or the FReLoN 4M detector was used (§ 2.2.2) for these measurements. Radiation damage tests showed no evidence of damage induced by X-rays to the bacteria within several seconds. The flux of the incident X-ray beam was always lower than $\sim 2 \times 10^{12}$ photons s^{-1}, with a FWHM beam size at the detector of 770 $\mu m \times 77\ \mu m$. Samples were contained in quartz or polycarbonate capillaries with sample thickness $\sim 1.85\ mm$ and, to maximise the precision of the background subtraction, a flow-through configuration was used. This allows to measure the sample and buffer at the same position with the same capillary, which was thoroughly cleaned prior to each measurement and control buffer measurements were performed before and after each bacterial sample.

SANS measurements were performed at the Large dynamic range SANS instrument D22 at the ILL. This set-up also employs a pin-hole collimation and a monochromatic beam. The experiments were performed at $\lambda = 0.45\ nm$ ($\Delta\lambda/\lambda \sim 0.1$) using three sample-detector distances: 17.6, 5.6 and 1.4 m covering a q-range of $(0.02-6)\ nm^{-1}$. Samples were contained in quartz

Hellma cuvettes with sample thickness 1 *mm*.

3.3. Modelling the Whole Cell Body

3.3.1. USAXS Measurements

The USAXS set-up (sample-detector distance of 30.8 *m*) allows the investigation of the micron scale structure. Even from low-contrast samples such as bacteria, it was possible to acquire measurements with a high-quality signal-to-noise ratio in the q-range $(2\times10^{-3}-10^{-1})\ nm^{-1}$. Figure 3.3 presents USAXS data from *Escherichia Coli* at such low q-values. The data are fitted using the scattering form factor $\langle P_{cap}(q,R,H)\rangle_{\Omega,\sigma_R}$ in Equation 3.3, that describes a cylinder of length H and average radius R with hemispherical caps at both ends (capped-cylinder). The scattering amplitude $A_{cap}(q,R,H,\theta)$ of a capped-cylinder was calculated by Kaya and de Souza [139] which is given by:

$$\begin{aligned}\frac{A_{cap}(q,R,H,\theta)}{\Delta\rho} =& \pi R^2 H \frac{sin[q\cos(\theta)H/2]}{q\cos(\theta)H/2}\frac{2J_1[q\sin(\theta)R]}{q\sin(\theta)R}+\\ &+4\pi R^3\int_0^1 \cos[q\cos(\theta)(Ry+H/2)]\times\\ &\times(1-y^2)\frac{J_1[q\sin(\theta)R\sqrt{(1-y^2)}]}{q\sin(\theta)R\sqrt{(1-y^2)}}\,\mathrm{d}y\end{aligned} \tag{3.1}$$

In the sample, the cell orientations are isotropically distributed and the form factor is calculated by the orientation average:

$$\langle P_{cap}(q,R,H)\rangle_\Omega = \langle |A_{cap}(q,R,H,\theta)|^2\rangle_\Omega = \int_0^{\pi/2} |A_{cap}(q,R,H,\theta)|^2 \sin(\theta)\,\mathrm{d}\theta \tag{3.2}$$

Finally, a Gaussian PDF, with standard deviation σ_R, was taken into account to include the polydispersity of the radius:

$$\langle P_{cap}(q,R,H)\rangle_{\Omega,\sigma_R} = \int_0^{+\infty} \langle P_{cap}(q,r,H)\rangle_\Omega PDF(r,R)\,\mathrm{d}r \tag{3.3}$$

This model uses a constant X-ray scattering length density (XSLD) for the whole cell body, neglecting any features coming from the cytoplasm, the cell envelope or the flagella. The term $\Delta\rho$ represents the difference between the electron density of the cell and the buffer.

This assumption is confirmed *a posteriori* by the goodness of the fit, but it is significant to justify it with further details:

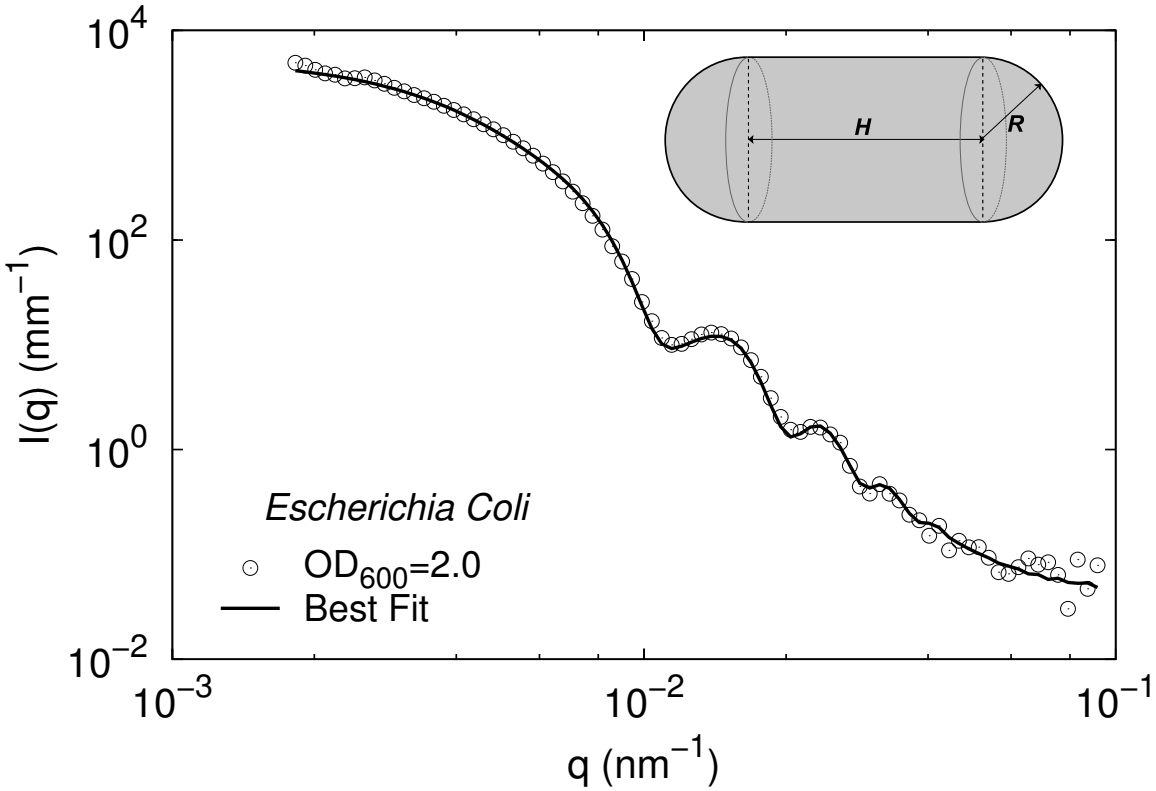

Figure 3.3.: USAXS data from *Escherichia coli* ($OD_{600} = 2.0$) suspended in PBS buffer (using FReLoN detector). The data are described by polydisperse capped-cylinder model with parameters listed in Table 3.1.

Table 3.1.: Results from the fit in Figure 3.3. σ_R is the standard deviation of a normal PDF for R.

E. coli	$\langle R \rangle$ (nm)	σ_R (nm)	H (nm)
$OD_{600} = 2.0$	351	25	940

i) In the non-nucleoid region of the cytoplasm, the largest objects are the ribosomes, which have a diameter $\sigma \simeq 20$ nm. The length of such macromolecules is smaller than the minimum dimension one can probe with $q_{max} \sim 0.1$ nm^{-1}, i.e. $l_{min} \sim 2\pi/q_{max} \sim 60$ nm. In the q-range of Figure 3.3, only scatterers with characteristic dimensions, $\tilde{R}$, larger than $\tilde{R}_{min} \sim q_{max}^{-1} \sim 10$ nm would nearly exhibit a plateau coming from the low-q region of the Guinier approximation, in which $q\tilde{R} \sim 1$. Similar considerations are valid for the nucleoid, consisting of proteins and a very long folded-ring of DNA. Any features that might contribute to the scattering signal, if visible, would be present in the q-range $(0.1 - 10)$ nm^{-1}, spanning from ~ 60 nm down to a few atomic sizes. The DNA strand could have a total length of up to 1 mm, however it occupies a tiny fraction of the total volume of the cell (up to $\sim 0.6\%$), having a negligible contribution compared to the total scattering intensity.

ii) The cell envelope takes up to 20% of the total volume. Therefore the total mass of the lipid content of the membranes could contribute significantly in the scattering pattern, even considering that the XSLD of a phospholipid is low (see Table 3.4). The contribution from the cell envelope could be included describing the bacterium with a core-shell model (§ 2.1.3), i.e. using a XSLD average value for the cytoplasm and another average XSLD value for the cell envelope. The former is an average value for proteins, DNA and water; the latter instead an average for phospholipids, proteins and water. These two values cannot be so different, with proteins and water being the main constituents. Furthermore, the shell thickness is lower than ~ 35 *nm*, considering two membranes of ~ 5 *nm* each and a periplasmic width around $(10-25)$ *nm* [78]. These values are much lower than the radius of the capped-cylinder core. In this situation, if the data does not span over a large q-range including the characteristic length scale of both radius and shell-thickness, parameters such as the two XSLDs, the shell thickness, the radius and the polydispersity, are highly correlated. Hence, a core-shell approach does not give more information than the simple-core model and could even be misleading.

iii) The flagella are very long $(2-15)$ μm and compact protein-based cylinders. Their radius is ~ 10 *nm* [136], making any local structure visible around $q \sim \tilde{R}^{-1} \sim 0.1$ nm^{-1}, which is at the edge of the USAXS q-range. The shape of a flagellum describes a helix, whose coil length changes depending on the cell motion [138, 140]. Nevertheless, at low q-values, such objects could be described using a polymer model, such as a Gaussian-chain. The scattering contribution in the USAXS range might be low or even negligible, as the volume-ratio between the flagella and the cell body is $(0.2-8)\%$.

3.3.2. Limitations of the Model

It is worth noting, that the sample is not monodisperse. It is composed of a distribution of bacteria with different sizes (both in length and diameter), as a consequence of their growth cycle. A culture of *E. coli* grows in number by binary fission. Each cell grows in length until it separates into two new individuals. Usually, for elongated geometries such as the capped-cylinder model, it is not worthwhile to use polydispersity in both radius and length, unless the sample has a low polydispersity (lower than 5%) and the available q-range shows many oscillations. For these bacteria instead only the first three oscillation are visible and the capped-cylinder model is only an approximation, especially considering that the bacteria are not even rigid rods (they have a certain degree of flexibility). The polydispersity included in the fit of Figure 3.3 describes all these sources of smearing of the curve. Hence the value σ_R cannot be taken as real measurement of the variance of the radius.

There are two more effects that could smear the form factor minima. The first is due to the instrumental smearing. For the measurement in Figure 3.3, the maximum σ_q (calculated from

the horizontal FWHM of the beam size at the detector) is around $7 \times 10^{-4}\ nm^{-1}$, making it negligible. The second one concerns the background subtraction. The difference between XSLD values of bacteria and suspension medium is low. In this case, the scattering signal from the sample is close to the measured background and the subtraction may overestimate (or underestimate) the effective depth of the minima. This effect has to be considered in the USAXS set-up. A compromise between the lowest q-values desired and the increased background must be taken into account, alongside the photon flux. Hence, the quality of the signal can be enhanced not only by increasing the bacterial concentration, but also by reducing the intensity level of the background. Practically, this is achievable by increasing the size of the beam-stop to sacrifice a portion of the Guinier region to obtain good signal-to-noise ratio at higher q-values. Finally, for an accurate background subtraction, the use of the flow-though cell sample-configuration is mandatory with such weak-scattering samples.

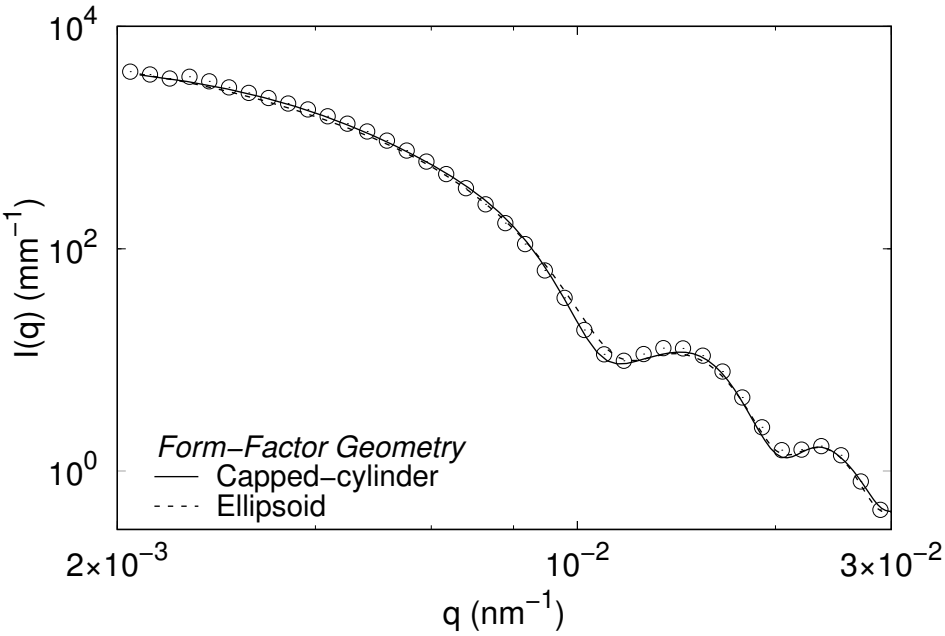

Figure 3.4.: USAXS data fitted by a capped-cylinder (*solid line*) and an ellipsoid (*dashed line*) model. The radius obtained with ellipsod-model is $\langle R \rangle \simeq 365\ nm$, roughly 15 *nm* bigger than the estimation by the capped-cylinder model.

The capped-cylinder model describes the scattering form factor of the *E. coli* cell body well. The radius value could be biased by a less accurate estimation of the polydispersity or by the fact that it is not possible to discern between the simple-core and core-shell models as discussed earlier. The curve clearly defines the radius value by the position of the first minimum, whereas the length of the cell has a different impact on the form factor. Cylinder or capped-cylinder form factors exhibit the effects of the length parameter in the Guinier region at low-q and on the high-order oscillations at high-q in the case of low polydipersity, which is not the case for

E. coli. Unfortunately, the scattering from the bacterium at low q-values is comparable to the signal from the background, hence the subtraction may lead to a lack of precision for values lower than 0.002 nm^{-1}. As a result, the length value in Table 3.1 may not be accurate. The same conclusion is obtained by fitting the low-q region with the Guinier law (see Equation 2.13), indeed the condition $qR_g \ll 1$ is not fulfilled as $q_{min}R_g = 1.7$. As a consequence of the apparent polydispersity of the sample and the lack of the low-q region, it is possible to model the USAXS data also with a simple cylinder or an ellipsoid (prolate), whose scattering amplitudes are respectively $A_{cyl}(q,R,H,\theta)$ and $A_{ell}(q,R,e,\theta)$:

$$A_{cyl}(q,R,H,\theta) = \Delta\rho\pi R^2 H \frac{sin[q\cos(\theta)H/2]}{q\cos(\theta)H/2}\frac{2J_1[q\sin(\theta)R]}{q\sin(\theta)R} \tag{3.4}$$

$$A_{ell}(q,R,e,\theta) = \Delta\rho 4\pi R^3 e \frac{\sin(u) - u\cos(u)}{u^3} \quad \text{with} \quad u = qR\sqrt{\sin^2(\theta) + e^2\cos^2(\theta)} \tag{3.5}$$

where e is the ratio between minor and major radii of the ellipsoid, i.e. $e > 1$ for prolates and $e < 1$ for oblates. The shape of *E. coli* is known and visible by microscopy techniques, the capped-cylinder model is the most adequate description of the system. A cylinder model can fit the data as well, but polydispersity on both radius and length must be added to compensate the lack of accuracy. For this reason there is no gain in computational speed (see Appendix A). Instead a prolate geometry can be a convenient choice. It is less accurate than the capped-cylinder, but is a good alternative due to gain in speed for the calculation (Fig. 3.4). It cannot describe the high-order oscillation of a cylindrical geometry, but works well in the case of polydispersity. Both models suffer from the same disadvantage in the length parameter and have the same precision for the radius.

3.3.3. Possible Applications

E. coli is able to sense if the available nutritional elements start to become insufficient. The decrease in volume is one of the strategies they apply to be able to survive for longer [141]. While bacteria are suspended in a nutrient-rich medium, they start doubling their number by cell division every $\sim$ 25 minutes at 37 $°C$ (*exponential growth phase*). When the amount of nutrients is low, the cell division rate is drastically reduced and the number of bacteria remain almost constant over time (*stationary phase*). The cycle of exponential/stationary sequence starts over if new nutrients are added to the suspension.

The changes in length and diameter of cells during the growth-cycle were reported [142–145]. The advantage of transferring cells from the LB medium to the nutrient-free PBS buffer is that they stop the cell-division cycle and the concentration remains constant over time. A sample of

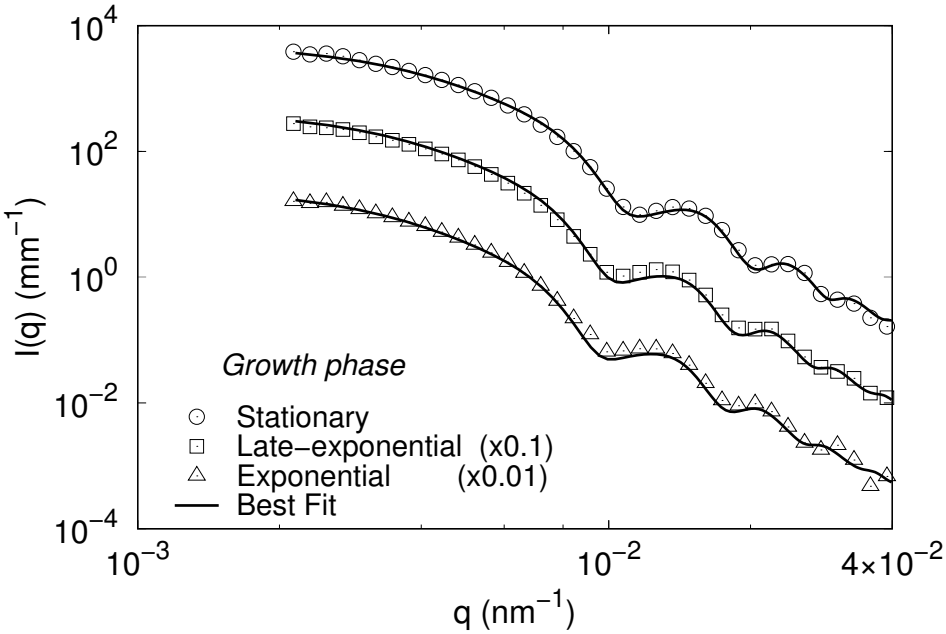

Figure 3.5.: Best fit of *E. coli* samples re-suspended in PBS buffer. The cells were taken from the same culture in three different stages, corresponding to distinct growth phases.

cells re-suspended in PBS is a "snapshot" of the specific condition of the system in the growth curve of the bacterial culture.

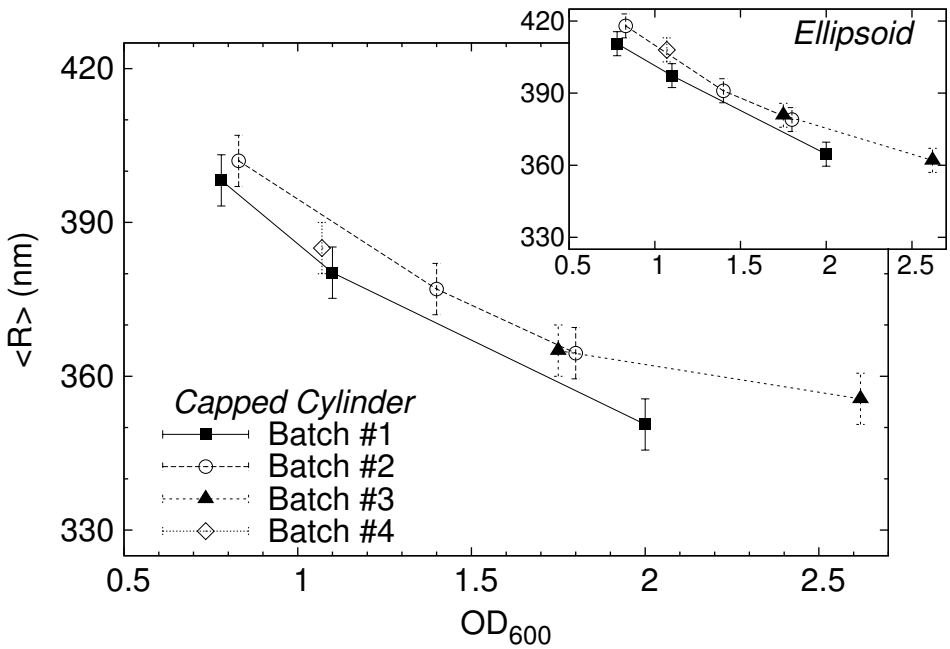

Figure 3.6.: Plot of the average cell radius as a function of the concentration in the bacterial culture. The inset shows the radius values obtained by fitting the data by an ellipsoid model. The curve is systematically overestimated by ~ 15 *nm*.

Figures 3.5 and 3.6 show the proof of concept for the study by USAXS, the evolution of the radius in a bacterial culture. The same idea could be applied to monitor any change in the *E. coli* geometry in various external conditions, such as changing temperature, pressure, pH, etc. The method offers a complete statics, probing more than 10^5 cells in one single measurement.

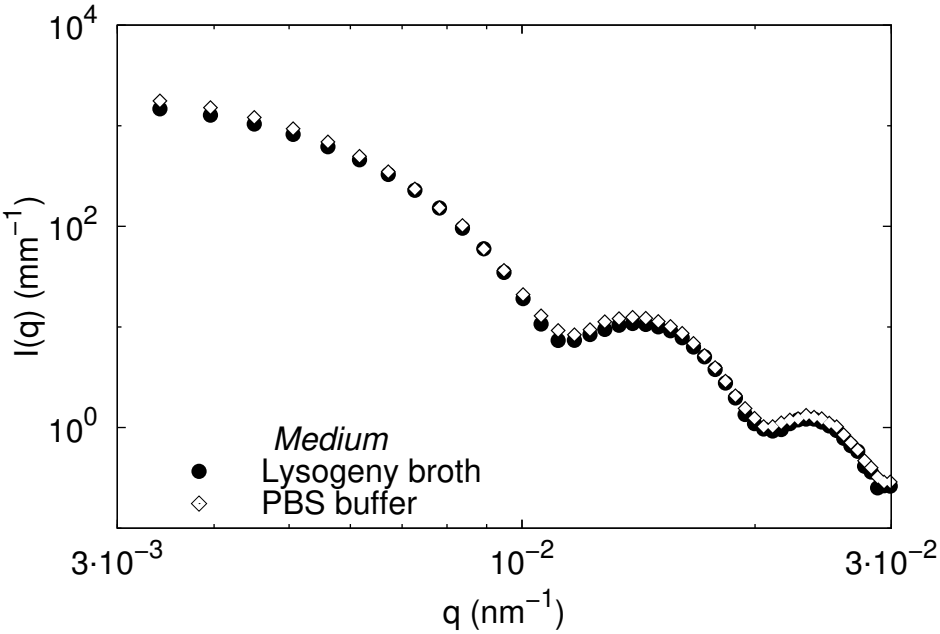

Figure 3.7.: Measurements of *E. coli* suspended in LB medium (*full circles*) and in PBS buffer (*empty diamonds*). Cells in the two media have the same radius, defined by the positions of the minima.

Another example of use of this technique concerns the measurement of the cell radius in suspension at different ionic strengths. Cell membranes are permeable to water and the shape of the cells is strongly affected by the concentration gradient of solutes across them. In isotonic conditions, the flow of water through the lipid bilayer is balanced and the cell shape is unaffected. In suspensions of hypotonic or hypertonic solutions though, cells experience swelling or shrinking respectively. This is due to the unbalanced water flow through the semi-permeable membrane. The PBS solution has the same tonicity as the LB medium, as displayed in Figure 3.7. In Table 3.2 instead radius values for suspension of cells in hypotonic solutions are presented.

The results point out the difference in radius between suspensions in PBS and in low ionic-strength buffers. The latter exhibits similar values ($\pm 2\%$). Even suspended in pure water, bacterial systems are able to survive for many hours, resulting in cells having the same radius measured in the phosphate and Tris buffers at 4 and 10 mM. For the *E. coli* these latter media are hypotonic solutions and they all show an increase in radius of around 30 nm as a result of cell swelling. Therefore, as additional instance, USAXS technique can be used to study the effects of osmotic pressure on the geometry of any cell in the sub-micron range or to characterise the

radius variation as a function of the ionic strength with a resolution of a few nanometres.

Table 3.2.: Values of cell radius for *E. coli* suspensions. Bacteria were harvested from the culture at $OD_{600} \simeq 1.4$, during the late-exponential growth phase. Due to background subtraction issues, the estimation of the errors on these values is 5 *nm*.

Suspension	$\langle \boldsymbol{R} \rangle$ **(*nm*)**
PBS buffer $pH \sim 7.2$	377
Phosphate buffer $4m\ M\ pH \sim 7.4$	406
Phosphate buffer 10 $mM\ pH \sim 7.4$	400
Tris buffer 4 $mM\ pH \sim 7.4$	407
Tris buffer 10 $mM\ pH \sim 7.4$	409
Water	409

3.4. X-ray and Neutron Scattering: Investigating the Internal Structure of *E. coli*

3.4.1. USAXS/SAXS Measurements

In the previous section the choice of the model has been justified by claiming that all the main structural detail of the *Escherichia coli* would contribute to the scattering intensity at high q-values, specifically from values higher than $\sim 0.1\ nm^{-1}$. Hence it would be very interesting to use complementary scattering techniques, SAXS and SANS, to obtain high-quality measurements at the nano-scale. There are various challenges, because the cells are complex, inhomogeneous and from individual small-angle scattering measurements it is hard to decouple the contributions coming from cytoplasm, membranes, flagella, etc.

Table 3.3.: Estimations of volume ratios with respect the whole cell body.

Cell Elements		$V/V_{Cell\ body}$ **%**
Cytoplasm		$81-84$
	- Proteins	$3-16$
	- Ribosomes	$1-6$
	- DNA	< 0.6
Cell Envelope		$16-19$
	- Periplasm	$11-12$
	- Membranes	$5-7$
Flagella		$0.2-8$

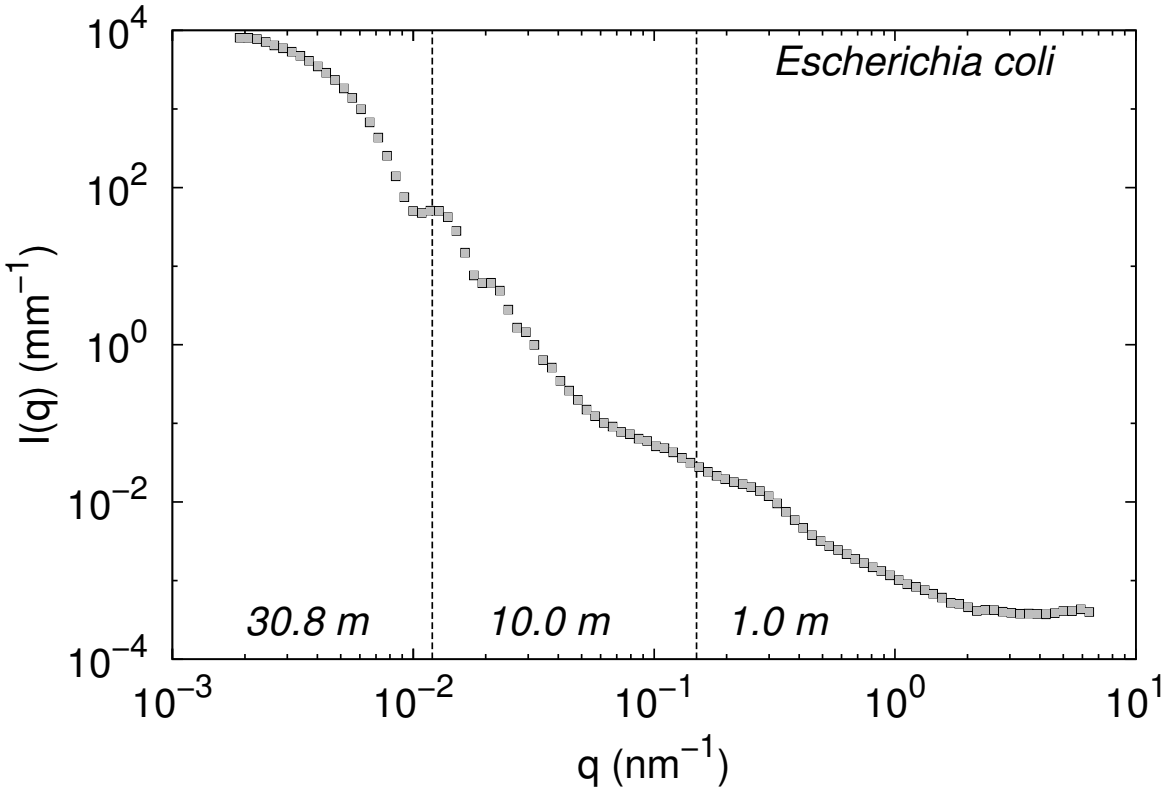

Figure 3.8.: USAXS/SAXS measurements of *E. coli* suspended in PBS buffer. Bacterial concentration $OD_{600} = 10$, artificially concentrated from a culture stopped at $OD_{600} = 1$ (late-exponential growth phase). The curve is obtained merging three measurements (using Rayonix detector) at three different sample-detector distances and interpolating the data into a logarithmic-spaced q-array.

In Figure 3.8 the complete USAXS/SAXS scattering curve from an *E. coli* system is shown. It spans 4 orders of magnitude in the q-axis, describing cells from the sub-micron to the nanometre scale. The curve is the result of merging three measurements at different sample-detector distances: 30.8, 10 and 1 metres. Therefore modelling the bacterium as a simple homogeneous colloid is no longer sufficient. There is a variation in slope at $q \sim 0.06\ nm^{-1}$ and a peak at $q \sim 0.27\ nm^{-1}$. The latter feature suggests the presence of a well-defined structure with a characteristic length of $l \sim 2\pi/0.27 \sim 23\ nm$. This very number could represent many sizes or distances inside the cell. As earlier discussed it is compatible with the ribosome diameter, but also with the flagellum diameter and the periplasm width. However it is not possible to exclude something else, such as a peculiar repetition length coming from the folded DNA in the nucleoid. Finally, it might be that all of these contributions are entangled in the scattering curve.

The first step, before modelling the system, is to estimate the scattering intensity coming from each class of elements in the cell, in order to have an idea of what can be realistic and

what should be neglected. By putting together all the information discussed in the previous section, in Table 3.3 bacterial elements are listed by the volume ratios with respect to the cell body.

Table 3.4.: Typical values for the X-ray and neutron scattering length density of the main components need to describe the system. Water and heavy water values refer to room temperature (25°C).

Scatterer	$XSLD \times 10^{-4}$ (nm^{-2})	$NSLD \times 10^{-4}$ (nm^{-2})
H_2O	9.39	-0.56
D_2O	9.38	6.37
Phospholipid	$8.7-9.6$	0.23
- Head group	$13.4-15.8$	$2.2-2.5$
- Acyl chain	7.7	$-(0.36-0.30)$
Protein	$11.6-12.4$	1.9
Ribosome	15	3.1
DNA/RNA	$16.6/16.9$	$3.5/3.6$

A natural choice for the model would follow a hierarchical ranking based on the volume percentage, but, for an estimation of the scattering intensity, volumes are not enough, as $I(q = 0) \propto V^2(\rho - \rho_{medium})^2$. In Table 3.4 estimations for both X-ray and neutron scattering length densities are listed. Here density values for macromolecules are estimations, used as starting points and boundaries to guide the parameters needed to describe the scattering model. For a precise assessment of the model, one should account for differences in SLD values, and the contrast with respect to the medium. Hence, for example, the membranes with low SLD contrast could contribute as much as the protein-based flagella.

To conclude, the cytoplasmic space is the biggest region of the bacterium, it contributes the most to scattering and it has already been described as a homogeneous core in the previous section, successfully fitting the USAXS data. The cell envelope is the second main component and cannot be neglected any longer. The cytoplasmic core model can be completed with different shells, depicting the ultrastructure of the gram-negative cell wall. Whereas cytoplasm and cell envelope scattering contributions are certain, the visibility of flagella, DNA strands and proteins is not clear. Proteins, ribosomes and DNA make the cytoplasm itself dense and compact, but without more information it is not possible to draw conclusions. Same principle for flagellar contribution, their presence could be absolutely negligible as well as pivotal.

3.4.2. SANS Measurements: Contrast Matching Method

SANS measurements were used to obtain more information about the different scattering contribution in the system. To prove or to invalidate the previously discussed estimations, the contrast matching method was used (see § 2.1.6). In principle, by suspending bacteria in a buffer comprising of the proper mixture of water and D_2O, it is possible to "match" the NSLD of a particular component and remove the corresponding scattering contribution from the whole SANS curve.

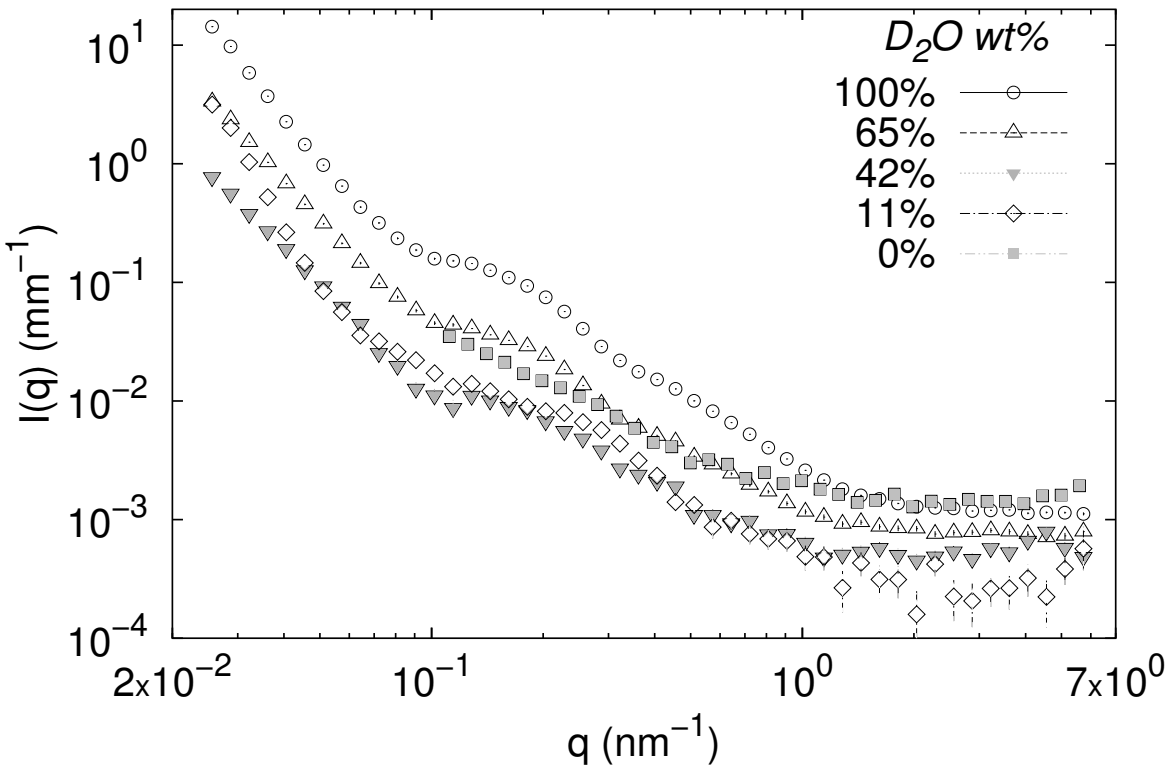

Figure 3.9.: SANS measurements of *E. coli* suspended in mixtures of PBS and D-PBS buffers. Bacterial concentration $OD_{600} = 10$, artificially concentrated from a culture stopped at $OD_{600} = 1$ (late-exponential growth phase). The curves are obtained by merging three measurements at different sample-detector distances (17.6, 5.6 and 1.4 *m*) and interpolating data into logarithmically spaced *q*-range.

The bacterial sample was harvested from the culture during the late-exponential growth phase ($OD_{600} \sim 1$) and re-suspended in 5 different buffers: in PBS and in D-PBS to have two references at 0 and 100% in D_2O weight ratio; in a mixture at 65 *wt%* to match the DNA/RNA contributions; at 42 *wt%* to equal the average NSLD of proteins and protein complexes; at 11 *wt%* to match the scattering signal coming from the phospholipid membranes (see Figure 2.5).

Normalised and background subtracted SANS data are shown in Figure 3.9. USAXS/SAXS

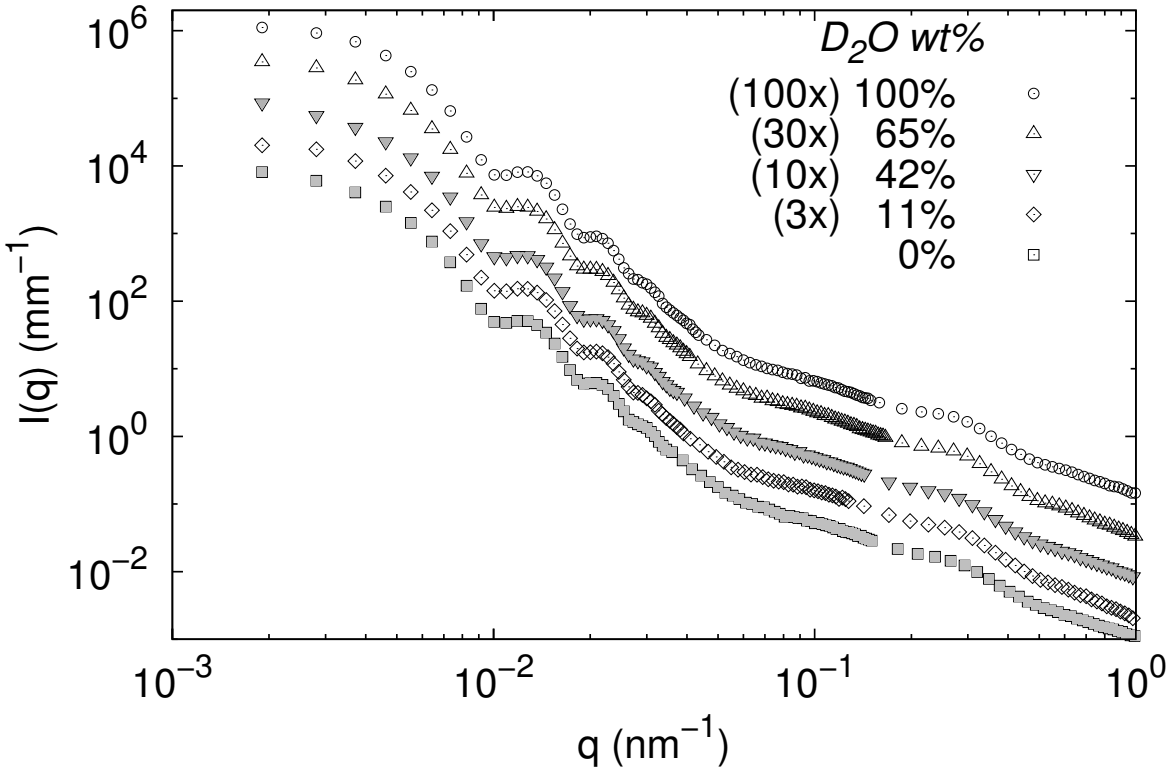

Figure 3.10.: USAXS/SAXS measurements of *E. coli* suspended in mixtures of PBS and D-PBS buffers. The measurements were acquired using the same samples employed to obtain SANS curves in Figure 3.9. The curves are obtained by merging three measurements at different sample-detector distances (30.8, 10.0 and 1.0 *m*).

measurements (Fig. 3.10) were performed on the same samples. This technique comparison is very useful to exclude any artefacts from X-ray radiation damage or possible toxic effects of the D_2O on the cells. X-ray data can be superimposed on a unique curve, thus no toxic effect due to heavy water is visible. Moreover, SAXS and SANS data at 11 *wt%* can be superimposed in the q-range $0.06 - 1\ nm^{-1}$, suggesting that X-ray findings are not influenced by the radiation damage. It is worth noticing that the latter superimposition was expected. Indeed the XSLD value for PBS (about 0.8% higher than pure water) is comparable with the contrast of phospholipids (see Tables 3.4 and 3.5).

Some qualitative information can be extracted by comparing SANS and SAXS curves. *i)* Data from samples at 11 and 42 *wt%* in D_2O exhibit the lowest total intensity in the q-range of primary interest $(0.1 - 1)\ nm^{-1}$. It confirms that lipid- and protein-like objects are the main scatterers here. This observations suggests that phospholipid membranes (rich in protein complexes) have a pivotal role in the description of the scattering curve in this range. *ii)* The curve at 42 *wt%* shows the lowest $I(q)$ values in the low-q region, where the contrast from the cytoplasmic core matters the most. Whereas membranes comprise both lipids and proteins, the

Table 3.5.: Equivalent D_2O *wt%* in buffer composition required to attain contrast matching condition. As an approximation, NSLD linearly increases as a function of D_2O *wt%* .

D_2O *wt%*	$NSLD \times 10^{-4}$ (nm^{-2})	**Component matched**
0% [H_2O]	-0.558	
11.3%	$+0.225$	Phospholipid
42%	$+2.353$	Protein
65%	$+3.947$	DNA
100% [D_2O]	$+6.373$	

cytoplasm contains no lipids. Hence one can infer that protein-like scatterers are mainly responsible for the core of the bacterium, confirming the goodness of the USAXS model in the previous section. *iii)* There are no differences except a scale factor between curves at 65 and 100 *wt%*, therefore any DNA/RNA contribution could be discarded. *iv)* Curves at 42, 65 and 100 *wt%* display a wiggle with maximum intensity at $q \sim 0.18\ nm^{-1}$ while at 11 *wt%* the peak shifts to $q \sim 0.27\ nm^{-1}$. It implies that the NSLD-description of the model has to include a major change in the range $(11-42)$ D_2O *wt%*.

3.4.3. Modelling of Gram-Negative Bacterium

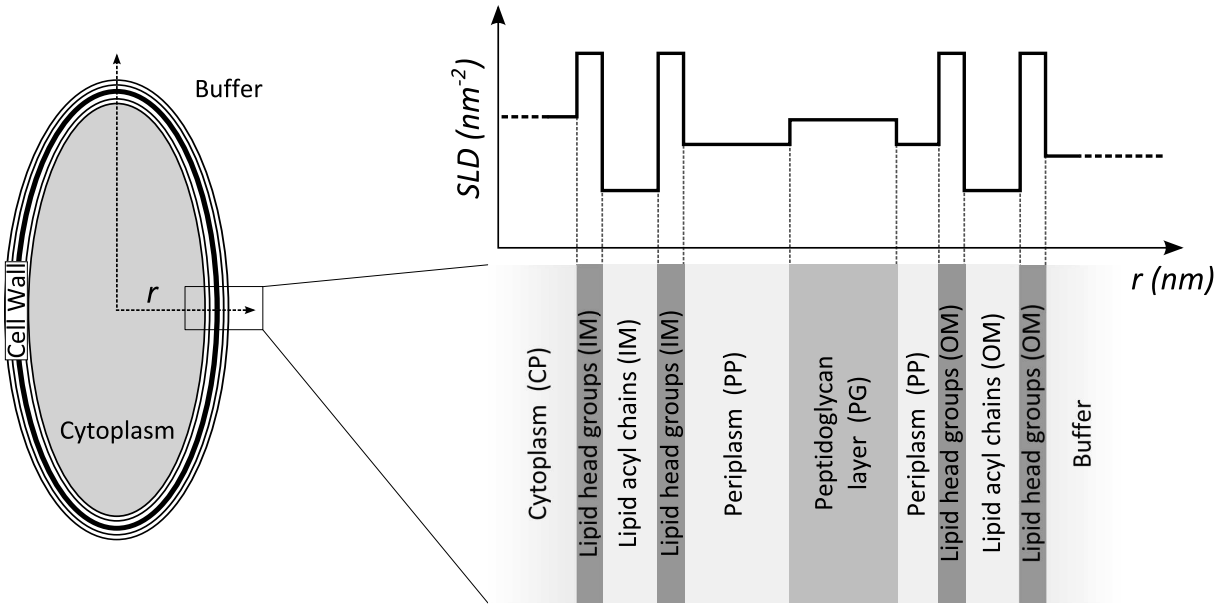

Figure 3.11.: Scheme of the core-multiple-shell geometry used to model the bacterial scattering form factor. Uniform SLD average values are used to approximate the cytoplasmic core and the shells describing a gram-negative cell wall.

The simple *E. coli* scattering form-factor discussed in § 3.3 need to be improved to include the presence of the cell wall. A scheme of a gram-negative bacterium is shown is Figure 3.11.

A cytoplasmic ellipsoidal-core with uniform density is surrounded by a series of layers describing the structure of the cell wall. Each layer is represented by an ellipsoidal-shell of uniform average density. The composition of the whole cell is very dynamic, small elements freely diffuse in the cytoplasm, in the periplasm and through the peptidoglycan stratum as well [132]. Membranes allow lateral diffusion of macromolecules and functional clusters, e.g. proteins and lipid rafts, as described in the revised fluid mosaic model [96]. Because of this continuous compositional fluctuations, inside each compartment no lateral structure is expected and each layer is approximated as a region with an homogeneous average XSLD or NSLD. For instance, a single phospholipid membrane involves three shells: two of them correspond to high-SLD regions consisting of lipid head-groups (full of phosphate groups), intra and inter-membrane proteins and hydration water; these enclose a low-SLD layer consisting of fatty acid chains from both inner and outer lipid leaflets and membrane proteins.

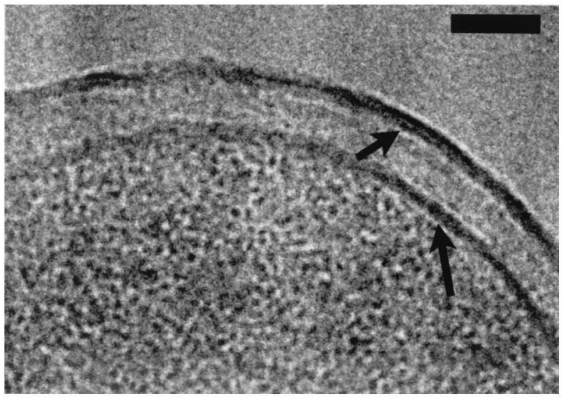

Figure 3.12.: Cryo-TEM image of a frozen thin section of *E. coli* K-12. The arrows point out the two inner and outer phospholipid membranes, defining the periplasmic space in between. Inside, a darker gray layer describe the peptidoglycan layer (Bar, 50 nm). Reproduced from [80] (DOI: 10.1128/JB.185.20.6112-6118.2003) with permission from the American Society of Microbiology.

The membrane model depicted in Figure 3.11 is based on cryoTEM measurements [77–80] on thin sections of vitrified bacteria, including *Escherichia coli* B, *Escherichia coli* K-12 (Fig. 3.12) and *Pseudomonas aeruginosa*. Therefore, in theory, this membrane model can be used to describe any gram-negative bacterium.

$$P_{shell}(q) = \left| \sum_{i=1}^{N} (\rho_i - \rho_{i+1}) \tilde{A}_{ell}(q, R_i, e, \theta) \right|^2 \quad \text{with} \quad \rho_{N+1} = \rho_{buffer} \tag{3.6}$$

Equation 3.6 refers to a core-multiple-shell form factor, where $\tilde{A}_{ell}(q, R_i, e, \theta)$ is the scattering amplitude of an ellipsoid, defined in Equation 3.5 (normalised by the SLD), with minor radius R_i and scattering length density ρ_i (R_1 and ρ_1 values define the core). To note that the width of each shell $R_{i+1} - R_i$ is constant over the entire surface and it is not deformed by the ratio e. The choice of a scattering amplitude related to an ellipsoid rather than a capped-cylinder lies on the numerical instability in the oscillations at high q-values for cylindrical-like form-factors (see Appendix A). To fix this issue requires an increase of computational time by several order of magnitude. Differences between these two geometrical shapes do not affect the analysis of the

inter-membrane structure. Structural characteristics from core and shells occur in a large spatial-scale, thus scattering features of the cell-envelope are not affected by the precise geometry of an elongated object.

In order to complete the picture, the presence of the flagella is included. Along with the membrane model, flagella could be described by using the formalism of a polymer-solution structure. The easiest representation of a polymer is the so-called Gaussian-chain [146, 147]. The model describes a polymer of contour length L as a chain consisting of N monomers placed on a pure random-walk (RW) trajectory. Here the repetition length $b = L/N$ of the polymer is depicted by the modulus of the displacement in the RW. By including excluded volume effects, a self-avoiding walk (SAW) is used for the description of self-avoiding polymers.

Needless to say, SAW description is more appropriate than RW for flagella: their function is to rotate and self-propel the cell-body, and a severe entanglement of these long filaments would not lead to any motion. The tendency to the flagella to form a bundle is a consequence of the hydrodynamics of the system [68] during the "run" phase of the run and tumble dynamics.

The R_g value of SAW polymers is given by:

$$R_g = \frac{1}{\sqrt{(2\nu+1)(2\nu+2)}} bN^{\nu} = \sqrt{\frac{25}{176}} bN^{3/5} \tag{3.7}$$

where ν is the excluded volume parameter, which is $\sim 3/5$ in the SAW description [148]. Flagella are very long and considering, for example, short and wavy filaments ($L/b = 2000/20$), an estimation for the smallest radius of gyration is $R_g \sim 110$ nm. It means that the shortest flagella will mostly contribute to the scattering signal in the same q-region of the cell-body or at even lower q-values. Thus, if visible, flagella may participate to the scattering curve by the asymptotic dependence as $q \to \infty$:

$$P_{SAW}(q) = B_{SAW} q^{-1/\nu} \simeq B_{SAW} q^{-1.7} \tag{3.8}$$

where $B_{SAW} \propto (\rho_{SAW} - \rho_{buffer})^2$. The value ρ_{SAW} is expected to be very close to protein values, as the flagellum is a purely protein-based assembly. It is worth mentioning that at high-q values a local structure may be visible and contribute to the scattering curve. However, as the flagellum radius is ~ 10 nm, the first visible maximum for a cylinder-like form-factor is at $q \sim 5/R \sim 0.5$ nm^{-1}, where the measured scattering patterns start becoming featureless. The high-q region shows no visible features and it could result from the presence of a multitude of small objects.

Finally, the model including cell-body, cell-envelope and flagella is given by Equation 3.9:

$$I(q) = n\left[< P_{shell}(q) >_{\Omega,\sigma_{CP},\sigma_{PP}} + P_{SAW}(q)\right] + Constant \tag{3.9}$$

where n is the number density of bacteria; a constant value is introduced as background to include the scattering at high-q from unidentified contributions; brackets $< \cdots >$ represent the orientation average and other two averages which include polydispersity in core radius (σ_{CP}) and periplasmic width (σ_{PP}). The former has been discussed in the previous section, while the latter includes the spatial fluctuation over the distances between inner and outer membrane. Both polydispersities are modelled using a normal PDF where σ_i values are the standard deviations. Both values are not meant to give a quantitative value for polydisersity and fluctuation or a study of the effective PDF, they are rather used as smearing functions based on real characteristic of the cell.

Before moving to the next section, it is worth spending a few words about the implementation of this approach. Bacteria are a very complex system and, for this reason, the model in Equation 3.9 must be as simple as possible and contain the smallest number of parameters. For example, the membrane profile to be used, schematised in Figure 3.11, is rectangular. It would be pointless adding any degree of complexity to it, in other words, more elaborated membrane-models, usually required to fit data from model vesicles [89, 97], are out of scope. Their application would increase the number of parameters and lead to false-positive results. Even the use of Gaussian-like or Fermi-Dirac-like profiles [98] enters in the same category. The membrane profile used here represents a minimal model for the description of the density profile of a gram-negative bacterium. This rectangular profile could be simplified if some features show no role in the data analysis, but it will not be further reduced *a priori*.

In order to get a genuine model, the number of parameters required to fully describe the system must be minimum. A famous saying among physicists, quoted from Enrico Fermi in 1953, is that "*I remember my friend Johnny von Neumann used to say, with four parameters I can fit an elephant, and with five I can make him wiggle his trunk*" [149, 150]. It is superfluous to say that Equation 3.9 demands much more than four parameters. The complete list of parameters is shown in Table 3.6. Excluding fixed terms, the number of free parameters necessary to describe the model is 17, that is a huge number. A single model has to be valid for the description of a set of five curves, one from SAXS and four from SANS from 100 to 11 D_2O *wt%* (the partial curve at 0 *wt%* will not be included in the preliminary analysis, but is as a cross-check). This means that each curve needs 7 local, 8 global and 2 partially-global parameters, bringing the total number of "effective" free parameters per curve to $\frac{8}{5} + \frac{2}{4} + 2 + 7 = 11.1$.

Jumping from 17 to 11.1 parameters is a good gain, but it is still more than twice the value needed to "fit the elephant". To make a realistic fit, each number needs *strict boundary-conditions* prior to fitting the data, and a *self-consistency check has to be performed* on the results. These two expedients are really important to select the solutions and discard any false-positive set of results. For example, SLD values for both IM and OM acyl-chain layer must result as an average between known average values of fatty acid chains and proteins. As well,

Table 3.6.: List of the 20 parameters involved in the bacterial model. They are classed in Global (10), Local (7) and Fixed (3) parameters. C_{IM} value represents the distance between the IM centre of mass and the centre of the elliptical core along the minor radius.

	Parameters	**Function**
Global	C_{IM} (nm)	Mean centre of mass of IM layer (distance from 0)
	D_{IM} (nm)	Centre-to-centre distance of the head-group layers in IM
	C_{OM} (nm)	Mean centre of mass of OM layer (distance from C_{IM})
	D_{OM} (nm)	Centre-to-centre distance of the head-group layers in OM
	C_{PG} (nm)	Centre of mass of the PG layer (distance from C_{OM})
	W_{ME} (nm)	Width of the head-group layers for both IM and OM
	W_{PG} (nm)	Width of the PG layer
	ρ_{TI} (nm^{-2})	Average SLD of the tail-group layer in IM
	ρ_{TO} (nm^{-2})	Average SLD of the tail-group layer in OM
	R_M (nm)	Major radius of the elliptical core ($C_{IM} \times e$)
Local	n (ml^{-1})	Cell number density
	ρ_{CP} (nm^{-2})	Average SLD of the CP core
	ρ_{PP} (nm^{-2})	Avelage SLD of the PP layer
	ρ_{ME} (nm^{-2})	Average SLD of both IM and OM head-group layers
	ρ_{PG} (nm^{-2})	Average SLD of the PG layer
	B_{SAW} $(nm^{-2.7})$	Intensity factor for SAW polymers
	Con (mm^{-1})	Constant value
Fixed	ρ_{BF} (nm^{-2})	SLD of the buffer solution
	σ_{CP} (nm)	Standard deviation of the C_{IM} distribution
	σ_{PP} (nm)	Standard deviation of the C_{OM} distribution

the distance between PG and OM cannot be larger than 8.3 *nm*, i.e. the length of the Braun's Lpp that bind together these two layers [134]. Any set of results that deviates from a confident physical model is rejected.

To fit SAS data with membrane models, where variables have a high degree of correlation, is usually hard because of the huge number of local minima in the χ^2 function. The fits could easily converge to a local χ^2 minimum and never reproduce the data or, even worse, might converge to a local minimum very close in value to the global one. The latter case is dangerous because it is more likely to lead to false results. To avoid this instance, the only way to judge the solution is to have a robust physical and structural model of the system and checking the self-consistency of the final result. Anyway, in the case of convergence to a local minimum far from the real solution, the actual problem is the feasibility of the analysis. The standard minimization algorithm used by most of the fitting routine, the Levenberg-Marquardt method, is not apt for this kind of situations. When the function comprises such number of highly-correlated variables, the set of results is greatly related to the set of initial free parameters.

Essentially, the only way to skip the local minima is to start with an initial set of values that is already the set of solutions. In this work, this issue was overcome by using the Genetic Selection algorithm [100]. It is particularly suitable for solving problems with a high number of variables and, above all, it is designed to avoid false convergences in local minima. More details of this method are provided in Appendix B.

3.4.4. Data Analysis and Discussion

In this section, the application of the model and the fit results are discussed. Global parameters were recursively refined and improved to have the best agreement with all the concerned curves, while local parameters were obtained independently. Every outcome that did not follow the model criteria, defined in sections § 3.4.2 and § 3.4.3, was discarded. In the same way, every series of outputs able to describe only a sub-set of curves was rejected. Finally, every not-self-consistent set of results was also excluded.

In this section the best results are shown in Figures 3.13 and 3.15. Here the term "best" implies that the complete set of values is able to represent the entire model by meaningful values; to give an optimum cumulative χ^2 value; to fulfil the self-consistence criteria (discussed in the following). Results are listed in more detail in Table 3.7. Figures 3.14 and 3.16 show the contribution of the SAW polymers compared to the core-shell signal.

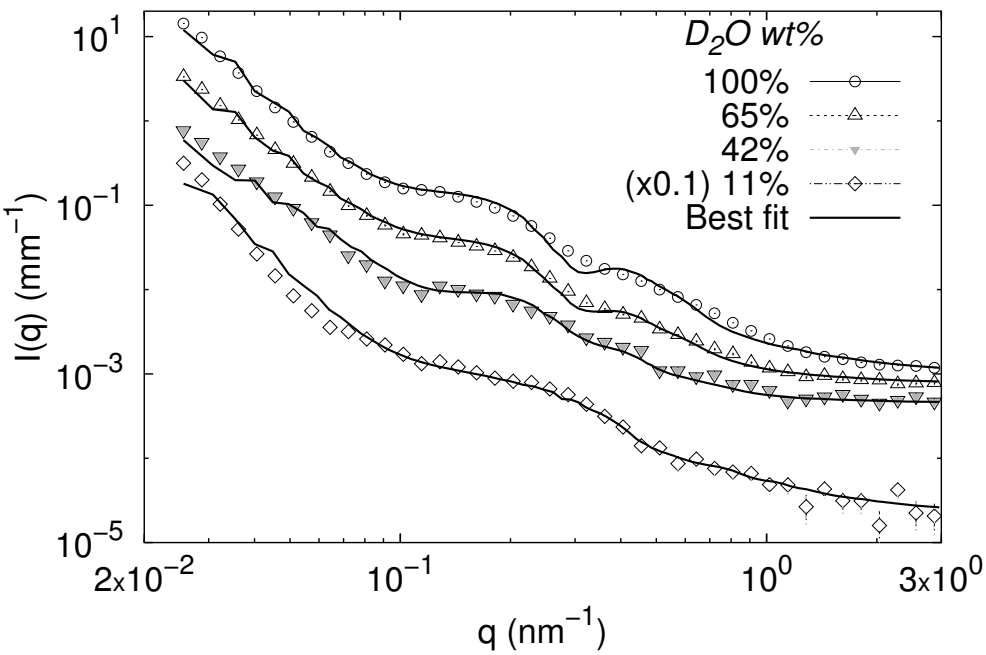

Figure 3.13.: SANS data fitted with Equation 3.9. Data concern samples at 11, 42, 65 and 100 D_2O *wt%* in the suspension medium.

Table 3.7.: Set of results from five fits on SANS curves at 11, 42, 65 and 100 D_2O *wt%* and the USAXS/SAXS curve at 0 D_2O wt% in buffer composition. Shared columns refer to global parameters.

(*nm*)	**Global**
C_{IM}	395
D_{IM}	4.3
C_{OM}	29.7
D_{OM}	6.3
C_{PG}	11.0
W_{ME}	0.94
W_{PG}	6.9
R_M	910
σ_{CP}	10
σ_{PP}	4

Local

	SANS (D_2O wt%)				*USAXS/SAXS*
$\times 10^{-4}$ (nm^{-2})	**11**	**42**	**65**	**100**	
ρ_{CP}	1.01	2.13	2.78	4.08	10.26
ρ_{PP}	0.26	2.04	3.39	5.64	9.51
ρ_{ME}	1.91	2.49	2.93	3.66	12.16
ρ_{PG}	1.65	2.22	2.75	3.72	11.64
ρ_{TI}		0.93			8.56
ρ_{TO}		-0.11			8.00
ρ_{BF}	0.20	2.04	3.64	5.91	9.47
$n \times 10^9$ (ml^{-1})	7.3	6.2	6.3	6.7	7.4
$B_{SAW} \times 10^{-11}$ ($nm^{-2.7}$)	30.0	9.0	33.8	131	119
$Con \times 10^{-4}$ (mm^{-1})	2.1	5.0	5.8	9.7	3.6

In the context of this analysis, *a set of results is self-consistent if it is able to describe the model in its entirety, including features that are not directly incorporated in Equation 3.9.*

As a first step, the values of ρ_{CP}, ρ_{PP}, ρ_{ME} and ρ_{PG} from SANS measurements are supposed to be linear with the D_2O content in the buffer (which in turn scales linearly with ρ_{BF}). This is expected due to the semi-permeability of the membranes. The mixture of water and D_2O is free to diffuse into the cytoplasm, the periplasm and through the peptidoglycan. For the same reason D_2O concentration is also in equilibrium with the hydration water of the lipid head-groups in both the inner and outer membranes. Furthermore, every carboxyl (–COOH $\rightleftharpoons$ –COO^-) and amine (–NH_2 $\rightleftharpoons$ –$NH_2{}^+$) groups accessible to the solvent (present in DNA and proteins as instance) are free to exchange labile H^+ and D^+ with the solvent.

The linearity of these parameters is then the first self-consistency control. In Figure 3.17

linear fits of NSLD values as a function of D_2O concentration are presented. The error bars in these plots were obtained by repeating the Genetic Selection algorithm 4 times with fixed global parameters, and considering half of the range $\Delta x = \frac{|x_{MAX} - x_{min}|}{2}$.

Linear regressions are also necessary in order to proceed to the second step in testing the model. From there, NSLD values at 0 D_2O *wt%* are extrapolated. Those, together with global

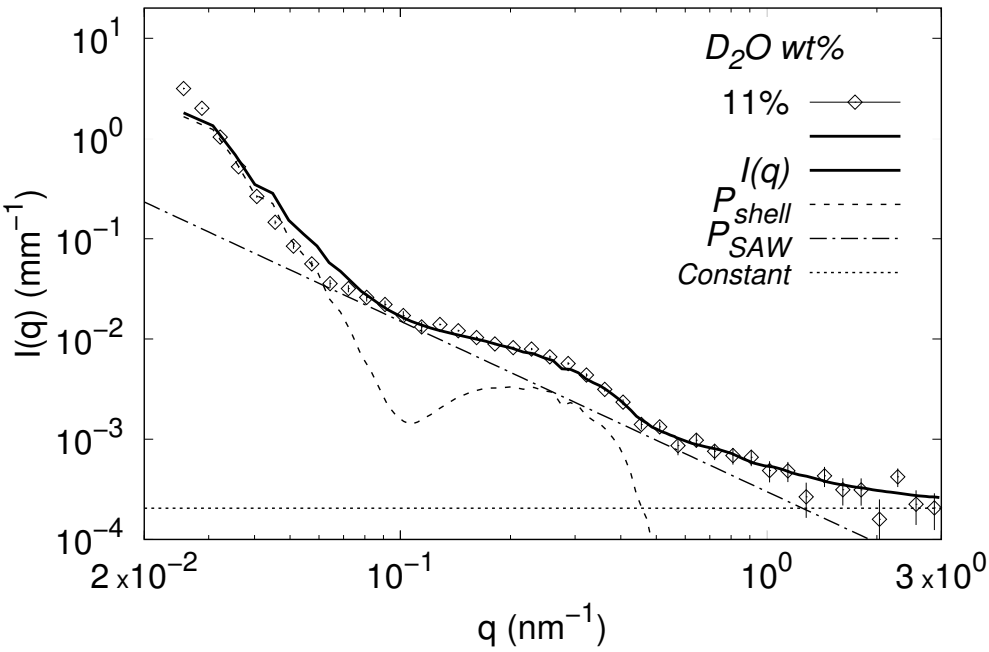

Figure 3.14.: SANS data fitted with Equation 3.9. Data concern the sample at 11 D_2O *wt%* in the suspension medium. The best fit (solid line) is the sum of the membrane model $< P_{shell}(q) >$, the SAW polymer model $P_{SAW}(q)$ with slope $q^{-1.7}$ and the constant value.

Table 3.8.: Summary of the parameters describing the partial SANS curve at 0 D_2O *wt%*. SLD values were recovered from a linear extrapolation. Values of n, B_{SAW} and Con were obtained by fitting the SANS curve (global and extrapolated parameters were fixed).

From Extrapolation	
Parameter	**NSLD** $\times 10^{-4}$ (nm^{-2})
ρ_{CP}	0.623 ± 0.007
ρ_{PP}	-0.38 ± 0.01
ρ_{ME}	1.69 ± 0.01
ρ_{PG}	1.40 ± 0.05
From Fit	
$n \times 10^{9}$ (ml^{-1})	7.0
$B_{SAW} \times 10^{-11}$ $(nm^{-2.7})$	54 ± 2
$Con \times 10^{-4}$ (mm^{-1})	12

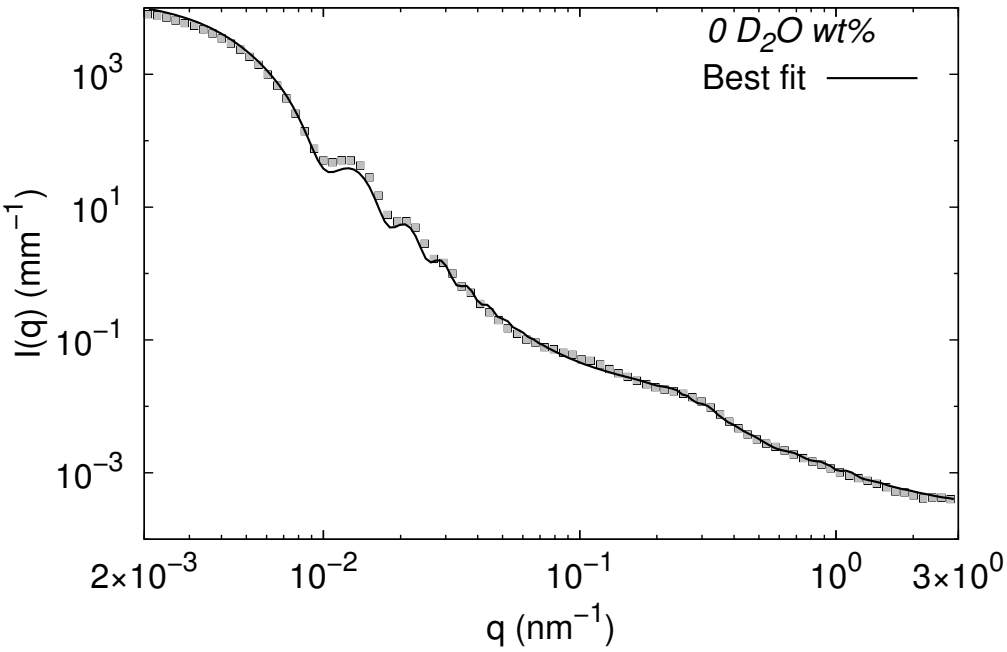

Figure 3.15.: USAXS/SAXS data fitted with Equation 3.9. Data concern the sample at 0 $D_2Owt\%$ in the suspension medium.

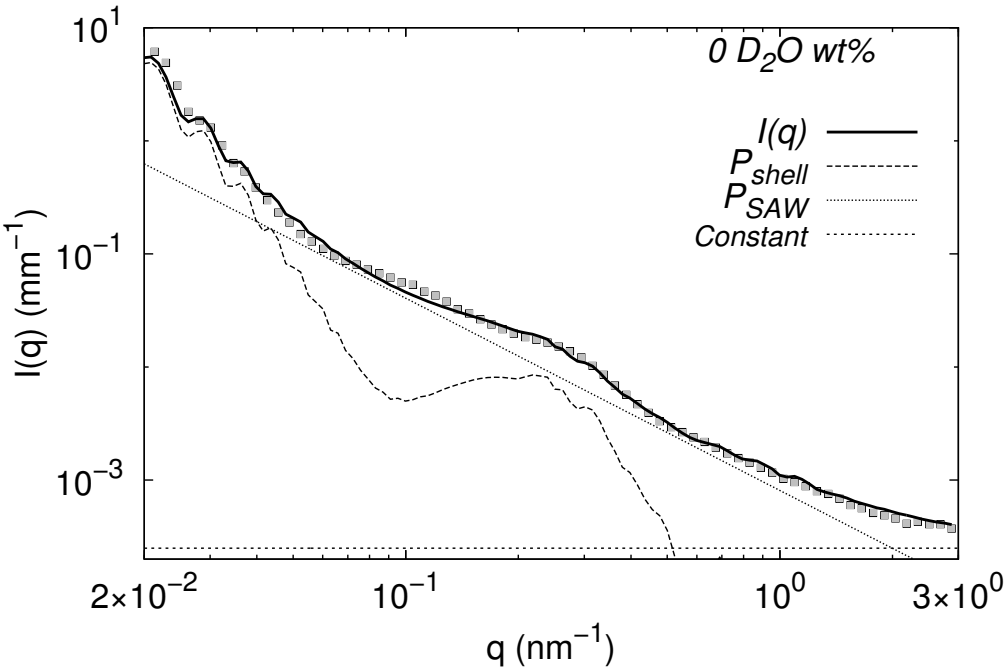

Figure 3.16.: USAXS/SAXS data fitted with Equation 3.9. Data concern the sample at 0 D_2O $wt\%$ in the suspension medium. The best fit (solid line) is the sum of the membrane model $< P_{shell}(q) >$, the SAW polymer model $P_{SAW}(q)$ with slope $q^{-1.7}$ and the constant value. To notice that the low-q region is fully described by $< P_{shell}(q) >$.

parameters, have to be apt to fit the corresponding SANS curve. The fit (Figure 3.18) was performed leaving only n, B_{SAW} and Con as free parameters.

From this last fit, n and B_{SAW} parameters are obtained and used as further control. The bacterial concentration n is adjusted to be the same for all the curves, the five SANS and the USAXS/SAXS as well. All the samples were prepared at a nominal concentration of $\tilde{n} \sim 8 \times 10^9\ ml^{-1}$ ($OD_{600} = 10$). The six n values obtained from the fits are expected to be the same, reflecting the confidence of the sample preparation. In Tables 3.7 and 3.8 the six n values are tabulated. They are comparable and give an average of $\langle n \rangle = (6.8 \pm 0.6) \times 10^9\ ml^{-1}$ (the error is half of the range). The sample concentration is a prefactor in the scattering intensity function,

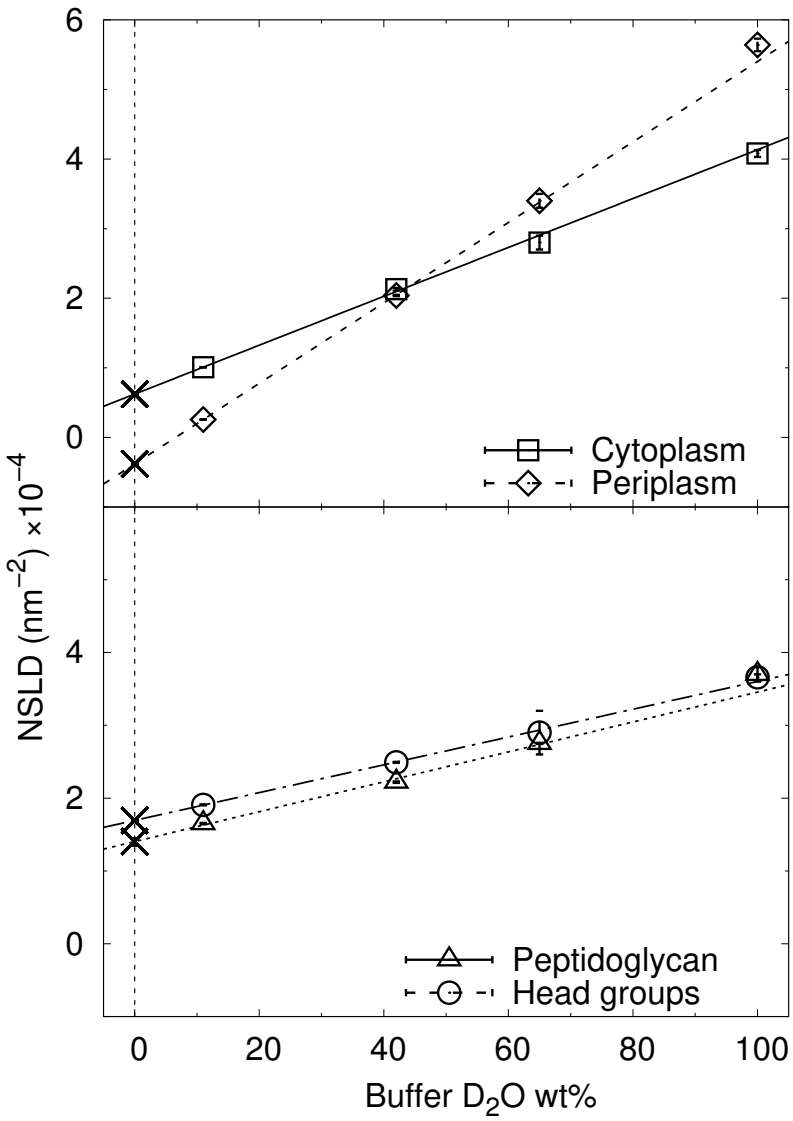

Figure 3.17.: NSLD values for CP, PP, PG and phospholipid head groups as a function of the nominal D_2O concentration. A weighted linear regression is used to extrapolate the respective values for the fit at 0 $wt\%$ in D_2O.

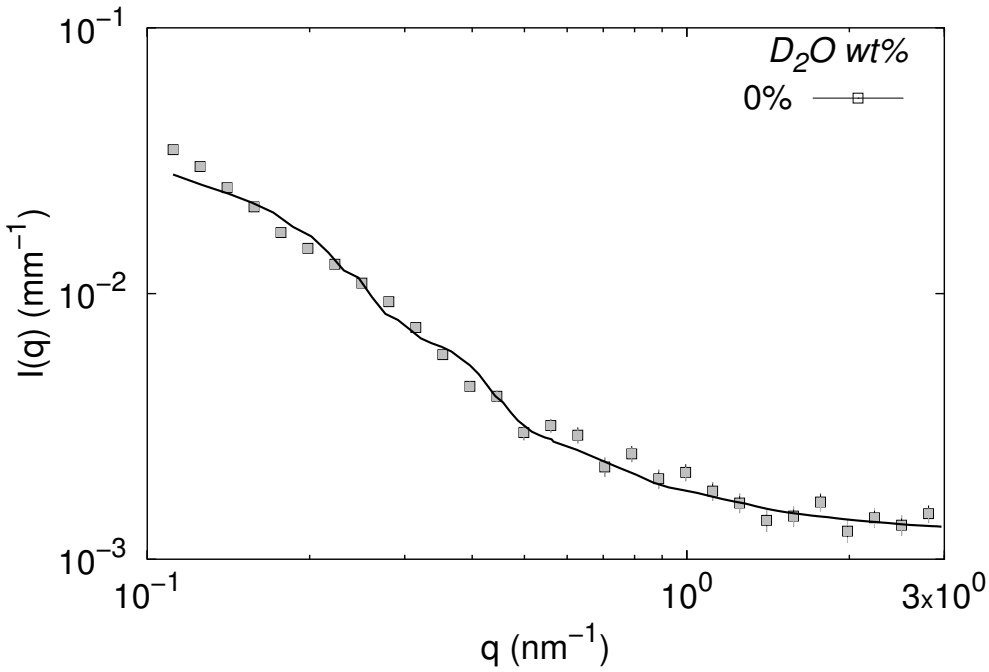

Figure 3.18.: Curve fitting of *E. coli* suspended in pure PBS (0 D_2O *wt%*). The solid line describes a fit obtained by fixing global and extrapolated parameters.

hence the relative error on n of $\pm 9\%$ can be considered as a maximum global error on each XSLD/NSLD profile. Furthermore it is worth noticing that the average measured value $\langle n \rangle$ is close to the nominal $\tilde{n}$, with a discrepancy of $\sim 15\%$.

Finally, as a last test of self-consistency, the contribution of the SAW polymer is taken into account. This term is assumed to describe the presence of flagella in the total scattering intensity. Flagella content is purely protein based, therefore, B_{SAW} values, normalised by n, are expected to have a quadratic dependence on the buffer NSLD, following the equation:

$$B_{SAW} \propto n(\rho_{SAW} - \rho_{BF})^2 \tag{3.10}$$

To confirm that this term is related to the presence of flagella, their contrast should be close to the typical protein value of $1.9 \times 10^{-4}\ nm^{-2}$. The fit is shown in Figure 3.19. It gives a matching point at $38.0 \pm 1.7\ D_2O\ wt\%$, equivalent to an NSLD value of $(2.08 \pm 0.12) \times 10^{-4}\ nm^{-2}$, and is in good agreement with the expectations.

Plots in Figures 3.17 and 3.19 display the nominal concentrations of D_2O along the x-axis. These values might be affected by possible pollution or D_2O lost, despite all the necessary precautions. Moreover, it is normal to expect a significant formation of HDO in dynamic equilibrium with H_2O and D_2O. Although, this has no effective impact on the contrast, indeed a mixture of H_2O/D_2O has the same number of H, D and O atoms, regardless of their molecular

arrangement. What matters in this case is the density of the mixture, but, considering that the density of pure H_2O and pure D_2O differs by 10% (respectively 0.997 and 1.107 $g\ cm^{-3}$ at 25 $°C$), one can assume that divergences in NSLD-buffer values are not significant. Accounting for all these reasons, ρ_{BF} values were allowed to vary during the fitting procedure (up to 10% from nominal values).

A further test for the consistency of the SAW term can also be performed from USAXS/SAXS data. In Figure 3.20 the SAW contribution, $P_{SAW}(q)$, is compared with evaluations calculated by accounting for cell concentration, flagella number $N = 7 - 10$, volume V and difference in XSLD. This simulation were performed using the OZ equation (see Eq. 2.18), with exponent $p = d_f = 1.7$, as determined by the SAW model. The intensity $I(0) = nNV^2\Delta\rho^2$ was calculated using bacterial concentration n from fits while the other parameters were taken from estimations in Tables 3.3 and 3.4. The correlation distances ξ were calculated following Equations 2.19 and 3.7 considering two extreme R_g values, short/wavy ($L/b = 2000/20$) and long/smooth ($L/b = 15000/500$) flagella, respectively $R_g = 113\ nm$ ($\xi = 71\ nm$) and $R_g = 1393\ nm$ ($\xi = 873\ nm$). From these values, lower and higher simulated scattering profiles were used to describe a possible contribution of the presence from flagella. The fitted $P_{SAW}(q)$ compares with the asymptotic trends of simulated data that behave as boundary limits of it for $q > 0.06\ nm^{-1}$.

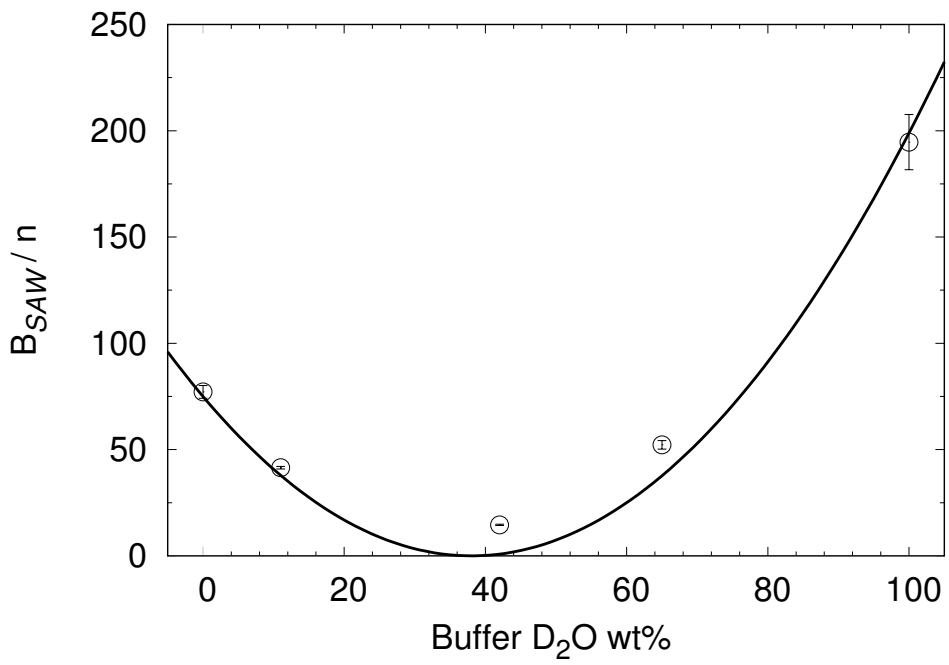

Figure 3.19.: Fitting of B_{SAW}/n values as a function of the nominal D_2O concentration. The minimum of the parabola is close to the matching point for protein systems, that is roughly 36 D_2O $wt\%$ ($1.9 \times 10^{-4}\ nm^{-2}$).

In Figure 3.21 both X-ray and neutron SLD-profiles of the cell envelope are displayed, summarising the fitting results in Tables 3.7 and 3.8. Besides the SAW contribution, these profiles fully describe the entire cell. The values are physical and supported by the descriptions in § 3.1 and in Table 3.4 but, in the interest of estimating confidence, they will be thoroughly discussed.

The most important and quantitative results are C_{OM} and C_{PG}. Together, these two distances entirely define the two peak position at $q \sim 0.18\ nm^{-1}$. C_{OM} is a key distance for SANS data from 42 to 100 *wt%*, where both *IM* and *OM* acyl-chain layers appear as two deep wells over a high SLD profile. Indeed this width dominates over the other features of the SLD profile and, by itself, delineates the position of the peak in these three curves. The effective average width of the periplasmic space is then 23 *nm*, in perfect agreement with the expected range $(11-25)$ *nm* [78] and with the most recent cryo-TEM observations (21 ± 3) *nm* [80]. Instead, the value of C_{PG} is fundamental to the shift observed in the peak in SANS data at 11 *wt%*. This peak at $q \sim 0.27\ nm^{-1}$, observed also in SAXS data, results from a combination of three high-contrast layer, i.e. the two membranes and the peptidoglycan region. Once the C_{OM} value is fixed, C_{PG} is univocally obtained. Thus, the peak shift is due to the interference of the high-contrast *PG* layer on the membrane-membrane distance. Because no change in SLD of the acyl chain is expected as a function of the hydration, this effect is visible only in SAXS data and SANS

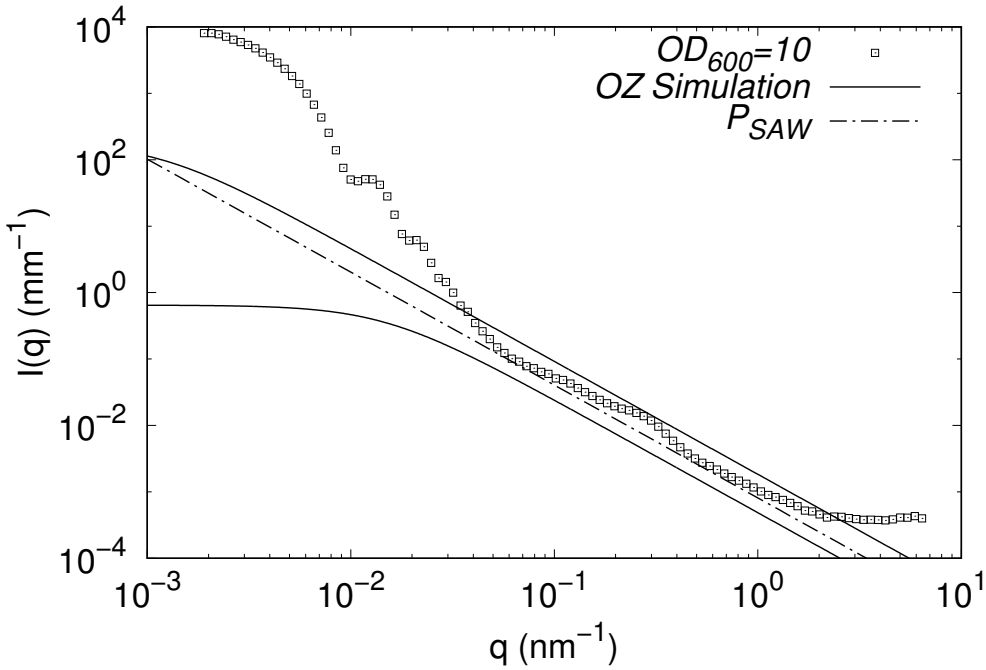

Figure 3.20.: Comparison between the fitted $P_{SAW}(q)$ term and simulated minimum and maximum contributions from flagella. Those are modelled using Ornstein-Zernike equation for SAW polymers with correlation length $\xi = 71$ *nm* and $\xi = 1393$ *nm*. Concentration, volume and contrast values are consistent with the known structural description of the flagella.

at 11 *wt%*, where the contrast of IM, OM and PG layers is comparable, whereas, with more heavy-water diffused into the cell, IM and OM acyl-chain contrast is far more emphasised than the one in the PG layer. Considering PG and OM widths, the periplasm region in between these two layers is 4 *nm*, consistent with the range (5.3 ± 0.9) *nm* found using cryo-TEM [80], while the centre-to-centre distance of PG and OM layers is 11 *nm*. These results are also consistent with the length of the cylindrical Braun's lipoprotein (Lpp-56) of 8.3 *nm* [134], confirming that these proteins are partially embedded in the outer membrane.

C_{IM} and R_M values entirely result from the USAXS data at low-q and they do not affect the membrane geometry. R_M suffers from the same issues discussed in § 3.3.2 and C_{IM} is represented by the positions of the minima in USAXS data. C_{IM} is the minor radius of the cell core and hence, describing the extension of the cytoplasm, it is linked to the "weight" of the cytoplasmic SLD in the core/envelope system. It means that the C_{IM} value is determined by minima position only once a specific membrane-profile is given. For this reason, a test membrane-profile was firstly recovered from the set of SANS data and then verified and refined on the USAXS/SAXS curve. The result C_{IM} is in agreement with USAXS data previously shown (see Fig. 3.6).

Values for σ_{CP} and σ_{PP} can be considered as empirical parameters. They are related to real polydispersity in cell size and fluctuation in inter-membrane distance respectively, but, as discussed in § 3.3.2, more sources of curve-smearing and more information are needed to obtain precise polydispersity estimations. As a matter of fact, σ_{CP} and σ_{PP} cannot be used to extrapolate quantitative information on the PDF of C_{IM} and C_{OM}.

The two intra-membrane distances, D_{IM} and D_{OM}, together with W_{ME}, represent the two total widths of the inner and outer membranes. These widths are, in the order, 5.2 and 7.2 *nm*, and they match with the observed values of (5.8 ± 0.4) *nm* and (6.9 ± 1.0) *nm* respectively. Similarly, the width of the PG layer (6.9 *nm*) is compatible with (6.4 ± 0.5) *nm* [80]. In spite of this agreement, the parameters could be strongly correlated with ρ_{TI}, ρ_{TO}, ρ_{ME} and ρ_{PG} values. Theoretically, the scattering contribution coming from a single layer of the SLD profile is described by its centre of "mass" C_i and the area outlined in the rectangular profile, i.e. $\rho_i \times WIDTH_i$. Previously, C_{OM} and C_{PG} were assigned to the positions of the scattering peaks observed in the curves. Now instead, D_{IM} and D_{OM} values cannot be ascribed to any visible features (expected around $q \sim 1\ nm^{-1}$), so cannot account for precise intra-membrane distances. However, they also represent the widths of the acyl-chain regions centred at C_{IM} and C_{OM}, so, together with ρ_{TI}, ρ_{TO} values, they are essential for the presence of the peak at $q \sim 0.18\ nm^{-1}$. A realistic error in both D_{IM} and D_{OM} is ± 1 *nm*.

An analogous discussion regards W_{PG} and W_{ME}. The lack of resolution at $q \sim 1\ nm^{-1}$, due to the complexity of the system, affects the determination of W_{PG} and, even more, W_{ME}. The former has also a confidence of ± 1 *nm*, while the latter is compatible with known values of

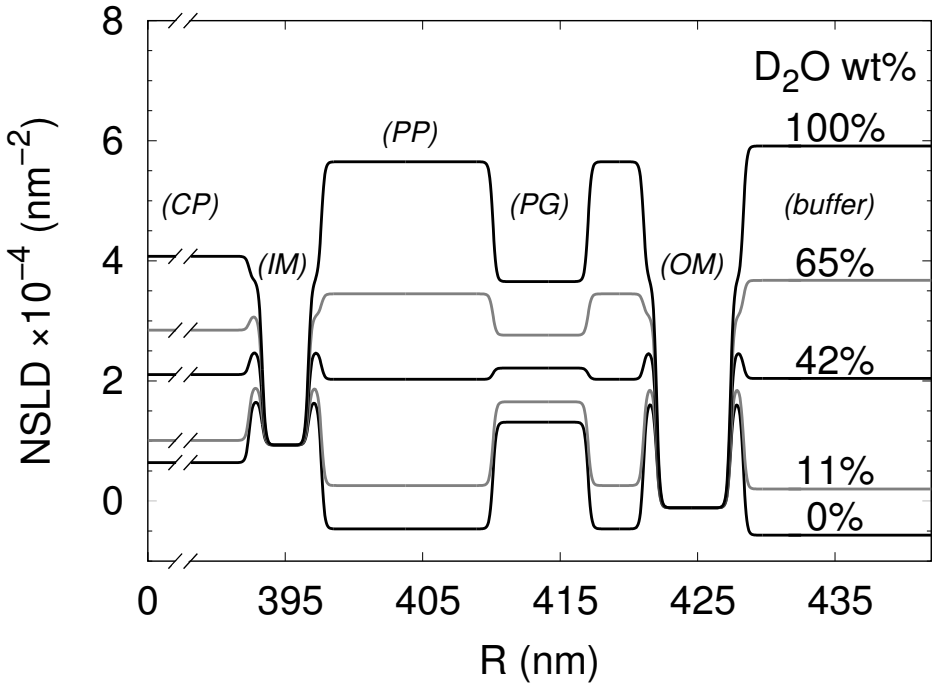

(a)

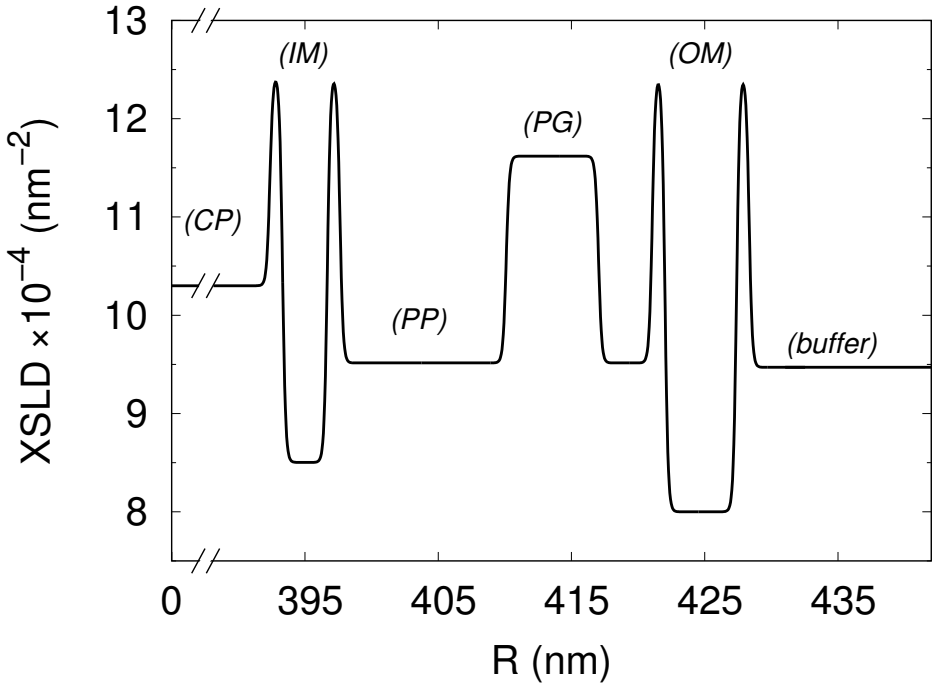

(b)

Figure 3.21.: a) NSLD profile for five different contrast match-point. The x-axis refers to the short radii of the ellipsoid. The same profile is applied all over the ellipsoid. b) XSLD profile for the system suspended in PBS buffer. In both figures, the smearing of the rectangular SLD-profile is only used for a better visibility.

head-groups in phospholipid membrane of $(0.7-1)$ nm, which can be used as an interval of confidence, considering the fact that it includes the presence of LPS in the asymmetric OM. Looking at the NSLD profiles in Figure 3.21(b) for 100 and 65 $wt\%$, it would be legitimate to question the possibility of discerning head-group from acyl-chain SLD values and then to try using single average SLD values for the whole IM or OM. This scenario had been explored but it did not give either consistent results or proper curve fits. In order to describe the peak-shift from 0.18 to 0.27 nm^{-1}, an average SLD for the membranes is not suitable to obtain an interference among IM-PG-OM layers. To get it, the sets of pairs (W_{PG}/ρ_{PG}) and (W_{ME}/ρ_{ME}) must depict well-pronounced and separated peaks in the SLD profiles. This leads to restrictions in broadening for W_{PG} and to the observation of the pair (W_{ME}/ρ_{ME}). Once it is achieved, as ρ_{TI} and ρ_{TO} values are the same in all the fitted SANS profiles, the visibility of the head-group layers becomes feasible also for the curves at 42, 65 and 100 $wt\%$, as it was confirmed in the self-consistency check in Figure 3.17.

A rough estimation of confidence for the whole set of SLD values could be done comparing the XSLD and NSLD profiles at 0 $wt\%$ in D_2O content. For model lipid-bilayer systems, consisting of one single species of lipid with known specific volumes of head-group and acyl-chains, it is possible to recover the volume fraction of the hydration water x_w in the head-group region, by using the relation:

$$\rho_{obs} = x_w\rho_w + (1-x_w)\overline{\rho} \quad \Rightarrow \quad x_w = \frac{\rho_{obs}-\overline{\rho}}{\rho_w-\overline{\rho}} \tag{3.11}$$

where ρ_{obs} is the measured value of the head-group layer, $\overline{\rho}$ comes from the effective volume occupied by the head-groups and ρ_w is the contrast of water. The more the measured SLD profile is realistic, the more this relation becomes precise. In a complex system such as a bacterium several phospholipid species are present, the protein content varies from one region to another and the knowledge of each $\overline{\rho}_i$ value can only be estimated. Therefore, the relation 3.11 becomes a big approximation and it can still be used as a conceptual exercise. For the IM and OM acyl-chain layers (ρ_{TI} and ρ_{TO}), where buffer molecules cannot enter, the same approach is used but the hydration is substituted by the protein content x_p and average protein $\overline{\rho}$ values are used. As well, all the $\overline{\rho}_i$ values are taken from Table 3.4. The aim is to compare x_w or x_p values from the XSLD and NSLD profiles for each layer, including the core, and extract an over-estimation of the errors from the discrepancies.

In Table 3.9 mean values for x_w and x_p are reported and listed in ascending order by the relative error δ_r. This exercise, though for the estimation of the confidence for the SLD values, is considered conceptual because x_w and x_p values cannot be considered quantitative evaluations of the water content or protein content. Actually, the relative errors shown in Table 3.9 could be overestimated depending on how much the test $\overline{\rho}_i$ values are far from the actual quantities.

Table 3.9.: Estimation of the water content (x_w) or protein content (x_p) for each layer. The error is calculated as half or the discrepancy between the two values from the XSLD and NSLD profiles. Raws are ranked by the relative error δ_r.

Layer	$x_w(x_p)$ from NSLD	from XSLD	**mean values and confidence**
Periplasm	0.93	0.98	0.95 ± 0.03 (3%)
Cytoplasm	0.64	0.84	0.74 ± 0.10 (13%)
OM acyl-chains	0.11	0.08	0.095 ± 0.016 (17%)
Peptidoglycan	0.20	0.14	0.17 ± 0.03 (17%)
Head-groups	0.22	0.45	0.33 ± 0.12 (40%)
IM acyl-chains	0.57	0.21	0.39 ± 0.18 (50%)

The periplasm ρ_{PP} evaluation is the most accurate ($\delta_r \leq 3\%$). The $\overline{\rho}$ value here is fully approximated to a protein-like contrast, neglecting any other kind of smaller solute in the whole periplasmic space. The PP contrast is very close to the buffer, representing a space that is almost empty. This result is in contradiction with the concept of a dense "periplasmic-gel" observed by cryo-TEM [77, 79] and FRAP (Fluorescence Recovery After Photo-bleaching) [151] measurements. With the former technique, the freeze-substitution method introduce a staining that biases the estimations of the actual electron densities; the latter instead may have been an ill-conditioned method for the determination of the effective viscosity in the periplasmic region. In this paper Mullineaux et al. [151] described an experimental design that requires the introduction of many biochemical variants into the cell, in order to express GFP protein (used as probe) and make it interact with a protein responsible of the exportation in the periplasm. The mechanism of the interaction of proteins or external bodies with the complexes in the inner membranes and with the peptidoglycan layer are manifold and not fully understood. Moreover the high oxidative conditions of the periplasm add more questions about the native nature of the protein used as a probe. Recent cryo-TEM observations by Matias et al. [80] were performed avoiding the staining due to the freeze-substitution method and stabilizing the hydrated, frozen sample using a high concentration of sucrose as cryo-protectant. In this case they also reported the detection of a quite empty periplasmic space.

The evaluation of the error associated to the average cytoplasmic contrast ρ_{CP} ($\delta_r \leq 13\%$) was achieved with an $\overline{\rho}$ value obtained considering a fictitious volume proportion of 1:1 in DNA- and protein-like compounds from both nucleoid and non-nucleoid regions. This raw approximation gives a mean water content of $x_w = 0.74 \pm 0.10$ that could be associated to the estimation of the protein volume fraction of $\sim 30\%$ in the non-nucleoid region [125]. Values of ρ_{CP} are correlated to the radius C_{IM} and are very important in the fitting of the whole (U)SAXS curve. Likewise, for SANS curves, the difference between ρ_{CP} and ρ_{BF} is the primary origin of the different slopes in the lowest q-range.

The result about ρ_{PG} ($\delta_r \leq 17\%$) occurs along with the description of an empty periplasmic region. This SLD is correlated with the PG width D_{PG} and this two values, together with a low ρ_{PP}, define a very distinct peak in the SLD profile. As for the PP region, here $\overline{\rho}$ represent a full protein-based contrast, ignoring not only the rest of the periplasmic content but also the contribution of the peptidoglycan network. Due to its mesh-like structure, the estimation of the SLD of the murein region is tough. Using a surface density of murein monomers of 1.65 nm^{-2} [152] and a total layer volume from the current structural analysis, rough estimations of $XSLD = (0.5 - 1.2) \times 10^{-4}\ nm^{-2}$ and $NSLD = (0.8 - 1.8) \times 10^{-4}\ nm^{-2}$ are obtained. Comparing this values with the those in Table 3.4, it is clear that the PG network, at most, can contributes to the scattering as a protein system. Moreover, estimations of the volume occupied by the PG range from 30% to 60%, hence any misinterpretation of volume and SLD values are reflected in the x_w evaluation, making it not suitable for a proper measurement of water or protein content in the region. However, the measured ρ_{PG} value is close to a protein-like contrast, suggesting that, even for the most compact and dense PG, a relevant fraction of the PG layer is occupied by proteins.

The confidence of the ρ_{ME} estimation ($\delta_r \leq 40\%$) is obtained using $\overline{\rho}$ values from a fictitious volume proportion of 1:9 of protein and phospholipid head-groups. In this case the differences are negligible because of the similarity of the contrast of these two class of macromolecules. The information about the actual hydration content cannot be taken into account, especially because of low level of confidence and the strong correlation with the width W_{ME}. A possible source of error can be ascribed to the approximation of using a single value for the description of four different lipid leaflets, with big differences in particular in the outer one, full of rafts of LPSs.

Finally, the relative errors in ρ_{TI} and ρ_{TO}, respectively $\delta_r \leq 50\%$ and $\delta_r \leq 17\%$ are evaluated. Here $\overline{\rho}$ values are associated to the average contrast of the lipid acyl-chains and a possible protein content x_p is obtained. The results are strongly correlated with the widths D_{IM} and D_{OM} and, due to the very low confidence for the IM, no quantitative results can be obtained from these values. However, the main information is the difference in protein content between IM and OM, confirming that the OM contains less proteins than the IM [130].

3.4.5. Alternative Scattering Model

In the previous section, the criteria for the feasibility and the reliability of the analysis has been shown, highlighting the rules for the rejection of any unphysical and inconsistent set of results. Needless to say, all these methods refer to the use of a specific scattering model. For the sake of completeness an alternative bacterial model is presented in this section and, at the end, the same consistency checks are applied. The modeling of the membrane structure $P_{shell}(q)$ is preserved,

but, instead of considering the presence of the flagella, the scattering from the polydisperse protein population inside the bacterium is taken into account with a generic Guinier law.

$$I_G(q) = I_{pr} e^{-q^2 R_g^2/3} \tag{3.12}$$

where the relation $I_{pr} \propto (\rho_{protein} - \rho_{BF})^2$ contains the assumption that the cytoplasmic medium has a contrast similar to the buffer, and R_g is the average value of the radius of gyration of the proteins. The whole model now is expressed by:

$$I(q) = n\left[< P_{shell}(q) >_{\Omega,\sigma_{CP},\sigma_{PP}} + I_G(q)\right] + Constant \tag{3.13}$$

Fits of the SANS curves are shown in Figures 3.22 and 3.23. The fitting procedures used for this model were exactly the same described in the previous section. The four fits plotted in Figure 3.22 give good χ^2 values and an adequate agreement with the data. To notice that the curve fitting at 42 *wt%* in D_2O is comparable with the one obtained by the other model (see Fig. 3.13). This is expected due the same protein-like constrast assumed for the second term of the equations, either $P_{SAW}(Q)$ or $I_G(q)$, that is quite matched at 42 *wt%*.

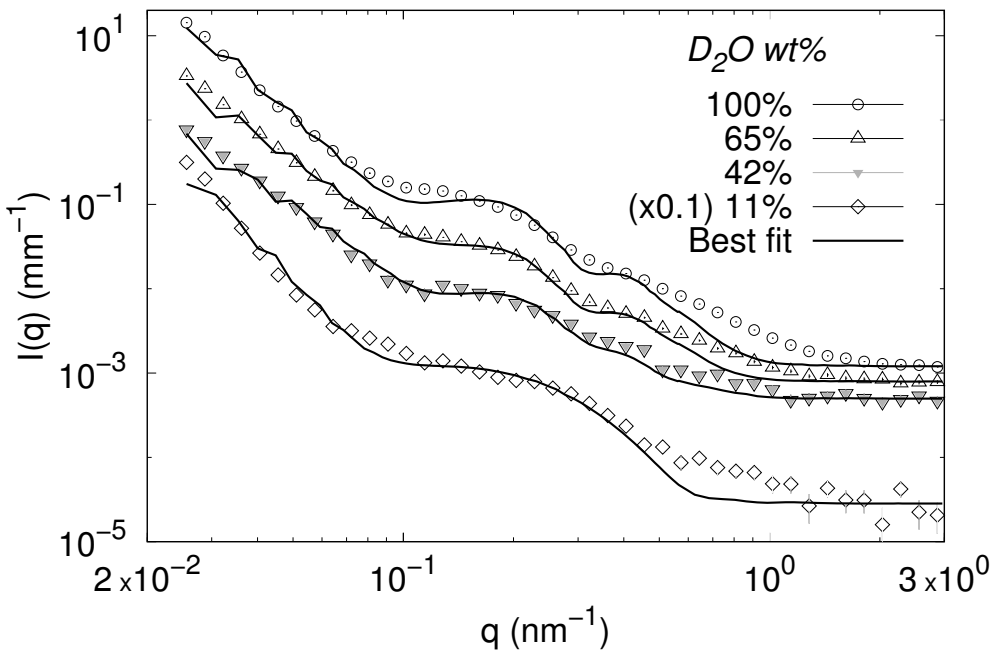

Figure 3.22.: SANS data fitted with Equation 3.13. Data concern samples at 11, 42, 65 and 100 D_2O *wt%* in the suspension medium.

As a matter of fact, matching the full protein content in the system is a way to visualise only the lipid compartments of the cell, because there is no trace of signal exclusively coming from DNA/RNA-like contrast objects. Hence, the curve for 42 D_2O *wt%* is completely fitted by

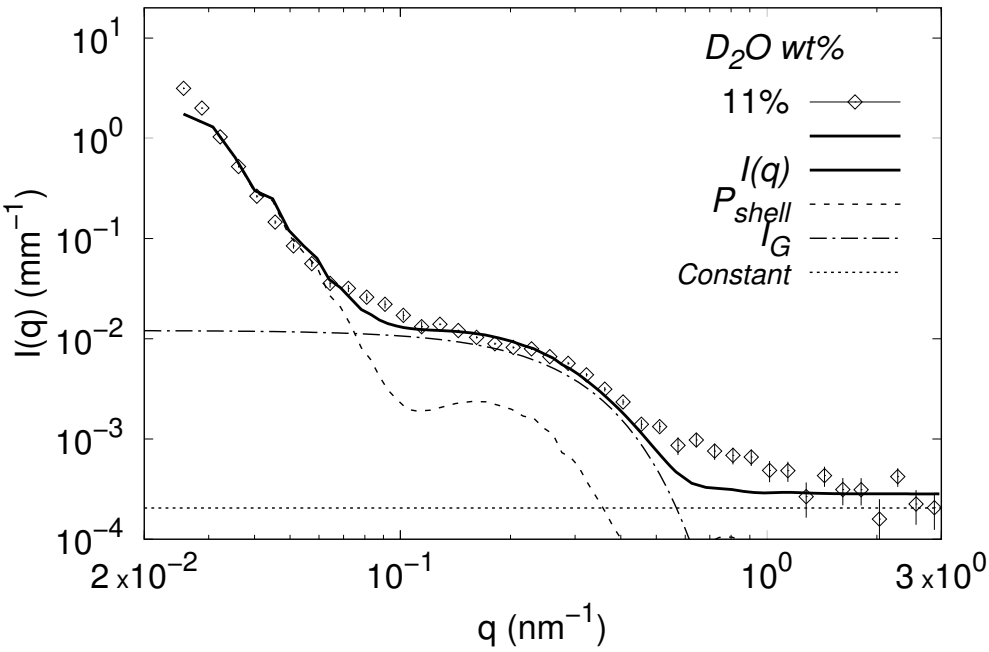

Figure 3.23.: SANS data fitted with Equation 3.13. Data concern the sample at 100 D_2O *wt%* in the suspension medium. The best fit (solid line) is the sum of the membrane model $< P_{shell}(q) >$, the Guinier term $I_G(q)$ and the constant value.

the $\langle P_{shell}(q) \rangle$ term, and, again, the oscillation is fully described by the centre-to-centre inter-membrane distance $C_{OM} = 29.7\ nm$. There are no instances of physical models or set of results that do exclude this result. For the same reason, the curve at 64 and 100 D_2O *wt%* are similarly described, but with the Guinier term acting as a protein-based background.

The main difference, in using this alternative model, concerns the SAXS and the SANS curve at 11 *wt%* (see Fig. 3.23). Here the peak at $q \sim 0.27\ nm^{-1}$ is fitted by the $I_G(q)$, with an average radius of gyration $R_g = 6.16\ nm$, value that seems reasonable as average radius for the protein population that is mainly located in the cytoplasm. The biggest proteins in the cytoplasm are the ribosomes, which have a radius of gyration of $R_g^{ribosome} = 8.7\ nm$[1] and occupy up to half of the total volume of all the proteins in the cell. However, two issues undermine this approach. (*i*) 70% of the mass of a ribosome consists of RNA, hence a consistent contribution to the intensity of the Guinier term is not coming from protein-like contrast scatterers, and this contribution may either be negligible or move the average SLD closer to ribosome-like values. (*ii*) The description of the peak by the Guinier term masks most of the information from the core-shell term. The fit is not sensitive to the parameter variations relative to the PG layer, i.e. C_{PG} and W_{PG}. For a coherent global model, the value $R_g = 6.16\ nm$, was fixed for all the fits, allowing

[1]This value was calculated performing a simulation with the software CRYSOL [153] based on crystallographic data saved in the Protein Data Bank (1ML5.pdb [154]).

the description of the Guinier term with one single parameter, I_{pr}. This approach allows a comparison with the previous model in term of number of necessary parameters to describe the complete system.

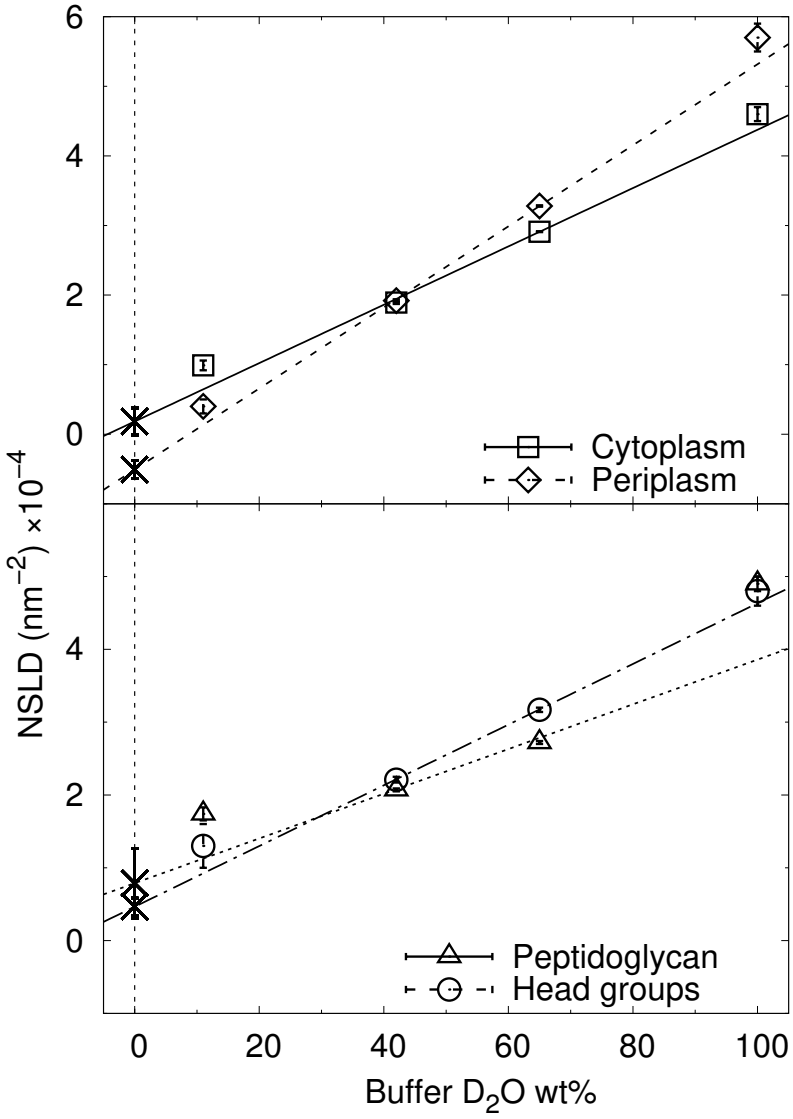

Figure 3.24.: NSLD values for CP, PP, PG and phospholipid head groups as a function of the nominal D_2O concentration. A weighted linear regression is used to extrapolate the respective values for the fit at 0 *wt%* in D_2O.

The consequences of this effects are visible in the extrapolation fits in Figure 3.24. The SLD values at four different D_2O concentrations systematically diverge from the linear trend, overestimating the linear fits at 11 and 100 *wt%*. The deviation is indeed more pronounced for the values concerning the PG layer. To note that in the fitting procedures for both models (Equations 3.9 and 3.13) similar boundary conditions were used for the free parameters. Extrapolated data are indicated in Table 3.10, along with the errors obtained from the linear fits. The discrep-

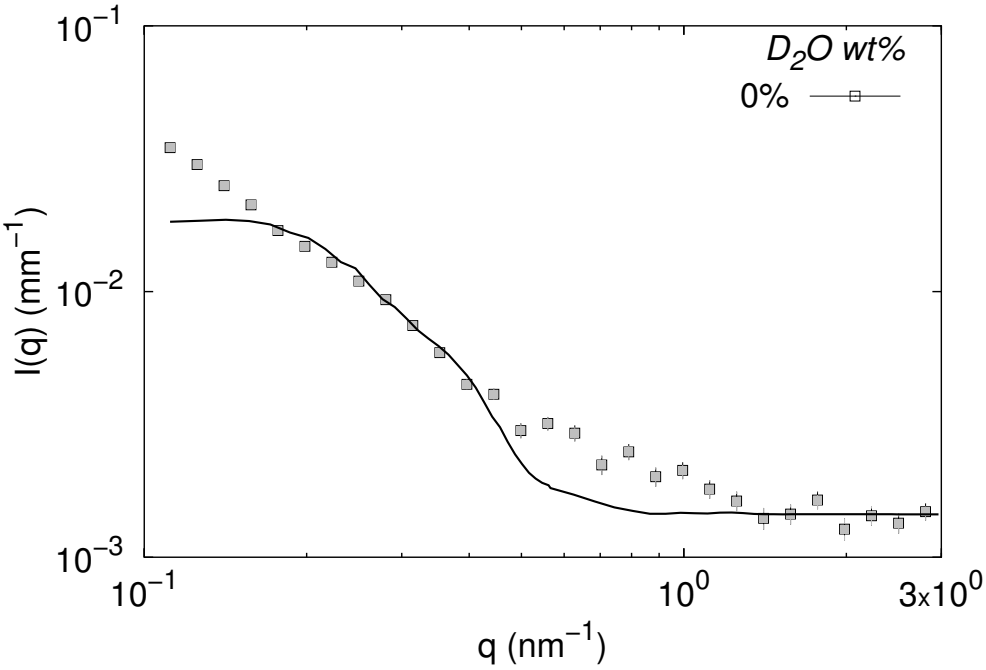

Figure 3.25.: Curve fitting of *E. coli* suspended in pure PBS (0 D_2O *wt%*). The solid line describes a fit obtained by fixing global and extrapolated parameters.

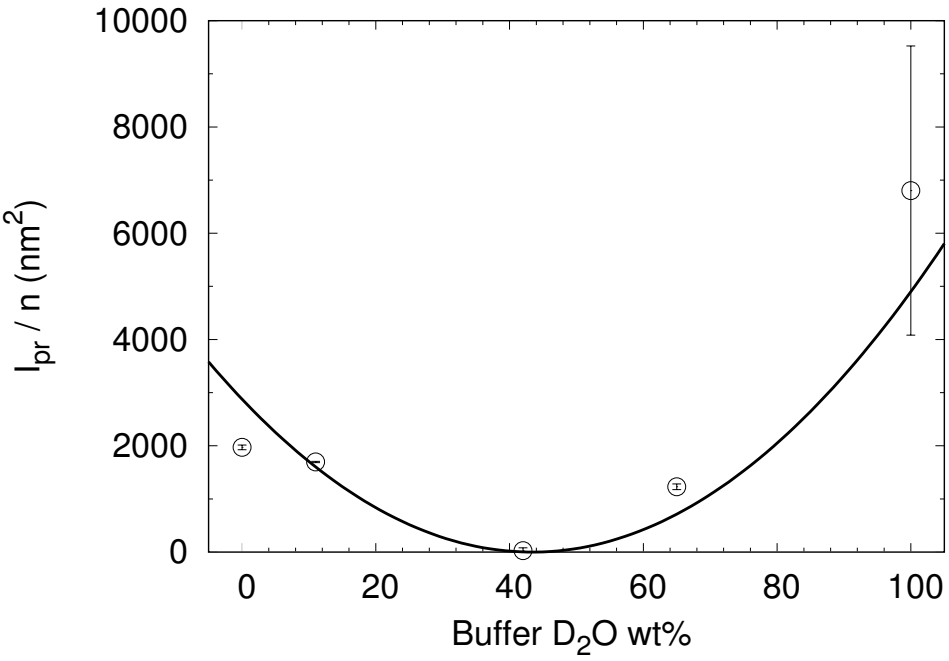

Figure 3.26.: Fitting of I_{pr}/n values as a function of the nominal D_2O concentration. The minimum of the parabola is higher than the matching point for protein systems, that is roughly 36 D_2O *wt%* (1.9×10^{-4} nm^{-2}).

ancy in the linear behaviour is clearly reflected in the confidence of these values (up to 100% in relative error), which are uniformly lower than the extrapolated values in Table 3.8.

To continue the self-consistency check, SLD parameters were extrapolated at 0 *wt%* and used to fit the pertinent curve with three free parameters, n, I_{pr} and a constant value. The curve fitting is shown in Figure 3.25. The quality of the agreement with the data is poor, leading to a concentration value, $n_{0\%} = 9.0 \times 10^9\ ml^{-1}$, that is overestimated by $\sim 20\%$ with respect to average of the other 5 curves $< n >= (7.4 \pm 0.2) \times 10^9\ ml^{-1}$.

Table 3.10.: Summary of the parameters describing the partial SANS curve at 0 D_2O *wt%*. SLD values were recovered from a linear extrapolation.

From Extrapolation	
Parameter	**NSLD** $\times 10^{-4}$ (nm^{-2})
ρ_{CP}	0.2 ± 0.2
ρ_{PP}	-0.50 ± 0.13
ρ_{ME}	0.46 ± 0.12
ρ_{PG}	0.8 ± 0.5

The result about I_{pr} is instead displayed in Figure 3.26, where the values are fitted with a parabolic curve in order to get the actual matching point associated to the Guinier term. The data actually show a minimum around 40 *wt%* but the fitting quality is much lower than the curve obtained including the SAW model. The matching point in fit is at (43 ± 6) *wt%* in D_2O, corresponding to an effective $\rho_0 = (2.4 \pm 0.4) \times 10^{-4}\ nm^{-2}$. This value may correspond to the typical protein-like contrast, considering the large interval defined by the error value, but the result remains inconclusive because of the intrinsic uncertainty in the expected value.

To conclude, this alternative formalism *does not* satisfactorily pass the self-consistency check principally because the global model is not suitable to fit the partial curve at 0 *wt%* in D_2O. The linear extrapolation of the NSLD values is the main cause of the failure and it also strongly biases the comparison with XSLD values, as they bring about up to 100% in relative error and a consistent membrane SLD-profile cannot be provided.

3.5. Summary and Conclusion

In this Chapter a high-quality signal-to-noise USAXS/SAXS measurements on the bacterium *Escherichia coli* are presented.

In the first part, a coarse-grained scattering form factor of the micron-sized bacterium was obtained by modelling USAXS data, covering a q-range of $(2 \times 10^{-3} - 10^{-1})\ nm^{-1}$. It is possible to model the data with an elongated shape, such as a capped-cylinder or a prolate ellipsoid, with a homogeneous scattering length density. In such low-q range the scattering is dominated

by the whole cell, which is visible as a single body of uniform density. The determination of the length is difficult, also because of the high polydispersity of the cells, whereas the measurement of the radius is precise, as it is related to the well-defined positions of the minima in the form factor oscillations. A low photon flux is sufficient to obtain a good quality signal-to-noise scattering curve with no visible effects of radiation damage. The USAXS technique can be used as an extension of standard optical microscopy techniques, allowing *in vivo* investigation in cellular systems on the micron scale with a resolution beyond the optical diffraction limits. A scattering curve describes a statistical ensemble of 10^5 to 10^7 cells in the illuminated volume, giving a proper average of the structure being studied. Moreover, two applications of the use of USAXS on bacterial systems were described: a study (*i*) of the evolution of the cell radius during the growth cycle of the *E. coli* culture and (*ii*) of the swelling effects on the cell radius due to osmotic pressure. These two examples can be considered as a proof of concept for the application of USAXS to the investigation of the effects on the shape of micron or sub-micron cells under different environmental conditions. The choice of the sample environment for scattering experiments is flexible, e.g. it will be possible to track the variations of a cell geometry in either physiological or stress conditions.

In the second part of this chapter, a multi-scale modelling of the bacterium was described. The combination of USAXS with SAXS measurements allows to span almost four orders of magnitude in scattering q-vector $(2 \times 10^{-3} - 7)\ nm^{-1}$. The complete scattering curve of an *E. coli* suspension brings information about the geometry of the whole micron-sized body and the details of the cell envelope in the nanometre scale. Contrast-variation SANS measurements were performed to add more constraints when modelling the bacterial ultrastructure and the comparison between SAXS and SANS measurements allowed the mutual exclusion of both X-ray radiation damage and toxic effect due to the suspensions in D_2O. Finally, a global model were formulated combining core-shell colloidal, membrane and polymer formalisms, respectively to describe the cell-body, the cell-envelope and the flagella. Fits were performed using the Genetic Selection algorithm as an effective minimisation method in solving systems with a high number of correlated parameter and a high density of local minima in the χ^2 landscape. The set of results is self-consistent and in agreement with the more recent cryo-TEM observations and this global analysis led to the determination of the membrane electron-density-profile and the inter-membrane distances on a quantitative scale. The most important results are the average centre-to-centre inter-membrane distance ($C_{OM} = 29.7\ nm$) and the SLD values of the periplasmic space ρ_{PP} and of the peptidoglycan layer ρ_{PG}. The C_{OM} value was univocally determined and sheds light on the identification of the precise periplasmic extension in the *E. coli* K-12 strain. In addition, ρ_{PP} and ρ_{PG} values reveal a very dilute periplasm, with a dense protein content trapped in (or closely interacting with) the peptidoglycan layer. This result is in contradiction with the current idea of a "periplasmic gel", concept that was primarily derived

from the cryo-TEM observations on frozen and chemically fixed bacteria [79], where staining compounds bias the determination of the effective electron-densities. Instead, it is in line with the last experiments of Matias et al. [80], also with cryo-TEM, where the experimental design aimed to a minimise the alterations on the samples.

These results add new material in the debate about the periplasm density. Structural information in biological systems are a powerful tool for the understanding of the functions or proteins or metabolic mechanisms in cells. For example, the highly-oxidative periplasmic region is supposed to be compared to the lysosomes in eukaryotic cells, whose function is to breakdown and dispose waste materials coming from both the cytoplasm or the exterior of the cell. This theory needs to be considered in the framework of this analysis, where the scenario of a dilute periplasm is strictly linked to a compact, dense murein layer. More measurements are needed to understand, for instance, if this latter density concerns the peptidoglycan layer itself, or if it describes a partition of macromolecules into it. Moreover, an empty region within the membranes changes also the current conjectures about the osmotic balance between inner and outer membrane. In any case, this arguments fall outside the aim of this work.

To conclude, this synergy of SAS techniques offers a powerful tool for the study *in vivo* of the ultrastructure of prokaryotic cells, avoiding invasive methods, such as staining or freezing, and can be used to study the effects of antibiotics, antimicrobial peptides or even detergents that affect the whole cell geometry as well as the cellular membranes [124, 155].

The USAXS investigation, even using highly concentrated *E. coli* suspensions, did not show any sign of the effective structure factor, also by considering the effects on the first minimum of the scattering curves. The latter did not exhibit significant changes varying the cell number density at a fixed growth phase, therefore effective interactions among bacterial systems, up to the concentrations probed here, were not observed. Moreover, the low-contrast of these bacteria precludes XPCS measurements at these optical densities.

4. Passive Colloids in Active Bacterial Medium: Interactions and Dynamics

In this chapter an investigation of the effective interactions and dynamics of passive silica colloids suspended in a medium of active *E. coli* using USAXS and XPCS is presented. The high scattering contrast of silica colloids allows the extraction of partial static structure factors of the interparticle interactions and obtaining the intensity-intensity autocorrelation functions corresponding to the colloidal dynamics.

Recently, works on micron sized passive colloids suspended in a bath of *E. coli* reported an effective attraction between colloids due to the bacterial activity [81] and an enhanced diffusion coefficient of passive particles [63,65]. In the experiments presented here, passive silica colloids have an average diameter of half a micron, so relatively small compared to the size of bacteria, and therefore the size ratio between colloids and bacteria is inverted. The systems studied is then a concentrated suspension of passive elements doped with active swimmers.

USAXS measurements were performed in order to get information on effective interactions between silica colloids. Scattering curves were analysed by structure factor models including multiple-scattering corrections. These were systematically investigated and tested on passive suspensions in pure water varying colloidal concentration and sample pathlength. Resulting corrections were then applied to overcome the influence of multiple-scattering on USAXS curves in colloidal mixtures with bacteria. For XPCS measurements, intensity-intensity autocorrelation functions, calculated from the 2D speckle pattern, were analysed with a single exponential decay representing a single relaxation process for all the systems.

Active systems showed little differences in effective interactions compared to passive references whereas the dynamics revealed a levelling-off of effective diffusion coefficients, where the system is simultaneously sped up and slowed down by a competitive effective-temperature and viscosity effects.

4.1. Materials and Methods

Samples were prepared with *E. coli* chemically-competent cells from Invitrogen (K-12 strain, close to DH10B^{TM} derivative), transformed with pUC19 DNA (Genbank Accession Number L09137) and plated on lysogeny-broth (LB) plates with ampicillin ($100\mu g/ml$). In order to maximize the mobility efficiency, bacteria were grown in LB medium at 25 $^{\circ}C$, instead of the standard temperature 37 $^{\circ}C$, and then were harvested during the exponential growth-phase, around $OD_{600} \sim 0.5$ [28] (measured with the OD-meter GeneQuant-1300). *E. coli* cells were artificially-concentrated by centrifugation at 4 $^{\circ}C$ in sterilized centrifugation-tubes at 1000 g for 25 minutes, the supernatant was removed, pellets were transferred in 50 ml falcon tubes and spun down again at 1000 g using a tabletop Eppendorf centrifuge for 35 minutes. To minimise the damage to flagella, the pipetting procedures were minimised as much as possible. Then, bacterial pellets were gently re-suspended in nutrient-free and sterile filtered 10 mM phosphate buffer at $pH \sim 7.2$ containing 0.1 mM EDTA, with a final concentration of the bacterial stock suspension up to $OD_{600} \sim 15$.

Silica colloids suspended in water were purchased from Bang Laboratories. They were centrifuged at room temperature in 1.5 ml Eppendorf tubes using a Eppendorf Centrifuge 5430 at 120 g for 10 minutes to obtain a concentrated stock suspension of volume fraction $\phi \simeq 0.48$.

Ampicillin sodium salt and EDTA disodium salt dihydrate, were purchased from Euromedex and LB medium, D-glucose, Tween20 and phosphate salts were purchased from Sigma Aldrich.

USAXS and XPCS measurements were performed on TRUSAXS beamline (ID02) at the ESRF. The incident X-ray wavelength was $\lambda = 0.0995$ nm and the sample-detector distance was set to 30.8 m. The pinhole configuration of the optics is extremely important for XPCS measurements, as the beam size has to be small to reach the required degree of coherence but, at the same time, has to maintain an adequate photon flux to obtain a good intensity statistics. XPCS acquisitions were taken with a maximum FWHM beam size of around 40×40 μm^2, as defined by the slits (see 2.2.2) and a photon flux of 2×10^{11} $photons\ s^{-1}$. The Pilatus 300K detector was used at the maximum frame rate of 400 Hz, equivalent to a time resolution of 2.5 ms. Intensity-intensity autocorrelation functions were calculated using the PYXPCS software (developed at ID10, ESRF) from a series of up to 500 frames with an exposure time of 0.2 ms and a read-out period of 2.3 ms, corresponding to a continuous irradiation of the sample for 1.25 s. Samples were contained in quartz capillaries with various pathlengths.

USAXS static measurements for the multiple-scattering study were performed with FReLoN Kodak CCD detector, with an effective FWHM beam size of 321×106 μm^2 on the detector.

Viscosity measurements were done using the rheometer Haake RS6000 with a polycarbonate cuvette and a titanium rotor in coaxial-cylindrical geometry, with inner and outer radii of

12.5 *mm* and 13.5 *mm*, respectively, and a sample volume of 6 *ml*.

4.1.1. Preliminary Data and Experimental Considerations

The size of the colloids to be used for this experiment requires some considerations that must be taken into account. If the colloids are too small compared to the bacteria, the cells will experience an effective attractive interaction due to the depletion forces § 1.1. Instead, if they are too large, they could not be considered as diffusive colloids because of the strong influence of the gravitational forces. Half-micron colloids are a reasonable compromise as they have a size that is roughly the radius of the bacteria but are big enough to limit the depletion effect. Even if these colloids, as the bacteria, sediment due to gravity, they are diffusive as Brownian motions occur in a much smaller time-scale than sedimentation [156].

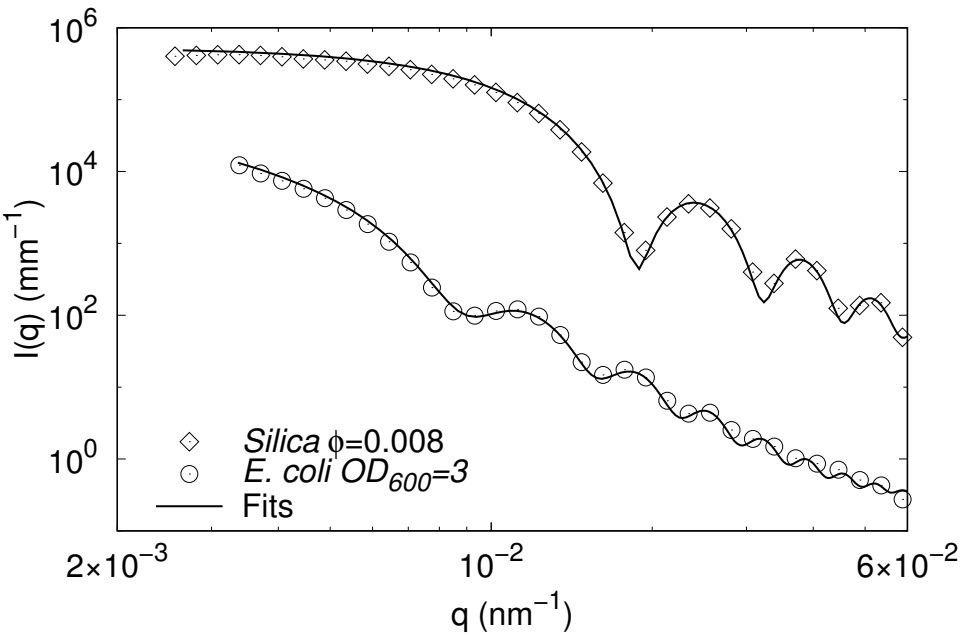

Figure 4.1.: Scattering Form Factors of silica colloids ($\langle R \rangle = 239$ *nm*) and *E. coli* bacteria ($\langle R \rangle = 460$ *nm*) suspensions. Data were fitted with a polydisperse sphere and a polydisperse ellipsoid respectively.

The material of the passive colloids is also fundamental. The density of silica is ~ 2 *g cm*$^{-3}$, which gives a favourable difference in XSLD between silica colloids (1.69×10^{-3} *nm*$^{-2}$) and *E. coli*, that is within the lower limit of protein and lipid XSLD values, ($\sim 1 \times 10^{-3}$ *nm*$^{-2}$). This aspect makes the scattering from bacteria negligible compared to the signal of the passive colloids, as is presented in Figure 4.1, where a dilute suspension of silica colloids show a signal nearly two orders of magnitude higher than the bacterial system at $OD_{600} = 3$. Therefore, sub-micron colloidal silica spheres were used as the passive constituent of the system. These selected colloids have an average diameter $\langle \sigma \rangle = 478$ *nm* with polydispersity index (PDI) 0.045.

These data were obtained via a spherical form factor analysis using Equation 2.9 and 2.11, where a Gaussian PDF was applied (see Fig. 4.1).

Theoretically, a SAS curve from a mixture of silica colloids and bacteria with scattering amplitudes $A_s(q)$ and $A_b(q)$, using the decoupling approximation with monodisperse conditions, can be expressed by the following equation:

$$\begin{aligned} P_{sb}(q) = n_s \Delta\rho_s^2 |A_s(q)|^2 S_s(q) + \\ + n_b \Delta\rho_b^2 |A_b(q)|^2 S_b(q) + \\ + \sqrt{n_s n_b} \Delta\rho_s \Delta\rho_b A_s(q) A_b(q) S_{sb}(q) \end{aligned} \tag{4.1}$$

where $S_s(q)$, $S_b(q)$ and $S_{sb}(q)$ respectively are the structure factors corresponding to interparticle interactions between colloid-colloid, bacterium-bacterium and colloid-bacterium. The first two terms correspond to the scattering intensities coming from silica colloids (s) and bacteria (b), treated as independent systems. The third one is a cross term that appears only if the two components interact with one another, otherwise it is negligible as $S_{sb} \simeq 0$ in absence of cross interactions. Experiments conducted in Chapter 3 excluded the presence of a static interaction in bacterial systems up to $OD_{600} = 10$ and, thanks to this high difference in XSLD, the information obtained via USAXS (and XPCS) were exclusively attributed to silica colloids:

$$P_{sb}(q) \approx n_s \Delta\rho_s^2 |A_s(q)|^2 S_s(q) \tag{4.2}$$

where the cross-term was neglected in a first approximation.

Stability versus Mobility

Another key consideration for this experiment is the medium used for the colloids/bacteria suspension. Cells, and silica colloids, are resuspended in the "motility" buffer [66, 81], consisting of 10 *mM* phosphate buffer at $pH \sim 7.2$, 0.1 *mM* EDTA, 0.002 wt% Tween20 (equivalent to 0.16 *mM* of polysorbate 20) and 0.5 *mM* Glucose. The composition of such a buffer aims to maximise the efficiency of the motility of *E. coli*, as it was reported by Adler and Templeton [28]. A pH value between 6 and 7 is important for the motility, as well as the presence of EDTA which can chelate heavy metal ions that could bias the *E. coli* motion. The Tween20 is necessary to prevent the cells sticking to the hydrophilic capillary walls during the measurements. Finally, the glucose is the energy source for the bacteria and it is also needed as osmoprotectant to reduce the osmotic stress due to the low concentration of salt in the buffer.

However an issue arises from this motility buffer. The conditions in which bacteria are in a native state as much as possible and manifest the most effective motion, are not suitable for the

stability of silica colloids. Silica, as well as *E. coli*, is negatively charged at the surface when suspended in water. This charge is needed for their colloidal stability to ensure a repulsive electrostatic interaction, but a problem arises when the motility buffer is used. Salts, glucose and Tween20 shield the long-range electrostatic repulsion which is stabilising against the van der Waals attractive forces. ζ-potential measurements on dilute suspensions of silica colloids in different buffers were performed using the Malvern Zetasizer Nano Z, in order to measure this effect and to find if the motility buffer is compatible with charged-stabilised silica colloids. The results are shown in Table 4.1 and Figure 4.2.

Table 4.1.: ζ-potential measurements on silica colloids suspensions with different buffer compositions. σ_ζ values is the standard deviation of a Gaussian profile representing the precision limit of the instruments, whilst the effective error in ζ is around 1%.

Suspension media	ζ (mV)	σ_ζ (mV)
Water	-55.3	6.3
Phos.Buffer/EDTA	-51.3	5.1
Phos.Buffer/EDTA/Glucose	-52.1	6.0
Phos.Buffer/EDTA/Tween20	-18.4	6.1
Phos.Buffer/EDTA/Glucose/Tween20	-19.3	5.0

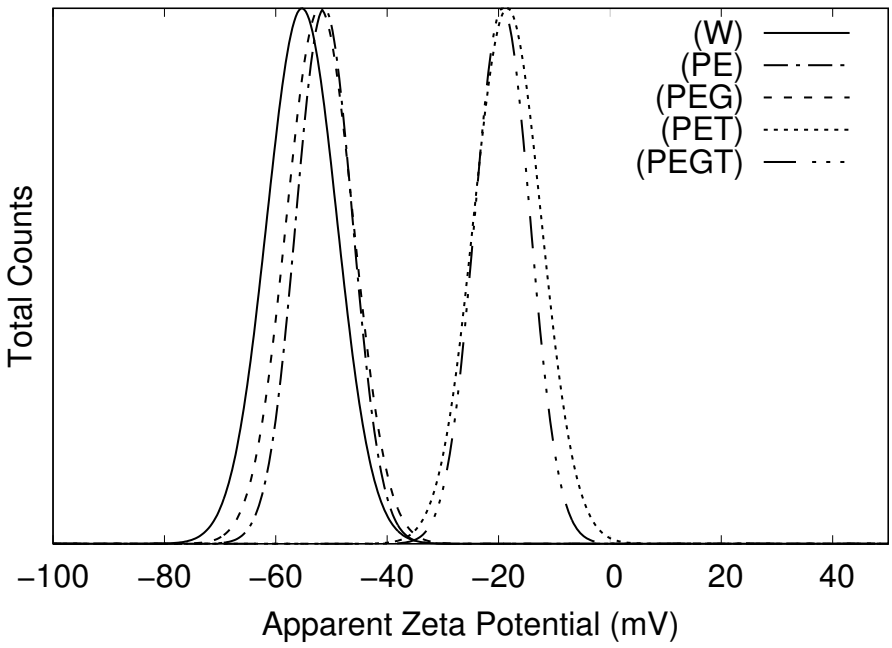

Figure 4.2.: ζ-potential measurements on silica colloids suspensions with different buffer compositions. Compared to pure water (W) suspensions, phosphate buffer (PE) media, with or without 0.5 *mM* of glucose (PEG), poorly affect the effective surface charge density of colloids. A significant screening is visible in presence of 0.16 *mM* Tween20 (PET and PEGT). All the samples contained 0.1 *mM* of EDTA.

From these measurements, one can notice that 10 *mM* of phosphate buffer at $pH \simeq 7.2$,

with or without glucose at 0.5 mM maintains the Coulomb repulsion between silica colloids, whereas the presence of Tween20 distinctly affects the colloidal stability. In these latter cases, ζ-potential values are typical of a weak stabilisation but it is not sufficient to determine if the van der Waals potential exceeds the Coulomb repulsion resulting in effective attractive interactions. USAXS measurements on silica colloid suspensions in pure water and in motility buffer, and the analysis of their effective potentials, are presented in the next section.

Swimming *E. coli*: Depletion of Energy Sources

The last aspect concerns the dynamical effects in bacterial mixtures and the time scale in which they can be observed. The activity of *E. coli* is due to the rotation of the flagella, whose motors are powered by pumping protons out of the cell [157]. This action needs energy and bacteria use different metabolic processes to transform the "fuel" available into kinetic energy. The most efficient process is the well-known citric acid cycle, in which bacteria consume glucose and oxygen and reach an average velocity of $15-20\ \mu ms^{-1}$, depending on the oxygen concentration. It is important that all USAXS and XPCS data have to be acquired before all the glucose is metabolised because, when it is exhausted, the cells make use of other metabolic processes, and the average velocity drops to $1-3\ \mu ms^{-1}$. For the sake of reproducibility, experiments have to be performed in the same time-frame, in order to compare data with similar activity. Schwarz-Linek et al. [157] reported the characterisation of the *E. coli* medium as an active bath. From their works it is possible to extrapolate the time window in which bacteria move efficiently before glucose depletion. With an initial glucose concentration of 0.5 mM, the cell velocity is preserved up to $\sim \frac{63\ \text{minutes}}{1\ OD_{600}}$, then, for example, with the maximum cell density used in these experiments, $OD_{600} = 5$, data were taken within the first 12 minutes. Stock solutions of glucose and Tween20 were kept separated from the stock suspensions of *E. coli*, so the final mixtures were mixed in Eppendorf vials just before each set of measurements. Samples were then moved into sealed capillaries containing a free portion of volume as an oxygen reservoir. The whole sample-preparation procedure lasts around $5-6$ minutes, leaving enough time for a set of XPCS measurements. Impurities present in commercial Tween20 may be metabolised too, yet the consumption of the polysorbate 20 species is not expected [157].

Bacteria in Crowded Suspensions: Physical Considerations

Active, bacterial mixtures were prepared with a volume fraction ϕ of silica colloids at 0.08, 0.16 and 0.32. These values were used to cover a suitable concentration range for the study of the effective interactions, indeed, no information can be obtained about the interparticle potential with lower concentrations, as $S(q) \approx 1$. A sample with $\phi \simeq 0.008$, both with and without bacteria, was investigated to obtain size and polydispersity from the scattering form

factor analysis (see Fig. 4.1) and also to perform XPCS measurements on a dilute system. As a matter of fact, systems with colloids occupying 0.08, 0.16 and 0.32 of the available volume force bacteria to swim in a very crowded environment.

Table 4.2.: Crowding conditions of the medium in which bacteria swim. n_s, $\sqrt[3]{1/n_s}$ and $\langle d_s \rangle$ are, respectively, the concentration, the centre-to-centre distance and the average distance between the surfaces of silica colloids of diameter $\langle \sigma \rangle = 478\ nm$. n_s/n_b values represent the number of passive colloids per single bacterium in a system with cell concentration $OD_{600} = 3$.

ϕ	$n_s \times 10^{-9} (nm^{-3})$	$\sqrt[3]{1/n_s}\ (nm)$	$\langle d_s \rangle\ (nm)$	n_s/n_b @ $OD_{600} = 3$
0.008	0.14	1930	1452	58
0.08	1.39	896	418	579
0.16	2.78	711	233	1159
0.32	5.56	564	86	2317

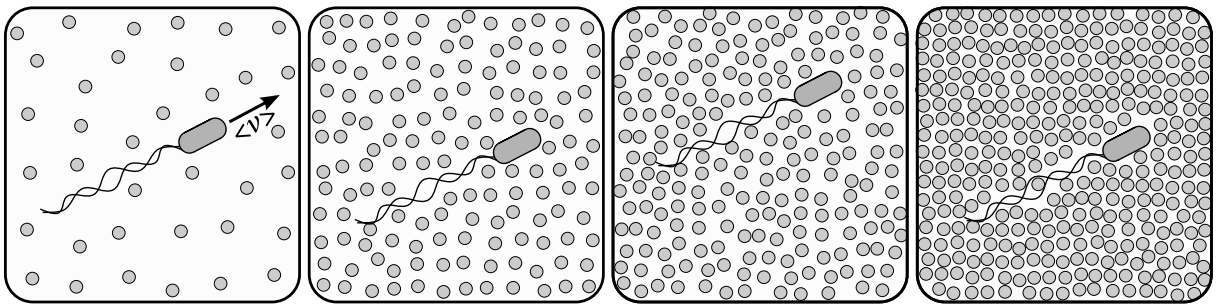

Figure 4.3.: Sketch of investigated systems. From left to right, pictures refer to 0.008, 0.08, 0.16 and 0.32. Sizes and distances are in scale as well as the number of particles per cell in the equivalent 2D geometry.

In Table 4.2 size and distance parameters are reported to visualise the system under study. Each sample is characterised by the volume fraction, ϕ, which influences the diffusion of silica particles in passive conditions, and the number of bacteria n_b. Looking at $\langle d_s \rangle$ values, a scenario in which *E. coli* could move without "'feeling" obstacles is possible only for $\phi < 0.01$ as their average diameter is $\sigma_b \simeq 900\ nm$. With higher concentrations, $\sigma_b > \langle d_s \rangle$ and each cell must push and move colloids apart in order to swim forward, as illustrated in Figure 4.3. This configuration is also highlighted by the number of passive colloids per cell, n_s/n_b, that reaches up to ~ 2300 in the most concentrated system.

It would be interesting to compare also the ratio ϕ_s/ϕ_b, including the effective volume fraction occupied by the bacteria ϕ_b, but the calculation of ϕ_b is not trivial. Considering a radius of 450 nm and a total length around 4 μm for the cell body, a concentration of $OD_{600} = 1$ corresponds to $\phi_b^{body} \sim 0.002$. Including the flagella as a single bundle with the same radius of the cell and an average length of 10 μm, $OD_{600} = 1$ is equivalent to $\phi_b^{full} \sim 0.007$. Although, the mean distance between two cells at $OD_{600} = 1 \equiv n_b = 8 \times 10^8 cells/cm^3$ can be estimated as $\sqrt[3]{1/n_b} \simeq 10800\ nm$, that is a length comparable to the flagella. Therefore, even if the apparent

volume fraction is low, it is not possible to exclude a partial overlap of the regions interested by the flagella, especially at higher cell concentrations, and then almost all the colloids may physically interact with bacteria via the flagella.

The concentration of cells that are actually motile is not straightforward. It was observed that $20-40\%$ of the bacterial population is non-motile as a native state [65]. If the fraction of cells stuck to sample-holder walls due to a reduced presence of Tween20 is also included, it is reasonable to assume that a significant fraction of cells is not swimming freely in the suspensions.

Viscosity measurements on *E. coli* suspensions in a glucose-free motility buffer were performed. The results indicated that the viscosity of the bacterial suspensions, spanning the concentration OD_{600} range $1-5$ is roughly 15% higher than the water-like motility buffer. Notice that fascinating measurements of "zero-viscosity" in super-fluidic suspensions of motile bacteria have been reported [158]. The two results are not in contradiction. The super-fluidic condition is the result of cells alignment along the shear flow in the rheometer cuvette in a specific low shear-stress range $\dot{\gamma} < 1\ s^{-1}$, where bacteria swim parallel with the flow field drastically reducing the measured friction within the cuvette walls. For higher $\dot{\gamma}$ values instead, the viscosity is roughly 10% higher than the viscosity of the suspension medium, displaying the effect of a classical passive system. Therefore, the viscosity of a bacterial suspensions can be distinguished from an "apparent", or "effective", viscosity when active motions are taken into account.

Finally, the high XSLD of silica colloids helps to simplify the analysis of USAXS and XPCS data, in which the signal is completely dominated by their scattering, but the drawback is that there are no information about the colloid/cell interactions and about the cell dynamics. This low-contrast cells do not allow reliable XPCS measurements on systems only consisting of bacteria, because the low signal-to-noise ratio. A repulsive interaction is assumed between silica and cell surfaces, as they are both negatively charged. Instead the actual average speed $\langle v \rangle$ of *E. coli* in these specific concentrated systems in unknown. A reduced translational and rotational diffusion in crowded systems is an established phenomenon [159–162], where a random-walk object can be trapped by its neighbours. For the same reasons, the "run&tumble" dynamics of bacteria should be affected and the actual average velocity of the "run" and the change in direction during the "tumble" should differ between dilute and crowded conditions. In this work, the actual dynamics of bacteria is not investigated but it is assumed that cells are active when the glucose and oxygen are present, those are consumed to power the flagellar rotors and, then, the same amount of energy, equivalent to the kinetic energy of bacteria in dilute environments, is released in the system.

4.2. Statics: Results and Discussion

4.2.1. Investigation of Multiple-Scattering Effects

USAXS measurements of the sub-micron colloidal silica suspended in pure water were performed prior to mixing with bacteria and the use of the motility buffer. Information about their repulsive interactions were extracted via scattering structure factor models of concentrated suspensions at three different volume fractions, $\phi \simeq 0.08,\ 0.16,\ 0.33$. Unfortunately, USAXS curves of concentrated silica colloids of $\langle R \rangle = 239\ nm$ exhibited anomalous features that could be ascribed to multiple-scattering. Therefore, the same suspensions were measured using up to three pathlengths of the used capillaries, nominally $W^* = 0.2,\ 0.5,\ 1.7\ mm$, aiming to verify the presence of multiple-scattering and study it as a function of the colloid concentration and the sample pathlength crossed by the X-ray beam.

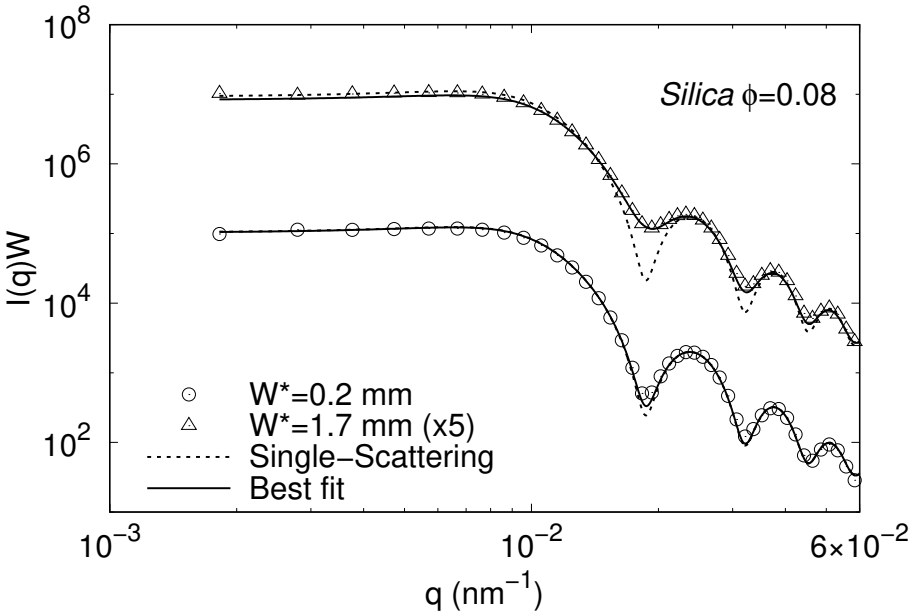

Figure 4.4.: Fits of USAXS curves of colloidal silica suspensions (volume fraction 0.08) in pure water using two capillaries with thicknesses W. Data were modelled using a repulsive Yukawa potential as structure factor and applying multiple scattering corrections.

Data and fits are shown in Figures 4.4, 4.5 and 4.6, where the ordinate is the total intensity expressed as the product of the scattering intensity $I(q)$ and the effective sample pathlength W. Data were fitted using the scattering structure factor model $S(q)$ for one-term Yukawa potential (within MSA closure relation) [111]. Polydispersity was included using the decoupling approximation (Eq. 2.30). The Coulomb repulsive potential, dominating over the dispersion forces, is approximated by the Yukawa potential $U(r)$ with the function:

$$\frac{U(r)}{k_B T} = \begin{cases} +\infty, & 0 < r \leq \sigma \\ \frac{K}{r} e^{-Z(r-\sigma)}, & r > \sigma \end{cases} \tag{4.3}$$

where σ is the colloid diameter meant as coordinate for the HS repulsion and K and Z are, respectively, the strength and the inverse range of screening length.

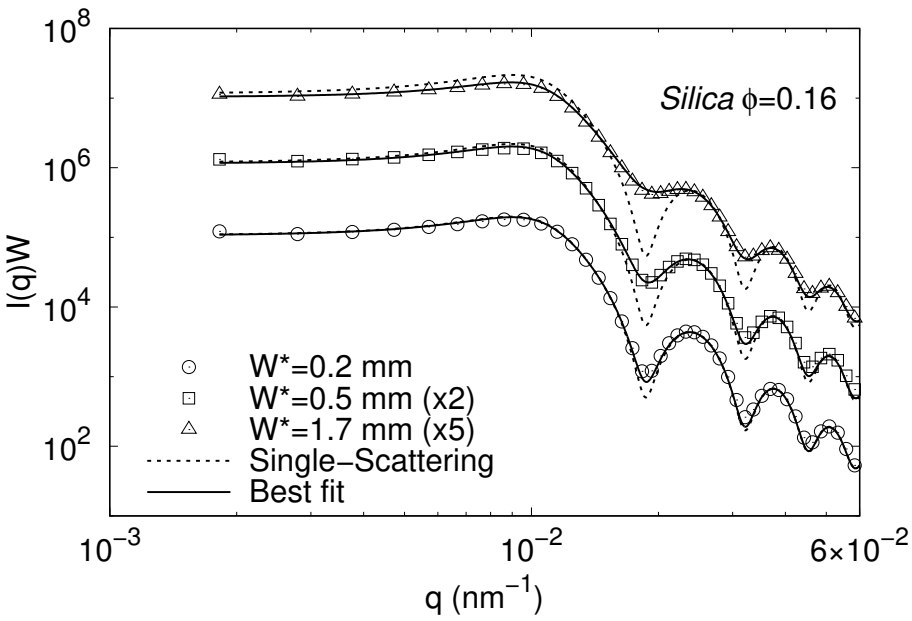

Figure 4.5.: Fits of USAXS curves of colloidal silica suspensions (volume fraction 0.16) in pure water using three capillaries with thicknesses W. Data were modelled using a repulsive Yukawa potential as structure factor and applying multiple scattering corrections.

Corrections for multiple scattering were applied using the model proposed by Schelten and Schmatz [88], which accounts for the single-scattering intensity $I^s(q)$, the wavelength λ of the incident beam and the sample thickness W. Formalising the multiple-scattering correction as a transformation $\mathscr{F}[\lambda, \cdots]$ to be applied on $I^s(q)$, fits were performed with the equation:

$$WI(q) \equiv WI^m(q) = N_r \mathscr{F}[\lambda, WI^s(q)] + Constant \tag{4.4}$$

where $I^m(q) \equiv I(q)$ is the measured intensity and N_r is a normalisation factor that takes into account possible discrepancies in the multiple-scattering model. Fits were performed using a single set of global parameters for the description of $I^s(q)$, while N_r, W and the constant values were considered as local parameters.

Parameters of the repulsive Yukawa potential are shown in Figure 4.7 and Table 4.3. A description of the effective interactions via a single exponential decay is possible as the Coulomb repulsion dominates over the van der Walls attraction in pure water suspensions. The discrep-

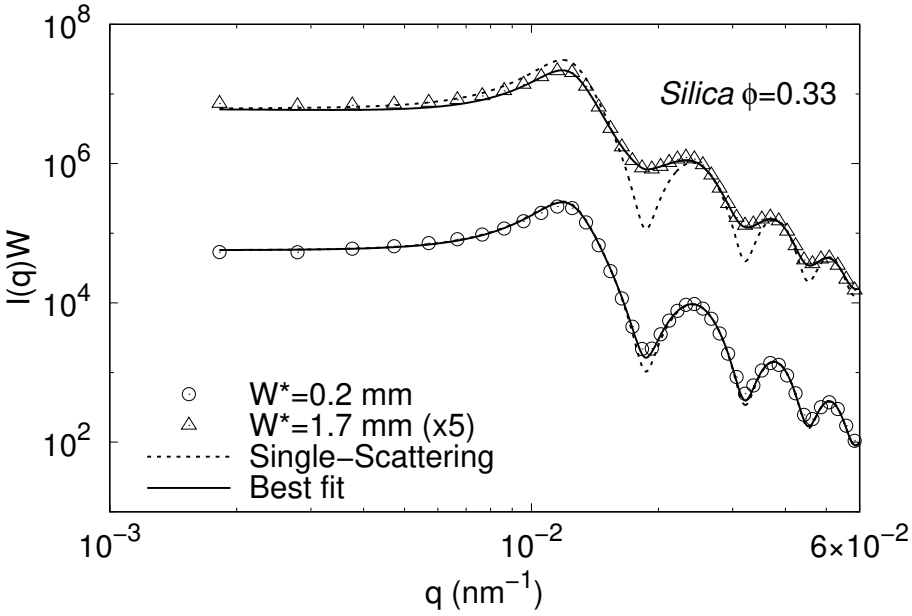

Figure 4.6.: Fits of USAXS curves of colloidal silica suspensions (volume fraction 0.33) in pure water using two capillaries with thicknesses W. Data were modelled using a repulsive Yukawa potential as structure factor and applying multiple scattering corrections.

ancy of K and Z values, between $\phi = 0.33$ and the lower 0.17 and 0.08, could be due to an effect of the decoupling approximation applied to data from such a high concentration of colloids, as it is valid up to $\phi < 0.1$.

Table 4.3.: Results from the global fitting of $I^s(q)$. $\langle R \rangle$ and PDI values were obtained from the fit in Figure 4.1.

Fitting Results: Global Parameters

$\langle R \rangle$ (nm)	239		
PDI	0.045		
ϕ	0.084	0.162	0.332
K (nm)	1.98	2.30	4.11
Z (nm^{-1})	7.8	7.7	4.8

About the multiple-scattering model, results display a good agreement between experimental data and the model for the whole set of combinations of concentrations and sample path-lengths. Compared to the theoretical single-scattering curves, scattering minima were significantly smeared in the whole q-range when using thick capillaries, whereas the effects are weak at $W^* = 0.2$ mm, where they are only visible as a smearing of the first minimum. This latter effect can be taken into account by applying an "effective" instrumental smearing to the single-scattering curve, using an unrealistic smearing σ_q three times bigger than the maximum horizontal instrumental smearing of $\sigma_q \simeq 3 \times 10^{-4}$ nm^{-1} measured from the horizontal FWHM of the direct beam at the detector. Fits at $W^* = 0.2$ mm did not include the instrumental smearing

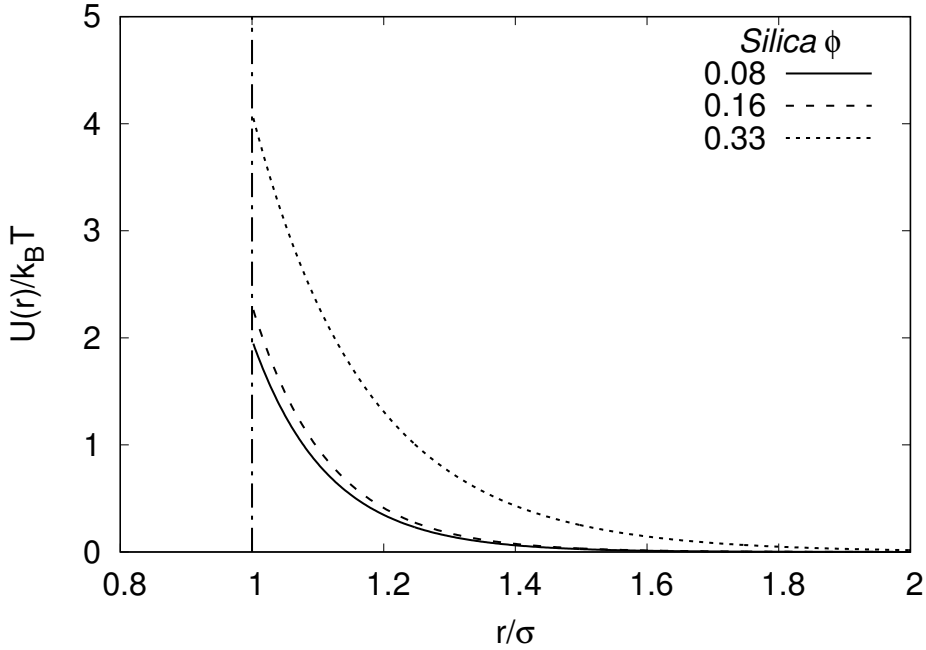

Figure 4.7.: Plot of the repulsive Yukawa potential curves obtained from the fits. The vertical dashed line represents the hard-sphere limit at the colloid surface.

Table 4.4.: Results about the local parameters W and N_r.

Sample		***Fitting Results: Local Parameters***	
ϕ	W^* (mm)	W (mm)	N_r
0.084	0.2	0.10	1.00
	1.7	1.44	1.24
0.162	0.2	0.10	1.02
	0.5	0.49	1.15
	1.7	1.45	1.53
0.332	0.2	0.10	1.03
	1.7	1.42	1.57

because, in this circumstance, actual σ_q and W values are strongly correlated as they affect scattering curves in the same manner. As a consequence, the more single- and multiple-scattering curves are close to each other the more W values are underestimated. The instrumental smearing was not applied also in the other cases, $W^* = 0.5,\ 1.7\ mm$, given that its effect is negligible compared to the distortion caused by multiple-scattering.

Results presented in Figure 4.8 show W values as a function of the nominal inner thickness W^* of the sample holders. Sample pathlengths W obtained from fits are expected to lie below the bisector, $W < W^*$, taking into account the thickness of the walls of the capillaries. The overestimation of $W \simeq W^* = 0.5\ mm$ may suggest that the precision in the determination of the actual sample thickness has the order of magnitude of the wall thickness of the capillar-

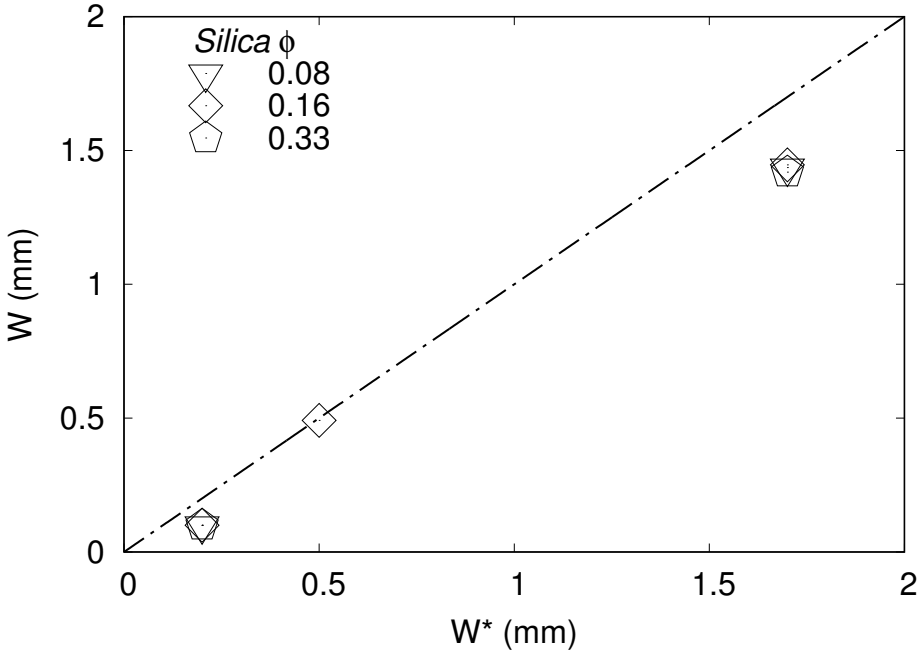

Figure 4.8.: Calculated thickness values W compared with the nominal values W^*. The dashed line represents the bisector.

ies. Moreover, measured W values affect the scattering intensity by smearing the curve but also by acting as a scale factor, hence they are partially correlated to the normalisation factor N_r, that increase up to about 57%. For data at $W^* = 0.2$ *mm*, when curves are very close to standard single-scattering conditions, the normalisation factor N_r is not needed ($N_r \simeq 1$) as data acquisitions were calibrated to have USAXS curves in absolute scale.

Deviations from the unitary value are dependent on the sample concentration and this multiple-scattering model does not account for the attenuation of the transmitted beam due to absorption. The beamline setup permits to normalise and correct the output from the detector by the sample transmission. Therefore, the trend of N_r values as a function of the colloid concentration and the sample thickness could be a compensation of the lower photon count due to absorption. This relationship is shown in Figure 4.9, where N_r values are linear with significantly the inverse of the measured transmission except for the most absorbing system ($\phi = 0.33$

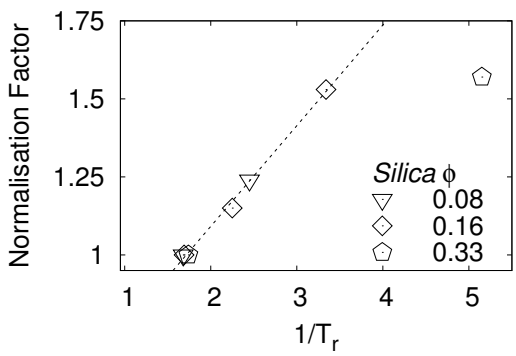

Figure 4.9.: Normalisation factor N_r as a function of the inverse transmission of the sample $1/T_r$. The dashed line is a guide to show the linear trend for $1/T_r < 4$.

and $W^* = 1.7$), which diverge from the linear trend.

4.2.2. Static Interactions in an Active Bacterial Medium

In this section a USAXS study of the effective static interactions between passive silica colloids in a bacterial medium is presented. Experiments were performed on three different silica volume fractions, nominally $\phi = 0.08,\ 0.16,\ 0.32$. In a first series of experiments (E1), samples were suspended in the motility buffer with a concentration of *E. coli*, $OD_{600} = 1,\ 2,\ 3$. A second set of measurements (E2) was done on mixtures where the stock suspensions of colloids were let ageing around ~ 4 hours with an excess of Tween20 concentration 0.24 *mM* (0.003 *wt%*), with the aim of further destabilising the colloidal suspension prior to the mixing with bacteria. In this case, the bacterial concentration span in the range $OD_{600} = 3,\ 4,\ 5$. In both experiments, USAXS measurements of passive silica colloids without bacteria were indispensable as they provided a reference about the static interactions in the passive system.

E1: Hard-Sphere Interactions

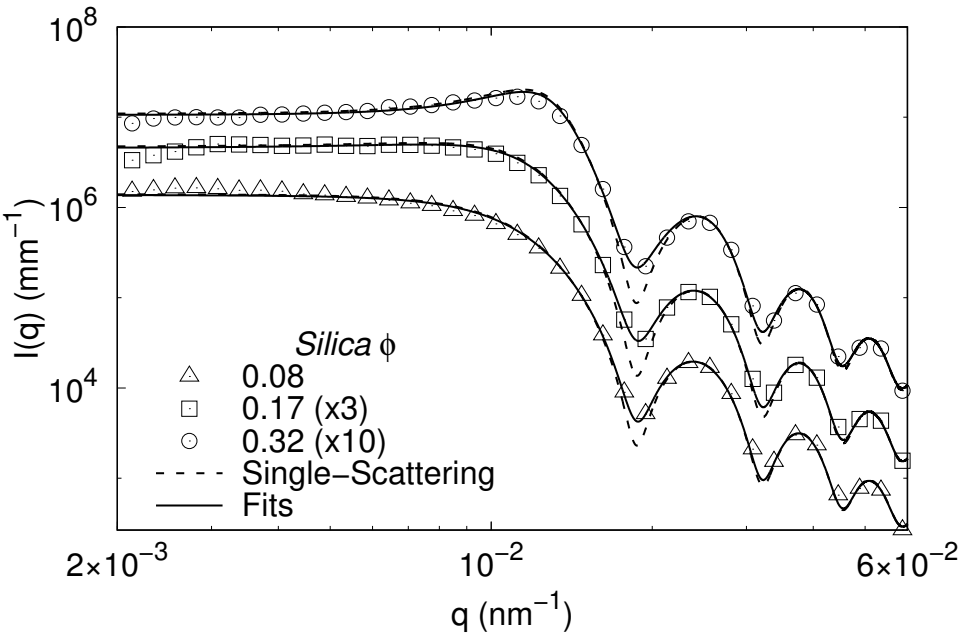

Figure 4.10.: Fits of USAXS curves of colloidal silica suspensions in motility buffer at various volume fractions (fitted values of 0.08, 0.17 and 0.32) using capillaries with thickness $W^* = 0.2$ *mm* (fitted value $W = 0.24$ *mm*). Data were modelled using effective HS potential for structure factor, where $\sigma_{HS} = \sigma$, and applying multiple scattering corrections.

In Figure 4.10, USAXS measurements of three different concentrations of passive suspensions are plotted. The decoupling approximations were used to include the polydispersity

and data were fitted with the structure factor $S(q)$ adopted for a HS repulsive potential in the Percus-Yevick closure relation (see Eq. 2.25). Samples were contained in $W^* = 0.2$ mm thick capillaries to reduce multiple-scattering effects on USAXS curves, which exhibit a restrained smearing mostly in the first minimum. The same analysis can be performed without including the multiple-scattering model and applying an effective instrumental smearing with $\sigma_q = 9.4 \times 10^{-4}$ nm^{-1}. This value is too large, as the FWHM of the beam size at a sample-detector distance of at 30.8 m is around $\Delta q \simeq 1.1 \times 10^{-3}$ nm^{-1} (considering the pixel size of the Pilatus detector), which is translated in a Gaussian smearing with $\sigma_q = 4.5 \times 10^{-4}$ nm^{-1}.

The HS potential is an adequate choice for the description of these USAXS curves. Hence the effect of the motility buffer, mainly of the presence of Tween20, results in an attenuation of the repulsive potential down to an effective HS interaction that maintains a stable suspension.

The presence of bacteria added in the suspensions apparently does not affect USAXS curves regardless of colloid and cell concentrations. Accordingly, the approximation in Equation 4.2 is fulfilled but there is no visible difference in the static interactions among passive colloids due to the presence of active *E. coli*. The comparison between the passive colloidal suspensions and the comparable active ones is shown in Figure 4.11, where systems with bacteria at $OD_{600} = 3$ are used as an example. Comparisons of systems at $OD_{600} = 1$ and 2 are not displayed.

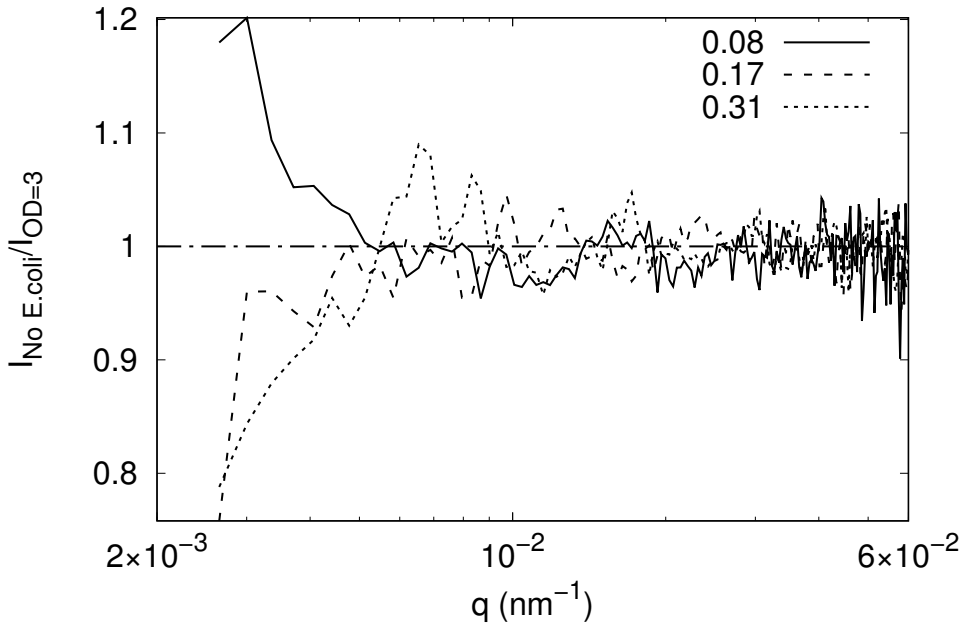

Figure 4.11.: Ratio of the scattering intensity values of passive and active suspensions of silica colloids at three volume fraction $\phi = 0.08$, 0.17 and 0.32. Active suspensions refer to the mixture at $OD_{600} = 3$.

Discrepancies for $q < 5 \times 10^{-3}$ nm^{-1} depend on the uncertainty due to the background subtraction and cannot be used to considered as differences in the structure factors, which should

also appear around the shoulder at $q \simeq 0.14\ nm^{-1}$. Data were acquired from samples with path-length $\sim 0.2\ mm$ resulting in low scattering intensities close to the background signal in the low-q region.

Finally, by looking at these data, it is possible to affirm that variations in the static interaction in a HS fluid consisting of silica colloids due to the motility of *E. coli* are either absent or small enough to not be visible even with such a high sensitivity. This result is comparable with simulations carried out by Loi et al. [69] where the structure factors from liquid, concentrated, passive and active systems are compared. Moreover, it is possible to confirm a posteriori the absence of the cross-term in Equation 4.2.

E2: Tuning the Interactions

From the data in experiment E1, it is reasonable to assert that the static interactions are not affected by the presence of bacteria, regardless of their motility. The effective static interaction between colloids leads to a weak stabilisation, which could be easily perturbed by small modifications of the chemistry in the suspension medium induced by the presence of *E. coli*. Effective HS potential results as a balance of repulsive and attractive contributions, hence, it should be possible to tune the interactions towards an attractive state by modifying the chemical composition of the motility buffer or the procedure of the sample preparation.

This tuning was achieved by let ageing stock suspensions of colloids with an excess of Tween20 concentration 0.24 *mM* (0.003 *wt%*) prior the mixing with *E. coli* and glucose.

Data of passive reference samples in Figures 4.12 and 4.13 present a big alteration due to the multiple-scattering, as thick capillaries of $W^* = 1.5\ mm$ were used. Here, the application of the multiple-scattering model did not require variations of the normalisation factors at different colloid concentrations as observed for suspensions in pure water (Table 4.4). In both E1 and E2 experiments, is was used a small beam-stop of 1.6 *mm* that does not include the pindiode employed to measure the transmitted intensity of the beam (see § 2.1.1). Compared to the experiment in § 4.2.1, data in Figures 4.12 and 4.13 were not corrected for sample transmission. In this case the normalisation factor was obtained as a global parameter for the six curves and obtained as a free parameter (the same procedure was adopted for E1). This was possible because when $\sigma = \sigma_{HS}$ the actual volume fraction ϕ is both a scaling factor of the scattering intensity and also a a key parameter for the structure factor $\phi = \phi_{HS}$. In this case, then, features from the structure factor analysis are strongly related to the absolute intensities. The comparison of the data in the current section and in § 4.2.1 suggests that the dependency of the normalisation factor N_r on sample pathlength and concentration may result as a compensation of the sample transmission.

Looking at the USAXS data it is not clear if there are significant changes in structure factors

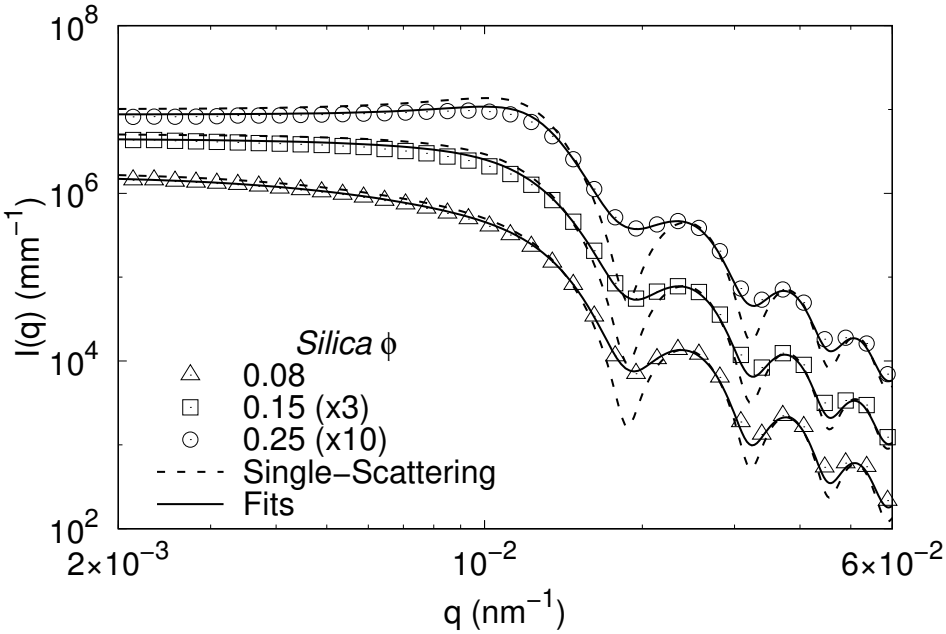

Figure 4.12.: Fits of USAXS curves of colloidal silica suspensions in motility buffer at various volume fractions (fitted values of 0.076, 0.150 and 0.254) using capillaries with thickness $W^* = 1.5$ (fitted value $W = 1.15$ *mm*). Data were modelled using an attractive Yukawa potential as structure factor and applying multiple scattering corrections.

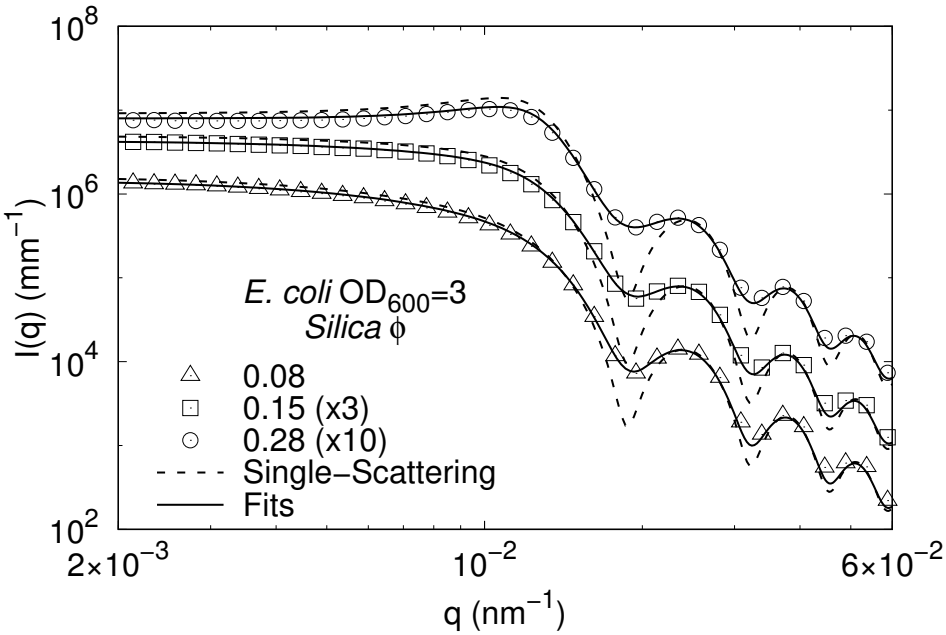

Figure 4.13.: Fits of USAXS curves of mixtures of colloidal silica and *E. coli* at $OD_{600} = 3$ in motility buffer at various volume fractions (fitted values of 0.077, 0.154 and 0.275) using capillaries with thickness $W^* = 1.5$ *mm* (fitted value $W = 1.15$ *mm*). Data were modelled using an attractive Yukawa potential as structure factor and applying multiple scattering corrections.

for systems with and without active bacteria. The comparison of each measured structure factor $S_M(q)$ (see Eq. 2.30) is shown in Figures 4.14 and 4.15 and in Table 4.5.

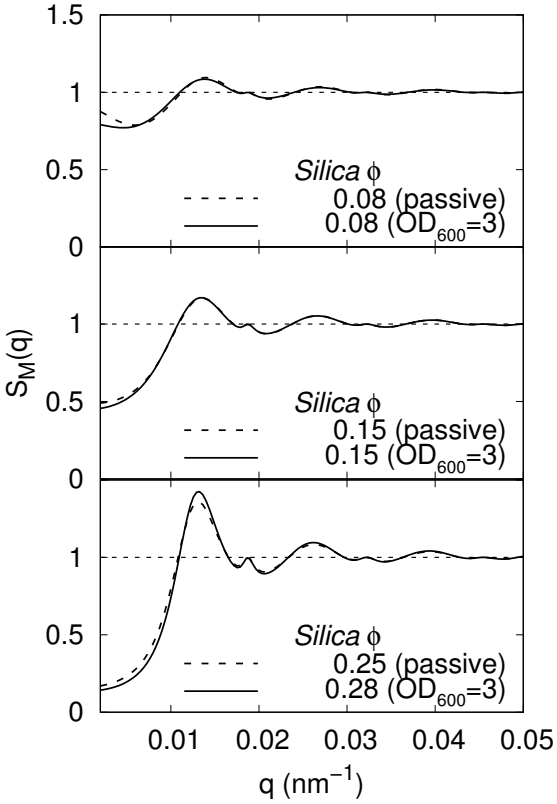

Figure 4.14.: Comparison of measured structure factors $S_M(q)$ obtained from the fits in Figures 4.12 and 4.13. Solid lines represent $S_M(q)$ curves for the colloidal mixtures with bacterial concentration $OD_{600} = 3$, dashed lines refer to passive systems without active cells.

Table 4.5.: Fit results for plots in Figures 4.14 and 4.15.

Passive System (No Bacteria)			
ϕ	0.076	0.150	0.254
$K\ (nm)$	-3.2	-1.7	-0.35
$Z\ (nm^{-1})$	11	10	15
Mixture at $OD_{600} = 3$			
ϕ	0.077	0.154	0.275
$K\ (nm)$	-2.5	-1.5	-0.15
$Z\ (nm^{-1})$	11	10	13

Results shown a decrease of the attractive interaction. The effect is weak but systematically present at all concentrations. Results for higher bacterial concentration ($OD_{600} = 4$ and 5) are not reported to avoid redundancy, as they exhibit the same USAXS profiles of the ones at $OD_{600} = 3$. Therefore, differences within the range $OD_{600} = 3 - 5$ seem to have no visible impact on the data.

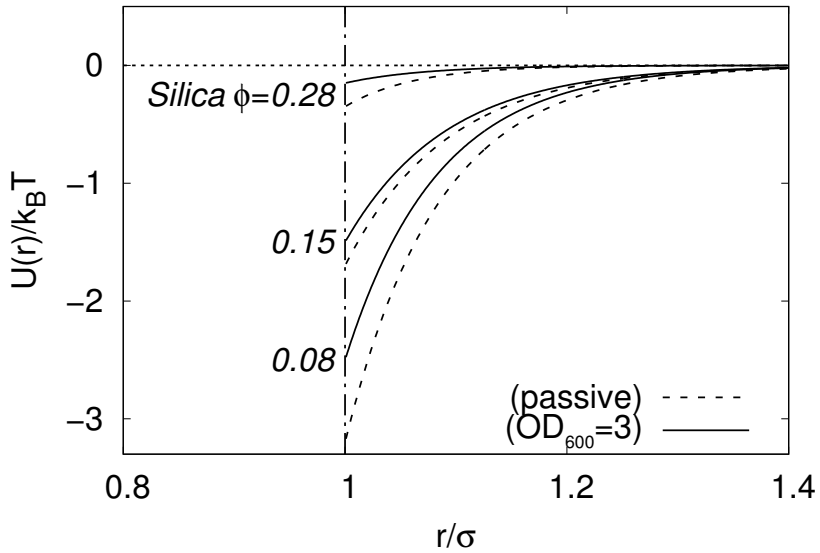

Figure 4.15.: Comparison of the attractive Yukawa potential $U(r)/k_BT$ obtained from the fits in Figures 4.12 and 4.13. Solid lines represent colloidal mixtures with bacterial concentration $OD_{600} = 3$, dashed lines refer to passive systems without active cells. The vertical dashed line represents the HS limit at the colloid diameter σ.

Summary

Mixtures of silica colloids and active *E. coli* were studied using USAXS. Data were analysed by means of structure factor of interactions and multiple-scattering models. Colloids suspended in motility buffer are considered as a HS fluid with or without the addition of bacteria (E1). Here, the presence of *E. coli* does not significantly affect the static interactions between colloids. Instead differences were found in a weakly attractive system (E2), where the presence of motile cells decrease the attractive strength of the interaction potential. This difference seems unconnected to the bacterial concentration in the range $OD_{600} = 3 - 5$ and linked to the presence of the motile cells. It should be noted that the reduction in the strength of the attractive potential in weakly attractive systems does not correspond to an increase in the repulsive interactions in the equivalent HS ones.

4.3. Dynamics: Results and Discussion

USAXS and XPCS measurements in experiments E1 and E2 were simultaneously performed on the same samples. XPCS measurements resulted from 500 frames of exposure time 0.2 *ms* spaced by a read-out of 2.3 *ms*, from which intensity-intensity autocorrelation functions were calculated, and USAXS curves were obtained making an average of these frames.

In this section the dynamics of active bacterial suspensions were investigated and compared to static results from USAXS. In experiment E1, a reference, dilute systems at $\phi = 0.008$, with

and without *E. coli*, were taken into account to compare the effects of the bacterial motion on both dilute and crowded systems.

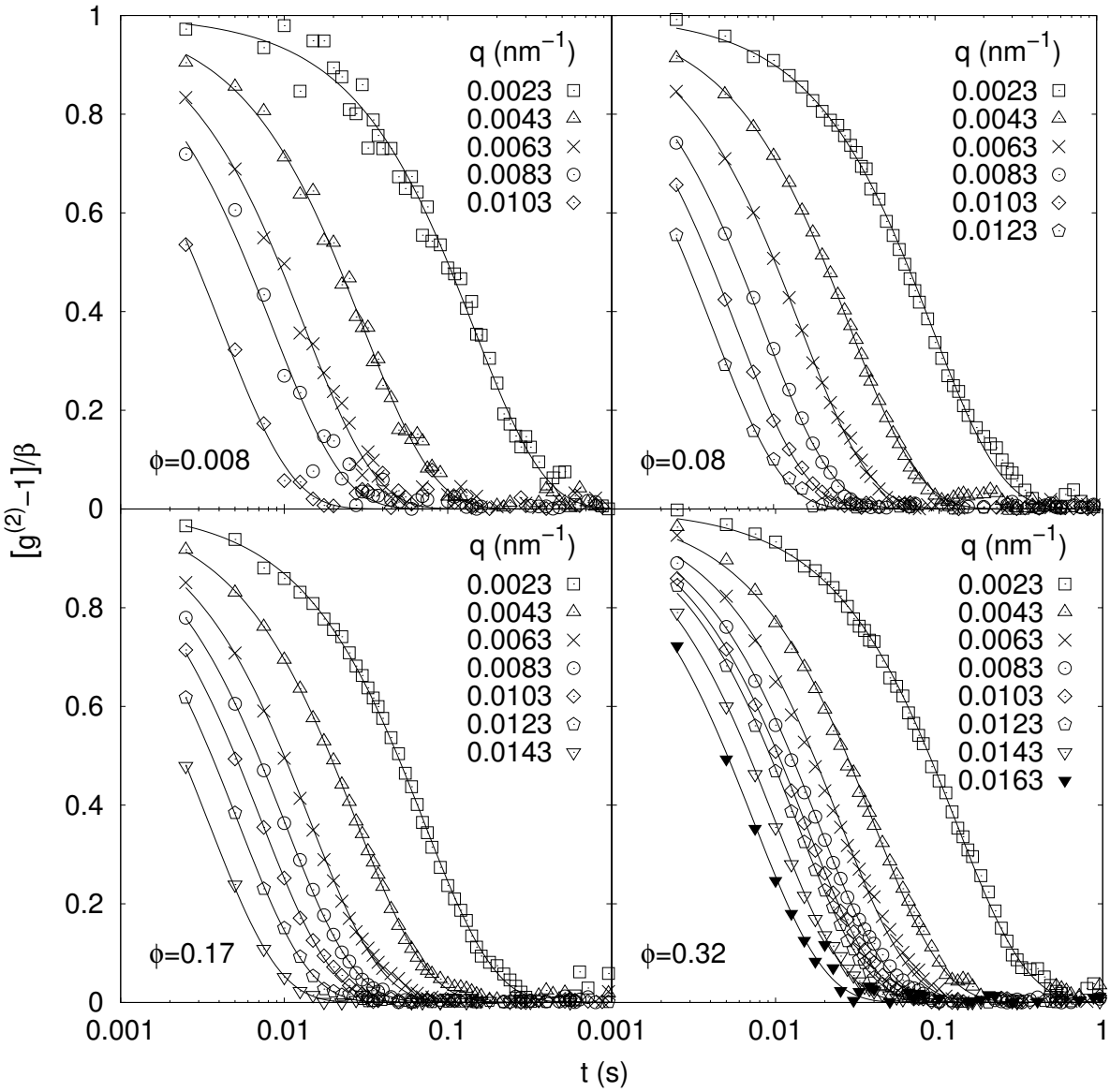

Figure 4.16.: Intensity-intensity autocorrelation functions $g^{(2)}(q,t)$ data fitted with Equation 4.5. Data refer to passive colloidal concentrations of $\phi = 0.008, 0.08, 0.17$ and 0.32.

Intensity-intensity autocorrelation functions $g^{(2)}(q,t)$ were analysed with a single exponential decay, as shown in Equation 2.34 and 2.35:

$$g^{(2)}(q,t) = 1 + \beta e^{-2\Gamma(q)t} \tag{4.5}$$

where $\Gamma(q)$ is the mean decay rate of the exponential function and β is the contrast factor that depends on the coherence properties of the X-ray beam. This approach was used for both

dilute and concentrated samples, as all systems displayed a single exponential behaviour. Fits concerning the passive, reference systems are reported in Figure 4.16.

In Figure 4.17, $\Gamma(q)$ values are plotted as a function of q^2. Only the system at $\phi = 0.008$ displays a linear trend in q^2, where the slope is the diffusion coefficient D (see Eq. 2.36). In this case of concentrated systems, instead, the decay rate is a more complex function of q and it is inversely proportional to the hydrodynamic structure factor, $H(q)$, given by:

$$H(q) = \frac{D_{eff} q^2}{\Gamma(q)} \tag{4.6}$$

where D_{eff} can be considered as an effective diffusion coefficient for colloids in concentrated systems. $\Gamma(q)$ values for ϕ from 0.08 to 0.32 are systematically lower than the dilute system. The dynamics are slower and slower due to the crowded environment, where a pure random-walk is affected by the interactions among colloids. For low-q values, $\Gamma(q)$ is similar for the whole set of concentrations because the correlations correspond to the long-time range. In this case, they are equivalent to the Brownian motion of non-interacting colloids, whereas for higher q values, as shorter distances are probed, $\Gamma(q)$ curves show crowding effects due to the interactions with the closest neighbours.

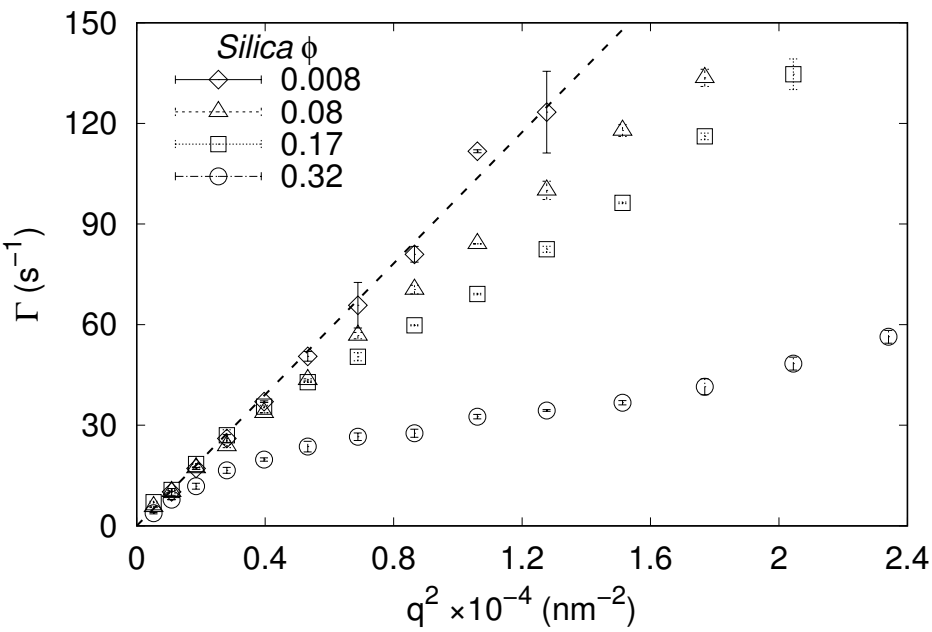

Figure 4.17.: Decay rate $\Gamma(q)$ as a function of q^2. Data refer to the passive systems of reference, without bacteria. The dashed line represents the linear fit $\Gamma = Dq^2$ for the diffusion of passive colloids in the dilute system at $\phi = 0.008$

Multiple-scattering, observed in static USAXS curves in E1 and E2 (respectively with sample thickness $W^* = 0.2$ and 1.5 *mm*), affects also XPCS measurements but it just results in a

reduction of the contrast factor β because of a mixing effect involving different single- and multiple-scattering signals coming from the sample. Indeed values of β were around 0.1 in E1 and 0.04 in E2. Results about dynamics and hydrodynamic structure factors are not influenced [163].

E1: Hard-Sphere Fluid

The passive dynamics shown in Figure 4.17 are compared with $\Gamma(q)$ curves obtained from the bacterial mixtures at $OD_{600} = 1$, 2 and 3. In Figure 4.18, $\Gamma(q)$ of passive and active systems are presented. The active system refers to the suspension at $OD_{600} = 3$, lower bacterial concentrations are not shown for the clarity of the plots. The linear fits were performed using the equation $\Gamma(q) = D_{eff}q^2$, where the average slope, D_{eff}, gives a measure of the effective diffusion in concentrated systems.

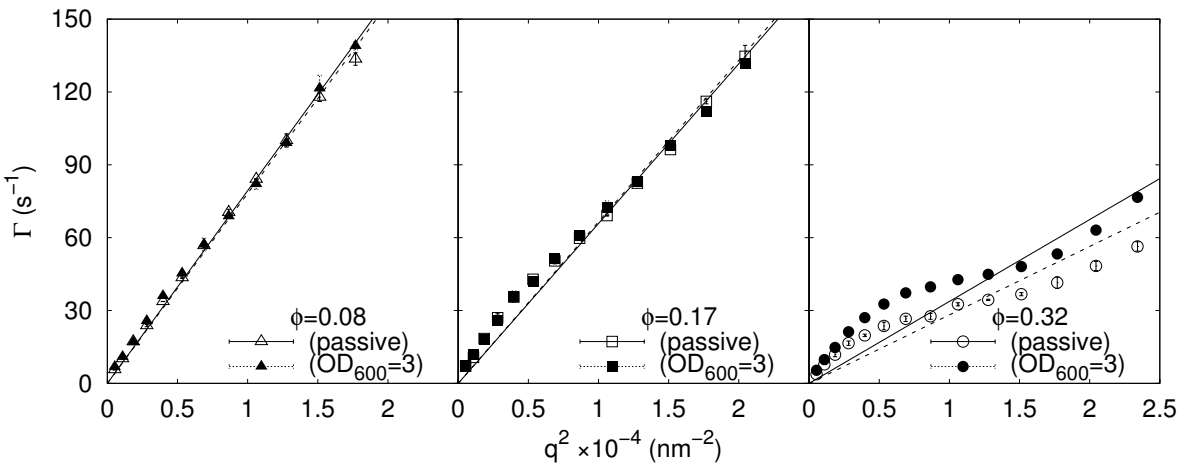

Figure 4.18.: Plots of $\Gamma(q)$ values as a function of q^2 for systems with volume fraction $\phi = 0.08$ (left), 0.17 (centre) and 0.32 (right). Linear fits were used to determine the effective diffusion D_{eff}. Empty symbols and dashed lines concern passive systems whereas full symbols and solid lines refer to samples with bacterial concentration $OD_{600} = 3$.

Each set of data was obtained by averaging 5 XPCS acquisitions over different spots of the samples and the error bars were associated to the mean square deviations. $\Gamma(q)$ curves at $\phi = 0.08$ and 0.17 do not show real differences in dynamics instead at 0.32, the active system do exhibit an enhanced diffusion compared to the passive reference.

D_{eff} values are also used to normalise the inverse of $\Gamma(q)$ and obtain the hydrodynamic structure factor $H(q)$, as shown in Figure 4.19. There is no significant difference in $H(q)$ for any combination of colloidal and bacterial concentrations. Moreover, the peak of static structure factor $S_M(q)$ fitted from USAXS curves correspond to the peak position of $H(q)$ at $\phi = 0.32$ [at lower concentration $H(q)$ peaks are not well-defined and the comparison is not precise]. These

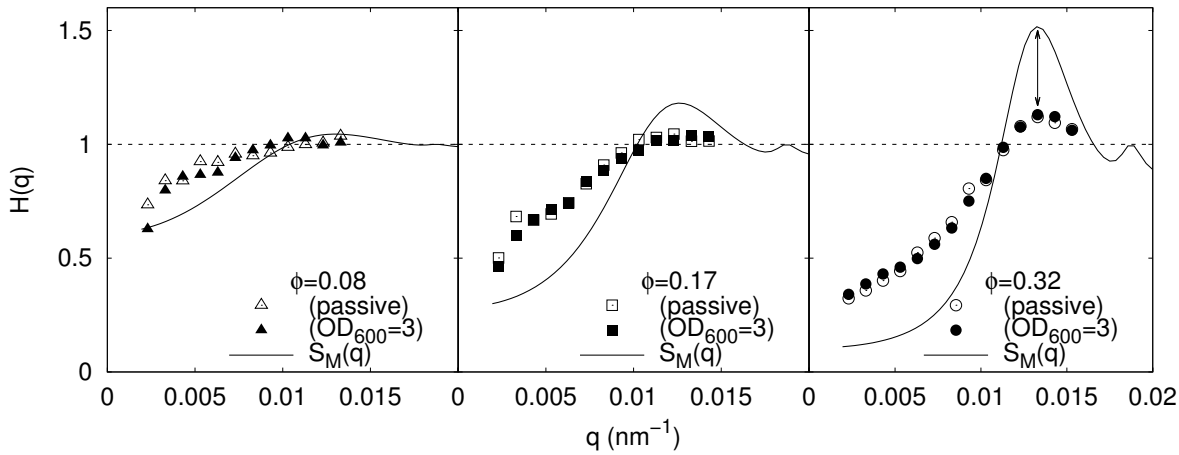

Figure 4.19.: Plots of hydrodynamic structure factors $H(q)$ for systems with volume fraction $\phi = 0.08$ (left), 0.17 (centre) and 0.32 (right). Empty symbols concern passive systems whereas full symbols refer to samples with bacterial concentration $OD_{600} = 3$. Solid lines are the measured static structure factors of the passive systems obtained from fits in Figure 4.10.

results suggest that the hydrodynamic interactions between colloids for passive and active systems are comparable and in turn, they are also consistent with the static interactions. Hence, the presence of motile bacteria does not significantly affect both static and hydrodynamic interactions among passive colloids under these conditions.

Results about the effective diffusion D_{eff} as a function of the bacterial concentration are shown in Figure 4.20 (top panel) and compared with the passive dynamics. The diffusion is weakly affected for low and medium concentrations, whilst at $\phi = 0.32$, where the passive diffusion is drastically hindered, the presence of bacteria speeds up the dynamics, probably linearly with the bacterial concentration. An opposite behaviour is observed in the dilute system at $\phi = 0.08$, where the effective diffusion of the active sample at $OD_{600} = 3$ is slower than the passive ones. Although, values at $OD_{600} = 1$ and 2 are comparable with the passive dynamics. In the bottom panel of Figure 4.20, the same results are presented as the inverse of the ratio between effective diffusion of the system containing bacteria, D_{eff}, and the reference $D_{passive}$. Using the Stokes-Einstein equation (see Eq. 1.6), value of D_{eff} can be considered as inversely proportional to an effective viscosity η_{eff}:

$$\left(\frac{D_{eff}}{D_{passive}}\right)^{-1} \equiv \frac{\eta_{eff}}{\eta_{passive}} \tag{4.7}$$

where $D_{passive}$ and $\eta_{passive}$ represent effective diffusion and viscosity of the passive systems. With this representation, values $(\eta_{eff}/\eta_{passive}) < 1$ describe the enhancement of dynamics and, vice versa, for slower dynamics.

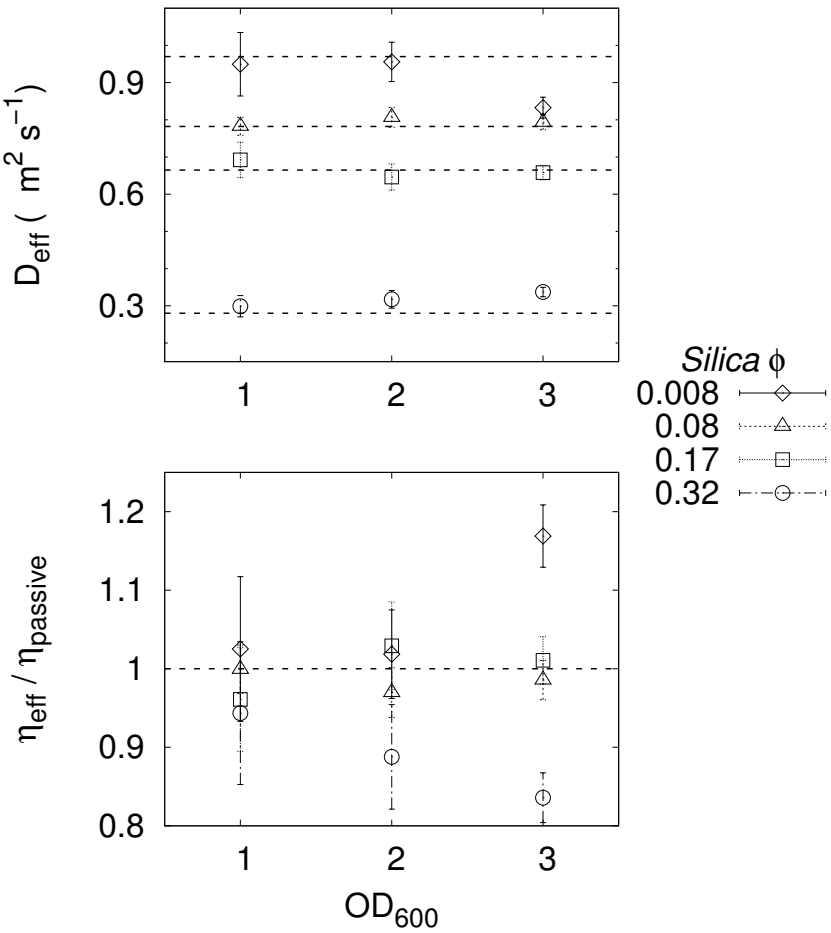

Figure 4.20.: (Top figure) Effective diffusion coefficients D_{eff} as a function of the bacterial concentrations. Dashed lines represent the effective diffusion of the respective passive systems. (Bottom figure) Ratio between effective viscosities of the system containing bacteria (η_{eff}) and the reference one ($\eta_{passive}$).

E2: Weakly Attractive System

In experiment E2, the dynamics of weakly-attractive systems is studied using bacterial mixtures at $OD_{600} = 3$, 4 and 5. In Figure 4.21, results about the effective diffusion D_{eff} are presented (top panel) and compared with the passive dynamics.

In this case, the diffusion in active systems is systematically higher than passive D_{eff} values for the three colloidal concentrations but, the enhancement is not linear with the bacterial concentration. Viscosity ratios in the bottom panel of Figure 4.21 highlight these differences. The stronger enhancement of dynamics is again observed in the slowest, most concentrated, system. For each concentration, viscosity ratios at $OD_{600} = 3$ and 4 are comparable and get closer to 1 for samples at $OD_{600} = 5$. Data suggest that $OD_{600} = 3$ is an optimal concentration for these experiments, considering that with this concentration effects on dynamics due to *E. coli* presence are maximised. The decrease in efficiency at $OD_{600} = 5$ could be ascribed to the fact that,

at such a concentration but in absence of colloids, bacteria start interacting and swimming in clusters, though, no clean evidence of such a behaviour could be extracted from both USAXS and XPCS data presented in this work. Another possible explanation is that with a bacterial concentration of $OD_{600} = 5$, the depletion of glucose and oxygen is fast and experiments might have been performed at the limit of the permitted time window, when the energy source for the motility was running out.

This consideration was exploited in order to have further comparison with passive dynamics. Samples at $OD_{600} = 5$ were re-measured after a delay Δt longer than one hour to allow a complete glucose consumption. USAXS data were again indistinguishable from curves at $\Delta t = 0$ but the differences in dynamics are presented in Figure 4.22.

For all the three concentrations, dynamics slowed down around one hour after the first measurements at $\Delta t = 0$. It was expected as, in this situation, the bacterial motion is quite sup-

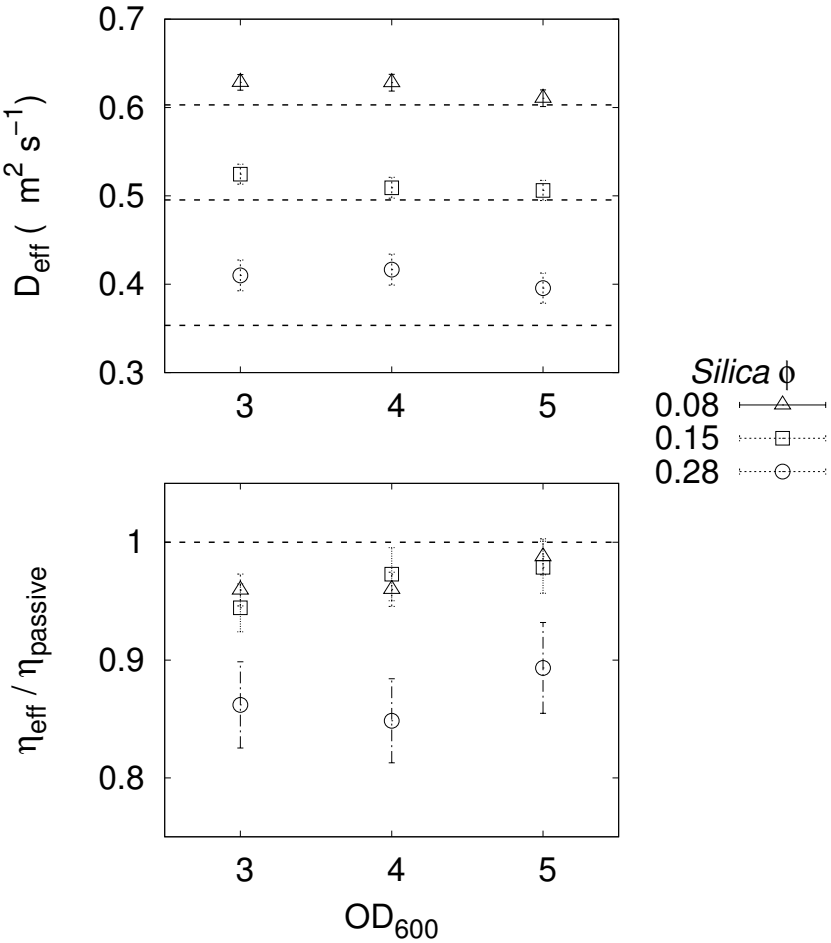

Figure 4.21.: (Top figure) Effective diffusion coefficients D_{eff} as a function of the bacterial concentrations. Dashed lines represent the effective diffusion of the respective passive systems. (Bottom figure) Ratio between effective viscosities of the system containing bacteria (η_{eff}) and the reference one ($\eta_{passive}$).

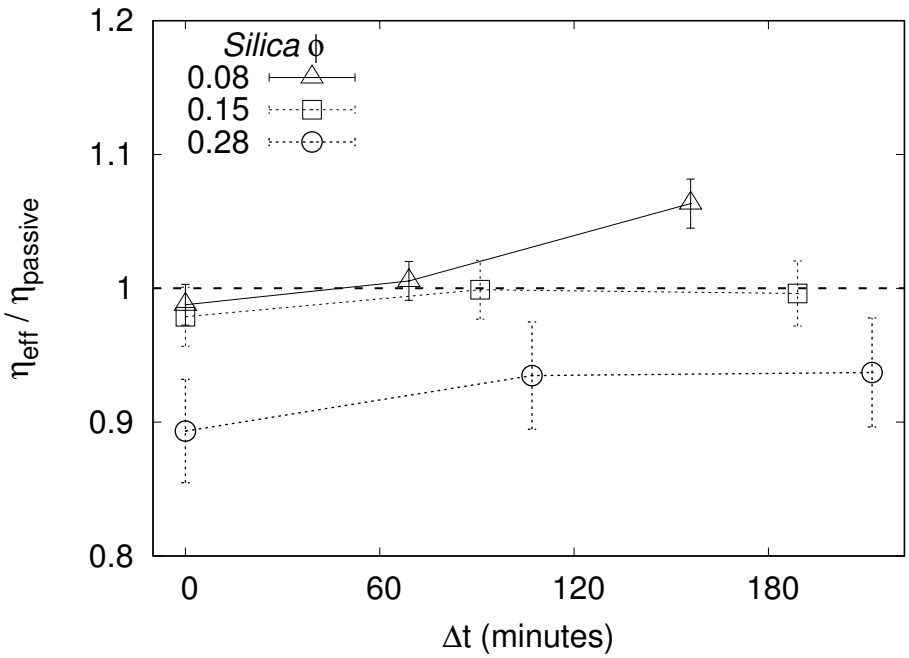

Figure 4.22.: Time evolution of the ratio between effective viscosities of the system containing bacteria (η_{eff}) and the reference one ($\eta_{passive}$). Systems at $OD_{600} = 5$ were measured just after mixing with glucose ($\Delta t = 0$).

pressed. However, the dynamics at $\phi = 0.28$ (assumed to be comparable for values around $\phi \sim 0.3$) remain faster than the passive system whilst at $\phi = 0.08$ the effective viscosity becomes even higher than the reference value, reminding the slowing down effect observed in the hard-sphere system (E1) for $\phi = 0.08$ at $\Delta t = 0$.

Summary

XPCS measurements on both hard-sphere fluid (E1) and weakly-attractive systems (E2) were performed. In general, the presence of motile *E. coli* has a small, but distinguishable effect on the dynamics of silica colloidal suspensions. These effects are pronounced in concentrated systems such as at $\phi = 0.32$ (E1) and 0.28(E2) but seems not present for intermediate values (0.08 and 0.17 in E1). The passive dynamics in experiments E1 and E2 for matching concentrations are not comparable, as weakly attractive systems show slower dynamics than equivalent hard-sphere fluids due to the attractive interactions.

A nice comparison seems achievable by plotting viscosity ratios as a function of the effective diffusion of passive systems $D_{passive}$, as it is presented in Figure 4.23. This representation appears to condense all the results in a single trend, where the presence of bacteria speeds up slow-systems but slows down dilute-suspensions and finds a balance at intermediate dynamics.

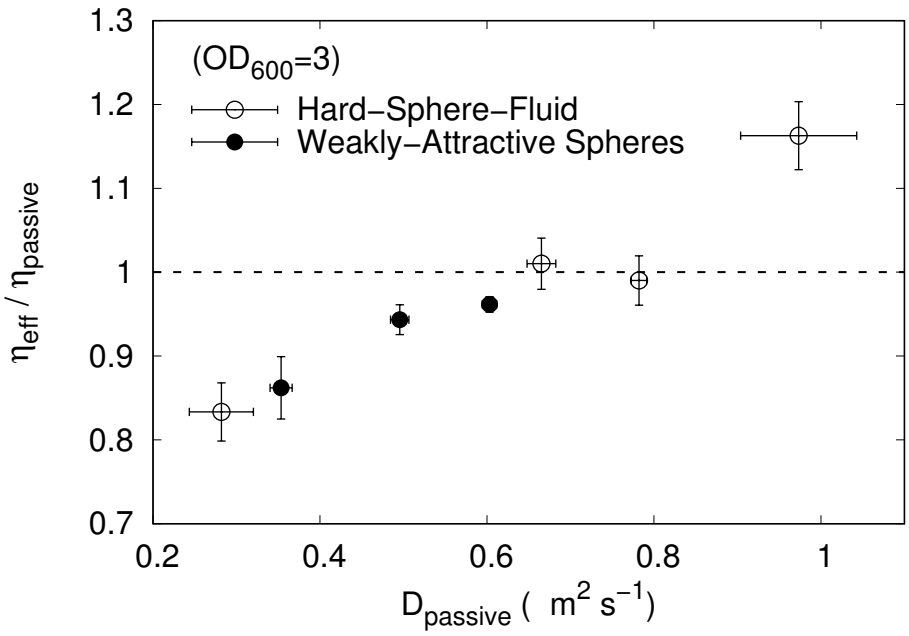

Figure 4.23.: Ratio between effective viscosities of the system containing bacteria (η_{eff}) and the reference one ($\eta_{passive}$) as a function of the effective diffusion coefficients $D_{passive}$ of the passive systems of reference. η_{eff} values refer to systems at $OD_{600} = 3$.

4.4. Summary and Conclusion

In this section, USAXS and XPCS measurements and analysis of sub-micron, concentrated passive silica colloids in active *E. coli* medium have been presented.

USAXS curves from high-contrast silica colloids exhibited alteration due to the presence of multiple-scattering, which was investigated by varying colloid concentration and beam path-length of the sample. Multiple-scattering data were modelled using the model proposed by Schelten and Schmatz [88] and tested with three different structure factor models describing distinct potentials: short-range repulsion, hard-sphere repulsion and short-range attraction. The multiple-scattering model was tested on passive suspension of silica colloids in pure water prior to the application on data from active systems containing bacteria.

From USAXS curves, a comparison among static structure factors of passive and active systems were presented. Silica colloids used in this experiments displayed effective hard-sphere repulsion when suspended in the motility buffer and no significant changes were observed in combination with the presence of active bacteria in the range of concentrations $OD_{600} = 1-3$. Tuning the static interactions in the passive system, by using an excess of Tween20 (main component responsible for the colloidal destabilisation), results in an effective long-range attraction between colloids. In this case, motile bacteria attenuate the strength of attractive interactions generating a contribution for the stabilisation. Notice that in hard-sphere systems, there was no

enhanced repulsion, indicating that the activity of the bacteria does not add a repulsive contribution to the effective interaction potential but reduces the attractive one, suggesting an enhanced effective temperature-like effect on the interaction potential of the colloids. A resembling effect was observed by Schwarz-Linek et al. [164], where they reported a reduction of depletion attraction forces in active *E. coli* suspensions compared to the passive reference samples. In the current work, it is not easy to deduce information on the nature of the colloidal destabilisation due to commercial Tween20 (polysorbate 20), that is a polar surfactant. Finally, variation in static interactions observed in E2 do not depend on the bacterial concentration. At the same time, the lack of visible changes in E1 suggests that the interaction potential is not affected by possible chemical alteration of the suspension medium induced by the addition of bacteria.

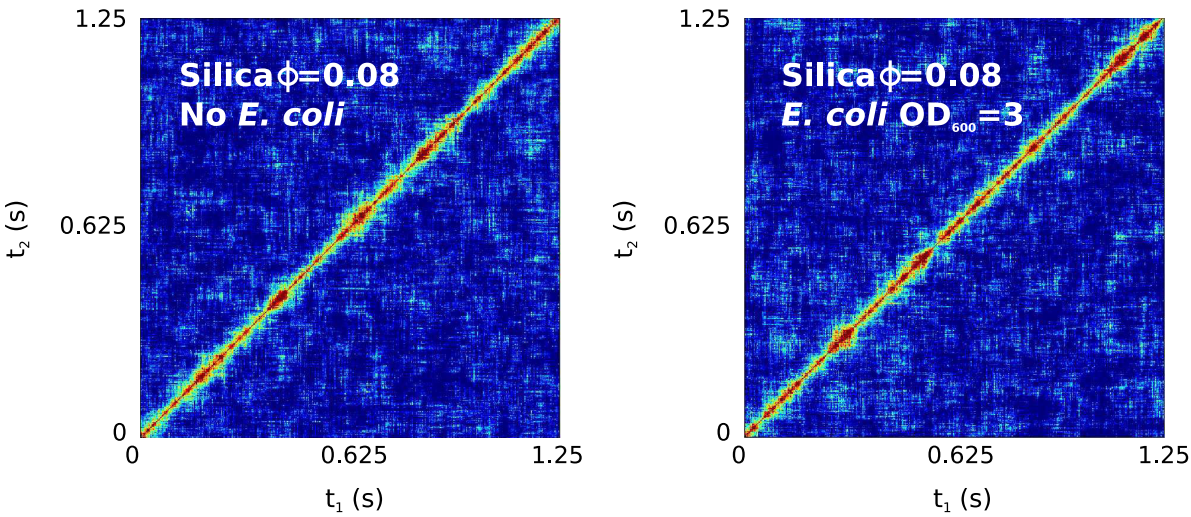

Figure 4.24.: 2-time correlation functions plots for silica colloids at $\phi \simeq 0.08$ with (left) and without bacteria (right) at $OD_{600} = 3$. The colour scale goes from blue to red, respectively representing $g^{(2)}(t) = 1$ and $g^{(2)}(t) = 1.1$. Data refer to $q = 0.0043\ nm^{-1}$.

The analysis of the intensity-intensity autocorrelation functions from XPCS measurements also excluded the presence of visible radiation damage. XPCS acquisitions were performed on either the same or different spots of the capillaries giving reproducible results. Moreover, the 2-time correlation functions (Eq. 2.32), as is shown in Figure 4.24, did not exhibit any variation in the system dynamics over time, such as ageing-like effects.

The comparison between hydrodynamic and static structure factors did not display significant variations. Hydrodynamic interactions between colloids are comparable in both active and passive systems, hence the influence of active bacteria does not seem to have a hydrodynamic contribution among silica colloids.

The colloidal Brownian motion is affected depending on respective passive dynamics of the suspension, that in turn depend on the concentration and the interaction potential. The presence of *E. coli* speed up slow-diffusive systems, either concentrated hard-sphere fluids or weakly-

attractive systems, while intermediate concentration of hard-sphere seems not affected or even slowed down in the dilute case. A single trend for both E1 and E2 is recovered when plotting the ratios of effective viscosities over passive values as a function of the effective diffusion of passive systems. This plot in Figure 4.23 displays a levelling-off in the dynamics caused by the presence of bacteria.

These results, along with the increase in viscosity ratios observed after glucose depletion, suggest that two mechanisms are simultaneously in action. The first could be directly ascribed to the active dynamics of swimming bacteria that enhances the dynamics and static interactions of colloids via a temperature-like effect defining an effective temperature T_{eff} in the system. The second mechanism is most probably not related to the cell motility and concerns a viscosity term added by the presence of *E. coli* that slows down colloids. These two effect are not separable if only the effective diffusion is taken unto account, as evident from the relation:

$$\left(\frac{D_{eff}}{D_{passive}}\right)^{-1} \equiv \frac{\eta_{eff}}{\eta_{passive}} \frac{T}{T_{eff}} \tag{4.8}$$

Effective temperature and viscosity effects operate in the opposite directions, finding a balance for specific combination of concentrations and interactions, as observed in HS systems with volume fractions of $\phi = 0.08$ and 0.17. In systems where the colloidal motion is heavily hindered by trapping effects (high concentrations or attractive interactions), the slow dynamics of passive colloids could dominate over the viscosity contribution due to the presence of bacteria and the effective temperature effect starts to be visible. In this current work it is not possible to separate and quantify effective temperatures and viscosities, so a single concept of "variation in effective viscosity" is accounted for a comparative description of the systems.

Considering a single bacterium moving at the maximum velocity $\langle v \rangle_{MAX} = 20\ \mu ms^{-1}$, the cell body would physically encounter no more than ~ 40 particles per second in the most concentrated case $\phi = 0.32$. This value is far from the numbers of colloids per cell in these systems, which are of the order of several hundreds, or thousands depending on the concentration. If only a HS, pushing interaction is taken into account, the activity of bacteria should not be visible. Therefore a long-range effect has to be associated with the reported results. As a matter of fact, flagella extension can close the gap between two cells, interacting with much more colloids than the bacterial cell bodies. Moreover the flow field generated by a single cell has a dipole pattern that decays in the long-range as $\propto r^{-2}$ [67, 68]. Hence, long-range hydrodynamic effects and the presence of rotating flagella, also essential part for the dipole flow field, can explain how all colloids are entirely affected by such a few cells.

5. Colloids in a Phase Separating Medium: Microstructure and Dynamics

In this chapter a USAXS/XPCS investigation of the microstructure and the dynamics of bare silica, and silica/nickel Janus, colloids which mimic active motion is reported. The study concerns sub-micron-sized silica colloids (used as a reference system) and half-coated silica/nickel Janus colloids suspended in a quasi-binary mixture of 3MP/H_2O/D_2O undergoing liquid-liquid phase separation. This mixture has limited miscibility at an intermediate temperature range, characterised by a closed-loop coexistence curve, but it forms a homogeneous phase at room temperature [40]. When charge-stabilised silica colloids are suspended in this medium, it is possible to observe a wetting-induced reversible aggregation of colloids as a function of the temperature and the 3MP concentration. These effects are due to the preferential adsorption of 3MP on the silica surface and, in the two phases region, colloids partition into the preferred phase. Preliminary XPCS experiments on silica colloids suspended in 3MP mixtures were performed by quenching the sample to the two-phase region and monitoring the colloid dynamics as a function of time. Then, similar XPCS experiments were performed on half-coated silica/nickel Janus colloids, which were synthesised using a sputtering technique.

5.1. Materials and Methods

Monodisperse silica colloids (average diameter $\langle\sigma\rangle = 427\ nm$ and PDI< 0.05) were synthesised via the Stöber method [23]. Specifically, a solution of 6 *ml* of ammonium hydroxide in 25 *ml* of ethanol was added step-wise in a 100 *ml* round-bottom flask containing a solution of 6 *ml* of tetraethyl orthosilicate (TEOS) in 25 *ml* of ethanol while the flask was being agitated. This final solution was shaken with a Flask Shaker (Stuart Scientific) for 20 hours in order to fully complete the reaction. The Stöber colloids were allowed to sediment to the bottom of the container and ethanol was exchanged with pure water. This solvent exchange was repeated several times to thoroughly remove any trace of ethanol, TEOS and ammonia. Silica/nickel

Janus colloids were synthesised by a surface science approach [165] using the Stöber colloids as a colloidal template and partially coating them with a thin layer of nickel using a Cressington 108 auto sputter coater. More details about this synthesis are given in § 5.1.1 and illustrated in Figure 5.1. Samples of both Stöber and Janus colloids were suspended in two different media, consisting of a mixture of 1:4 H_2O:D_2O by mass and a different amount of 3MP, 25 and 35 *wt%*. 3MP, TEOS and ethanol were purchased from Sigma Aldrich, ammonium hydroxide 28% v/v was purchased from Alpha Aesar and the nickel target 57×0.1 mm^2 was purchased from Ted Pella, Inc..

USAXS and XPCS measurements were performed at the TRUSAXS beamline (ID02) at the ESRF. The incident X-ray wavelength was $\lambda = 0.0995$ *nm* and the sample-detector distance was set to 30.8 *m*. XPCS acquisitions were taken with a Pilatus 300K detector and the maximum FWHM beam size was around 40×40 μm^2 (defined by the slits) and an incident intensity of 2×10^{11} *photons* s^{-1}. The Pilatus 300K detector was used at the maximum frame rate of 400 *Hz*, equivalent to a time resolution of 2.5 *ms*. Intensity-intensity autocorrelation functions were calculated using the PYXPCS software (developed at ID10, ESRF) from a series of up to 500 frames with an exposure time of 0.2 *ms* and a read-out time of 2.3 *ms*, corresponding to a continuous irradiation of the sample of 1.25 *s*. An inhouse-built thermal stage with *mK* temperature control was used to perform slow temperature scans [$\Delta T = (0.3 - 0.5)$ °*C* every 60 *s* to permit stabilisation] which allowed characterising the phase transition temperatures, while fast *in situ* temperature quenches were obtained by heating the samples at a rate of 0.33 °*C* s^{-1} using a Mettler Toledo heating stage. Samples were contained in flat-walled pyrex capillaries of wall thickness 0.1 *mm* and pathlengths of 0.5 or 1 *mm*.

5.1.1. Synthesis of Silica/Nickel Janus Colloids

Polished 2×2 cm^2 $\langle 100 \rangle$ silicon wafers were uniformly coated with ~ 9 μl of Stöber silica colloids suspended in ethanol, at $\phi < 0.01$. After solvent evaporation under vacuum, the substrates were further dried for 10 minutes and dry monolayers of colloids were obtained (see Fig. 5.1). Brighter regions on the substrates were carefully removed manually, in order to eliminate multi-layers of colloids that accumulate on the borders of the wafer because of Marangoni flow (coffee ring effect). The quality of colloidal monolayers were verified by Atomic Force Microscopy (AFM) using an AFM-MFP3D Asylum Research instrument [Fig. 5.2(a)]. Then, the monolayers were coated by sputtering with a very thin layer of nickel (100 *s* exposure at 10 *mA*). During the sputtering, an argon atmosphere with partial pressure 0.055 *mbar* was necessary to avoid the formation of nickel oxide. Most likely, a percentage of metal were oxidised in the next phases of the synthesis or in later stages in stock suspensions. The sputtering conditions

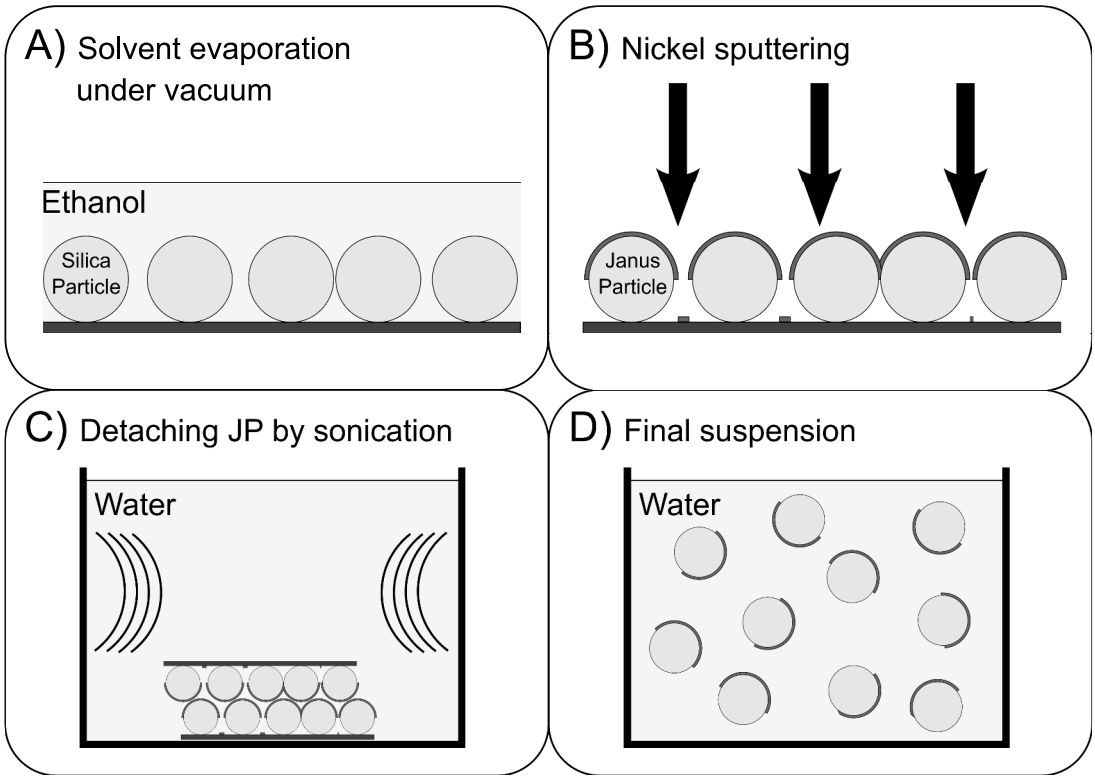

Figure 5.1.: Sketch of the JP synthesis using the sputtering method.

were determined by carrying out a series of ellipsometry measurements (using a Beaglehole Picometer Light Ellipsometer) on silicon wafers coated with nickel at different conditions of pressure, time and current during the coating. This enabled a nickel layer that was as thin as possible to be obtained. Coated colloids were released from the wafer in water by bath sonication (Bioblock Scientific 88154) at 45 $°C$ for 15 minutes. The silicon wafer was removed and a further, more intense, sonication was then applied for 2 minutes (with a probe sonicator Vibracell 75185 from Sonics & Materials) to break possible particle clusters formed during the nickel coating procedure. The sputtering process was repeated on up to 200 substrates to increase the number of Janus particles produced. Finally 500 ml of a very dilute suspension of Janus colloids was obtained. This dilute suspension was centrifuged at 500 g for 25 minutes in 50 ml falcon tubes, the supernatant was removed and saved, and the concentrated suspension was separated from silicon debris stuck on the relatively hydrophobic surfaces of the tubes. The supernatant was further centrifuged at 100 g for 2 hours in 50 ml falcon tubes. Janus colloids from both centrifugation cycles were transferred in 1.5 ml Eppendorf vials and the same centrifugation procedure repeated (using smaller time-scales) until a single stock suspension was contained in a single 1.5 ml vial. The suspension was then further concentrated by removing supernatant upon sedimentation down to 100 μl and a final volume fraction of Janus colloids estimated to $\phi \sim 0.03$ was achieved.

Characterisation

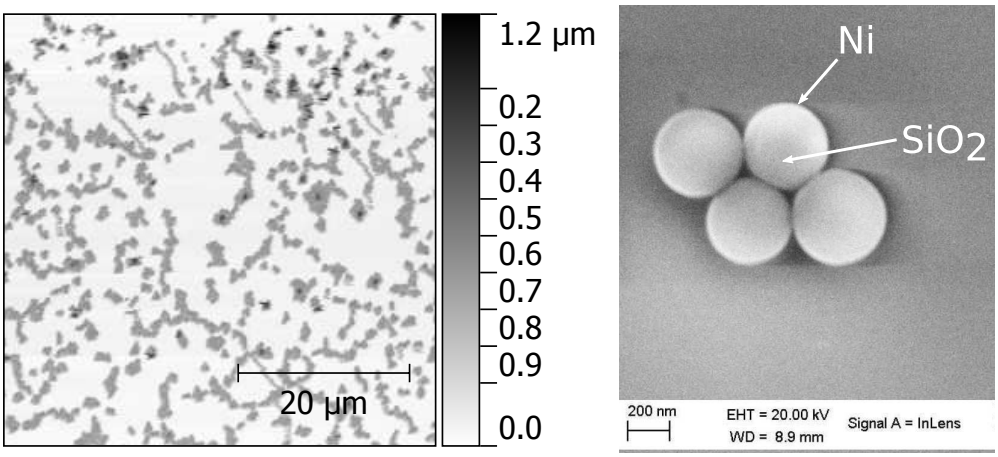

(a) (b)

Figure 5.2.: (a) AFM measurements of dry silica colloids on a silicon substrate. Light-gray areas display the monolayer whilst the black spots represent the presence of a few colloids on a second layer. (b) SEM measuremets on silica/nickel Janus colloids. For the measurements, a drop of dilute suspension in water was let dry on a silicon wafer.

Silica/nickel Janus colloids were characterised by Scanning Electron Microscopy (SEM) and SAXS. SEM measurements (carried out with a LEO 1530 Scanning Electron Microscope) were used to verify the thickness of the nickel layers, visible as brigther regions in Figure 5.2(a). However, in the SAXS range, the scattering amplitude A_{JP} of a half-coated sphere was modelled following the same procedure applied to a spherical core-shell geometry (see Eq. 2.12) but using a hemispherical shell to describe the partial coating of the core as depicted in Figure 5.3.

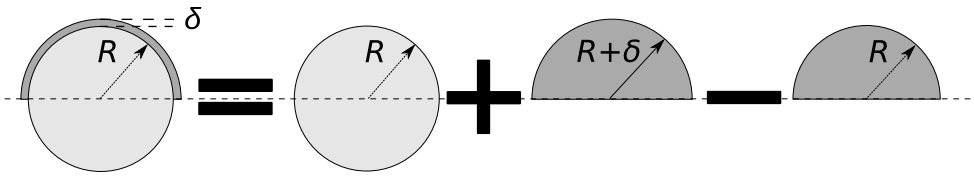

Figure 5.3.: Building-up of a half-shell Janus geometry, where R is the radius of the core colloids and δ is the thickness of the half-shell. The different XSLD of the materials is represented by the colour, light-grey for a silica core and a dark-grey for the nickel coating.

The scattering amplitude of a hemisphere A_{hemi} was modelled in cylindrical coordinates adopting the strategy used by Kaya and de Souza [139] to obtain the spherical caps for the capped-cylinder scattering amplitude.

$$A_{hemi}(q,R,\theta) = \Delta\rho 2\pi R^3 \left[\mathscr{C}(q,R,\theta) - i\mathscr{S}(q,R,\theta)\right] \tag{5.1}$$

where the real $\mathscr{C}(q,R,\theta)$ and imaginary $\mathscr{S}(q,R,\theta)$ terms in Equation 5.1 are described as:

$$\mathscr{C}(q,R,\theta) = \int_0^1 \cos[q\cos(\theta)Ry](1-y^2)\frac{J_1[q\sin(\theta)R\sqrt{(1-y^2)}]}{q\sin(\theta)R\sqrt{(1-y^2)}}\,\mathrm{d}y$$
$$\mathscr{S}(q,R,\theta) = \int_0^1 \sin[q\cos(\theta)Ry](1-y^2)\frac{J_1[q\sin(\theta)R\sqrt{(1-y^2)}]}{q\sin(\theta)R\sqrt{(1-y^2)}}\,\mathrm{d}y \tag{5.2}$$

The imaginary part $\mathscr{S}(q,R,\theta)$ comes from the asymmetry of the hemisphere along the integration z-axis in cylindrical coordinates and vanishes when calculating the scattering form factor P_{JP} from the complex product of the amplitude (Eq. 5.3). An orientation average (see Eq. 3.2) is necessary as a Janus colloid does not have a spherical symmetry. Finally, the form factor P_{JP} is given by the equation:

$$P_{JP}(q,R,d) = \langle \left|\Delta\rho_c A_{sph}(q,R) + \Delta\rho_h\left[A_{hemi}(q,R+\delta,\theta) - A_{hemi}(q,R,\theta)\right]\right|^2\rangle_\Omega \tag{5.3}$$

where $\Delta\rho_c$ and $\Delta\rho_h$ are the XSLD with respect to the suspension medium for the core and the half-shell respectively, R is the radius of the spherical core and δ is the thickness of the coating. The discontinuity of the edges of the hemisphere is not physical, but for $\delta << R$ this description offers a good geometrical approximation of the system.

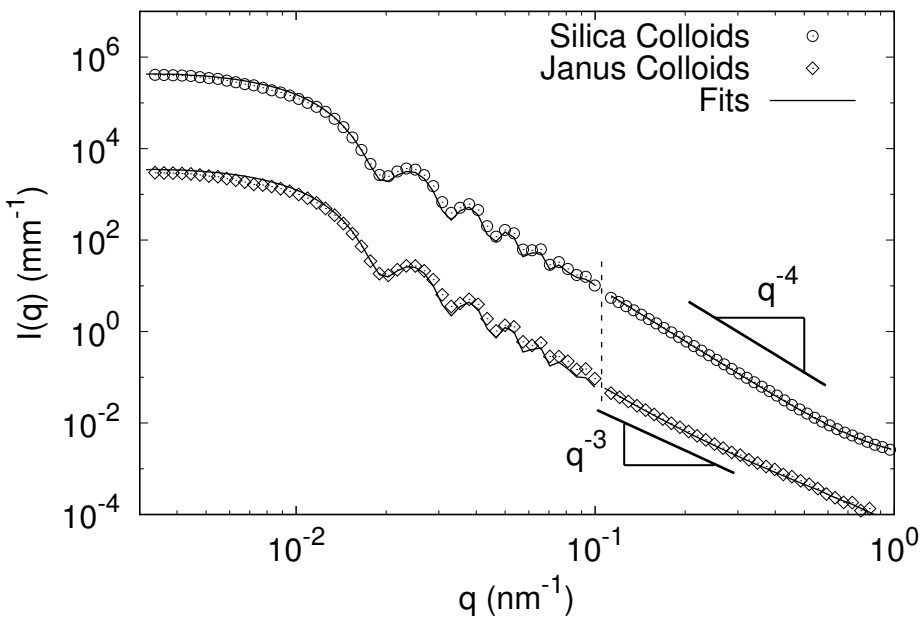

Figure 5.4.: SAXS measurements on silica and half-coated silica/nickel Janus colloids. Fits were perfomed by using Equations 2.10 and 5.3 and applying polydispersity and intrumental smearing. The vertical dashed line divides data obtained with sample-detector distances of 10 and 0.9 *m*.

Table 5.1.: Fit results from Figure 5.4. σq values refer to the instrumental smearing related to two sample-detector (SD) distances. $^*\rho$ values were used as fixed parameters.

Parameters	
$\langle R \rangle$ (nm)	242
PDI	0.035
δ (nm)	0.9
$^*\rho_{water}(nm^{-2})$	0.942×10^{-3}
$^*\rho_{silica}(nm^{-2})$	1.69×10^{-3}
$\rho_{nickel}(nm^{-2})$	6.14×10^{-3}
σ_q (nm^{-1}) (SD 10 m)	1.8×10^{-3}
σ_q (nm^{-1}) (SD 0.9 m)	4.8×10^{-3}

SAXS measurements on as-synthesised Janus colloids, and Stöber silica as a reference, were performed with sample-detector distances of 30, 10 and 0.9 m and are reported in Figure 5.4. These scattering form factors are comparable in the lower q-region whereas a substantial difference arises in the asymptotic trend for $q \to \infty$. A slope of q^{-4}, characteristic for smooth surfaces, well-describes the behaviour of data from silica colloids, instead Janus colloids are fitted with a decay proportional to q^{-3}. Fit results (reported in Table 5.1) are compatible with a nickel layer of a few atoms thick while the contrast is underestimated, as $\rho_{nickel} \simeq 7.21 \times 10^{-3}\ nm^{-2}$. This discrepancy could be explained considering the simplicity of the scattering model proposed. It accounts for a complete hemispherical cap, but a smaller area may have covered by the coating. Moreover, the theoretical ρ_{nickel} values concerns the structure of bulk nickel, while such a thin layer of metal could have a different atomic arrangement.

5.2. Silica colloids: Results and discussion

5.2.1. Microstructure in the Quasi-Binary Mixture

Suspensions of charged silica colloids in binary mixtures of 2,6-lutidine, have been thoroughly investigated over the last 30 years [3,166–170]. The 3MP/H_2O/D_2O system is also similar with a LCST below which the mixture is (Fig. 5.5). Above this transition temperature the mixture separates into two coexisting phases, a water-rich and a 3MP-rich phase. The presence of D_2O is pivotal, as a 3MP/H_2O system is miscible at every temperature and at ambient pressure. Moreover, the critical temperature T_c is a function of the D_2O concentration and the higher concentration is the lower the phase boundary lies [40].

When silica colloids are suspended in such a mixture they are stable, but it becomes unstable and aggregate in the proximity of the phase separation temperature (T_s) above an aggregation temperature (T_A) and in a well-defined 3MP-concentration range below the critical concentra-

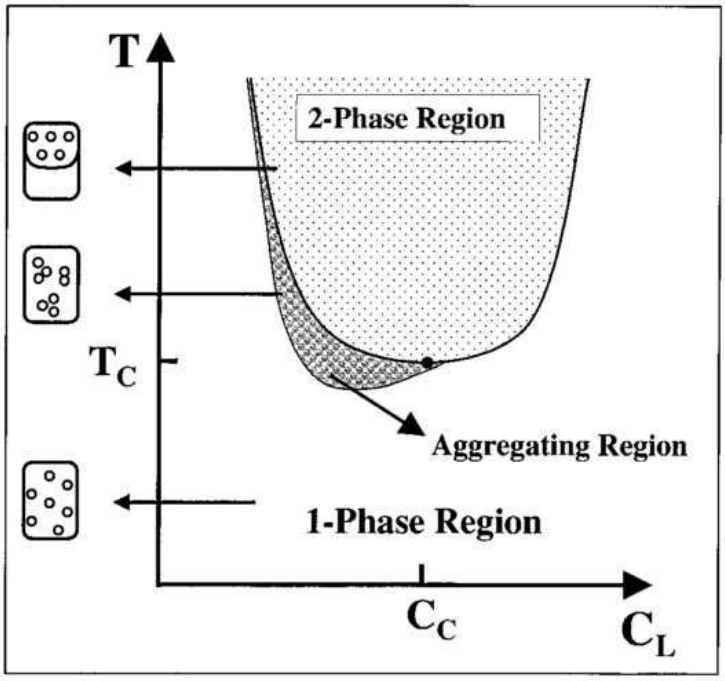

Figure 5.5.: Schematic phase diagram of silica colloids in 2,6-lutidine/H_2O or 3MP/H_2O/D_2O systems displaying the phase-separation temperature (T_s) boundaries as a function of the lutidine (or 3MP) concentration (C_L). T_C and C_C are, respectively, the critical temperature (LCST) and the critical concentrations. Both 3MP and lutidine water-mixture exhibit the same features. The boxes of the left are sketches of the colloidal distribution in three different areas: a stable suspension in the 1-phase region (*bottom*), clusters in the aggregation region (*centre*) and stable, fragmented-clusters redispersed into the lutidine-rich (or 3MP-rich) phase upon phase separation (*top*). Reproduced from Ref. [166] (DOI: 10.1023/A:1004506601807) with permission from Springer.

tion (C_c), $C_c \simeq 30$ *wt%* [166, 167, 171]. This aggregation is reversible and colloids redisperse upon lowering the temperature. When the system is separated into two phases, above T_s, clusters experience a complete fragmentation and stable colloids partition into the 3MP-rich phase. This behaviour is due to the preferential adsorption of 3MP on silica colloid surfaces [172, 173]. For temperatures lower than the phase separation temperature, $T < T_s$, silica colloids are surrounded by a 3MP layer adsorbed on the surface. For $T > T_s$, when the system separates itself in two distinct phases, in spite of gravitational forces colloids migrate toward the top of the sample into the 3MP-rich phase, whose density is lower than water. This phenomenon is enthalpy-driven as a partition at the equilibrium reduces the entropy. For 3MP concentrations $C < C_c$, an aggregation region is visible in the phase diagram in the temperature range $T_A < T < T_s$.

The phase separation temperatures T_s at 25% and 35% were observed by monitoring the bulk concentration of silica colloids during a temperature scan. Here, the value n_0 represents the initial concentration of silica colloids at 30 $°C$ and the increasing ratio n/n_0 after the transition at $T_s \simeq 44.8$ $°C$ denotes the partitioning into the 3MP-rich phase probed by the X-ray beam.

In Figure 5.6 selected USAXS curves of a silica colloids suspended in 25 *wt%* 3MP are reported showing the microstructure of the system in three different regions of the phase diagram.

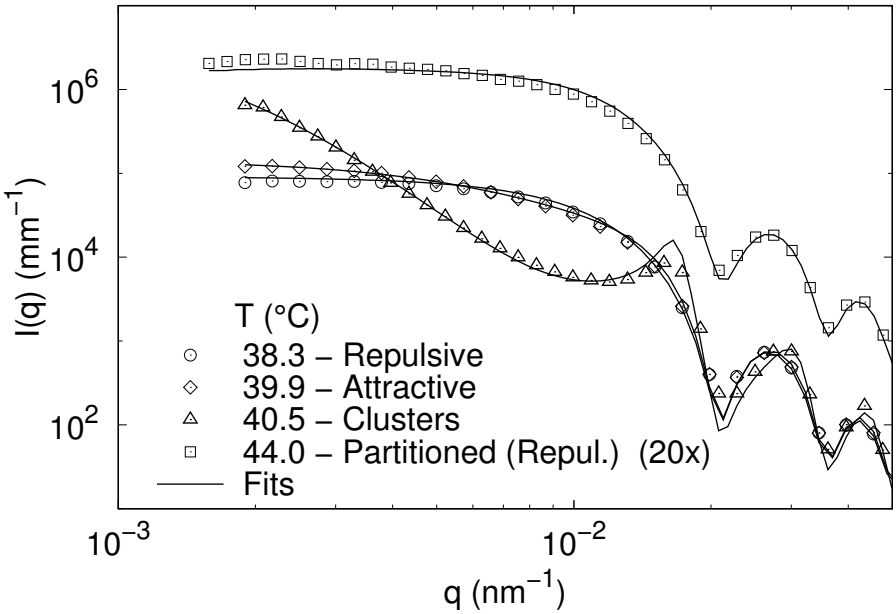

Figure 5.6.: Selected USAXS curves from silica colloids in 25 3MP *wt%* as a function of temperature. The curves represent the stable dispersion of colloids in the 1-phase region at 38.3 °C (circles); just after the onset of attractive interaction at 39.9 °C (diamonds); in the aggregation region, showing clusters, at 40.5 °C (triangles); in the 3MP-rich phase at 44 °C (squares) after a complete phase separation. Volume fractions at 38.3 and 44 °C are, respectively, $\phi = 0.02$ and 0.056.

Curves at 38.3 and 44.0 °C refer to the stable suspensions in the 1-phase at $T < T_A < T_s$ and 3MP-rich phase at $T > T_s$, respectively, and were fitted with a polydisperse spherical form factor (Eq. 2.9 and 2.11) and a hard-sphere repulsive potential with the decoupling approximation (Eq. 2.30 and 2.25). Scattering curves at 39.9 and 40.5 °C, $T_A < T < T_s$, describe the system in the aggregation region. The structure factor to be used in this case is obtained from a SW potential model [109] in the Percus-Yevick closure relation. The SW pontential is defined as:

$$\frac{U(r)}{k_B T} = \begin{cases} +\infty, & 0 < r \leq \sigma_{HS} \\ -\varepsilon, & \sigma_{HS} < r \leq \sigma \\ 0, & r > \sigma \end{cases} \tag{5.4}$$

where σ_{HS} is the diameter of the hard-sphere repulsive core and σ represents the actual diameter that include the well width $\Delta\sigma = \sigma - \sigma_{HS}$ of depth ε. Finally the curve at 40.5 °C was fitted using Equation 5.5

$$I(q) = n\Delta\rho^2 \langle |A(q)|^2 \rangle \left[I_{DB}(q) + S_M(q) \right] \tag{5.5}$$

were $I_{DB}(q)$ is the DB scattering function described in Equation 2.16, needed to describe the

scattering from clusters, and $S_M(q)$ is the SW structure factor in the monodisperse approximation for polydispersity (Eq. 2.29). Fit results are reported in Table 5.2.

Table 5.2.: Results from fits in Figure 5.6. $\langle R \rangle$ and PDI values refer to the form factor analysis. ϕ_{eff} is the effective packing fraction of colloids in the aggregates, $\langle \sigma_{HS} \rangle$, ε and $\Delta\sigma$ define the SW potential quantities and R_g is the radius of gyration of the aggregates.

Parameters		
$T\,(^\circ C)$	39.9	40.5
$\langle R \rangle\ (nm)$	213.6	
PDI	0.05	
ϕ_{eff}	0.02	0.47
$\langle \sigma_{HS} \rangle\ (nm)$	428.2	
$\varepsilon\ (k_B T)$	1.88	
$\Delta\sigma\ (nm)$	35	
$R_g (nm)$	-	1450

Curves at 38.3 and 44.0 $^\circ C$ in Figure 5.6 give an indication of the colloidal concentration difference before and after the partitioning into the 3MP-rich phase.

5.2.2. Dynamics upon Quenching

The aim of this experiment is to study the dynamics via XPCS of a dispersion of silica colloids in a phase separating quasi-binary mixture of 3MP/H_2/D_2O upon quenching. In this case, colloids mimic active motions for a short period. USAXS measurements were used to obtain the precise transition temperatures T_s for mixtures at 25 and 35 *wt%* 3MP in order to impose a small temperature jump ΔT across the phase boundary. The sample at 25% was quenched from 38 to 44 $^\circ C$ ($T_A = 39.8\ ^\circ C$, $T_s = 42.2\ ^\circ C$) while the system at 35% was quenched from 42.5 to 48 $^\circ C$ ($T_s = 44.8\ ^\circ C$) with a temperature jump, from T_s to the final value, $\Delta T = 1.8$ and 3.2 $^\circ C$ respectively.

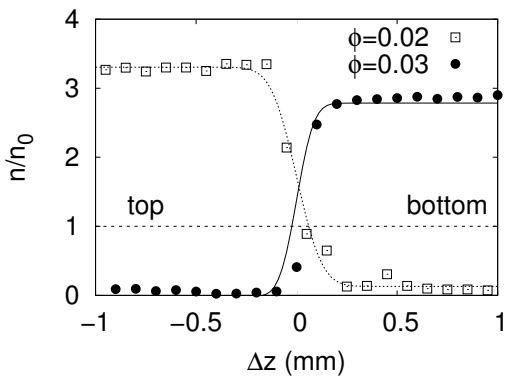

Figure 5.7.: Phase inversion. The colloidal-rich 3MP phase move to the bottom of the sample holder for higher volume fractions $\phi \geq 0.03$ and about 500 *s* after the end of the temperature quench.

Various colloidal concentration ϕ were investigated, as high concentrations give better signal-to-noise measurements, essential for the XPCS investigation. For $\phi \geq 0.03$, a phase inversion of the 3MP-rich and water-rich phases was observed at about 500 *s* after the temperature quench.

The silica-3MP interaction is so strong that the whole 3MP-rich phase with colloids, becomes denser than water, resulting in an inversion in position of the two phases as shown in Figure 5.7.

XPCS acquisitions on colloidal suspension at $\phi \sim 0.02$ (to avoid the phase inversion) were done prior to the temperature quench to have reference dynamics for a Brownian system. Time-dependent measurements were performed starting from the end of the quench with at an interval of 70-110 s. This time delay is due to the time necessary to save 500 2D scattering patterns (taken in total time-window of 1.25 s) from which intensity-intensity autocorrelation functions were calculated. To reduce this delay, the experiments were repeated on the same, but rejuvenated samples brought at a lower temperature, and applying a time delay of 20 and 40 s between the end of the quench and the first XPCS acquisition. Three to four XPCS series with different delays were then merged to be able to probe the evolution of the dynamics with a finer time resolution. This procedure made use of the excellent reproducibility of the experiments.

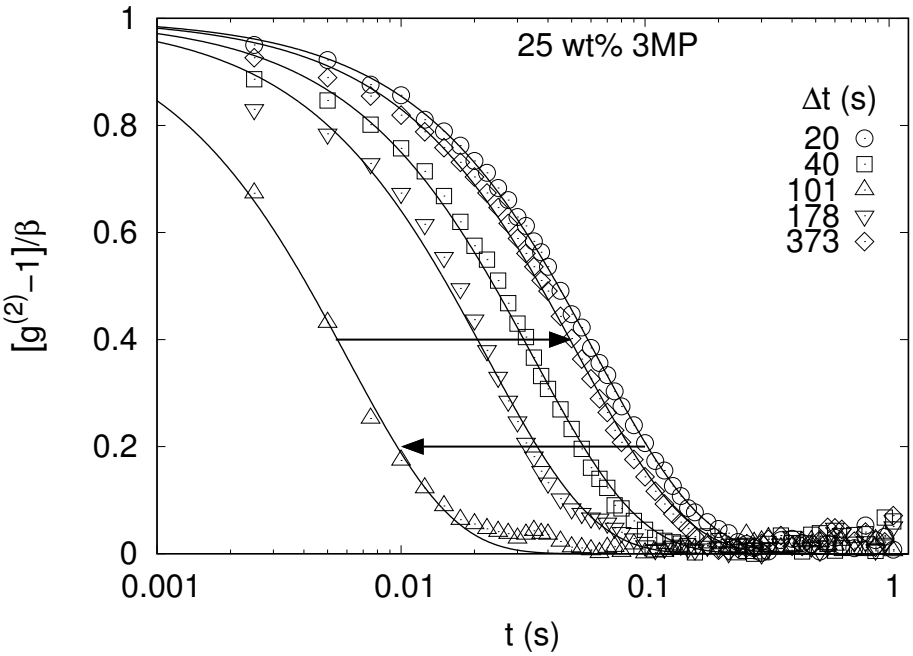

Figure 5.8.: Intensity-intensity autocorrelation functions for the 25 $wt\%$ sample at $q = 3.3 \times 10^{-3}\ nm^{-1}$ at different times Δt from the end of the temperature quench. Fits were done using Equation 5.6. The arrows highlight the speeding-up of the dynamics until $\Delta t = 101\ s$ followed by a relaxation to a slower colloidal motion for longer periods.

The measured intensity-intensity autocorrelation functions $g^{(2)}(t)$ were analysed by simple exponential decay, making use of Equations 2.34 and 2.35:

$$g^{(2)}(q,t) = 1 + \beta e^{-2\Gamma(q)t} \tag{5.6}$$

An example of the progression of $g^{(2)}(t)$ as a function of time delay Δt from the end of the temperature quench is presented in Figure 5.8. Fits were performed using Equation 5.6 and for

both 25 and 35% samples the contrast factor β was around 0.12. In this figure, $g^{(2)}(t)$ functions decay faster and faster as a function of Δt until about 100 s and then return to show dynamics close to those at the end of the quench for longer times.

From the analysis of $g^{(2)}(t)$ data, values of Γ as a function of q were deduced for each time delay Δt. The curves for samples at 25 and 35% are shown in Figure 5.9 where the variations in dynamics are associated with changes in the slope. In particular, at the beginning and at the end of the time series, the curves are described by $\Gamma \propto q^2$, which is typical for diffusive behaviour instead, close to 101 s for the colloids in 25% 3MP and to 219 s for 35%, the trend is $\Gamma \propto q^1$, which corresponds to advective dynamics.

An important aspect has to be pointed out. The intensity-intensity autocorrelation functions $g^2(t)$ for each q value were calculated from the full 2D speckle patterns performing an azimuthal integration. The same operation were performed with a partial integration, selecting only the speckles in a vertical or horizontal direction and obtaining $g^2(t)_{ver}$ and $g^2(t)_{hor}$ that respectively refer to the dynamics in the z-axis (normal to gravity) and xy-plane § 2.1.1. By comparing the data for each value of q and Δt, it turned out that $g^2(t) \sim g^2(t)_{ver} \sim g^2(t)_{hor}$ in early and final stages of the time series and there are no preferential directions for colloidal motions. However, the more the dynamics get faster, the more $g^2(t)_{ver}$ diverges from $g^2(t)_{hor}$ with a difference of up to $\sim$ 30% (see Fig. 5.10).

When $g^{(2)}(t)$ is described by a purely exponential decay, even for the case of more complex motion, Γ can be expressed in terms of MSD, $\langle \Delta r^2(t) \rangle$ [174]. In this case, with colloids executing phoretic motions, the decay rate $\Gamma(q)$ is a function of both effective diffusion D_{eff} and velocity fluctuations Δv. Assuming that the diffusion and advection terms are decoupled [175], when the dynamics are isotropic, the decay rate can be expressed as:

$$\Gamma(q) = D_{eff} q^2 + \Delta v q \tag{5.7}$$

In order to assess these quantities, $\Gamma(q)$ curves were fitted with the factorised relation 5.7 and the results are displayed in figure 5.11, alongside the colloidal concentration changes [obtained by static $I(q)$], as a function of the time difference Δt after the end of the quench. As an approximation, the same fits were performed on data with fast decay which displayed differences between horizontal and vertical dynamics. In Figures 5.11(a) and 5.11(b), the system at 25 $wt\%$ 3MP exhibits a monotonic enhancement of the effective diffusion coefficient D_{eff} alongside an increase in velocity fluctuations Δv until around 130 s. This trend is then sharply interrupted when the beam is probing an area of the sample in which the 3MP-rich phase is formed and colloids are partitioned into it ($n/n_0 \simeq 2.5$), as shown in Figure 5.11(c) where n_0 refers to the concentration value before the quench. Here both D_{eff} and Δv values relax to the equilibrium, i.e. D_{eff} becomes the expected Brownian diffusion coefficient, related to the viscosity in the

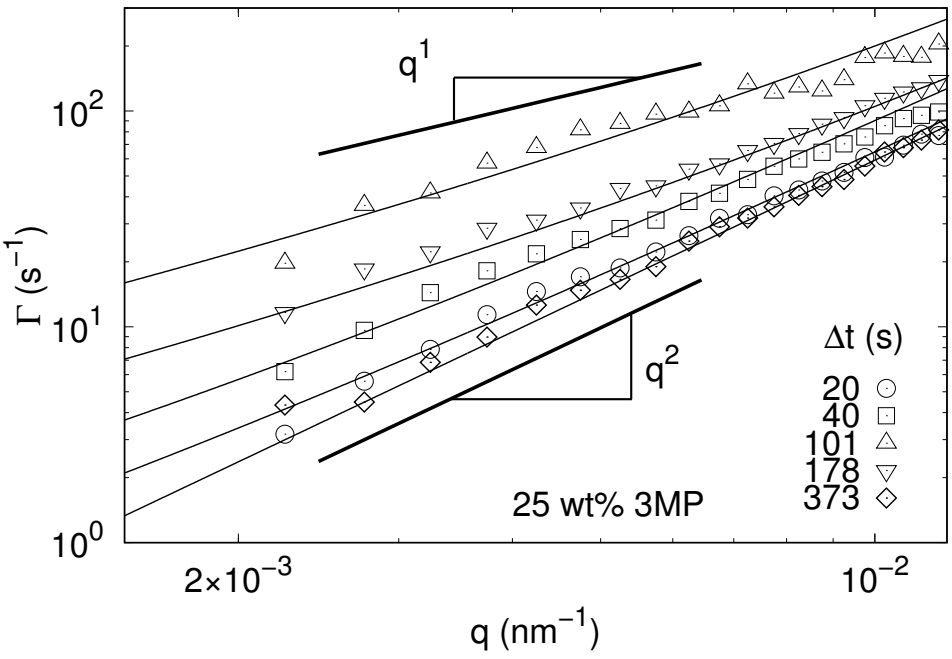

(a)

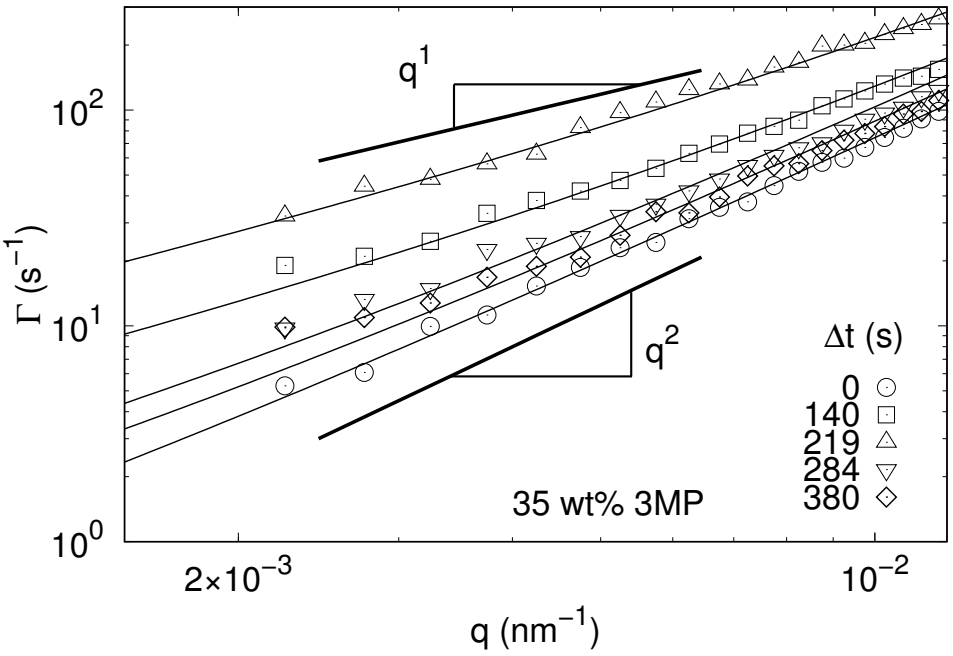

(b)

Figure 5.9.: Mean decay rate Γ as a function of q for (a) 25 and (b) 35 *wt%* 3MP at different Δt. Data were fitted with Equation 5.7.

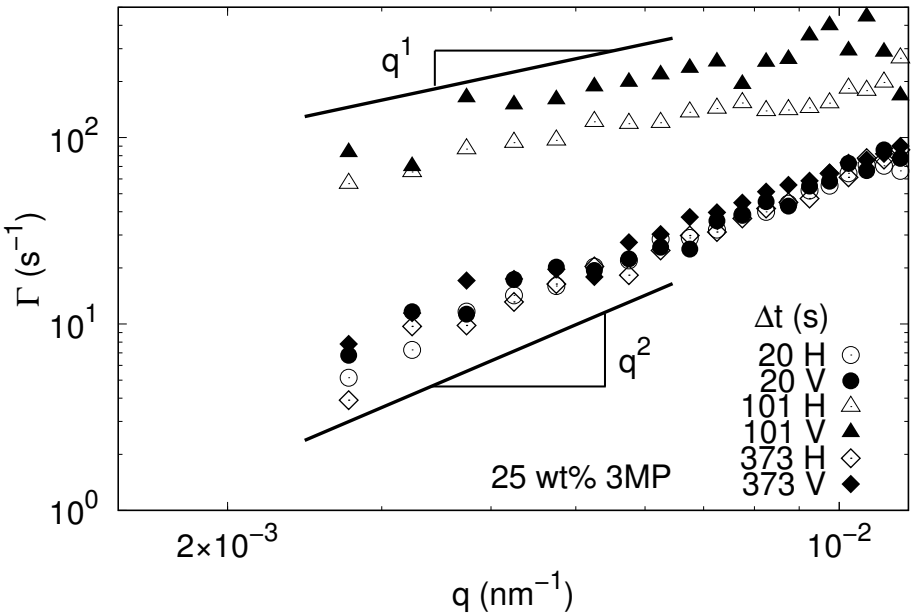

(a)

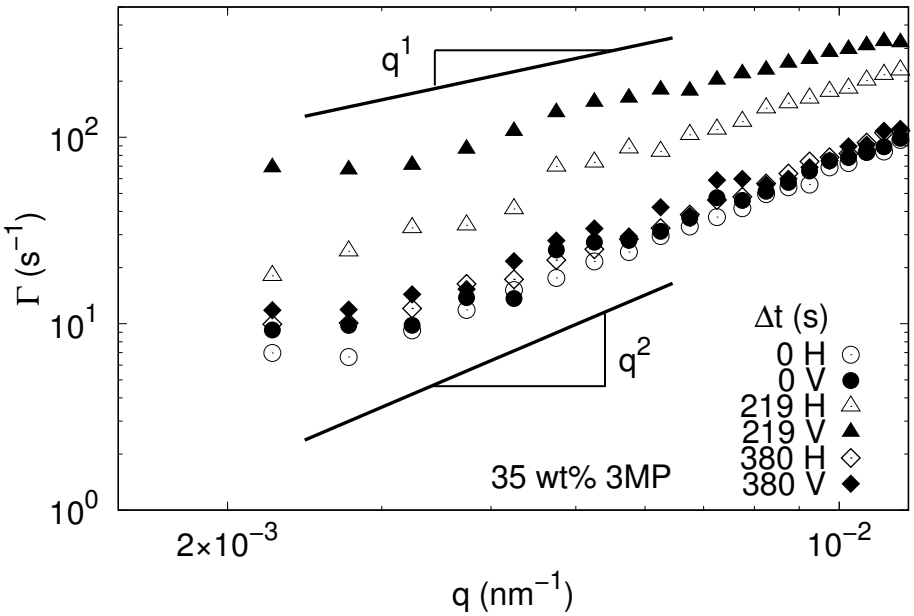

(b)

Figure 5.10.: Mean decay rate Γ as a function of q for (a) 25 and (b) 35 *wt%* 3MP at different Δt. Empty and full symbols represent horizontal (H) and vertical (V) dynamics respectively. Circles and diamonds, in the order, describe data taken at the beginning and at the end of the series, while triangles refer to data acquired with the fastest decay rate.

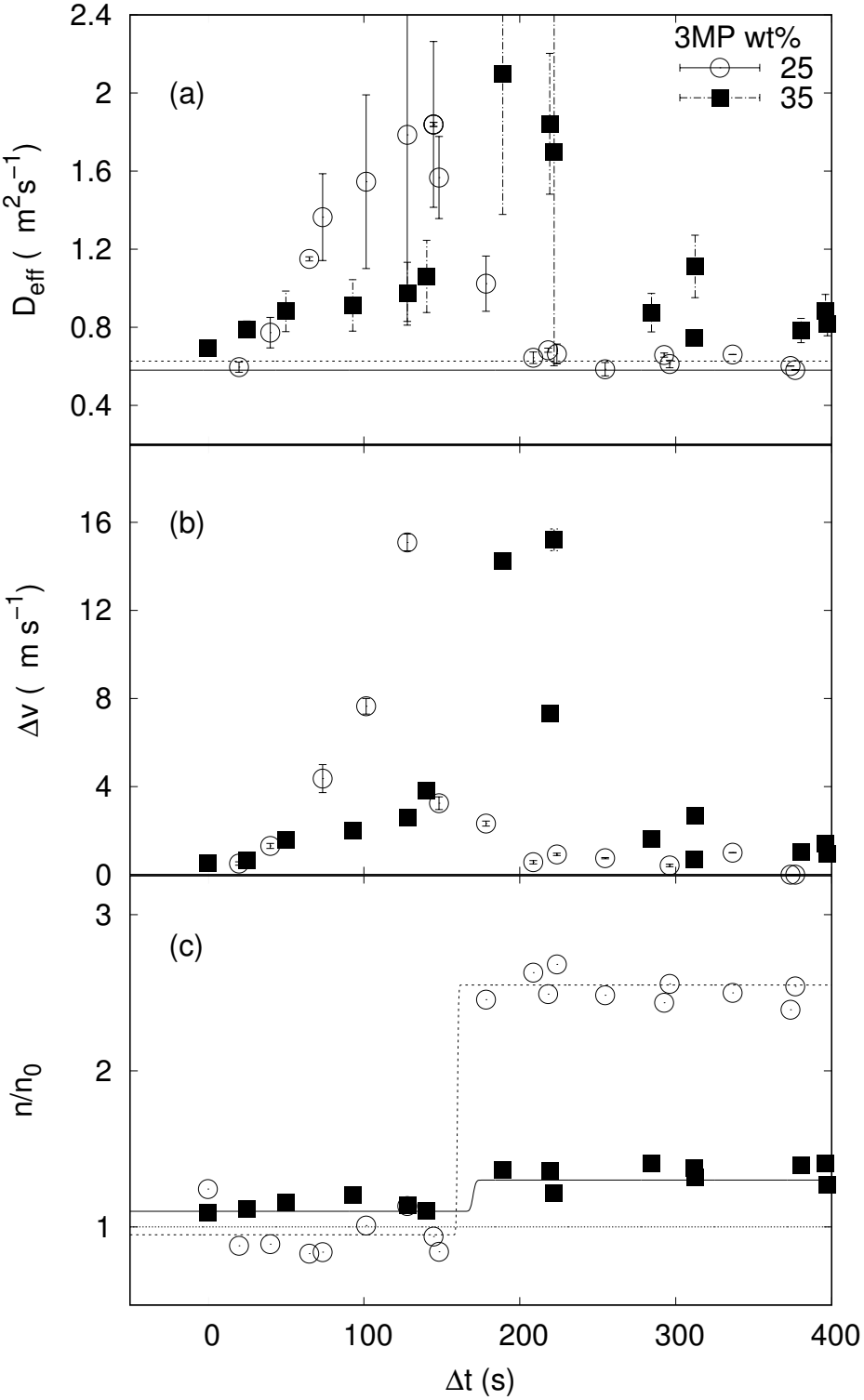

Figure 5.11.: Curves of the (a) effective diffusion coefficient D_{eff}, (b) velocity fluctuations Δv and (c) concentration ratio $\frac{n}{n_0}$ as a function of time delay Δt from the end of the temperature quench for 25 and 35 $wt\%$ 3MP. Dashed (25%) and solid (35%) lines in (a) represent the diffusion coefficient of the silica colloids prior to the temperature quench and in (c) are guides to the eye to show the partitioning that occurs during the phase separation.

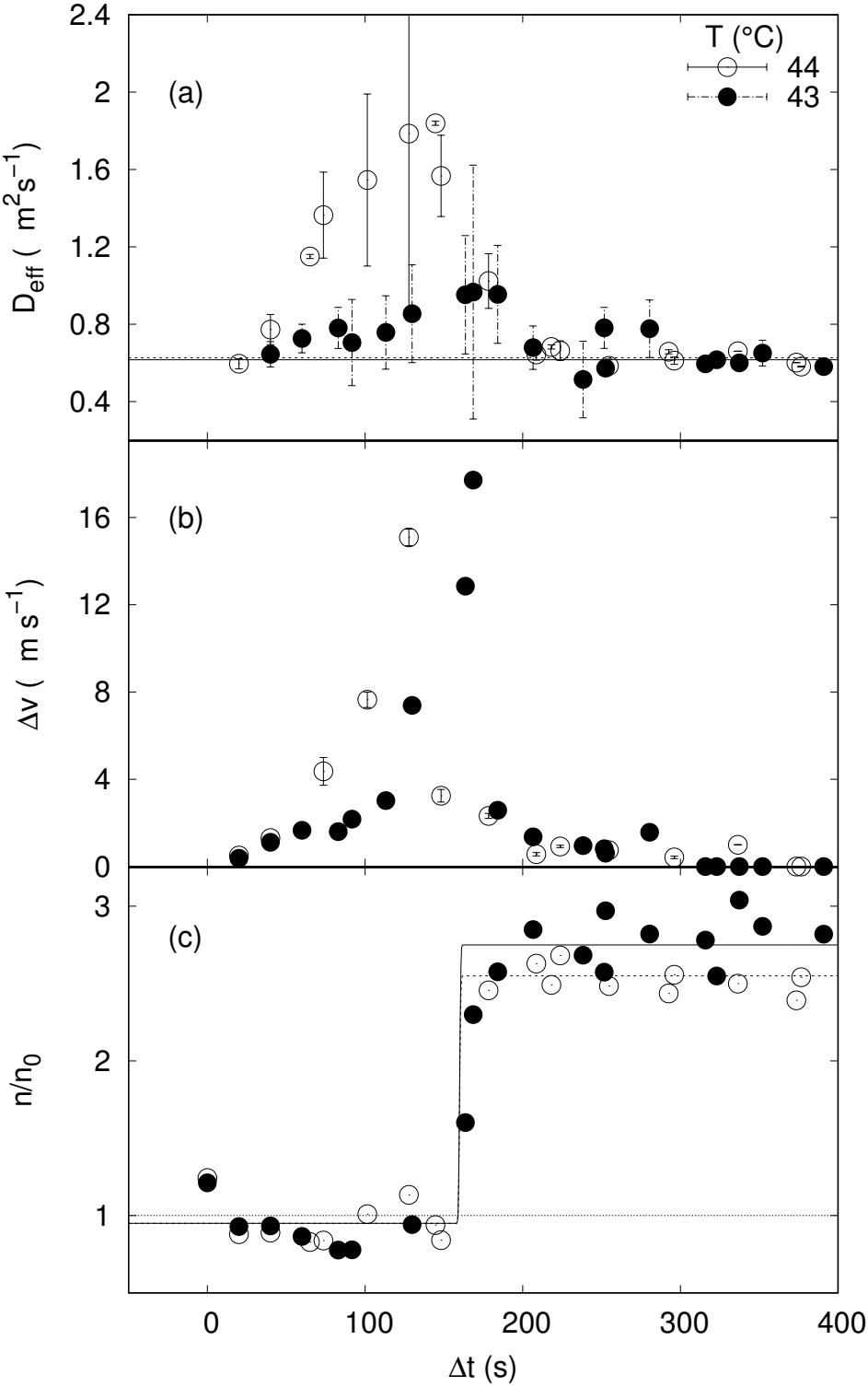

Figure 5.12.: Curves of the (a) effective diffusion coefficient D_{eff}, (b) velocity fluctuations Δv and (c) concentration ratio $\frac{n}{n_0}$ as a function of time delay Δt from the end of the temperature quench for two different $\Delta T = 44$ and 43 $°C$. Dashed (44 $°C$) and solid (43 $°C$) lines in (a) represent the diffusion coefficient of the silica colloids prior to the temperature quench and in (c) are guides to the eye to show the partitioning that occurs during the phase separation.

3MP-rich phase, and the velocity fluctuations vanish as advective motion is no longer present. The system at 35 *wt%* in 3MP shows a similar behaviour, with a reduced n/n_0 value due to the bigger volume of the 3MP component ($n/n_0 \simeq 1.3$). In Figure 5.11(c) it is also possible to see how, prior a complete partitioning, n/n_0 values are slightly smaller or bigger than the unity value for 25 and 35% system respectively. This lower concentration at 25% could be due to the migration of colloids to 3MP phases that tend to move toward the top of the sample holder, a region not probed by the X-ray beam, whereas at 35%, with n/n_0 values higher than 1, the partitioning occurs in the same area of the capillary explored since the beginning. Notice that for the highest values of D_{eff} the error bars are considerable. These errors may also result from the approximation of full isotropy that was assumed for the analysis of the entire set of data.

These enhanced dynamics cannot be ascribed to a reduced-viscosity effect. Using the measurements reported by Wang et al. [176], at 50 $°C$ systems at 20 and 40 *wt%* in 3MP (equivalent concentration of the 3MP-rich phases reported here) have viscosity values η of 0.7921 *mPa s* and 1.0485 *mPa s*, respectively. Hence colloids move in an environement with a higher viscosity, making the faster dynamics even more noticeable as the diffusion coefficient is inversely proportional to the viscosity $D \propto \eta^{-1}$.

Aggregate fragmentation before the completion of the quench of the systems at 25% can be easily excluded thanks to static USAXS measurements. In addition, the similarity of the results for the two systems at 25 and 35% gives an interesting information. The main difference between these two systems is the presence of the aggregation region in the phase diagram, therefore one can assume that the attractive interactions experienced by the colloids during the early stage of the quench do not affect the dynamics during phase separation.

For sake of completeness, a systematic investigation of the effect of different ΔT used in the quench was performed. In Figure 5.12, plots of the effective diffusion, D_{eff}, velocity fluctuations Δv and concentration ratio n/n_0 as a function of Δt for quenches to 43 and 44 $°C$ are displayed as an example. The evolutions of Δv and D_{eff} follow the same trend for different ΔT values as the main difference is the shift of the moment Δt in which the peak of the phoretic motion occurs. It depends on the rate of the phase separation via a binodal decomposition, with advection phenomena that last longer or less as a function of ΔT. For bigger ΔT values, phoretic phenomena are not observable as the fast motion takes place during the quench itself and through a spinodal decomposition. Small ΔT values, instead, cause phase separations that last a few minutes and allow the visualisation of the colloidal dynamics.

5.2.3. Summary

To conclude, isotropic phoretic dynamics of silica colloids in both 25 and 35 *wt%* 3MP mixtures are observed during the binodal phase separation in the microscopic scale, where 3MP (or

water) nucleation sites effectively attract (or repel) colloids. These motions are not due to the macroscopic migration of the colloids toward the top of the sample holder, which occurs in a much longer time scale (minutes) compared to the time-decay of $g^{(2)}(t)$ functions and it is just the consequence of the final state of the system at the equilibrium. This behaviour is schematised in Figure 5.13 for systems at both 25 and 35 *wt%* 3MP. When the mixture starts phase-separating, silica colloids start partitioning on a microscopic scale, moving toward the 3MP-rich nuclei at 25% or away from the water-rich ones at 35%. These motions increase in intensity as a function of time and then cease when the partitioning is completed, as the colloids are firmly dispersed in the 3MP-rich phase and follow Brownian motion.

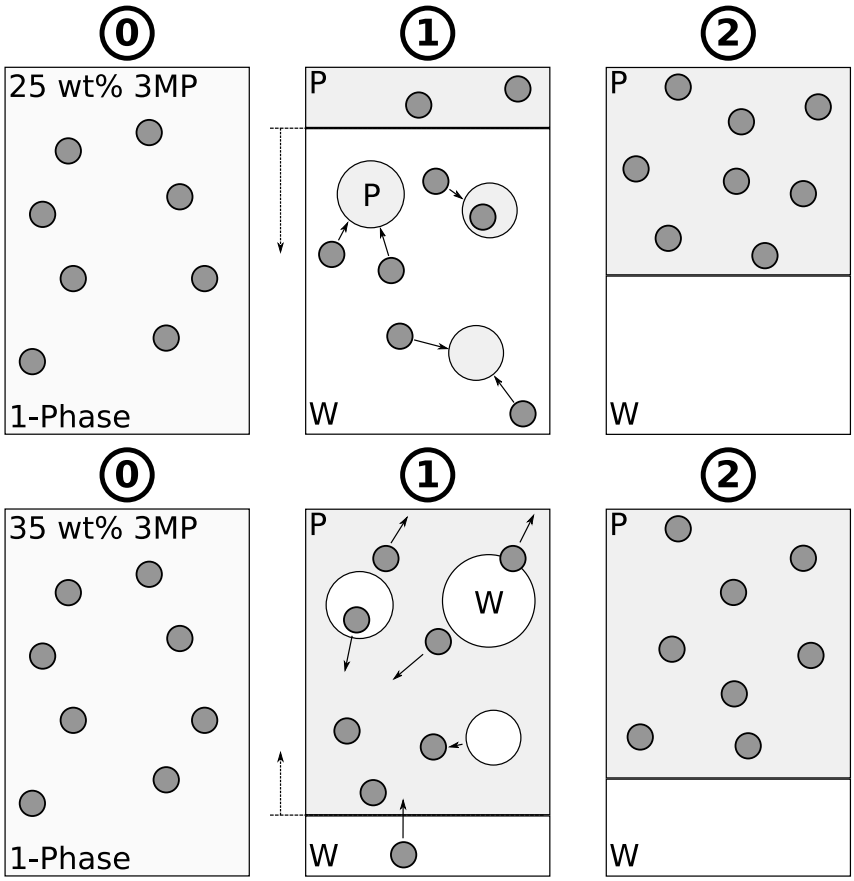

Figure 5.13.: Sketch of the mechanism inducing phoretic motion of silica colloids in the phase separating system. Stage (0) represent the 1-phase system before quenching. During the phase separation, stage (1), isotropic phoretic motions are induced by the binodal decomposition of the mixture, where silica colloids are forced to move toward the 3MP-rich areas (P) and away from the water-rich regions (W). When the system is at equilibrium, stage (2), colloids are partitioned in the 3MP-rich phase and move by Brownian diffusion. Dashed arrows outside the boxes represent the movement of the 3MP/water interface.

These dynamics are reminiscent of active motions. Even if they are not due to *self*-phoresis effects, colloids experience an ordinary diffusiophoresis by following 3MP-concentration gradients that are isotropically dispersed all around the system during the phase separation.

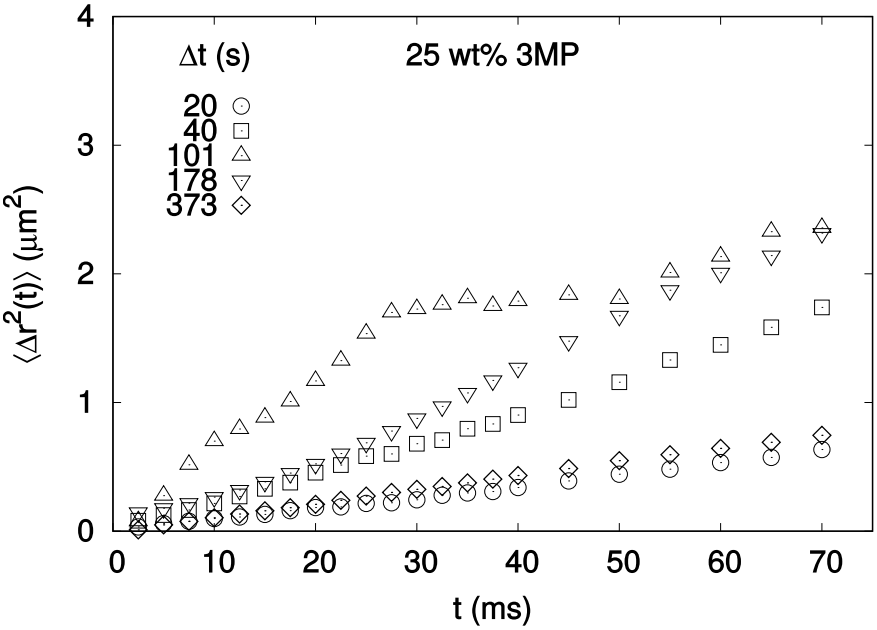

(a)

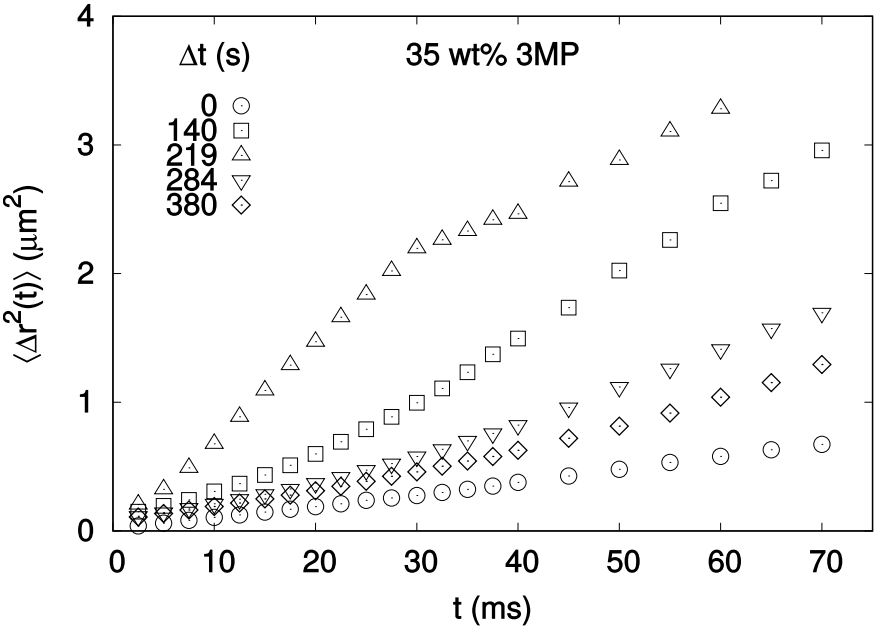

(b)

Figure 5.14.: MSD curves $[\langle \Delta r^2(t) \rangle]$ for silica colloids in (a) 25 and (b) 35 *wt%* 3MP as a function of time from the end of the temperature quench Δt. Data at $q = 2.8 \times 10^{-3}\ nm^{-1}$.

In Figure 5.14 the mean square displacement (MSD) curves for the systems at 25 and 35% are displayed as a function of time. MSD values were calculated using Equations 1.4 and 2.34 and show a deviation from the linear behaviour. The linear trend $[\langle \Delta r^2(t) \rangle \propto t^1]$ visible at early times is distinctive for Brownian motion but, as soon as colloids start migrating towards the 3MP-rich regions, there is a change to nonlinear behaviour similar to reported MSDs in systems of

Janus colloids in H_2O_2 experiencing self-phoresis motions [35]. These nonlinearity of the MSD for the fastest motions are reminiscent of the anomalous time dependences [$\langle \Delta r^2(t) \rangle \propto t^{3/2}$] behaviour predicted for symmetric active colloids [44].

5.3. Janus colloids: Results and discussion

5.3.1. Asymmetric Static Interactions

Janus colloids suspended in the quasi-binary mixture of 3MP/H_2O/D_2O display a much richer scenario of static microstructures upon phase separation of the solvent. The most striking effect is shown in Figure 5.15. Here, the concentration-ratio profile n/n_0 along the hight of the capillary Δz is monitored in the long time range after the application of a temperature quench to 50 $^\circ C$ in a system at 25 $wt\%$ 3MP. At this temperature the system separates into two phases and the colloids migrate toward the liquid-liquid interface. This behaviour is different to the bare Stöber colloids as seen in the previous section § 5.2. Whereas silica colloids completely partition into the 3MP-rich phase because of the preferential interaction with the solvent, in this case silica/nickel(-oxide) Janus colloids are mostly redistributed along the interface leaving both 3MP- and water-rich regions empty. This behaviour is typical of surfactants and, since silica/3MP preferential interaction is well-established, suggests that the nickel-oxide surface rather prefers water than 3MP. Indeed, USAXS measurements were performed with dried silica colloids without nickel coating, in order to exclude a significant modification of the silica/3MP interaction due to the processes of the Janus synthesis. Upon resuspension these colloids exhibited a partitioning behaviour similar to the Stöber particles.

In Figure 5.16 both 25 and 35 % concentration profiles in the phase separated mixtures are reported. The system at 35 $wt\%$ 3MP behaves in an even different way. Here, Janus colloids partially partition in the water-rich phase, leaving a lower concentration in the 3MP-rich one, where $n/n_0 \simeq 0.2$.

These behaviours can be better understood by investigating the colloid microstructure in the 3MP- and water-rich phases and next to the interface between them. USAXS measurements were performed in these three regions in samples at 25 and 35% in the phase separated systems (at 50 $^\circ C$) and presented in Figure 5.17. Data were fitted using the SW model and the OZ scattering function, $I_{OZ}(q,p)$, (Eq. 2.18) which account for the presence of clusters with fractal dimension d_f. In this q-range, the scattering form factors for a simple sphere and for the Janus geometry (see Fig. 5.3) are comparable, therefore calculations were simplified using the equation:

$$I(q) = n\Delta\rho^2 \langle |A(q)|^2 \rangle \left[I_{OZ}(q,p) + S_M(q) \right] \tag{5.8}$$

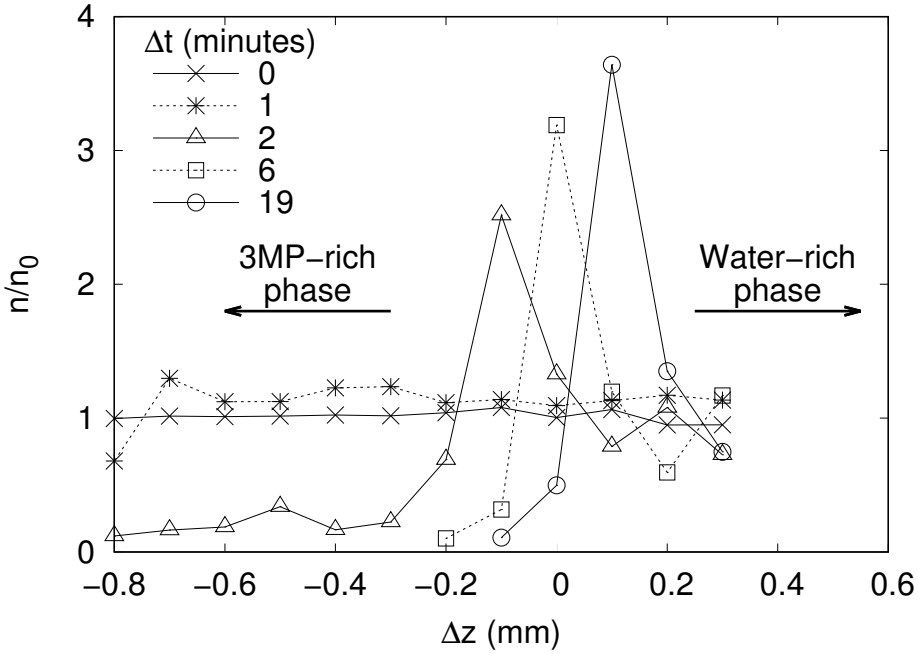

Figure 5.15.: Concentration ratio $\frac{n}{n_0}$ as a function of the capillary height Δz from the interface at different time delays Δt after a quench from 36 to 50 $°C$ in a system at 25 *wt%* 3MP. The peak in concentration is due to an accumulation of colloids at the interface between the phases. The value of n_0 refers to the systems at 30 $°C$.

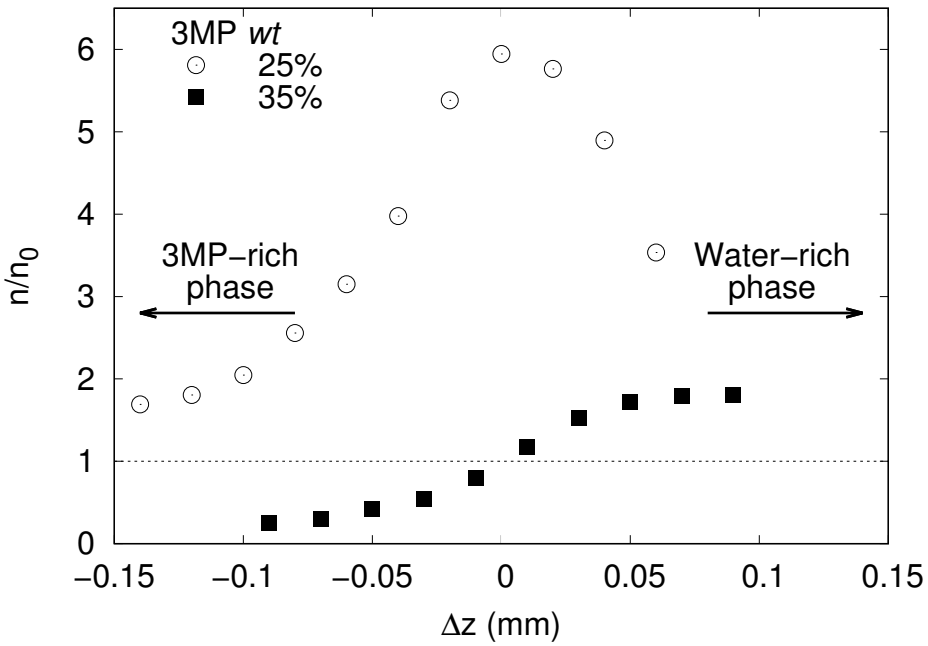

Figure 5.16.: Concentration ratio $\frac{n}{n_0}$ as a function of the capillary height Δz from the interface or systems at 25 and 35 *wt%* 3MP at 50 $°C$. The value of n_0 refers to the systems at 30 $°C$.

where $\langle |A(q)|^2 \rangle$ is a polydisperse spherical form factor. $S_M(q)$ is the SW structure factor in the monodisperse approximation for polydispersity (Eq. 2.29). Results are shown in Table 5.3.

Data from the system at 25% 3MP display the presence of highly packed ($\phi_{eff} = 0.45 - 0.47$) aggregates around the 3MP/water interface, as it was measured at $\Delta z \simeq 0,\ +1,\ -1$ *mm*, where 0 is the capillary position very much close to the interface. The most interesting information is that the concentration at the interface is 10 times higher than in both 3MP- and water-rich phase, as shown in Figure 5.17(a). The power law decay, p, of the OZ function suggests that the aggregates are more compact in the 3MP-rich phase (surface fractal, $p = 3.2 \leftrightarrow d_f^s = 2.8$) than at the interface or in the water-rich region (mass fractals, $p \equiv d_f^m = 2.7$ and $p \equiv d_f^m = 2.3$ respectively).

Data from the system at 35% 3MP, instead, show a different microstructure along the z-axis of the capillary. A partitioning was observed but, as opposed to silica colloids which fully migrate to the 3MP-rich phase forming a stable suspension, Janus colloids partially partition in the water-rich phase forming highly-packed clusters ($\phi_{eff} = 0.39$). In this phase, fluctuations in concentration were observed, comparable to the ones in the 3MP-rich phase at 25%. Here instead, in the 3MP-rich phase, colloids seem stable and have a low concentration of $n/n_0 \simeq 0.2$ with respect to the initial n_0 before the phase separation. In Figure 5.17(b), USAXS measurements of the system in the proximity of the interface are shown. At $\Delta z \simeq -0.1$ *mm*, the system is rather stable despite attractive interactions as the presence of aggregates is not significant, but at the interface, $\Delta z \simeq 0$ *mm*, clusters are formed. A little deeper in the water-rich phase, $\Delta z \simeq +0.1$ *mm*, the concentration is twice the initial one, $n/n_0 \simeq 2$ and the effective volume fraction of the clusters reaches higher values. The exponent p at the interface and in the water-rich phase are equal or close to the value used in the DB scattering function ($p = 4$), therefore similar to compact aggregates of bare silica colloids embedded in a 3MP matrix.

The SW model was used to describe the attractive interactions between Janus colloids in both 25 and 35% 3MP as the same kind of solvent-mediated interaction found in bare silica colloidal systems is assumed. It is important to remind that such a structure factor model takes into account interactions in spherical symmetry, while it is very plausible that a Janus colloid differently interacts with its two faces. As the spherical symmetry is broken, the results from a structure factor analysis may give an effective representation of the average interactions. Parameters in Table 5.3 offer a useful base for a comparison though, also including the results for silica colloids in Table 5.2. The attractive strength ε between Janus colloids in almost all circumstances is roughly twice the value for silica clusters in the aggregation region, which is comparable with the value found in the system at 25% in water-rich region. The range of the interaction $\Delta\sigma$ is instead much smaller, around 3 and 5 for the systems at 25 and 35% respectively. Finally, Janus colloids seem to experience a stronger interaction than silica ones in the aggregation region. This conclusion, alongside the assumption of solvent-mediated interactions, are consistent with the macroscopic observations about the stability of the separated system when cooled at room temperature.

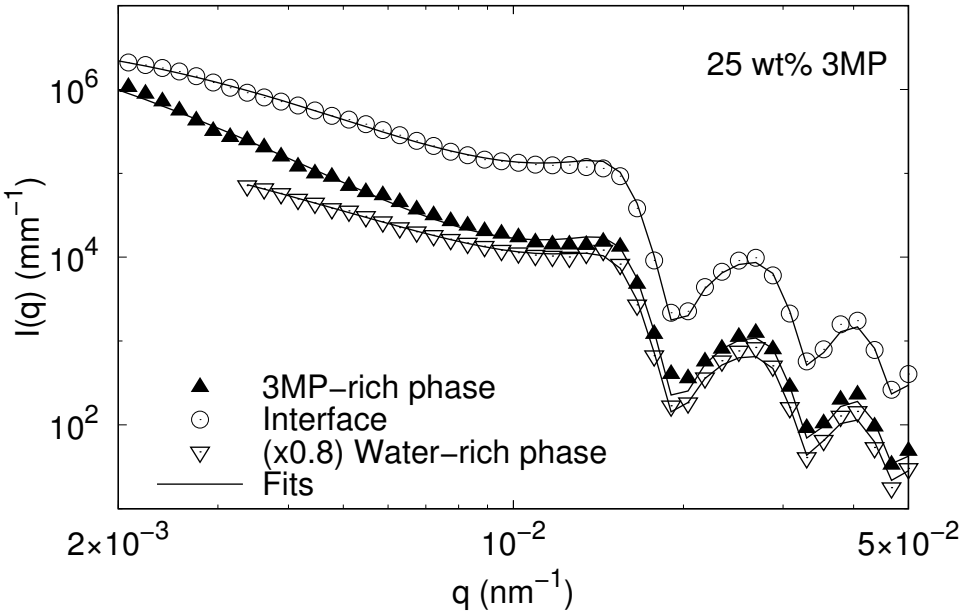

(a)

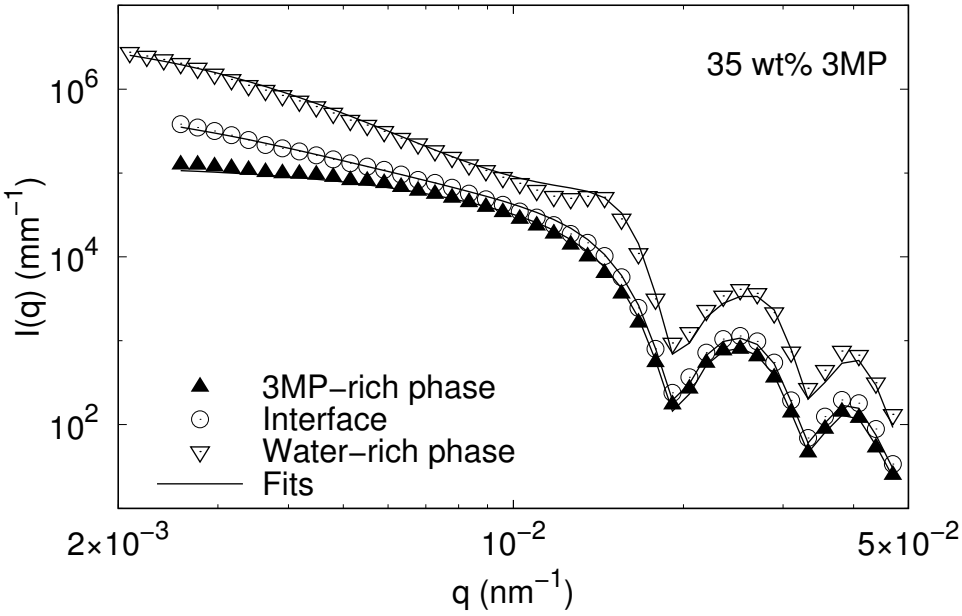

(b)

Figure 5.17.: USAXS measurements performed in the 3MP- and water-rich phases and next to the interface between them for samples at 25 (a) and 35 *wt%* 3MP (b) in the phase separated systems. Fits refer to Equation 5.8, except for data concerning 3MP-rich phase, where just a spherical form factor was used.

In order to rejuvenate a silica colloid sample after a quench, the capillaries were shaken by hand at room temperature. Janus colloid samples needed instead a much stronger shaking, for

longer times and a mild bath-sonication to break a few aggregates still in suspension.

Table 5.3.: Fit results from Figure 5.17, where P, I and W respectively refer to the curves in 3MP-rich phase, interface and water-rich regions. ϕ_{eff}, $\langle\sigma_{HS}\rangle$, ε and $\Delta\sigma$ are the effective volume fraction, the hard-sphere diameter, the depth and the width of the SW potential, respectively. R_g and p are the radius of gyration and the exponent of the cluster term I_{OZ}. The fractal dimension is linked to either surface, d_f^s, or mass, d_f^m, fractals. (*) The value $d_f^s = 2$ is equivalent to a spatial dimension $d_s = 2$, describing a smooth surface.

Parameters						
$\langle R\rangle$ (nm)	230.9					
PDI	0.05					
	25 $wt\%$			35 $wt\%$		
	P	I	W	P	I	W
ϕ_{eff}	0.47	0.47	0.45	0.08	0.12	0.39
$\langle\sigma_{HS}\rangle$ (nm)	462	462	462	462	462	462
ε (k_BT)	2.7	2.7	2.7	2.7	2.7	2.7
$\Delta\sigma$ (nm)	6.2	6.2	6.2	11	11	11
R_g (nm)	1760	880	1070	-	710	690
p	3.2	2.7	2.3	-	4.0	3.7
Dimension	$d_f^s = 2.8$	$d_f^m = 2.7$	$d_f^m = 2.3$	-	$d_f^s = 2^*$	$d_f^s = 2.3$

Phase transition

The phase diagram for silica colloids in 3MP/H_2O/D_2O mixtures presented in Figure 5.5 is not valid for the Janus systems. The presence of the aggregating region was not observed as the cluster formation occurs in a different way and is part of the equilibrium state after phase separation. Moreover, the different dependencies of the concentration and of the cluster properties on the capillary position made the observation of the phase separation temperature T_s more difficult. Performing a temperature scan (with steps of $\Delta T = 0.2$ °C every 30 s to permit stabilisation) on the system at 25% 3MP, with the beam passing above the imminent interface, no changes in the USAXS curves were observed for temperatures lower than 36.4 °C, then the concentration decreased and aggregates appeared. The 3MP/water interface originated on the top of the capillary at $T_s \sim 42.5$ °C, as it was detected by macroscopic observations, and it is at a temperature comparable to the value for the silica colloids system. No clear sign about a possible aggregation region, prior to the interface formation, was detected.

The system at 35% 3MP has a behaviour which is closer to silica colloids. Here, the same scheme for the temperature scan was used, but with the X-ray beam passing far below the imminent interface. A decrease in concentration at 44 °C and a subsequent formation of clusters at 46 °C were observed. The separation temperature was determined to be $T_s = 47.5$ °C, when the partitioning became evident.

Ageing

Janus colloids are by definition composed by two compounds that differently interact with the solvent and this feature, that leads to self-phoretic motions, can also be a source of instability for the suspension. As a matter of fact, suspensions of colloids which have both solvophilic and solvophobic properties could self-assemble by enthalpy-driven phenomena [177] as surfactant systems do. This latter example is an extreme case, as the asymmetry in the interaction may be small and the minimisation of the free energy could not favour clustering phenomena. Moreover, even if an aggregate state is energetically favourable, clustering kinetics may be too slow and keep a Janus dispersion stable.

Nevertheless, suspension of Janus colloids may not be effective in term of stability in the long-time range. Stock suspensions of half-coated silica/nickel colloids in pure water were stable for weeks, but when suspended in 3MP systems are subject to ageing, as the observed form factors showed small but continuous variations with time in hours during the experiments. This deviation from a simple spherical shape was attributed to the formation of dimers, whose orientation-averaged form-factor is easily described by the following equation:

$$|A_d(q,R)|^2 = 2|A_s(q,R)|^2 \left[1 + \frac{\sin(q2R)}{q2R}\right] \tag{5.9}$$

where R is the radius of the touching spheres. A mixture of spheres and dimers composed by the same colloids is expressed by the combination:

$$I(q) = \Delta\rho^2 \langle \left[n_s|A_s(q,R)|^2 + n_d|A_d(q,R)|^2\right] \rangle \tag{5.10}$$

where n_s and n_d are the number densities of spheres and dimes respectively and the evolution of the dimerisation is monitored as the interchanging of the number fractions x_{JP} and x_{DI}, as is shown in Figure 5.18.

$$x_{JP} = \frac{n_s}{n_s + n_d} \quad x_{DI} = \frac{n_d}{n_s + n_d} \tag{5.11}$$

In Figure 5.18 USAXS curves of Janus colloids are displayed as a function of time and fitted with Equation 5.10. A fresh sample was initially stable and only spheres, as approximation of the Janus geometry, were visible. At about 24 hours, 2/3 of the colloids were already interacting and forming dimers that were not fragmented by vigorously shaking the capillaries and, after more then 48 hours, no more single colloids were present. In this latter case, the system could present more complex structures, such as trimers or other form of oligomers, but the polydispersity of these structures does not allow a clear determination of their distribution. However, this dimer representation distinctly express how the system ages toward a situation in which most

of the colloids are no longer in a monomeric state.

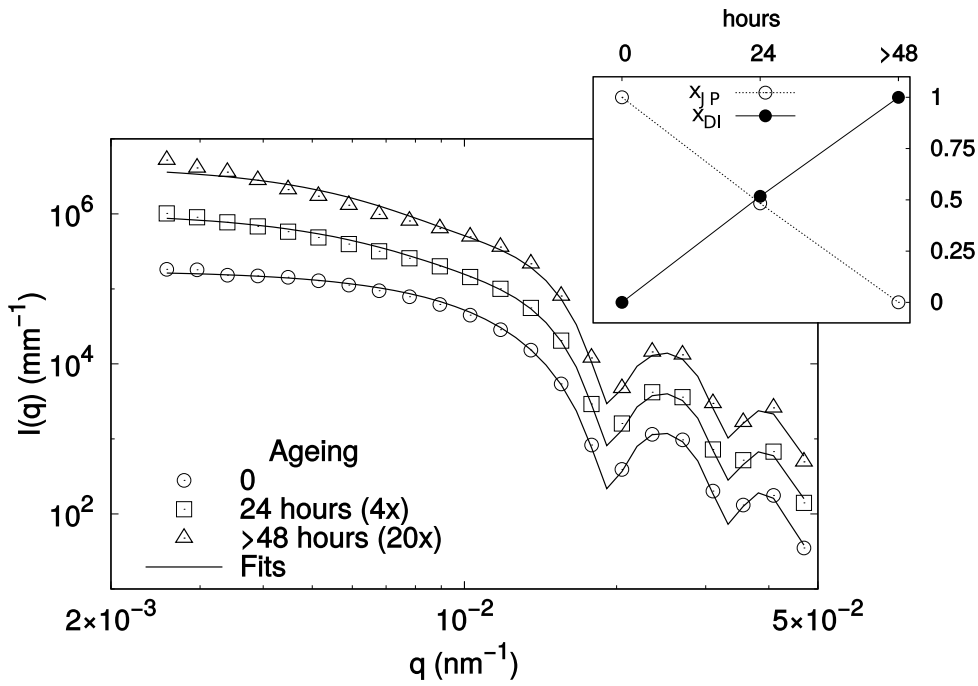

Figure 5.18.: Ageing of Janus colloids suspended in 25 *wt%* 3MP. The curves show a deviation from an initial stable suspension (circle), where data were analysed using a spherical form factor, to older systems (squares and triangles) that display the presence of dimers. Number fractions of spheres x_{JP} versus dimers x_{Di} is shown a function of time as an inset.

The nature of this ageing could still be due to solvent-mediated interactions, as also bare silica colloids showed aggregation, but in a longer time scale (roughly a month). Moreover, strong van der Waals interaction between the nickel faces of the colloids should not be the major cause of the ageing, as samples older than 48 hours still exhibited partitioning (depending on the 3MP concentration) in the phase separated system ($A_H^{silica} = 6.3 \times 10^{-20}$ J and $A_H^{nickel} = 22 \times 10^{-20}$ J [178]). When colloids rearrange along the 3MP/water interface, a surfactant behaviour is evident and such a microstructure should not be visible if most of the particles are forming dimers or oligomers where the nickel surface is engaged with metal-metal connections, as the geometry of the resulting objects would not bring about surfactant properties. However, a percentage of nickel-nickel van der Waals bonds cannot be excluded as further cause of ageing. Indeed, upon phase separation in both 25 and 35% 3MP, despite the concentration ratio profiles n/n_0 along the z-axis of the capillary were unchanged when comparing fresh and aged samples, the latter showed a clusters with reduced effective volume fractions (down to $\phi_{eff} \sim 0.2$) and smaller R_g values, as the I_{OZ} term was barely observable.

5.3.2. Dynamics in the Phase Separating System

As it was done for the bare silica colloidal system, the dynamics of a dispersion of Janus colloids in phase separating quasi-binary mixtures of 3MP/H_2/D_2O upon quenching were investigated via XPCS. The idea is add a directionality in the phoretic motion of the colloids by breaking the symmetry of the interactions with the phase separating medium and exploiting this asymmetry to further enhance the phoretic dynamics. The transition temperatures T_s for systems at 25 and 35 *wt%* 3MP were estimated in the previous section. The sample at 25% was quenched from 36 to 50 $°C$ ($T_s = 42.5$ $°C$) and the system at 35% was quenched from 42.5 to 50 $°C$ ($T_s = 47.5$ $°C$) with a temperature jump, from T_s to the final value, $\Delta T = 7.5$ and 2.5 $°C$ respectively. During the experiments, the X-ray beam passed close to the interface for 25% and in the 3MP-rich phase for 35%. These choices were made because of the stability in term of concentration fluctuations that these systems showed in these regions.

XPCS measurements on Janus colloidal suspension at $\phi \sim 0.01$ were performed prior to the temperature quench, to have a reference, and then time-dependent measurements at an interval of $\Delta t = 70 - 110$ seconds (determined by the saving time of 500 2D scattering patterns) were acquired following the quench. The experiments were repeated on the same, but rejuvenated samples brought at a lower temperature, and applying an initial time delay of 25 and 50 s between the end of the quench and the first XPCS acquisition in order to refine the Δt by merging from three to four XPCS series with different delays.

In Figure 5.19 an example of the progression of $g^{(2)}(t)$ as a function of time delay Δt from the end of the temperature quench is presented. Systems at both 25 and 35% showed a similar behaviour with respect to the silica colloids, except for intermediate Δt, 70 and 262 s respectively, where $g^{(2)}(t)$ deviates from a single exponential decay.

In this case, measured intensity-intensity autocorrelation functions $g^{(2)}(t)$ were analysed by a double exponential decays, making use of Equation 5.12:

$$g^{(2)}(q,t) = 1 + \beta \sum_{n=1}^{2} x_n e^{-2\Gamma_n(q)t} \tag{5.12}$$

where β is contrast factor, Γ_n are the decay rates related to two distinct dynamics and x_n are weighting factors related to the number fraction of objects that move according the two dynamics. This distinction were considering the second dynamics as resulting from the motions of single colloids and clusters, the presence of which was observed studying the microstructure in the phase separated system. The contrast factor β was around 0.12-0.13.

Janus colloids at 25% show fast dynamics in the beginning of the sequence which were fitted by a single decay rate Γ_1. Then, in the range $\Delta t = (70 - 200)$ s, the presence of a second decay, described by Γ_2, is visible as shown in Figure 5.20. For $\Delta t > 200$ s the system start

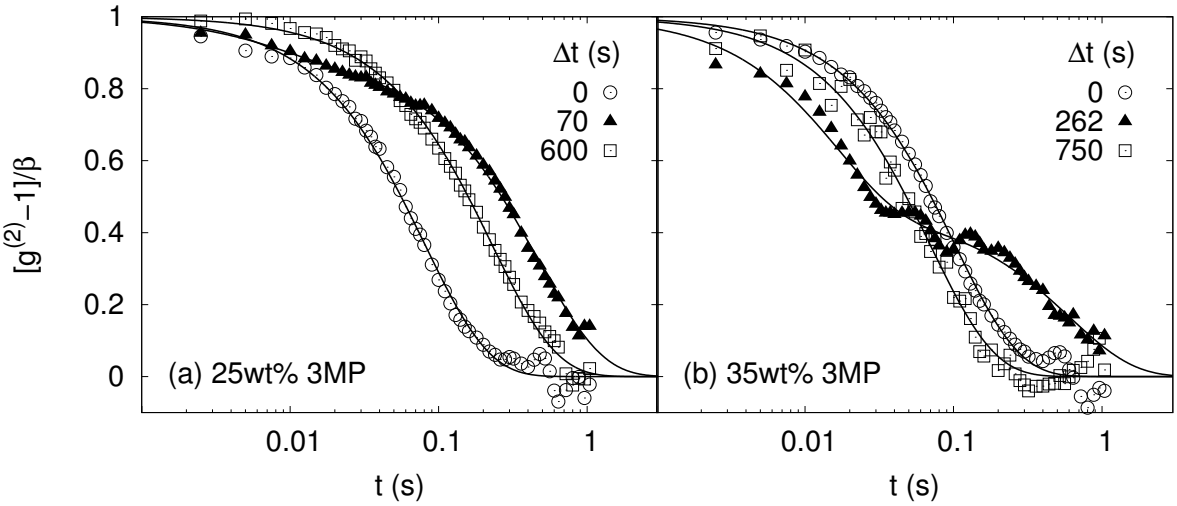

Figure 5.19.: Intensity-intensity autocorrelation functions for (a) 25 and (b) 35 $wt\%$ samples at $q = 3.3 \times 10^{-3}\ nm^{-1}$ at different times Δt from the end of the temperature quench. Fits were done using Equations 5.12.

relaxing to the equilibrium with slower dynamics. A similar behaviour occurred for 35% 3MP, here the decays get faster at later stages and show a double dynamics in the intermediate range $\Delta t = (200 - 480)\ s$, after which the system relax.

From the analysis of $g^{(2)}(t)$ data, values of Γ_1 and Γ_2 as a function of q were extracted for each time delay Δt. Γ_1 curves, plotted for samples at 25 and 35%, are shown in Figure 5.21 where the variations in dynamics are associated with changes in the slope between $\Gamma_1 \propto q^2$ (Brownian dynamics) and $\Gamma \propto q^1$ (advective dynamics). As for the case of silica colloids, a comparison, between intensity-intensity autocorrelation functions calculated from the full 2D speckle patterns and the ones obtained selecting only the speckles in a vertical or horizontal directions, indicated isotropic dynamics, $g^2(t) \sim g^2(t)_{ver} \sim g^2(t)_{hor}$, except for a short, intermediate stage corresponding to the time-range over Γ_1 decays fast (see Fig. 5.22). Here, as in the case of bare silica particles, vertical dynamics appeared systematically faster than the horizontal ones.

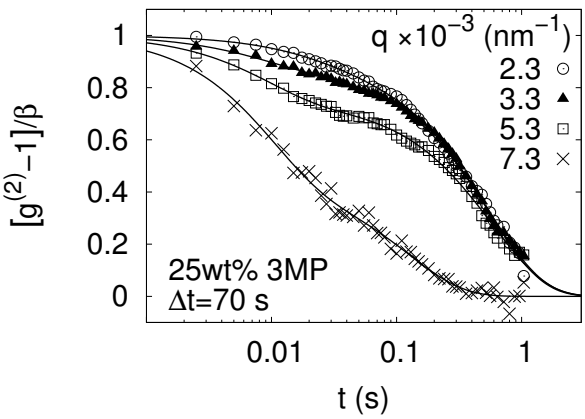

Figure 5.20.: Intensity-intensity autocorrelation functions for 25 $wt\%$ samples at $\Delta t = 70\ s$ at different times q values. Fits were performed using Equations 5.12.

Assuming that the diffusion and advection terms are decoupled, the decay rates Γ_i were fitted with Equation 5.7. From the analysis of Γ_1, as shown in Figure 5.21, both effective diffusion,

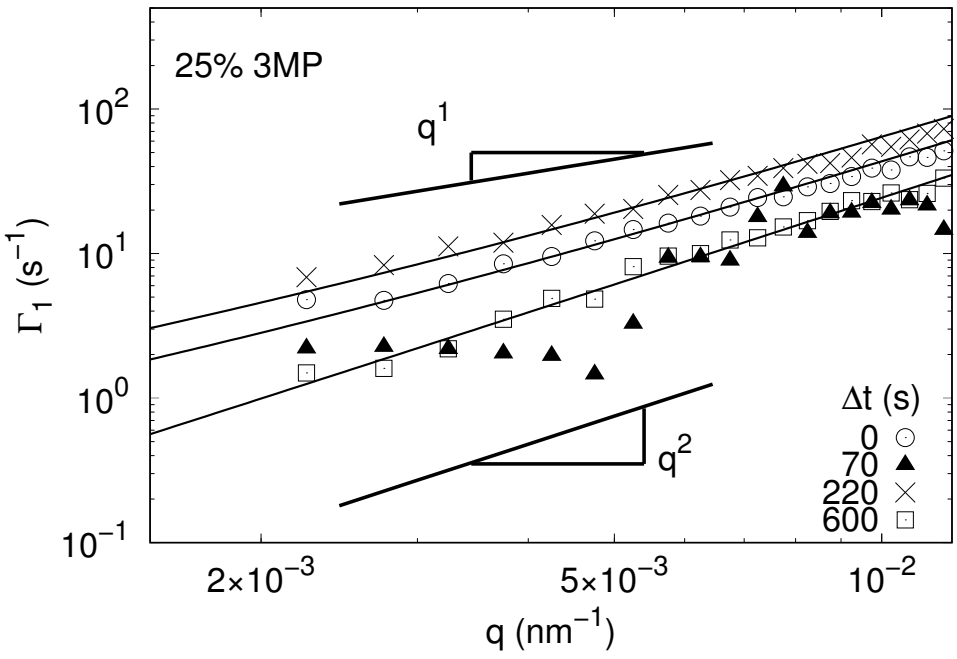

(a)

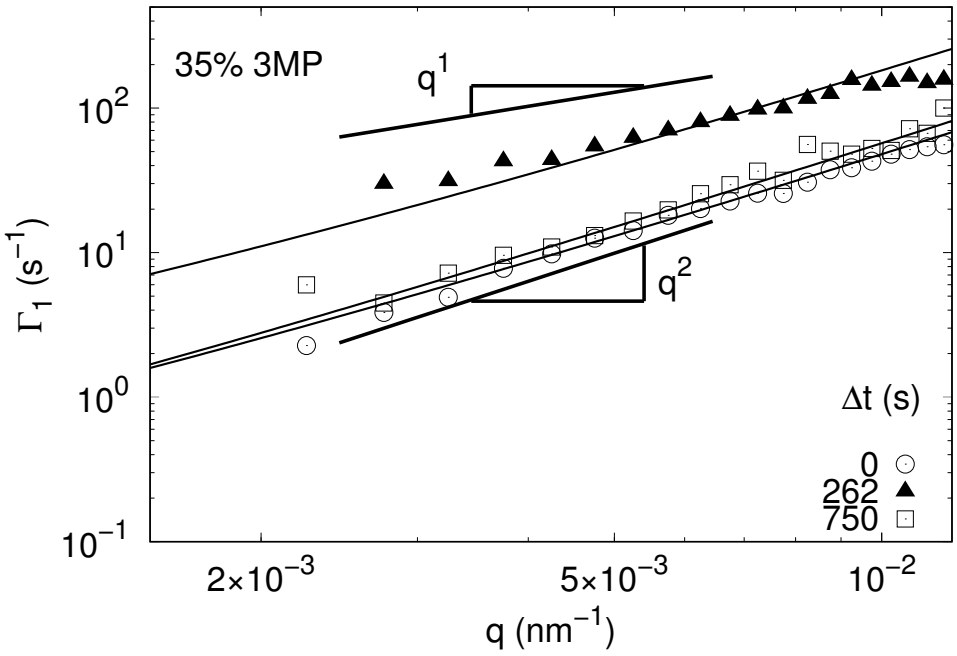

(b)

Figure 5.21.: Mean decay rate Γ_1 as a function of q for (a) 25 and (b) 35 *wt%* 3MP at different Δt. Data were fitted with Equation 5.12. Data for 25% and $\Delta t = 70$ were not fitted and are shown as an example.

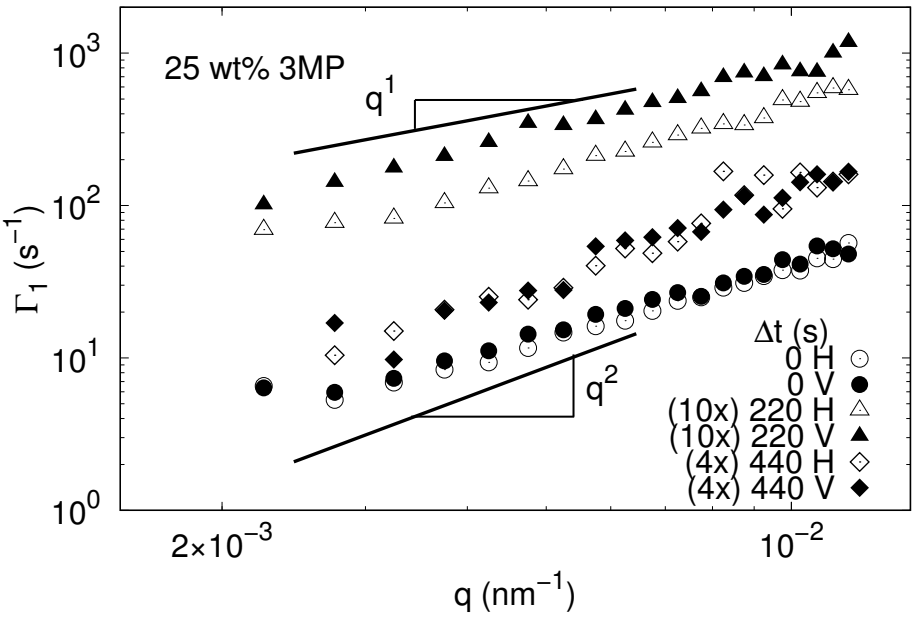

(a)

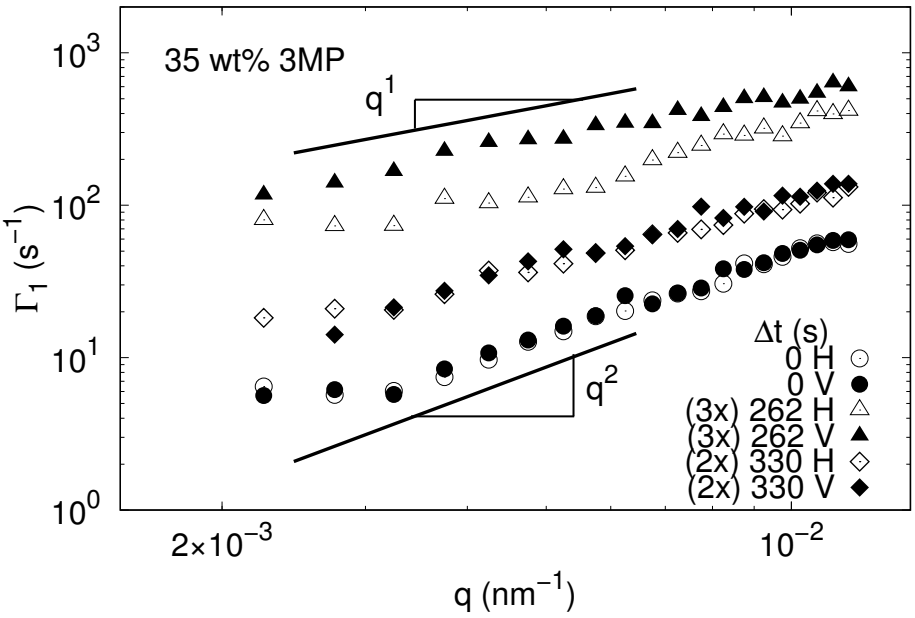

(b)

Figure 5.22.: Mean decay rate Γ as a function of q for (a) 25 and (b) 35 *wt%* 3MP at different Δt. Empty and full symbols represent horizontal (H) and vertical (V) directions respectively. Data show a isotropic dynamics except for an intermediate time range, where the decays related to vertical and horizontal motions do not overlap.

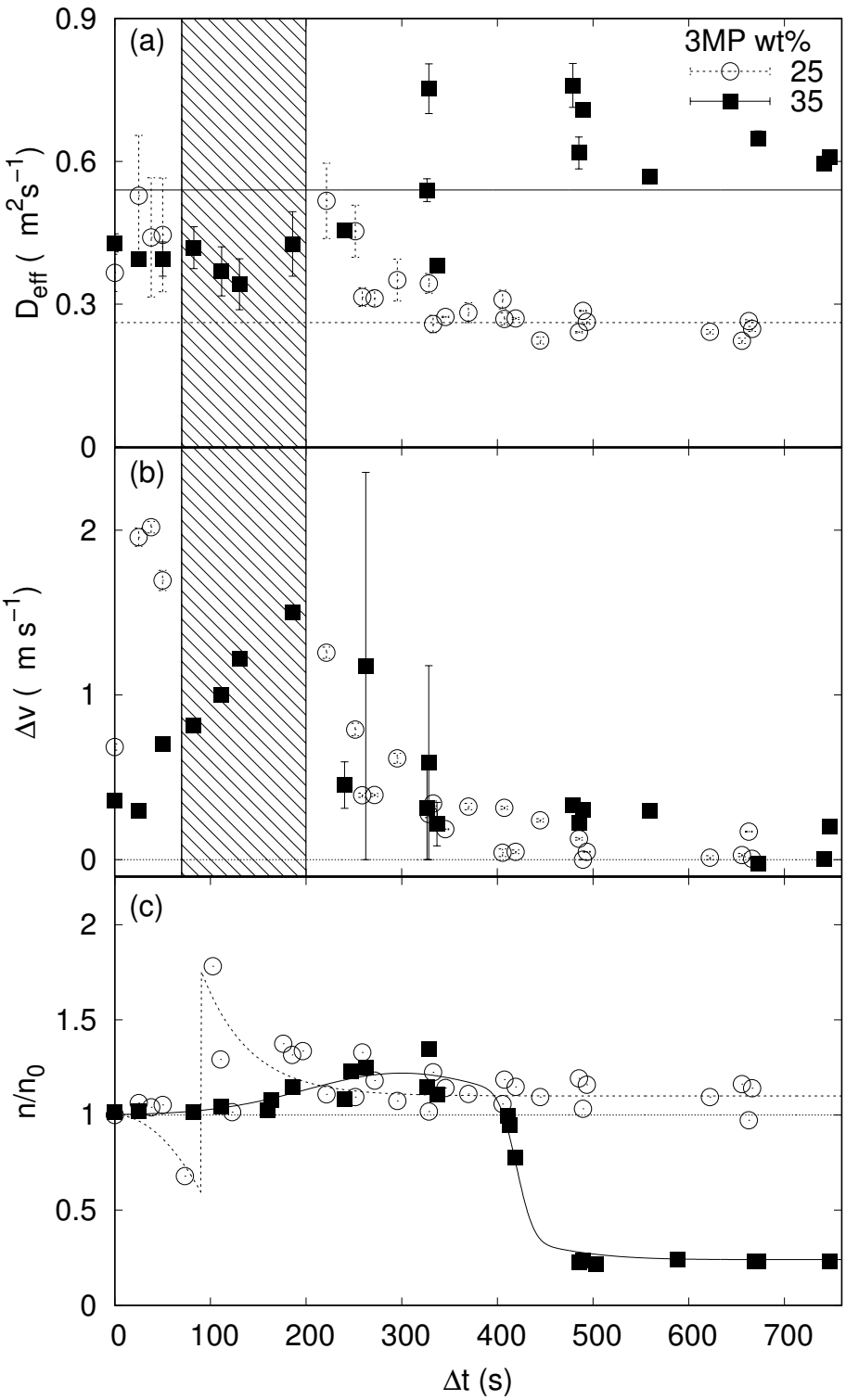

Figure 5.23.: Parameters for (a) effective diffusion coefficient, D_{eff}, (b) velocity fluctuations, Δv, and (c) concentration ratio, $\frac{n}{n_0}$, as a function of time delay Δt from the end of the temperature quench for 25 and 35 *wt%* 3MP, where n_0 is the initial concentration of the colloids at 30 $^\circ C$. Solid and dashed lines in (a) represent the diffusion coefficient of the Janus colloids prior to the temperature quench and in (c) are guides to the eye to show the partitioning that occurs during the phase separation. The dashed area in (a) and (b) refers to the missing data.

D_{eff}, and velocity fluctuations, Δv, were extracted for the Janus colloids at 25 and 35% 3MP. In the system at 25%, in the range $\Delta t = (70 - 200)\ s$, the q-dependence of Γ_1 (see Fig. 5.21) was uncertain while the trend of Γ_2 showed random slopes, ranging from $\propto q^{0.5}$ to $\propto q^2$. Unfortunately, the slower decay Γ_2 is too slow for the available time-window $t = (0.0025 - 1.25)\ s$, as for low q-values $g^{(2)}(t)$ curves do not exhibit the constant plateau at long time. At the same time these slow dynamics hinder the visibility of the fast one Γ_1, whose q-dependence is uncertain. In the system with 35 *wt%* 3MP instead, two decays were measured in the time range $\Delta t = (200 - 480)\ s$. Here, Γ_1 are well-represented but the q-dependences of Γ_2 curves are less reliable because of an unfavourable signal-to-noise ratio. The effective diffusion coefficient, D_{eff}, and an increase in velocity fluctuations, Δv, extracted from the analysis of Γ_1 are shown in Figure 5.23 as a function of the time difference Δt along with the evolution of the concentration n/n_0, where n_0 is the initial concentration of the colloids at 30 $^\circ C$.

The system at 25 *wt%* 3MP displays a marked enhancement of D_{eff} alongside an increase in Δv until around 70 s. Then, from 70 to 200 s, when two dynamics are present, results from Γ_1 are not available but it is interesting the discontinuity in the n/n_0 visible in the same time range. This discontinuity is the result of the interface crossing the X-ray beam during its movement from the top of the capillary. When the concentration decreases to the equilibrium value $n/n_0 = 1.1$ close to the interface at $\Delta t \sim 200\ s$ and one single decay is again dominating $g^{(2)}(t)$, enhanced D_{eff} and high Δv values slowly relax to the Brownian diffusion and zero respectively.

The system at 35 *wt%* 3MP displays an increase in Δv until around 200 s beside a reduced D_{eff} compared to initial D at 30 $^\circ C$. Thereafter, from 200 to 480 s, when two dynamics were observed, Δv values start relaxing to zero as D_{eff} start increasing and showing enhanced values. In this time range, when the water-rich phase is forming, n/n_0 values increase and, simultaneously, the second decay, Γ_2, appears describing together the beginning of the colloid partitioning and the cluster formation. After 480 s, when the interface crosses the X-ray beam during its movement from the bottom of the capillary, only one exponential decay is visible in $g^{(2)}(t)$ and D_{eff} relaxed to Brownian dynamics. Here, the concentration is reduced to $n/n_0 = 0.2$ as the scattering volume is firmly in the 3MP-rich phase.

In the case of silica colloid phoretic motion, it was reported that colloids showed an enhanced diffusion even in a solvent with a higher viscosity during the phase separation. Here the system at 35% seems to reflect this viscosity increase in the early stages of the separation as D_{eff} values are reduced. Simultaneously, advective phenomena are visible showing how D_{eff} and Δv are decoupled. This behaviour suggests that Janus colloid motions are extremely connected to the phase separation dynamics in the early stages for $\Delta t < 200\ s$. For $\Delta t = (200 - 480)\ s$, trends of D_{eff} and Δv are inverted when partitioning and clusters are visible as a consequence that the scattering volume is probing the water-rich phase and most of the separation process is over.

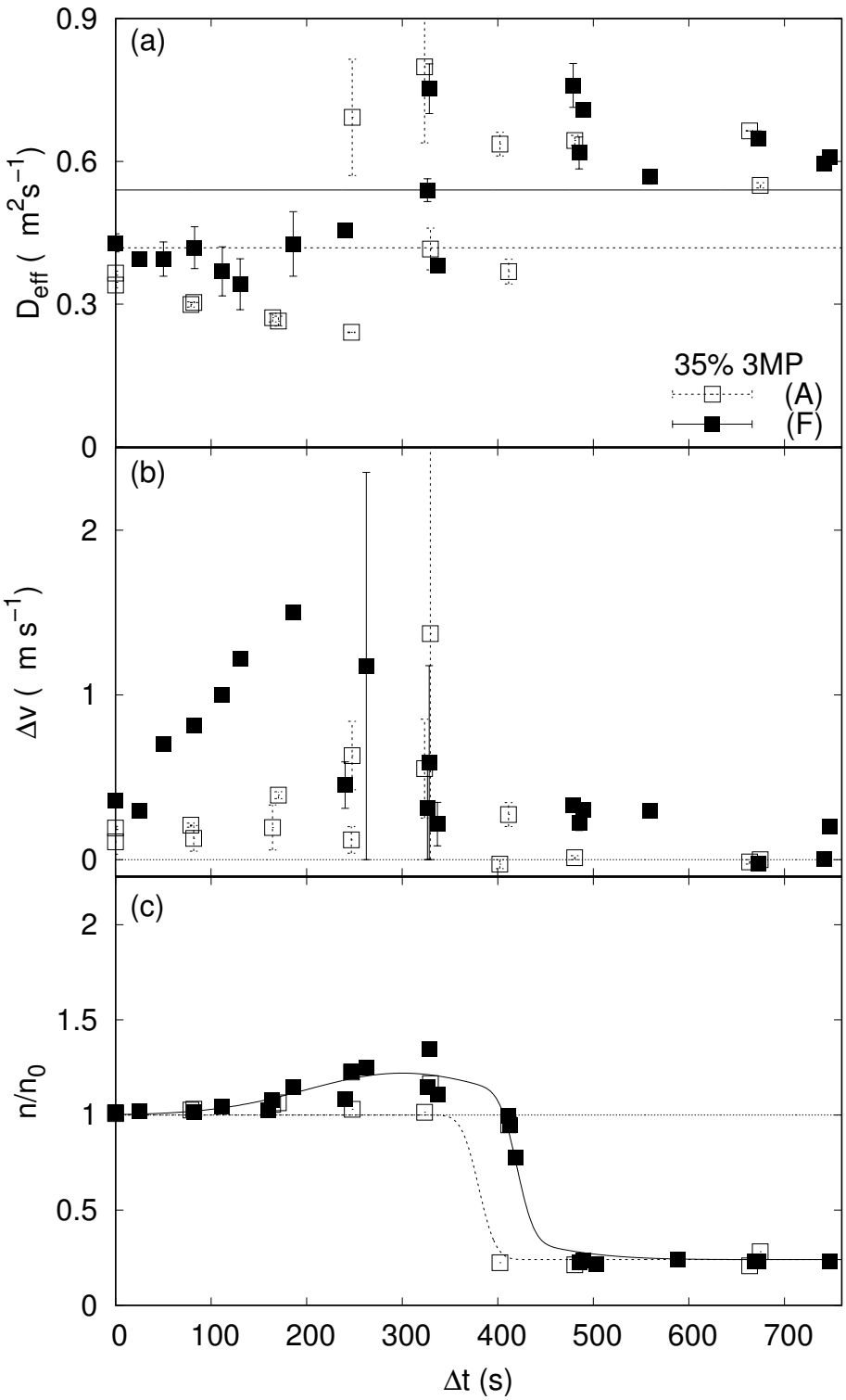

Figure 5.24.: Curves of the (a) effective diffusion coefficient D_{eff}, (b) velocity fluctuations Δv and (c) concentration ratio $\frac{n}{n_0}$ as a function of time delay Δt from the end of the temperature quench for 35 *wt%* 3MP, using samples at different ageing stages. (A) and (F) refer for aged and fresh samples. Solid and dashed lines in (a) represent the diffusion coefficient of the Janus colloids prior to the temperature quench and in (c) are guides to the eye to show the partitioning that occurs during the phase separation.

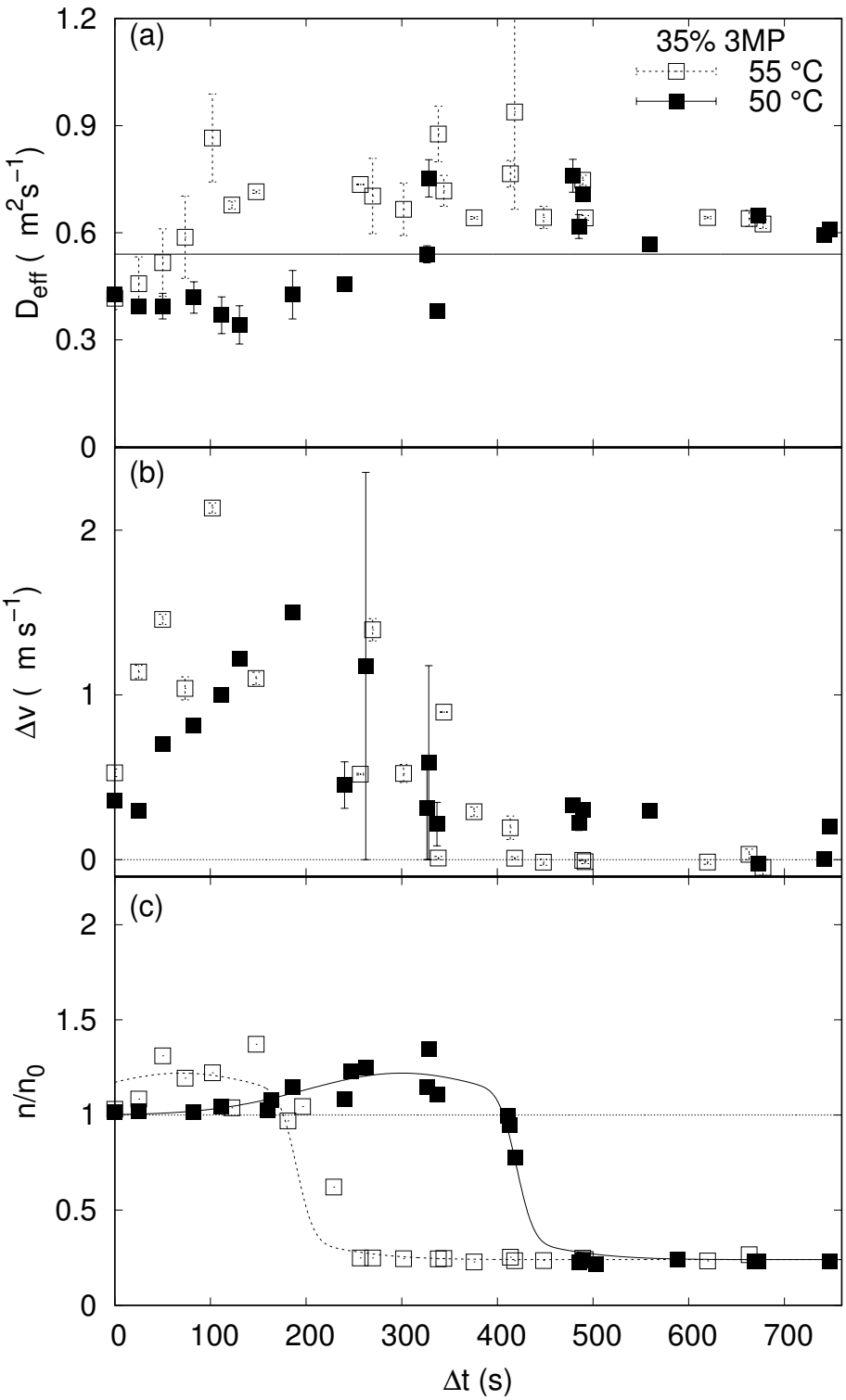

Figure 5.25.: Curves of the (a) effective diffusion coefficient D_{eff}, (b) velocity fluctuations Δv and (c) concentration ratio $\frac{n}{n_0}$ as a function of time delay Δt from the end of the temperature quench for 35 $wt\%$ 3MP with two different final temperatures, 50 and 55 $^{\circ}C$. The solid line in (a) represents the diffusion coefficient of the Janus colloids prior to the temperature quench and in (c) are guides to the eye to show the partitioning that occurs during the phase separation.

Note that the initial diffusion coefficient of the system at 25% is half of the expected one. This occurred because the sample used was already aged. Both fresh and aged systems at 25 and 35% were systematically investigated at different ageing stages and ΔT temperature jumps, as shown in the selected data presented in Figures 5.24 and 5.25. The comparison with aged samples does not show significant differences in the overall behaviour, however a reduced advection was detected (Fig. 5.24). Variations of ΔT gave the same results reported for silica colloids as the only effect is a shift in time of the completion of the phase separation (Fig. 5.25).

5.3.3. Summary

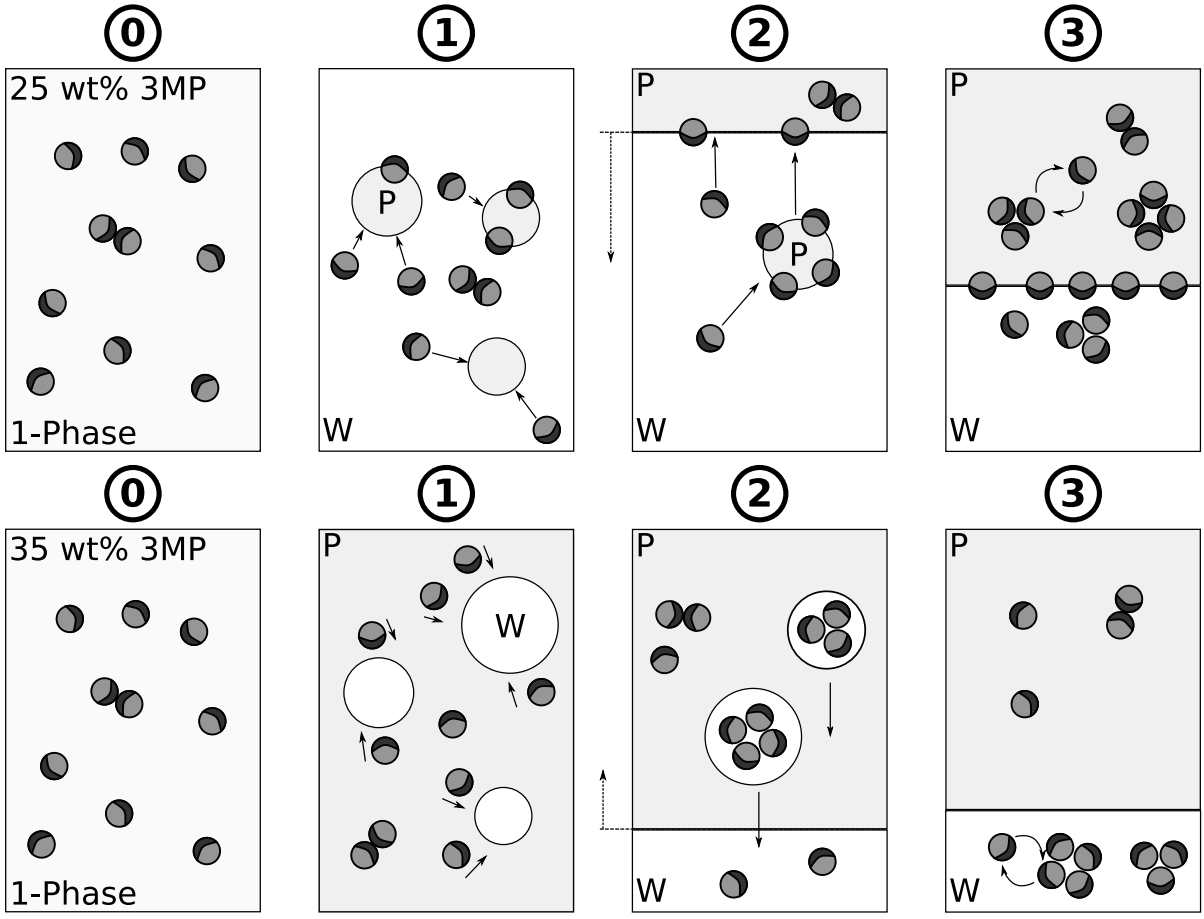

Figure 5.26.: Sketch of the mechanism inducing phoretic motion of Janus colloids in the phase separating system. Stage (0) represent the 1-phase system before quenching. During the phase separation, stage (1), isotropic phoretic motions are induced by the binodal decomposition of the mixture, where Janus colloids are forced to move toward the interfaces (25%) or the water-rich (W) areas (35%). When the two phase regions are defined, (2), clusters are visible and the phoretic motions start relaxing towards an equilibrium state, stage (3). A dimer is always drawn to remind the ageing effect.

Finally, isotropic dynamics of Janus colloids in both 25 and 35 *wt%* 3MP mixtures are controlled by phoretic phenomena occurring during the binodal phase separation at the microscopic

scale. This behaviour is schematically shown in Figure 5.26 for systems at both 25 and 35 *wt%* 3MP. At 25% 3MP, in which Janus colloids behave as surfactants, when the mixture start separating, stage ① ($\Delta t < 70\ s$), they probably start moving toward the interface of the 3MP-rich nuclei that strongly attract them. In stage ② ($\Delta t = (700-200)\ s$), when the macroscopic 3MP- and water-rich regions are formed and the colloids are concentrated at their interface, clusters are present and the evolution of the dynamics is not clear. In stage ③ ($\Delta t > 200\ s$), the system relax to the equilibrium.

At 35% 3MP, in stage ① ($\Delta t < 200\ s$), the motion of Janus colloids could be affected by the different solvent-preference of silica and nickel surfaces, and the reduced diffusion could results as a balance of the strong silica-3MP affinity and the water-rich phase nuclei facilitating the cluster formation. In this case the advective contribution may entirely comes from the dynamics of the media. In stage ② ($\Delta t = (200-480)\ s$), when the macroscopic 3MP- and water-rich regions are formed, the colloids are mainly concentrated in clusters in the water-rich areas as the advective term starts vanishing and the effective diffusion increases again. In stage ③ ($\Delta t > 480\ s$), system dynamics relax to the equilibrium.

5.4. Summary and Conclusion

This chapter shows the dynamics of colloids suspended in a system mimicking active motion far from the equilibrium. Phoretic motions and microstructures of sub-micron-sized silica colloids and half-coated silica/nickel Janus colloids suspended in a quasi-binary mixture of 3MP/H_2/D_2O undergoing liquid-liquid phase separation were investigated.

The suspension of silica colloids was used as a reference system. In the phase separated systems, such suspensions show a complete partitioning of silica colloids in the 3MP-rich phase due to the preferential wetting of 3MP on the silica surface. During phase separation, this same strong interaction with the solvent induce isotropic, phoretic motions of the colloids which are correlated to the dynamics of the phase-separating solvent. After a deep quench from an homogeneous phase to a two-phase region, silica colloids experience advection and enhanced diffusion, moving towards the evolving 3MP-rich phase nuclei or away from water-rich areas, depending to the 3MP concentration in the system. Moreover, MSD values as a function of time showed a deviation from the linear behaviour of Brownian motions, displaying dynamics that are reminiscent of active motions [35, 44]. In this experiments, colloids moved by diffusiophoresis effects, triggered by the local concentration gradients around the forming 3MP (or water) nuclei in the phase separating system.

Janus colloid systems displayed a much richer and more complex scenario compared to the case of bare silica colloids, where 3MP (or water) nucleation sites act as attractive (or repulsive)

regions. In the case of Janus particles, the microstructure is strongly dependent on the 3MP concentration as data suggested that the interactions of silica and nickel surfaces with the solvent bring about a behaviour similar to surfactants. In the system at 25%, indeed, Janus colloids migrate towards the 3MP/water interface forming a planar microstructure, whereas at 35%, colloids partially partition on the water-rich phase in the form of clusters which, in analogy with the surfactant behaviour at 25%, could have a micelle-like arrangement. The dynamics observed during the liquid-liquid phase separation is then very much associated to the peculiar microstructure. Advective phenomena are still present, but the effective diffusion coefficient are either enhanced or suppressed depending on the 3MP concentration and cluster formation. Specifically, at 35%, where the diffusion is reduced, colloids might probe the effective high viscosity of the system in the early stages of the phase separation.

The reference "passive" suspensions of bare silica colloids were found to move much faster than dispersions of Janus particles used for active systems. These results, both about microstructure and dynamics, are an eloquent demonstration that effective interactions in active systems matter. In this specific experiment, the asymmetry of the Janus colloids restrains the motility instead of speeding it up. This effect can be ascribed to the asymmetric interaction with the solvent in a binary system, where interparticle interactions similar to a surfactant system dominate over the phoretic motion induced by the phase separation. In other words, data suggested that enhanced dynamics are inhibited by dynamic clustering, reminiscent of the one observed in the phase diagram of some active systems [55]. In fact, during the binodal decomposition, colloid surfaces are probable nucleation points for 3MP-rich phase (or water), thus concentration monopoles created aside the Janus particles generate attractive interactions mimicking not only the dynamics, but also the interaction mechanism found in active systems [2].

X-ray scattering methods are a useful complement to direct 2D microscopy observations of dynamic clustering phenomena in active matter systems, as they offer the opportunity to probe 3D systems averaging a much higher number of colloids and investigate, simultaneously, the relation between effective interactions, microstructure and dynamics in concentrated systems.

6. Conclusion and Perspectives

This thesis presented an investigation of the effective interactions, microstructure and dynamics in colloidal systems exhibiting active behaviour, performed by using USAXS and multi-speckle XPCS.

A brief literature review about active colloidal dispersions was provided in **Chapter 1**, alongside a short introduction to colloids. **Chapter 2** describes some essential theoretical and experimental background of SAS techniques and the details of beamline ID02 at the ESRF.

As a first step, in **Chapter 3**, the size and morphology of active *E. coli* bacteria were obtained from the analysis of USAXS measurements by means of scattering form factor models. USAXS data covered a range of magnitude of scattering-vector $q = (2 \times 10^{-3} - 10^{-1})\ nm^{-1}$ and were analysed using a coarse-grained scattering form factor with a homogeneous SLD profile, demonstrating that in this q-range the enclosed cytoplasm dominates the scattering and the cell is visible as a uniform body. High-quality signal-to-noise *in vivo* measurements on *E. coli*, free from radiation damage, were used as a reference for the subsequent scattering experiments on active systems. The structure factor of interaction between *E. coli* cells was not measurable.

A further step towards the structural study of the cell involved the analysis of combined USAXS/SAXS data by a composite model. A wide range of q, from 2×10^{-3} to $7\ nm^{-1}$, of almost 4 orders of magnitude, allowed to enrich the structural model including the bacterial ultrastructure. Because of the complexity of the cell, contrast-variation SANS measurements were essential to add more constraints to the model and helped to develop a multi-scale structural model accounting for the entire size of the cell, in the micrometre scale, down to the details of the cell envelope of the order of a few tens of nanometres. The comprehensive multi-scale model was formulated blending formalisms related to core-shell colloids, lipid membranes and random-coil polymers. Particularly, flagella were described using the scattering structure factor of self-avoiding-walk polymers whilst the cell-body and cell-envelope were modelled by a core-multiple-shell form-factor consisting of an ellipsoidal core, representing the cytoplasm, and a specific rectangular SLD profile describing a generic gram-negative cell wall, respectively. Results were subjected to a self-consistency check accounting for a series of physical and mathematical requirements that were imperatives to turn the whole set of parameters into a single, congruent description.

The membrane electron-density-profile and the inter-membrane distances were obtained on

a quantitative scale. A striking results concerns the determination of the periplasm extension, (23 ± 2) *nm*, and electron-density, *in vivo* and without staining agents, namely without biasing the observations or actually affecting the envelope structure. These results are comparable with the most recent cryo-TEM observations [80] and add new evidences in opposition to the idea of "periplasmic gel" reported in the past [79]. These outcomes contribute to the debate about the physics of the periplasm. For this reason, it would be interesting to deepen small-angle scattering investigations and learn more about the nanometre scale, for example, by comparing data taken from *E. coli* with and without flagella. Moreover, scattering measurements on different strains of *E. coli* and other bacteria can be compared to verify if this multi-scale model can actually describe every gram-negative bacterium and, finally, the same approach could be tested to model gram-positive bacteria.

To conclude, the synergy of X-ray and neutron SAS techniques can be used as a non-invasive method for the *in vivo* study of the morphology and ultrastructure of gram-negative bacteria. This offers great opportunities for applied research on the mechanism of either detergents or antibiotics and antimicrobial peptides (such as the α-helical peptides [179, 180]) action on cellular membranes.

In **Chapter 4**, a combined USAXS and XPCS investigation was performed on passive, concentrated, sub-micron silica colloids suspended in active *E. coli* media, with the aim to observe and analyse variations on the effective interactions and dynamics of the passive particles induced by the motility of the active components. Concentrated systems ($\phi > 0.08$) of silica colloids of $\langle\sigma\rangle \sim 470$ *nm* exhibited multiple-scattering. The effect in the USAXS q-range was systematically investigated by varying colloid concentration and sample pathlength. Data were analysed by using the model proposed by Schelten and Schmatz [88]. The multiple-scattering also marginally affected XPCS data by reducing the contrast factor β. The knowledge gained from this study was used to complete the analysis of systems including bacteria, whose scattering contribution was neglected due to the high scattering contrast of silica.

Comparisons of effective interactions and dynamics of suspensions of silica colloids with (active) and without bacteria (passive) were performed by varying colloid and bacterial concentrations and tuning the "passive" interparticle interaction by changing solution conditions. The motility buffer, used to ensure an optimised cell swimming, affects the short-range repulsive interaction between negatively-charged silica colloids. This is turned into an effective hard-sphere potential resulting from a balance of attractive and screened repulsive contributions. These interactions can be tuned in favour of the attractive term and a second passive system with weakly-attractive interactions was obtained.

Results from the analysis of hard-sphere-like fluids suggested that the bacterial motility did not have a significant impact on both static [69] and hydrodynamic interparticle interactions. Instead, active *E. coli* reduced the attractive term in weakly-attractive systems, with a behaviour

similar to the one reported by Schwarz-Linek and co-workers [164].

Intensity autocorrelation functions of both hard-sphere-like and weakly-attractive systems were described by a single exponential decay, showing dynamics that were either enhanced or reduced depending on concentrations and static interactions of the passive reference systems. Changes in dynamics were represented by an effective-viscosity ratio $\eta_{eff}/\eta_{passive}$ which accounts for both viscosity variations and increase of the effective temperature, which is characteristic of some active systems [69–71]. It is interesting that $\eta_{eff}/\eta_{passive}$ values as a function of $D_{passive}$ showed a single, monotonic trend which seems to level-off the dynamics, where slow systems are sped up and fast suspensions are slowed down.

These results complement the picture described in reports about dilute, micron-sized colloids in a bath of swimming *E. coli* [63, 65, 81], where depletion-like interactions and enhanced dynamics of passive colloids due to the bacterial activity have been reported. It would be interesting to integrate this knowledge by performing a systematic investigation of the effective interactions and dynamics of such a system by varying the size ratio between passive/active colloids and verify if different sizes are sensitive to different dynamics occurring in the system, including the disparity between cell-body and flagella in terms of morphology, rotation [181, 182] and interactions with the environment [183]. This hypothesis follows the simulation carried out by Loi and co-workers [69], where a passive tracer in an active bath, used as a "thermometer" for the determination of the effective temperature, was sensitive to either fast- or slow-frequency dynamics depending on its mass.

X-ray scattering techniques were used to probe the influence of active bacteria on the effective interactions and dynamics of sub-micron, passive silica colloids, and allowed an appropriate ensemble averaging and the use of such concentrated systems, as they are too turbid to be probed by DLS due to a severe multiple-scattering. However, further improvements in XPCS are required to probe faster dynamics in dilute systems.

Multi-speckle XPCS measurements in the USAXS q-range were further exploited for the study of the effective interactions, microstructure and dynamics of suspension of half-coated silica/nickel Janus colloids in a quasi-binary mixture of 3MP/H_2O/D_2O upon phase separation. These results are presented in **Chapter 5**.

Investigations of the phase behaviour of charge-stabilised silica colloids in such a mixture were started by Beysens and co-workers [3, 166, 167, 171]. Colloids are stable in the homogeneous phase at low temperature while, above the LCST, they partition in the 3MP-rich phase towards the top of the sample holder, moving against the gravity. This behaviour is due to the wetting properties of silica, which preferentially adsorbs 3MP. This was exploited to generate the motion of sub-micron silica colloids, used as a reference system, in 3MP/H_2O/D_2O suspensions during a phase separation upon a temperature jump. Colloids showed a quasi-isotropic enhanced diffusion and advective phenomena during the phase separation. During the binodal

decomposition, 3MP-rich nuclei behave as effective attractive sites, triggering phoretic motions reminiscent of active dynamics that last for several minutes and slowly relaxing back to the equilibrium dynamics (Brownian) when the phase separation is completed. The similarity with active systems includes the evolution of the MSD of silica colloids observed during the phase separation, where MSD values exhibited deviations from the linear time-dependence, comparable to the anomalous diffusion predicted for symmetric active colloids [44].

The same reference silica colloids were used as templates for the synthesis of half-coated silica/nickel Janus particles using sputtering method. A systematic USAXS investigation of the microstructure of such asymmetric colloids in the 3MP/H_2O/D_2O mixture was performed prior to the XPCS experiments. Such a study revealed peculiar features, as Janus colloids in this binary mixture exhibit a behaviour similar to amphiphiles. Specifically, at 25 *wt%* 3MP colloids self-organised along the water/3MP interface, suggesting that the nickel surface prefers water more than the 3MP-rich phase. Instead, at 35% 3MP, colloids partially partitioned in the water-rich phase, as opposed to bare silica particles, and formed clusters, similar to surfactant micelles, to minimise the silica surfaces accessible to the solvent [177].

The Janus geometry, which is the key for the self-diffusiophoretic motion of active systems, was expected to boost the dynamics by adding directionality to phoretic motions. Instead, compared to the reference silica colloid systems, Janus particles displayed phoretic motions with more complex dynamics than their "passive" equivalent. In fact, the velocity of Janus colloids seemed hindered by the cluster formation, with a behaviour similar to the dynamic clustering observed in active systems [2,53]. In this case, USAXS and XPCS techniques permitted to monitor the microstructure and dynamics simultaneously and demonstrated their usefulness as they complement microscopy observations by allowing a better ensemble averaging and providing direct information about the effective interactions in the bulk.

With the expected improvements of the ESRF source and detector in the near future, the time resolution of the XPCS will be enhanced by several orders of magnitude. This, alongside a higher contrast factor β, will enable more quantitative static and dynamic studies of active systems.

7. Conclusion et Perspectives (Français)

Cette thèse a présenté une étude des interactions effectives, de la microstructure et de la dynamique dans les systèmes colloïdaux qui présentent un comportement actif, réalisée en utilisant USAXS et multi-speckle XPCS.

Une brève revue de la littérature sur les dispersions colloïdales actives a été fournie au **Chapitre 1**, ainsi qu'une courte introduction aux colloïdes. Le **Chapitre 2** décrit quelques informations théoriques et expérimentalles essentielles des techniques SAS et les détails de la ligne de lumière ID02 à l'ESRF.

Dans une première étape, au **Chapitre 3**, la taille et la morphologie de la bactérie active *E. coli* ont été obtenues à partir de l'analyse des mesures USAXS au moyen de modèles de facteur de forme. Les données USAXS ont recouvrent une gamme du vecteur de diffusion $q = (2 \times 10^{-3} - 10^{-1})\ nm^{-1}$ et ont été analysées en utilisant un facteur de forme avec un profil SLD homogène, démontrant que dans cette gamme de q le cytoplasme dans son ensemble domine la diffusion de rayons X et la cellule est visible comme un corps uniforme. Ces mesures *in vivo* de haute qualité (rapport signal/bruit) sur *E. coli*, exemptes de dommages radiatifs, ont été utilisées comme références pour les expériences de diffusion suivantes sur des systèmes actifs. Le facteur de structure inter-cellulaire n'a pas été observé.

Une autre étape vers l'étude structurelle de la cellule a impliqué l'analyse des données combinées USAXS/SAXS par un modèle composite. Une large gamme de q de presque 4 ordres de grandeur, de 2×10^{-3} à $7\ nm^{-1}$, a permis d'enrichir le modèle structurel incluant l'ultrastructure bactérienne. En raison de la complexité de la cellule, les mesures SANS de variation de contraste ont été essentielles pour ajouter plus de contraintes au modèle et ont aidé à développer un modèle structurel multi-échelle qui représente la cellule dans son ensemble, depuis l'échelle micrométrique jusqu'aux détails de l'enveloppe cellulaire de l'ordre du nanomètre. Le modèle multi-échelle complet a été formulé en associant des formalismes liés aux colloïdes de type noyau-enveloppe, aux membranes lipidiques et aux polymères à pelote aléatoire. En particulier, les flagelles ont été décrites en utilisant le facteur de structure de dispersion des polymères de type "self-avoiding-walk", tandis que le corps et l'enveloppe cellulaires ont été modélisés par un facteur de forme de type noyau-enveloppe-multiple constitué

d'un noyau ellipsoïdal, représentant le cytoplasme, et d'un profil SLD rectangulaire spécifique décrivant une paroi cellulaire générique typique des bactéries à Gram négatif. Les résultats ont été soumis à un contrôle d'auto-cohérence pour tenir compte d'une série d'exigences physiques et mathématiques impératives pour transformer l'ensemble des paramètres en une seule description congruente.

Le profil de densité électronique de la membrane et les distances inter-membranes ont été obtenus à une échelle quantitative. Un résultat remarquable concerne la détermination de l'extension périplasmique $(23 \pm 2\ nm)$ et de la densité électronique, *in vivo* et sans agents colorants, c'est-à-dire sans porter préjudice aux observations ou affecter réellement la structure de l'enveloppe. Ces résultats sont comparables aux observations cryo-TEM les plus récentes [80] et ajoutent de nouvelles informations qui contredisent l'idée de "gel périplasmique" rapportée par le passé [79]. Ces résultats contribuent au débat sur la physique du périplasme. Pour cette raison, il serait intéressant d'approfondir les études de diffusion au petit-angle et d'en apprendre davantage sur l'échelle nanométrique, par exemple, en comparant les données recueillies avec *E. coli* avec et sans flagelles. De plus, des mesures de diffusion sur différentes souches de *E. coli* et d'autres bactéries peuvent être comparées pour vérifier si ce modèle multi-échelle peut effectivement décrire chaque bactérie à Gram négatif; la même approche pourrait être testée pour modéliser des bactéries à Gram positif.

En conclusion, la synergie des techniques SAS des rayons X et des neutrons peut être utilisée comme un méthode non invasive pour l'étude *in vivo* de la morphologie et de l'ultrastructure des bactéries à Gram négatif. Ceci offre de grandes possibilités pour la recherche appliquée sur le mécanisme des détergents ou des antibiotiques et des peptides antimicrobiens (comme l'action des peptides α-hélicoïdes [179, 180]) sur les membranes cellulaires.

Dans le **Chapitre 4**, une étude combinée de USAXS et XPCS a été réalisée sur des colloïdes passifs concentrés de silice de taille sub-micrométriques en suspension dans une solution active de *E. coli*, avec l'objectif d'observer et d'analyser des variations des interactions effectives et de la dynamique des particules passives induites par la motilité des composants actifs. Les systèmes concentrés ($\phi > 0.08$) de colloïdes de silice de $\langle\sigma\rangle \sim 470\ nm$ ont présenté une diffusion multiple de rayons X. L'effet dans la gamme q de l'USAXS a été systématiquement étudié en faisant varier la concentration colloïdale et la longueur du trajet de l'échantillon. Les données ont été analysées en utilisant le modèle proposé par Schelten et Schmatz [88]. La diffusion multiple a également affecté marginalement les données XPCS en réduisant le facteur de contraste β. Les connaissances acquises dans le cadre de cette étude ont été utilisées pour compléter l'analyse des systèmes incluant les bactéries, dont la contribution à la diffusion a été négligée en raison du contraste élevé de diffusion de la silice.

Les comparaisons des interactions effectives et de la dynamique des suspensions de colloïdes de silice avec (active) et sans bactéries (passive) ont été effectuées en modifiant les concentra-

tions colloïdales et bactériennes et en ajustant l'interaction inter-particule "passive" en changeant les conditions de la solution tampon. La solution tampon de motilité, utilisé pour assurer une nage optimisée des cellules, affecte l'interaction répulsive à courte distance entre les colloïdes de silice chargés négativement. Ceci est transformé en un potentiel efficace de type sphère dure qui résulte d'un équilibre des contributions attractives et répulsives écrantées. Ces interactions peuvent être réglées en faveur du terme attractif et un second système passif avec des interactions faiblement attractives a été obtenu.

Les résultats de l'analyse du système sphère dure semblent indiquer que la motilité bactérienne n'a pas eu d'impact significatif sur les interactions inter-particule statiques [69] et hydrodynamiques. Au lieu de ça, les *E. coli* actifs ont réduit le terme attractif dans les systèmes avec une attraction faible, avec un comportement semblable à celui rapporté par Schwarz-Linek et collègues [164].

Les fonctions d'autocorrélation de l'intensité des systèmes sphère dure et faiblement attractifs ont été décrites par une seule décroissance exponentielle, montrant des dynamiques qui ont été accélérées ou ralenties en fonction des concentrations et des interactions statiques des systèmes de référence passifs. Les variations de la dynamique ont été représentées par un coefficient de viscosité efficace $\eta_{eff}/\eta_{passive}$ qui tient compte à la fois des variations de viscosité et des augmentations de la température effective, caractéristique de certains systèmes actifs [69–71]. Il est intéressant de noter que les valeurs passives $\eta_{eff}/\eta_{passive}$ en fonction de $D_{passive}$ ont montré une seule tendance monotone qui semble "stabiliser" la dynamique, où les systèmes lents sont accélérés et les suspensions rapides ralenties.

Ces résultats complètent le portrait décrit dans les rapports sur les colloïdes dilués de taille micrométrique dans un bain actif de *E. coli* [63, 65, 81], où des interactions similaires au type déplétion et une dynamique augmentée des colloïdes passifs en raison de l'activité bactérienne ont été rapportées . Il serait intéressant d'intégrer ces connaissances en effectuant une recherche systématique des interactions effectives et de la dynamique d'un tel système en faisant varier le rapport de taille entre les colloïdes passifs/actifs et en vérifiant si différentes tailles sont sensibles aux différentes dynamiques qui se produisent dans le système, telles que la disparité entre le corps cellulaire et les flagelles en termes de morphologie, de rotation [181, 182] et d'interactions avec l'environnement [183]. Cette hypothèse fait suite à la simulation effectuée par Loi et collègues [69], où un traceur passif dans un bain actif, utilisé comme thermomètre pour la détermination de la température effective, était sensible aux dynamiques à fréquence rapide et lente en fonction de sa masse.

Des techniques de diffusion des rayons X ont été utilisées pour étudier l'influence des bactéries actives sur les interactions effectives et la dynamique des colloïdes passifs de silice de taille sub-micrométrique, et ont permis une moyenne d'ensemble appropriée alors que ces systèmes concentrés sont trop turbides pour être sondés au moyen de la diffusion dynamique de la lumière

en raison d'une diffusion multiple sévère. Cependant, d'autres améliorations de la technique XPCS sont requises pour sonder la dynamique plus rapide dans les systèmes dilués.

Les mesures XPCS multi-speckle dans la gamme de q de l'USAXS ont été aussi exploitées pour l'étude des interactions effectives, de la microstructure et de la dynamique de la suspension de colloïdes de type Janus (silice partiellement couvert de nickel) dans un mélange quasi-binaire de 3MP/H_2O/D_2O pendant la séparation de phase. Ces résultats sont présentés au **Chapitre 5**.

Des recherches sur le diagramme de phase des colloïdes de silice stabilisés en charge dans un tel mélange ont été initiées par Beysens et collègues [3,166,167,171]. Les colloïdes sont stables dans la phase homogène à basse température tandis que, au-dessus de la LCST, ils se partagent dans la phase riche en 3MP vers le haut de l'échantillon, en se déplaçant contre la gravité. Ce comportement est dû aux propriétés de la silice, qui adsorbe préférentiellement 3MP. Ceci a été exploité pour générer le mouvement de colloïdes de silice de taille sub-micrométrique, utilisé comme système de référence, dans des suspensions 3MP/H_2O/D_2O, au cours d'une séparation de phase lors d'un saut de température. Les colloïdes ont montré une diffusion quasi isotrope et des phénomènes advectifs lors de la séparation de phase. Au cours de la décomposition binodale, les noyaux riches en 3MP se comportent comme des sites attractifs efficaces, provoquant des mouvements phorétiques rappelant des dynamiques actives qui durent plusieurs minutes et convergent lentement vers la dynamique d'équilibre (brownienne) lorsque la séparation de phase est terminée. La similarité avec les systèmes actifs inclut l'évolution du MSD des colloïdes de silice observée au cours de la séparation de phase, où ces valeurs présentent des déviations par rapport à la dépendance temporelle linéaire, comparable à la diffusion anormale prédite pour les colloïdes actifs symétriques [44].

Les mêmes colloïdes de silice de référence ont été utilisés en tant que matrices pour la synthèse de particules de type Janus en silice/nickel en utilisant des procédés de pulvérisation cathodique. Une étude systématique USAXS de la microstructure de tels colloïdes asymétriques dans le mélange 3MP/H_2O/D_2O a été réalisée avant les expériences XPCS. Une telle étude a révélé des caractéristiques particulières, par exemple les colloïdes Janus dans ce systèmes binaires présentent un comportement semblable à des amphiphiles. Spécifiquement, à 25 *wt%* 3MP, les colloïdes s'auto-organisent à l'interface eau/3MP, suggérant que la surface de nickel préfère l'eau plus que la phase riche en 3MP. Par contre, à 35 *wt%* 3MP, les colloïdes sont partiellement présents dans la phase riche en eau, par opposition aux particules de silice nues, et forment des clusters, semblables aux micelles des tensioactifs, pour minimiser les surfaces de silice accessibles au solvant [177].

La géométrie Janus, qui est la clé du mouvement auto-diffusiophorétique des systèmes actifs, aurais dû stimuler la dynamique en ajoutant de la directionnalité aux mouvements phorétiques. Au lieu de cela, par rapport aux systèmes de colloïde de silice de référence, les particules Janus présentent des mouvements phorétiques avec une dynamique plus complexe que leur équivalent

“passif”. En fait, la vitesse des colloïdes Janus semble gênée par la formation de clusters, avec un comportement similaire au regroupement dynamique observé dans les systèmes actifs [2,53]. Dans ce cas, les techniques USAXS et XPCS ont permis de surveiller simultanément la microstructure et la dynamique et ont démontré leur utilité car elles complètent les observations de microscopie en permettant une meilleure moyenne d’ensemble et fournissant des informations directes sur les interactions effectives.

Avec les améliorations attendues de la source de rayons X à l’ESRF et du détecteur dans un proche avenir, la résolution temporelle du XPCS sera améliorée de plusieurs ordres de grandeur. Ceci, à côté d’un facteur de contraste β plus élevé, permettra des études statiques et dynamiques plus quantitatives de ces systèmes.

Appendices

A. Numerical limits in the Porod Regime

Scattering form factors of cylindrical objects, including the capped-cylinder geometry (see scattering amplitudes in Equations 3.4 and 3.1) contain the Bessel function of 1st kind $J_1(x)$, which derives from the solution of the integral in Equation 2.7 by using cylindrical coordinates.

Scattering amplitudes for spherical coordinates (Equations 2.9 and 3.5) lead instead to the *spherical* Bessel functions of 1st kind, $j_n(x)$, including:

$$j_0(x) = \frac{\sin(x)}{x} \qquad j_1(x) = \frac{\sin(x) - x\cos(x)}{x^2} \tag{A.1}$$

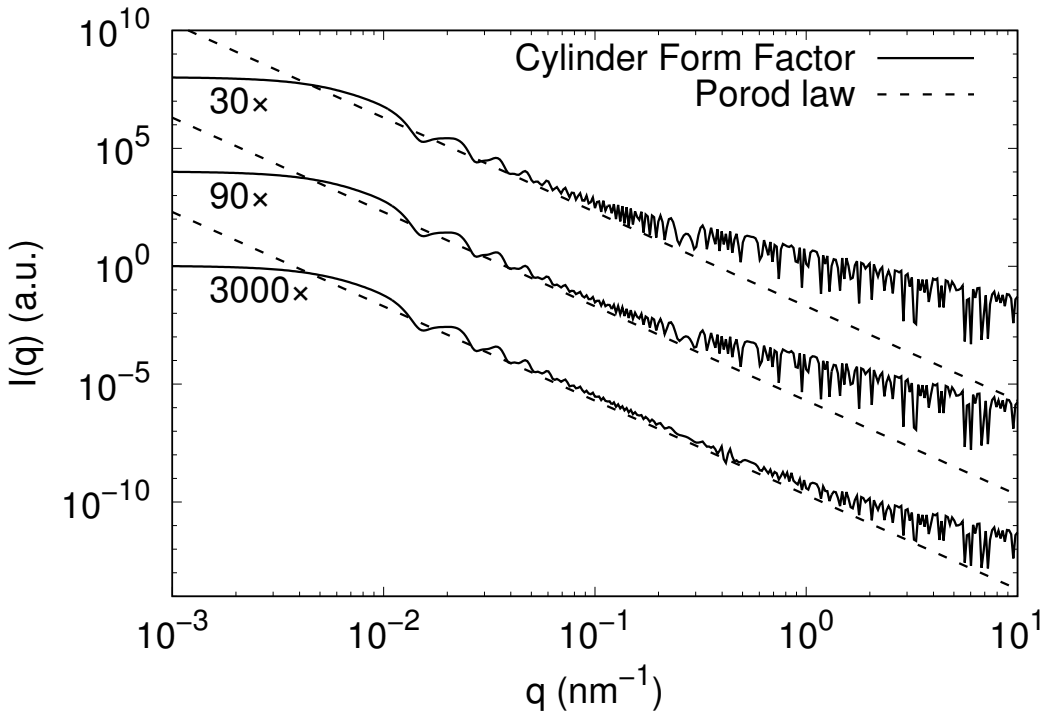

Figure A.1.: Simulated scattering form factors of a polydisperse cylinder (Gaussian PDF) with $\langle R \rangle = 250$ *nm*, $H = 1000$ *nm* and standard deviation $\sigma_R = 12.5$ *nm*. Curves are compared to the asymptotic trend of the Porod law $\propto q^{-4}$. The values 30, 90 and 3000× are the numbers of numerical integration steps (Simpson's rule) used during the orientation average (see Eq. 3.2).

From a numerical point of view, the main difference between $j_n(x)$ and $J_n(x)$ is that only the former can be reduced to a simple analytical form, whereas the latter are described by rather simple approximations that are coded in the libraries of a number of programming languages. Such approximations are precise, but when scattering form factors are computed, they enhance an intrinsic numerical instability that occur in the Porod regime at $qR \gg 1$, as it is shown in Figure A.1. Here, an example of instability for high q-values is presented. A cylindrical form factor requires an orientation average, which is numerically implemented by a discrete sum based on the trapezoidal rule (Simpson's rule). If a cylinder model is required, a (U)SAXS measure performed at one sample-to-detector distance, covering almost two orders of magnitude in q, can be analysed accounting for an orientation average with 30 to 90 steps within $[0, \frac{\pi}{2}]$. In this case, scattering curves are well-described up to 0.06 nm^{-1} and 0.1 nm^{-1}, respectively. From Figure A.1, it is clear that for a multi-scale model, which needs a larger q-range, even splitting the integral in 3000 steps is not sufficient for a perfect description, as the curve covers one order of magnitude more, but unwanted oscillations are still present.

The entity of such an issue depends on the specific scattering function and can be easily fixed by increasing the number of steps, N_O and N_P, of the orientation average and polydispersity integral (see Eq. 2.11). The instability can also disappear by adding a further polydispersity, such as in the length H of a cylinder, but, for practical purposes, this will significantly increase the computational time. To give the idea, consider a data set $\{x_i, y_i\}$ with M entries, and a time Δt necessary to compute $F(x_i)$ per step, regardless of the integral type. The time necessary to plot a function is $\Delta t \times M \times N_O \times N_P$, in the case of orientation average and polydispersity. Therefore, each increase of integration steps, or additional integrations, are directly reflected on the computational time and ordinary calculations of a few minutes can take several hours.

B. Minimization Algorithms

SAXS data presented in this thesis were reduced from two-dimensional scattering patterns by using *SPD programs* (developed by Dr. Peter Böseke, ID02 beamline [184]) and *saxsutilities.m* (developed by Dr. Michael Sztucki, ID02 beamline [123]). XPCS measurements were obtained by using *PYXPCS.py* (developed by Dr. Yuri Chushkin, ID10 beamline) software. Intensity-intensity autocorrelation functions were fitted with *getxpcs.m* (prepared by Dr. Johannes Möller, ID02 beamline).

All SAS curves were instead analysed with dedicated utilities and fitting routines written and developed as a part of this thesis work. The fitting routine has been written in Perl with the aim to have a unique and customized program able to implement specific scattering form factors associated to bacteria and Janus colloids. The routine makes use of a growing library of SAS functions, including polydisperse form and structure factors (with the exception of the Yukawa potential model, implemented in *saxsutilities.m*).

The program includes a few options, such as background subtraction, smearing convolution, data binning, plotting, saving history and choice of the most appropriate minimization algorithm. In particular, those methods are the *Levenberg-Marquardt*, *Simulated Annealing* and *Genetic Selection* algorithms.

A fitting procedure, given a specific test function F, consists in finding the correct set of parameters $\mathbf{u}$ which minimises the χ^2 function:

$$\chi^2 = \sum_{i=1}^{M} \left[\frac{y_i - F(x_i, \mathbf{u})}{e_i} \right]^2 \tag{B.1}$$

where $\{x_i, y_i\}$ is the data set comprising M entries, e_i is the error associated to y_i, F is the model function to be used, which depends on the coordinate x_i and a set of P parameters $\mathbf{u} = u_1, u_2, \ldots, u_P$. The term inside square brackets is called *residual*.

B.1. Levenberg-Marquardt Method

The Levenberg-Marquardt Algorithm (LMA) is the standard method used in many commercial and in-house-built fitting software.

Consider the vector $\tilde{\mathbf{u}}$ as the set of parameters for which the χ^2 function presents a minimum. In the proximity of $\tilde{\mathbf{u}}$, $\chi^2(\mathbf{u})$ is approximated by its Taylor series up to the second order:

$$\chi^2(\mathbf{u}) \approx \chi^2(\tilde{\mathbf{u}}) + (\mathbf{u}-\tilde{\mathbf{u}}) \cdot \nabla\chi^2(\tilde{\mathbf{u}}) + \frac{1}{2}(\mathbf{u}-\tilde{\mathbf{u}}) \cdot \mathbf{H} \cdot (\mathbf{u}-\tilde{\mathbf{u}}) \tag{B.2}$$

where $\mathbf{H}$ is called *Hessian* matrix of the χ^2 function at $\tilde{\mathbf{u}}$:

$$[\mathbf{H}]_{ij} = \left.\frac{\partial^2\chi^2}{\partial u_i u_j}\right|_{\tilde{\mathbf{u}}} \tag{B.3}$$

The gradient of $\chi^2(\mathbf{u})$ is then given by:

$$\nabla\chi^2(\mathbf{u}) \approx \nabla\chi^2(\tilde{\mathbf{u}}) + \mathbf{H} \cdot (\mathbf{u}-\tilde{\mathbf{u}}) \tag{B.4}$$

In the Newton method [185], accordingly to the Taylor series approximation, by setting the gradient to zero, $\nabla\chi^2(\mathbf{u}) = 0$, one can calculate $\tilde{\mathbf{u}}$, starting from an arbitrary vector $\mathbf{u}$. Hence, from Equation B.4, one obtains:

$$\mathbf{u}-\tilde{\mathbf{u}} \approx \mathbf{H}^{-1} \cdot \left[-\nabla\chi^2(\tilde{\mathbf{u}})\right] \tag{B.5}$$

The LMA makes use of the this concept. Let define the vector $\mathbf{b}$, associated to the gradient $\mathbf{b} = -\frac{1}{2}\nabla\chi^2(\mathbf{u})$, whose elements are:

$$[\mathbf{b}]_k = -\frac{1}{2}\frac{\partial\chi^2(\mathbf{u})}{\partial u_k} = \sum_{i=1}^{M} \frac{[y_i - F(x_i,\mathbf{u})]}{e_i^2}\frac{\partial F(x_i,\mathbf{u})}{\partial u_k} \tag{B.6}$$

and the *curvature* matrix $\mathbf{A}$, associated to the Hessian matrix $\mathbf{A} = \frac{1}{2}\mathbf{H}$, whose elements are given by:

$$\begin{aligned}[\mathbf{A}]_{kl} &= \frac{1}{2}\frac{\partial^2\chi^2(\mathbf{u})}{\partial u_k u_l} = \sum_{i=1}^{M}\frac{1}{e_i^2}\left\{\frac{\partial F(x_i,\mathbf{u})}{\partial u_k}\frac{\partial F(x_i,\mathbf{u})}{\partial u_l} - [y_i - F(x_i,\mathbf{u})]\frac{\partial^2 F(x_i,\mathbf{u})}{\partial u_k u_l}\right\} \approx \\ &\approx \sum_{i=1}^{M}\frac{1}{e_i^2}\frac{\partial F(x_i,\mathbf{u})}{\partial u_k}\frac{\partial F(x_i,\mathbf{u})}{\partial u_l}\end{aligned} \tag{B.7}$$

where the last approximation simplifies the algorithm, as it does not affect its efficiency and it rather avoids instability issues close to the minimum [185].

Given an initial set of test parameters, $\mathbf{u}_0$, the minimum χ^2_{min} is reached by calculating the corrections $\delta\mathbf{u}$ from the linear systems of equations which directly follow from Equation B.5:

$$\mathbf{A} \cdot \delta\mathbf{u} = \mathbf{b} \qquad \delta\mathbf{u} = \mathbf{C} \cdot \mathbf{b} \tag{B.8}$$

where $\mathbf{C} = \mathbf{A}^{-1}$ is called *covariance* matrix (Gauss-Newton method). If $\chi^2(\mathbf{u}_0)$ value deviates from the approximation in Equations B.2, the corrections are, instead, simply related to the gradient (gradient descent method) and are given by :

$$\delta\mathbf{u} \propto \mathbf{b} \tag{B.9}$$

The LMA mixes these two methods by defining a scalar parameter λ and a new curvature matrix $\mathbf{A}'$ as:

$$\begin{cases} [\mathbf{A}']_{kl} = [\mathbf{A}]_{kl} & \text{if } k \neq l \\ [\mathbf{A}']_{kl} = (1+\lambda)[\mathbf{A}]_{kl} & \text{if } k = l \end{cases} \tag{B.10}$$

For $\lambda \gg 1$ the curvature matrix is diagonally dominant and Equation B.8 is reduced to Equation B.9 with an *ad hoc* proportionality factor. This approximation is used when $\chi^2(\mathbf{u})$ values are far from the minimum whereas, close to it, $\lambda \ll 1$ values reactivate Equation B.8, as $\mathbf{A}' \simeq \mathbf{A}$, and a finer search around the minimum can be performed.

Specifically, in the Perl script used, the LMA was implemented as follows:

(1) Give an initial set of parameters $\mathbf{u} \equiv \mathbf{u}_0$ and compute $\chi^2(\mathbf{u}_0)$.
(2) Set boundary conditions, $\mathbf{u}^{(L)}$ and $\mathbf{u}^{(H)}$, for lowest and highest values, respectively.
(3) Set an initial $\lambda = 100$ and compute $\mathbf{b}$ and $\mathbf{A}'$.
(4) Solve the linear system of Equation B.8 using $(\mathbf{A}')^{-1}$, obtain the corrections $\delta\mathbf{u}$ and compute $\chi^2(\mathbf{u}+\delta\mathbf{u})$.
(5) Evaluate the new $\chi^2(\mathbf{u}+\delta\mathbf{u})$ value:
    - *accepted*: if $\chi^2(\mathbf{u}+\delta\mathbf{u}) < \chi^2(\mathbf{u})$, update $\mathbf{u}+\delta\mathbf{u} \to \mathbf{u}$, update $\lambda/10 \to \lambda$, re-compute $\mathbf{b}$ and $\mathbf{A}'$ and go back to step (4).
    - *rejected*: if $\chi^2(\mathbf{u}+\delta\mathbf{u}) \geq \chi^2(\mathbf{u})$, update $\lambda \cdot 10 \to \lambda$, re-compute $\mathbf{A}'$ and go back to step (4).
(6) Iterate until the following **ending criteria** are fulfilled:
    - *convergence*: $[\chi^2(\mathbf{u}) - \chi^2(\mathbf{u}+\delta\mathbf{u})] < \Delta\chi^2$ and $[\chi^2(\mathbf{u}) - \chi^2(\mathbf{u}+\delta\mathbf{u})] < 0$, where $\Delta\chi^2$ is a user defined threshold.
    - *oscillation*: the sign of $[\chi^2(\mathbf{u}) - \chi^2(\mathbf{u}+\delta\mathbf{u})]$ changes four times in a row. It occurs when the threshold $\Delta\chi^2$ is too small compared to the order of magnitude of the χ^2 oscillations around the minimum.
    - *divergence*: the condition $[\chi^2(\mathbf{u}+\delta\mathbf{u}) \geq \chi^2(\mathbf{u})]$ is realised four times in a row. It may happen when $\mathbf{u}_0$ is not an appropriate set of initial parameters.

In the case of *divergence*, a new set of initial parameters has to be chosen, whereas both *convergence* and *oscillation* give a final set of results, $\mathbf{u}$, which minimises $\chi^2(\mathbf{u})$. At the end of

the iterations (usually < 10), the covariance matrix, $\mathbf{C}$, brings information about the nominal errors associated to each parameter u_k. In particular, each diagonal value is equal to the variance $[C]_{kk} = \sigma_k^2$, assuming that errors e_i follow a Gaussian distribution around the measured y_i. Non-diagonal values measure the correlations among the parameters, $0 \leq \frac{[C]_{kl}}{\sigma_k \sigma_l} \leq 1$.

B.2. Monte Carlo Algorithms

The LMA is extensively used for its simplicity and speed. However, it has the disadvantage that it cannot discriminate a local to a global minimum in the $\chi^2(\mathbf{u})$ landscape and, therefore, it may not be a suitable choice for complex problems. In this context, a "complex problem" refers to the number of local minima in the χ^2-space [defined by data, $\{x_i, y_i\}$, and model function, $F(x_i, \mathbf{u})$], to the size P of the array of *free* parameters, $\mathbf{u}$, and to correlations among them.

For this situation, algorithms accounting for Monte Carlo approaches, i.e. based of randomly distributed entries, have been designed.

B.2.1. Simulated Annealing Algorithm

The Simulated Annealing Algorithm (SAA), used as a minimisation method, is an adequate tool to explore a number of $\mathbf{u}$ realisations and hence to probe the $\chi^2(\mathbf{u})$ space looking for the global minimum.

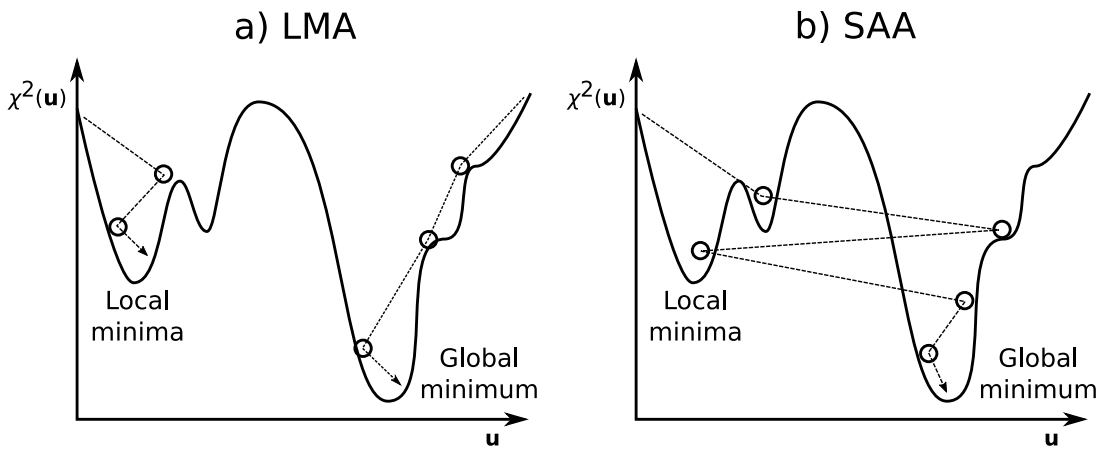

Figure B.1.: a) Two possible paths of the LMA minimisation of $\chi^2(\mathbf{u})$ as a function of the P-dimensional vector $\mathbf{u}$, where the one on the left is trapped in a local minimum. b) Possible path of the SAA minimisation of $\chi^2(\mathbf{u})$ as a function of the P-dimensional vector $\mathbf{u}$. Here the path can explore the χ^2 landscape to find the global minimum.

The SAA was inspired by the natural relaxation of some glassy systems towards the global minimum of free energy, the crystal state [185]. In this analogy, $\chi^2(\mathbf{u})$ is compared to the free energy associated to a peculiar atomic configuration and the set of parameters $\mathbf{u}$ simulates the conformational coordinates of such a configuration. The probability, π_i, of being in a specific

configuration i, depends on the energy related to it, E_i, and on the temperature of the system, T, through the Boltzmann distribution:

$$\pi_i \propto e^{-\frac{E_i}{k_B T}} \tag{B.11}$$

In the SAA, a series of $\mathbf{u}$ vectors are generated, where each element u_k is a random values within user defined boundaries. For each new set of parameters, $\mathbf{u}$, the condition $\chi^2(\mathbf{u}) < \chi^2_{min}$ is checked, where χ^2_{min} is a test minimum. If the condition is false, the new set $\mathbf{u}$ is rejected, otherwise, if true, $\mathbf{u}$ is saved as best realisation of a χ^2_{min} and the latter is updated (see Fig. B.1). The peculiarity of the SAA consists in introducing an artificial temperature parameter T. Every time a $\chi^2(\mathbf{u})$ value is rejected because it is higher than χ^2_{min}, it has a probability π, of being considered a new temporary minimum, equal to:

$$\pi = e^{-\frac{\chi^2(\mathbf{u})}{T}} \tag{B.12}$$

This procedure prevents the minimisation path to remain trapped in local minima and gives the possibility to probe other regions of the χ^2 space. For $T \gg \chi^2$, the entire landscape is explored and global and local minima are equally probed, instead, for $T \ll \chi^2$, the probability of jumping from one "valley" to another is negligible.

In the Perl script, the SAA was implemented as follows:

(1) Give an initial set of parameters $\mathbf{u} \equiv \mathbf{u}_0$ and assign $\chi^2(\mathbf{u}_0) \rightarrow \chi^2_{min}$.
(2) Set boundary conditions, $\mathbf{u}^{(L)}$ and $\mathbf{u}^{(H)}$, for lowest and highest values, respectively.
(3) Set an initial temperature, T, higher than, or of the same order of magnitude of $\chi^2(\mathbf{u}_0)$.
(4) Generate a "fluctuation" $\delta\mathbf{u}$, where each element δu_k is a pseudo-random number within 0 and $(u_k^{(H)} - u_k^{(L)})/10$.
(5) Compute $\chi^2(\mathbf{u}+\delta\mathbf{u})$ and evaluate it:
    - *accepted*: if $\chi^2(\mathbf{u}+\delta\mathbf{u}) < \chi^2_{min}$, update $\mathbf{u}+\delta\mathbf{u} \rightarrow \mathbf{u}$ as a best result, update $\chi^2(\mathbf{u}+\delta\mathbf{u}) \rightarrow \chi^2_{min}$ and go back to step (4).
    - *accepted*: generate a pseudo-random number $x \in [0,1]$; if $\chi^2(\mathbf{u}+\delta\mathbf{u}) > \chi^2_{min}$ and $x \leq e^{-\frac{\chi^2(\mathbf{u}+\delta\mathbf{u})}{T}}$, update $\mathbf{u}+\delta\mathbf{u} \rightarrow \mathbf{u}$ as a best result, update $\chi^2(\mathbf{u}+\delta\mathbf{u}) \rightarrow \chi^2_{min}$ and go back to step (4).
    - *rejected*: if $\chi^2(\mathbf{u}+\delta\mathbf{u}) > \chi^2_{min}$ and $x > e^{-\frac{\chi^2(\mathbf{u}+\delta\mathbf{u})}{T}}$ go back to step (4).
(6) Iterate until 100 instances of χ^2_{min} are accepted, then reduce the T by 10% and go back to step (4).
(7) Repeat until the the following **ending criteria** are fulfilled:
    - The reduced temperature is lower than 1% of the initial value.
    - 300 instances of rejection are realised before to 100 acceptances. It occurs when the

initial temperature is too low or no other χ^2_{min} is found.

This procedure is able to find the global minimum skipping possible local minima encountered during the minimisation. Unfortunately, for complex problems, where the LMA might fail, the probability of success is guaranteed if an infinite number of $\mathbf{u} + \delta\mathbf{u}$ realisations are probed.

Given a data set of M entries y_i and a model function F which requires P parameters, each iteration of the LMA needs F to be computed $(P+1) \times M$ times. In the SAA, F is computed only M times, but for hundreds of iterations, as opposed to the few ones necessary for the LMA. Finally, the SAA is to be preferred with respect to the LMA only if the latter fails due to trapping effect at local minima, otherwise the SAA is is too slow to be used as an efficient tool.

B.2.2. Genetic Selection Algorithm

Another Monte Carlo based method is the Genetic Selection Algorithm (GSA). In the same way the SAA is inspired to glassy systems, the GSA mimics the Darwinian evolution based on the natural selection.

In such an analogy, each set of parameters, $\mathbf{u}$, is associated to a *chromosome*, composed of P *genes* $\mathbf{u} = u_1, u_2, \ldots, u_P$, and each chromosome defines an *individual*, $\chi^2(\mathbf{u})$. The algorithm consists in creating an initial population — a set of $\chi^2(\mathbf{u}^{(i)})$ — where $\mathbf{u}^{(i)}$ vectors are different chromosomes, randomly generated within user defined boundaries. Such a population is evaluated on the base of the χ^2 minimisation, therefore, only the individuals with the lowest χ^2 realisations are selected to create an offspring, which inherits a random mixture of chromosomes, $\mathbf{u}^{(i)}$, from the best individuals. The offspring can be subjected to mutations, i.e. a few genes of their chromosomes can be randomly modified. Then, the process is iterated, as the new *generation* is the population to be evaluated, best genes are preserved and inherited and individuals *evolve* towards the optimum realisation of the global minimum.

The GSA can be written by using different options and criteria to evaluate, select and create each generation but, here, only the algorithm used in the analysis of Chapter 3 will be presented. Specifically, the GSA was implemented as it follows:

(1) Give an initial set of parameters (chromosome) $\mathbf{u} \equiv \mathbf{u}_0$.
(2) Set boundary conditions, $\mathbf{u}^{(L)}$ and $\mathbf{u}^{(H)}$, for lowest and highest values, respectively.
(3) *Create the population*: Generate 8 more sets, $\mathbf{u}^{(i)}$, where each parameter (gene), $u_k^{(i)}$, is a pseudo-random number within the boundaries $\mathbf{u}^{(L)}$ and $\mathbf{u}^{(H)}$.
(4) *Chromosome selection*: Rank $\chi^2(\mathbf{u}^{(i)})$ values from the smallest to the biggest and select the first 4 associated vectors $\mathbf{u}^{(i)}$ over a total of 9.
(5) *Generate the offspring* (*Chromosome recombination*): Randomly create 8 couples $\{\mathbf{u}^{(i)}, \mathbf{u}^{(j)}\}$

among the best 4 selected in step (4). Each couple generates a new set $\{\mathbf{u}^{(i)}, \mathbf{u}^{(j)}\} \rightarrow \mathbf{u}^{new}$, where every single parameter u_k^{new} is inherited from $\mathbf{u}^{(i)}$ or $\mathbf{u}^{(j)}$ with an equal probability of 50%.

(6) *Chromosome mutation*: Each single parameter $u_k^{(i)}$, among the 8 new sets, possesses a 20% probability to be "mutated", i.e. it is updated by a random fluctuation, $u_k^{(i)} + \delta u_k^{(i)} \rightarrow u_k^{(i)}$, where $\delta u_k^{(i)}$ is a pseudo-random number within 0 and $(u_k^{(H)} - u_k^{(L)})/10$.

(7) *Inheritance of the best*: The set $\mathbf{u}^{(i)}$ which realises the minimum χ^2_{min} value during the step (4) is not subjected to mutations and it is preserved to be part of the new *offspring*, restoring the initial number of individuals to 9.

(8) Go back to step (4) evaluating every new generation and iterate until the the following **ending criteria** are fulfilled:
   - $\chi^2_{min} < \chi^2_{thr}$, where χ^2_{thr} is a user defined threshold.
   - A user-defined maximum number of iterations is reached.

The number of individuals, 9, resulted to be a sufficient quantity to probe the χ^2 space in the fitting procedures encountered in Chapter 3 where, with an appropriate initial set $\mathbf{u}_0$, 25 generations were often enough to reach χ^2_{thr}. As well, a mutations probability of 20%, resulted as a suitable value to avoid an *evolutionary cul-de-sac*, which, following the analogy, describes trapping effects due to local minima found in the LMA.

The GSA suffers from the same disadvantage of the SAA, as it could reach the best χ^2_{min} only in the long time range. However, even if it is still slower than the LMA, results much faster than the SAA in most of the cases.

Neither SAA nor GSA provide an error estimation of the final $\mathbf{u}$, nevertheless, they are not deterministic methods as the LMA which, given one initial set $\mathbf{u}_0$, leads to specific results. By repeating a well-posed GSA (or SAA) several times, with the same initial array $\mathbf{u}_0$, slightly different results are obtained but all in the proximity of the global minimum of the χ^2 space. Hence, from the set of these results, calculated variances could give a measure of the width of such a valley.

List of Symbols and Acronyms

Symbols and Notations

$\mathbf{A}$	Curvature matrix
A_b	Beam cross section [mm^2]
A_H	Hamaker constant [J]
$A(q)$	Scattering amplitude [mm]
b	Scattering length [nm]
B	Brilliance [$s^{-1}\ mrad^{-2}\ mm^{-2}$]
c	Speed of light [$2.998 \times 10^8\ m\ s^{-1}$]
$c(r)$	Direct correlation function
$\mathbf{C}$	Covariance matrix
d_s	Spatial dimension
d_f, d_f^s, d_f^m	Fractal dimensions (Surface and mass fractals)
D	Diffusion coefficient [$\mu m^2\ s^{-1}$]
D_{eff}	Effective diffusion coefficient [$\mu m^2\ s^{-1}$]
D_r	Rotational diffusion coefficient [s^{-1}]
f	Scattering factor
$g(r)$	Pair correlation function
$g^{(1)}(\mathbf{q},t)$	Field-field autocorrelation function / normalised first-order intensity correlation
$g^{(2)}(\mathbf{q},t)$	Intensity-intensity autocorrelation function / normalised second-order intensity correlation
$G(\mathbf{q},t)$	Intensity correlation function
$\tilde{G}(\mathbf{r},t)$	Generalised time-dependent pair distribution function
h	Plank constant [$6.626 \times 10^{-34}\ J\ s$]
$h(r)$	Total correlation function
$\mathbf{H}$	Hessian matrix
$H(q)$	Hydrodynamic structure factor
I_0	Incident photon intensity [$mm^{-2}\ s^{-1}$]
$I(q)$	Scattering intensity [mm^{-1}]

$I_{DB}(q)$	Debye-Büche scattering function [mm^{-1}]
$I_{OZ}(q)$	Ornstein-Zernike scattering function [mm^{-1}]
k_B	Boltzmann constant [$1.380 \times 10^{-23}\ J\ K^{-1}$]
K	Amplitude of the interaction in the Yukawa potential [nm]
$\mathbf{k}_i$, $\mathbf{k}_s$	Wave vector of incident and scattered photons [nm^{-1}]
m_e	Electron mass [$9.109 \times 10^{-31}\ kg$]
n	Particle number density [ml^{-1}]
N	Number of particles
N_r	Normalisation factor
OD_{600}	Optical Density at $\lambda = 600\ nm$
p	Exponent of scattering power law
$P(q)$	Scattering form factor [mm^2]
$\mathbf{q}$; $q = \|\mathbf{q}\|$	Scattering vector; amplitude of $\mathbf{q}$ [nm^{-1}]
r_e	Classic electron radius [$2.818 \times 10^{-15}\ m$]
R	Radius of the colloid [nm]
$R(q)$	Effective smearing function
R_g	Radius of gyration [nm]
S	Surface area [nm^2]
$S(q)$	Static structure factor
$S_M(q)$	Effective static structure factor
$\mathbf{u}$	Array of free parameters used in a minimisation algorithm
$U(r)$	Effective interparticle interaction potential [J]
$U_C(r)$	Interparticle interaction: screened Coulomb potential [J]
$U_{vdW}(r)$	Interparticle interaction: Van der Waals attractive potential [J]
V	Particle volume [nm^3]
V_S	Scattering volume [nm^3]
T	Temperature [K]
T_A	Aggregation temperature [$^\circ\ C$]
T_C	Critical temperature [$^\circ\ C$]
T_S	Phase separation temperature [$^\circ\ C$]
T_{eff}	Effective temperature [J]
T_r	Transmission coefficient
W	Sample pathlength (fit parameter) [mm]
W^*	Sample pathlength (nominal) [mm]
Z, κ	Inverse Debye screening length (interaction length in the Yukawa potential) [nm^{-1}]

β	Contrast factor of the intensity-intensity autocorrelation function
γ	Lorentz factor
γ_f	Friction coefficient [$kg\ s^{-1}$]
$\gamma(r)$	Self-convolution of SLD fluctuation [nm^{-4}]
$\Gamma(q)$	Relaxation rate
$\delta(x)$	Dirac delta-function
$\langle \Delta r(t)^2 \rangle$	Mean square displacement [μm^2]
$\mathrm{d}\sigma/\mathrm{d}\Omega$	Differential scattering cross-section per unit solid angle [$nm^2\ sterad^{-1}$]
$\mathrm{d}\Sigma/\mathrm{d}\Omega$	$\mathrm{d}\sigma/\mathrm{d}\Omega$ per unit volume [$nm^{-1}\ sterad^{-1}$]
ε	Amplitude of the attractive interaction in the SW potential
ζ	ζ-potential [mV]
η	Viscosity [$Pa\ s$]
η_{eff}	Effective viscosity [$Pa\ s$]
λ	Photon/neutron Wavelength [nm]
$\Lambda(t)$	Langevin force [N]
ν	Photon frequency [s^{-1}]
ξ	Correlation length of SLD fluctuations [nm]
ρ	Scattering Length Density [nm^{-2}]
σ	Diameter of a spherical colloid [nm]
σ_{HS}	Hard-Sphere diameter [nm]
σ_i	Standard deviation of a Gaussian PDF associated to the quantity i
τ_r	Inverse rotational diffusion coefficient [s]
ϕ	Volume fraction
ϕ_{eff}	Packing density within clusters
χ^2	χ-squared function
χ_T	Isothermal compressibility [Pa^{-1}]
Ω	Solid angle [$sterad$]

Acronyms

AFM	Atomic Force Microscopy
PDF	Probability Distribution Function
DB	Debye-Büche
DLS	Dynamic Light Scattering
GSA	Genetic Selection Algorithm
HNC	Hyper Netted-Chain
HS	Hard-Sphere

LMA	Levenberg-Marquardt Algorithm
LCST	Lower Critical Solution Temperature
MSA	Mean Spherical Approximation
MSD	Mean Square Displacement
NSLD	Neutron Scattering Length Density
OZ	Ornstein-Zernike
PCS	Photon Correlation Spectroscopy
PDI	PolyDispersity Index
PY	Percus Yevick Approximation
RMSA	Rescaled Mean Spherical Approximation
RW	Random-Walk polymers (Gaussian chains)
RY	Rogers-Young
SAA	Simulated Annealing Algorithm
SANS	Small-Angle Neutron Scattering
SAS	Small-Angle Scattering
SAXS	Small-Angle X-ray Scattering
SAW	Self-Avoiding-Walk polymers
SEM	Scanning Electron Microscopy
SLD	Scattering Length Density
SW	Square-Well
USAXS	Ultra-Small-Angle X-ray Scattering
TEM	Transmission Electron Microscopy
XPCS	X-ray Photon Correlation Spectroscopy
XSLD	X-ray Scattering Length Density

List of Figures

1.1. MSDs as a function of time at different H_2O_2 concentrations. Reproduced from Ref. [35] (DOI: 10.1103/PhysRevLett.99.048102) with permission from The American Physical Society. 21

1.2. Dynamic clustering evolution monitored at different times. The colour map is maintained in both raw (a) and (b) in order to show the current colloid dynamics. Reproduced from Ref. [2] (DOI: 10.1103/PhysRevLett.108.268303) with permission from The American Physical Society. 22

1.3. Numerical velocity/concentration phase diagram of active particles. Dashed lines represent boundaries of the clustering phase and the red scale indicates the concentration fluctuation due to dynamics. Reproduced from Ref. [54] (DOI: 10.1016/j.jnoncrysol.2014.08.011) with permission from Elsevier. 22

2.1. Schematic illustration of SAS. The incident beam (wave vector $\mathbf{k}_i$), arriving on the sample, generates a scattered wave (wave vector $\mathbf{k}_s$) with $|\mathbf{k}_i| = |\mathbf{k}_s|$ at a scattering angle θ. 28

2.2. a) 2D scattering pattern acquired on a Pilatus 300k detector from a suspension of concentrated spherical silica colloids. Tics represent the magnitude of the scattering vector $|q|$ from the centre of the image in nm^{-1}. The colour scale displays the scattering intensity. b) Examples of partial azimuthal integration, only accounting for partial azimuthal sections of the 2D scattering pattern. . . . 29

2.3. Schematic illustration of the building-up of the core-shell scattering amplitude by summing, separately, the core and shell terms, where the latter is obtained by removing from a sphere ρ_s, R_s the equivalent volume of the core. Different SLDs are represented by light and dark grey, for ρ_c and ρ_s respectively. 31

2.4. Sketches of SLD profiles for two examples of lipid systems, a) a micelle and b) a lipid bilayer. In the plots, black lines represent the rectangular profiles of the simple core-shell approximation, whereas red lines depict more realistic gaussian SLD profiles $\Delta\rho(r)$. 32

2.5. Neutron scattering length density of biomolecules suspended in a mixture of H_2O/D_2O. Divergence from a constant trend is due to the exchange of hydrogen atoms in the solvent-accessible area of the macromolecules. Reproduced from Ref. [114] (DOI:10.1016/j.tifs.2009.07.008) with permission from Elsevier. . . 38
2.6. a) Schematic illustration of the frame acquisition over time. Two-dimensional multi-speckle patterns were acquired on a Pilatus 300k detector from a suspension of concentrated spherical silica colloids. b) Example of masking of the speckle pattern to selected a series of rings of thickness Δq. 41
2.7. Schematic illustration of the emission of an accelerated electron. Direction **a** and **v** describe the acceleration and velocity vectors normal and tangential to a circular trajectory, respectively, and γ is the relativistic Lorentz factor, which is a function of the electron energy. a) Dipole-field in the instantaneous reference frame of the electron. b) Deformed dipole-field in relativistic regime: photons are emitted alongside **v** with a narrow divergence with an angle equal to γ^{-1}. . 42
2.8. Schematic illustration of the USAXS/SAXS setup at the TRUSAXS beamline ID02. From the left to the right, ID02 beamline exploits the undulator radiation. The beam passes through a Si 111 monochromator and is focused by a double-mirror. The pinhole collimation of the beam is performed by a series of slits, from P to S5. After the interaction with a sample, the USAXS/SAXS intensity is measured by a detector placed in a motorised wagon inside a 34 *m* long detector tube under vacuum. Picture adapted from [16]. 43

3.1. Schematic diagram of an *E. coli* cell. The bacterium is a compact rod-like cell enclosed by the cell wall. A few flagella are anchored all around the cell body by trans-envelope machinery that cross the cell wall. The cytoplasm contains a nucleoid region mainly consisting of single folded DNA-ring and a non-nucleoid area densely packed with proteins and ribosomes. 48
3.2. Schematic diagram of the cell wall in gram-negative bacteria. These cells are distinguished by the presence of the periplasmic space, that is an external cellular compartment separated from the cytoplasm by the inner, or periplasmic, membrane. In turn, the periplasm is separated from the outside by a second coating, the outer membrane, that is firmly bound to the peptidoglycan layer inside. 49
3.3. USAXS data from *Escherichia coli* ($OD_{600} = 2.0$) suspended in PBS buffer (using FReLoN detector). The data are described by polydisperse capped-cylinder model with parameters listed in Table 3.1. 52

3.4. USAXS data fitted by a capped-cylinder (*solid line*) and an ellipsoid (*dashed line*) model. The radius obtained with ellipsod-model is $\langle R \rangle \simeq 365$ *nm*, roughly 15 *nm* bigger than the estimation by the capped-cylinder model. 54
3.5. Best fit of *E. coli* samples re-suspended in PBS buffer. The cells were taken from the same culture in three different stages, corresponding to distinct growth phases. 56
3.6. Plot of the average cell radius as a function of the concentration in the bacterial culture. The inset shows the radius values obtained by fitting the data by an ellipsoid model. The curve is systematically overestimated by ~ 15 *nm*. 56
3.7. Measurements of *E. coli* suspended in LB medium (*full circles*) and in PBS buffer (*empty diamonds*). Cells in the two media have the same radius, defined by the positions of the minima. 57
3.8. USAXS/SAXS measurements of *E. coli* suspended in PBS buffer. Bacterial concentration $OD_{600} = 10$, artificially concentrated from a culture stopped at $OD_{600} = 1$ (late-exponential growth phase). The curve is obtained merging three measurements (using Rayonix detector) at three different sample-detector distances and interpolating the data into a logarithmic-spaced q-array. 59
3.9. SANS measurements of *E. coli* suspended in mixtures of PBS and D-PBS buffers. Bacterial concentration $OD_{600} = 10$, artificially concentrated from a culture stopped at $OD_{600} = 1$ (late-exponential growth phase). The curves are obtained by merging three measurements at different sample-detector distances (17.6, 5.6 and 1.4 *m*) and interpolating data into logarithmically spaced q-range. 61
3.10. USAXS/SAXS measurements of *E. coli* suspended in mixtures of PBS and D-PBS buffers. The measurements were acquired using the same samples employed to obtain SANS curves in Figure 3.9. The curves are obtained by merging three measurements at different sample-detector distances (30.8, 10.0 and 1.0 *m*). 62
3.11. Scheme of the core-multiple-shell geometry used to model the bacterial scattering form factor. Uniform SLD average values are used to approximate the cytoplasmic core and the shells describing a gram-negative cell wall. 63
3.12. Cryo-TEM image of a frozen thin section of *E. coli* K-12. The arrows point out the two inner and outer phospholipid membranes, defining the periplasmic space in between. Inside, a darker gray layer describe the peptidoglycan layer (Bar, 50 nm). Reproduced from [80] (DOI: 10.1128/JB.185.20.6112-6118.2003) with permission from the American Society of Microbiology. . . . 64
3.13. SANS data fitted with Equation 3.9. Data concern samples at 11, 42, 65 and 100 D_2O *wt%* in the suspension medium. 68

3.14. SANS data fitted with Equation 3.9. Data concern the sample at 11 D_2O *wt%* in the suspension medium. The best fit (solid line) is the sum of the membrane model $< P_{shell}(q) >$, the SAW polymer model $P_{SAW}(q)$ with slope $q^{-1.7}$ and the constant value. 70
3.15. USAXS/SAXS data fitted with Equation 3.9. Data concern the sample at 0 $D_2O wt\%$ in the suspension medium. 71
3.16. USAXS/SAXS data fitted with Equation 3.9. Data concern the sample at 0 D_2O *wt%* in the suspension medium. The best fit (solid line) is the sum of the membrane model $< P_{shell}(q) >$, the SAW polymer model $P_{SAW}(q)$ with slope $q^{-1.7}$ and the constant value. To notice that the low-q region is fully described by $< P_{shell}(q) >$. 71
3.17. NSLD values for CP, PP, PG and phospholipid head groups as a function of the nominal D_2O concentration. A weighted linear regression is used to extrapolate the respective values for the fit at 0 *wt%* in D_2O. 72
3.18. Curve fitting of *E. coli* suspended in pure PBS (0 D_2O *wt%*). The solid line describes a fit obtained by fixing global and extrapolated parameters. 73
3.19. Fitting of B_{SAW}/n values as a function of the nominal D_2O concentration. The minimum of the parabola is close to the matching point for protein systems, that is roughly 36 D_2O *wt%* ($1.9 \times 10^{-4}\ nm^{-2}$). 74
3.20. Comparison between the fitted $P_{SAW}(q)$ term and simulated minimum and maximum contributions from flagella. Those are modelled using Ornstein-Zernike equation for SAW polymers with correlation length $\xi = 71\ nm$ and $\xi = 1393\ nm$. Concentration, volume and contrast values are consistent with the known structural description of the flagella. 75
3.21. a) NSLD profile for five different contrast match-point. The x-axis refers to the short radii of the ellipsoid. The same profile is applied all over the ellipsoid. b) XSLD profile for the system suspended in PBS buffer. In both figures, the smearing of the rectangular SLD-profile is only used for a better visibility. . . . 77
3.22. SANS data fitted with Equation 3.13. Data concern samples at 11, 42, 65 and 100 D_2O *wt%* in the suspension medium. 81
3.23. SANS data fitted with Equation 3.13. Data concern the sample at 100 D_2O *wt%* in the suspension medium. The best fit (solid line) is the sum of the membrane model $< P_{shell}(q) >$, the Guinier term $I_G(q)$ and the constant value. 82
3.24. NSLD values for CP, PP, PG and phospholipid head groups as a function of the nominal D_2O concentration. A weighted linear regression is used to extrapolate the respective values for the fit at 0 *wt%* in D_2O. 83

3.25. Curve fitting of *E. coli* suspended in pure PBS (0 D_2O *wt%*). The solid line describes a fit obtained by fixing global and extrapolated parameters. 84
3.26. Fitting of I_{pr}/n values as a function of the nominal D_2O concentration. The minimum of the parabola is higher than the matching point for protein systems, that is roughly 36 D_2O *wt%* (1.9×10^{-4} nm^{-2}). 84

4.1. Scattering Form Factors of silica colloids ($\langle R \rangle = 239$ *nm*) and *E. coli* bacteria ($\langle R \rangle = 460$ *nm*) suspensions. Data were fitted with a polydisperse sphere and a polydisperse ellipsoid respectively. 91
4.2. ζ-potential measurements on silica colloids suspensions with different buffer compositions. Compared to pure water (W) suspensions, phosphate buffer (PE) media, with or without 0.5 *mM* of glucose (PEG), poorly affect the effective surface charge density of colloids. A significant screening is visible in presence of 0.16 *mM* Tween20 (PET and PEGT). All the samples contained 0.1 *mM* of EDTA. 93
4.3. Sketch of investigated systems. From left to right, pictures refer to 0.008, 0.08, 0.16 and 0.32. Sizes and distances are in scale as well as the number of particles per cell in the equivalent 2D geometry. 95
4.4. Fits of USAXS curves of colloidal silica suspensions (volume fraction 0.08) in pure water using two capillaries with thicknesses W. Data were modelled using a repulsive Yukawa potential as structure factor and applying multiple scattering corrections. 97
4.5. Fits of USAXS curves of colloidal silica suspensions (volume fraction 0.16) in pure water using three capillaries with thicknesses W. Data were modelled using a repulsive Yukawa potential as structure factor and applying multiple scattering corrections. 98
4.6. Fits of USAXS curves of colloidal silica suspensions (volume fraction 0.33) in pure water using two capillaries with thicknesses W. Data were modelled using a repulsive Yukawa potential as structure factor and applying multiple scattering corrections. 99
4.7. Plot of the repulsive Yukawa potential curves obtained from the fits. The vertical dashed line represents the hard-sphere limit at the colloid surface. 100
4.8. Calculated thickness values W compared with the nominal values W^*. The dashed line represents the bisector. 101
4.9. Normalisation factor N_r as a function of the inverse transmission of the sample $1/T_r$. The dashed line is a guide to show the linear trend for $1/T_r < 4$. 101

4.10. Fits of USAXS curves of colloidal silica suspensions in motility buffer at various volume fractions (fitted values of 0.08, 0.17 and 0.32) using capillaries with thickness $W^* = 0.2\ mm$ (fitted value $W = 0.24\ mm$). Data were modelled using effective HS potential for structure factor, where $\sigma_{HS} = \sigma$, and applying multiple scattering corrections. 102
4.11. Ratio of the scattering intensity values of passive and active suspensions of silica colloids at three volume fraction $\phi = 0.08$, 0.17 and 0.32. Active suspensions refer to the mixture at $OD_{600} = 3$. 103
4.12. Fits of USAXS curves of colloidal silica suspensions in motility buffer at various volume fractions (fitted values of 0.076, 0.150 and 0.254) using capillaries with thickness $W^* = 1.5$ (fitted value $W = 1.15\ mm$). Data were modelled using an attractive Yukawa potential as structure factor and applying multiple scattering corrections. 105
4.13. Fits of USAXS curves of mixtures of colloidal silica and *E. coli* at $OD_{600} = 3$ in motility buffer at various volume fractions (fitted values of 0.077, 0.154 and 0.275) using capillaries with thickness $W^* = 1.5\ mm$ (fitted value $W = 1.15\ mm$). Data were modelled using an attractive Yukawa potential as structure factor and applying multiple scattering corrections. 105
4.14. Comparison of measured structure factors $S_M(q)$ obtained from the fits in Figures 4.12 and 4.13. Solid lines represent $S_M(q)$ curves for the colloidal mixtures with bacterial concentration $OD_{600} = 3$, dashed lines refer to passive systems without active cells. 106
4.15. Comparison of the attractive Yukawa potential $U(r)/k_BT$ obtained from the fits in Figures 4.12 and 4.13. Solid lines represent colloidal mixtures with bacterial concentration $OD_{600} = 3$, dashed lines refer to passive systems without active cells. The vertical dashed line represents the HS limit at the colloid diameter σ. 107
4.16. Intensity-intensity autocorrelation functions $g^{(2)}(q,t)$ data fitted with Equation 4.5. Data refer to passive colloidal concentrations of $\phi = 0.008, 0.08, 0.17$ and 0.32. 108
4.17. Decay rate $\Gamma(q)$ as a function of q^2. Data refer to the passive systems of reference, without bacteria. The dashed line represents the linear fit $\Gamma = Dq^2$ for the diffusion of passive colloids in the dilute system at $\phi = 0.008$ 109
4.18. Plots of $\Gamma(q)$ values as a function of q^2 for systems with volume fraction $\phi = 0.08$ (left), 0.17 (centre) and 0.32 (right). Linear fits were used to determine the effective diffusion D_{eff}. Empty symbols and dashed lines concern passive systems whereas full symbols and solid lines refer to samples with bacterial concentration $OD_{600} = 3$. 110

4.19. Plots of hydrodynamic structure factors $H(q)$ for systems with volume fraction $\phi = 0.08$ (left), 0.17 (centre) and 0.32 (right). Empty symbols concern passive systems whereas full symbols refer to samples with bacterial concentration $OD_{600} = 3$. Solid lines are the measured static structure factors of the passive systems obtained from fits in Figure 4.10. 111
4.20. (Top figure) Effective diffusion coefficients D_{eff} as a function of the bacterial concentrations. Dashed lines represent the effective diffusion of the respective passive systems. (Bottom figure) Ratio between effective viscosities of the system containing bacteria (η_{eff}) and the reference one ($\eta_{passive}$). 112
4.21. (Top figure) Effective diffusion coefficients D_{eff} as a function of the bacterial concentrations. Dashed lines represent the effective diffusion of the respective passive systems. (Bottom figure) Ratio between effective viscosities of the system containing bacteria (η_{eff}) and the reference one ($\eta_{passive}$). 113
4.22. Time evolution of the ratio between effective viscosities of the system containing bacteria (η_{eff}) and the reference one ($\eta_{passive}$). Systems at $OD_{600} = 5$ were measured just after mixing with glucose ($\Delta t = 0$). 114
4.23. Ratio between effective viscosities of the system containing bacteria (η_{eff}) and the reference one ($\eta_{passive}$) as a function of the effective diffusion coefficients $D_{passive}$ of the passive systems of reference. η_{eff} values refer to systems at $OD_{600} = 3$. 115
4.24. 2-time correlation functions plots for silica colloids at $\phi \simeq 0.08$ with (left) and without bacteria (right) at $OD_{600} = 3$. The colour scale goes from blue to red, respectively representing $g^{(2)}(t) = 1$ and $g^{(2)}(t) = 1.1$. Data refer to $q = 0.0043\ nm^{-1}$. 116

5.1. Sketch of the JP synthesis using the sputtering method. 121
5.2. (a) AFM measurements of dry silica colloids on a silicon substrate. Light-gray areas display the monolayer whilst the black spots represent the presence of a few colloids on a second layer. (b) SEM measuremets on silica/nickel Janus colloids. For the measurements, a drop of dilute suspension in water was let dry on a silicon wafer. 122
5.3. Building-up of a half-shell Janus geometry, where R is the radius of the core colloids and δ is the thickness of the half-shell. The different XSLD of the materials is represented by the colour, light-grey for a silica core and a dark-grey for the nickel coating. 122

5.4. SAXS measurements on silica and half-coated silica/nickel Janus colloids. Fits were perfomed by using Equations 2.10 and 5.3 and applying polydispersity and intrumental smearing. The vertical dashed line divides data obtained with sample-detector distances of 10 and 0.9 m. 123
5.5. Schematic phase diagram of silica colloids in 2,6-lutidine/H_2O or 3MP/H_2O/D_2O systems displaying the phase-separation temperature (T_s) boundaries as a function of the lutidine (or 3MP) concentration (C_L). T_C and C_C are, respectively, the critical temperature (LCST) and the critical concentrations. Both 3MP and lutidine water-mixture exhibit the same features. The boxes of the left are sketches of the colloidal distribution in three different areas: a stable suspension in the 1-phase region (*bottom*), clusters in the aggregation region (*centre*) and stable, fragmented-clusters redispersed into the lutidine-rich (or 3MP-rich) phase upon phase separation (*top*). Reproduced from Ref. [166] (DOI: 10.1023/A:1004506601807) with permission from Springer. 125
5.6. Selected USAXS curves from silica colloids in 25 3MP $wt\%$ as a function of temperature. The curves represent the stable dispersion of colloids in the 1-phase region at 38.3 $^\circ C$ (circles); just after the onset of attractive interaction at 39.9 $^\circ C$ (diamonds); in the aggregation region, showing clusters, at 40.5 $^\circ C$ (triangles); in the 3MP-rich phase at 44 $^\circ C$ (squares) after a complete phase separation. Volume fractions at 38.3 and 44 $^\circ C$ are, respectively, $\phi = 0.02$ and 0.056. 126
5.7. Phase inversion. The colloidal-rich 3MP phase move to the bottom of the sample holder for higher volume fractions $\phi \geq 0.03$ and about 500 s after the end of the temperature quench. 127
5.8. Intensity-intensity autocorrelation functions for the 25 $wt\%$ sample at $q = 3.3 \times 10^{-3}\ nm^{-1}$ at different times Δt from the end of the temperature quench. Fits were done using Equation 5.6. The arrows highlight the speeding-up of the dynamics until $\Delta t = 101\ s$ followed by a relaxation to a slower colloidal motion for longer periods. 128
5.9. Mean decay rate Γ as a function of q for (a) 25 and (b) 35 $wt\%$ 3MP at different Δt. Data were fitted with Equation 5.7. 130
5.10. Mean decay rate Γ as a function of q for (a) 25 and (b) 35 $wt\%$ 3MP at different Δt. Empty and full symbols represent horizontal (H) and vertical (V) dynamics respectively. Circles and diamonds, in the order, describe data taken at the beginning and at the end of the series, while triangles refer to data acquired with the fastest decay rate. 131

5.11. Curves of the (a) effective diffusion coefficient D_{eff}, (b) velocity fluctuations Δv and (c) concentration ratio $\frac{n}{n_0}$ as a function of time delay Δt from the end of the temperature quench for 25 and 35 *wt%* 3MP. Dashed (25%) and solid (35%) lines in (a) represent the diffusion coefficient of the silica colloids prior to the temperature quench and in (c) are guides to the eye to show the partitioning that occurs during the phase separation. 132
5.12. Curves of the (a) effective diffusion coefficient D_{eff}, (b) velocity fluctuations Δv and (c) concentration ratio $\frac{n}{n_0}$ as a function of time delay Δt from the end of the temperature quench for two different $\Delta T = 44$ and 43 $°C$. Dashed (44 $°C$) and solid (43 $°C$) lines in (a) represent the diffusion coefficient of the silica colloids prior to the temperature quench and in (c) are guides to the eye to show the partitioning that occurs during the phase separation. 133
5.13. Sketch of the mechanism inducing phoretic motion of silica colloids in the phase separating system. Stage (0) represent the 1-phase system before quenching. During the phase separation, stage (1), isotropic phoretic motions are induced by the binodal decomposition of the mixture, where silica colloids are forced to move toward the 3MP-rich areas (P) and away from the water-rich regions (W). When the system is at equilibrium, stage (2), colloids are partitioned in the 3MP-rich phase and move by Brownian diffusion. Dashed arrows outside the boxes represent the movement of the 3MP/water interface. 135
5.14. MSD curves $[\langle \Delta r^2(t) \rangle]$ for silica colloids in (a) 25 and (b) 35 *wt%* 3MP as a function of time from the end of the temperature quench Δt. Data at $q = 2.8 \times 10^{-3}\ nm^{-1}$. 136
5.15. Concentration ratio $\frac{n}{n_0}$ as a function of the capillary height Δz from the interface at different time delays Δt after a quench from 36 to 50 $°C$ in a system at 25 *wt%* 3MP. The peak in concentration is due to an accumulation of colloids at the interface between the phases. The value of n_0 refers to the systems at 30 $°C$. 138
5.16. Concentration ratio $\frac{n}{n_0}$ as a function of the capillary height Δz from the interface or systems at 25 and 35 *wt%* 3MP at 50 $°C$. The value of n_0 refers to the systems at 30 $°C$. 138
5.17. USAXS measurements performed in the 3MP- and water-rich phases and next to the interface between them for samples at 25 (a) and 35 *wt%* 3MP (b) in the phase separated systems. Fits refer to Equation 5.8, except for data concerning 3MP-rich phase, where just a spherical form factor was used. 140

5.18. Ageing of Janus colloids suspended in 25 $wt\%$ 3MP. The curves show a deviation from an initial stable suspension (circle), where data were analysed using a spherical form factor, to older systems (squares and triangles) that display the presence of dimers. Number fractions of spheres x_{JP} versus dimers x_{Di} is shown a function of time as an inset. 143
5.19. Intensity-intensity autocorrelation functions for (a) 25 and (b) 35 $wt\%$ samples at $q = 3.3 \times 10^{-3}\ nm^{-1}$ at different times Δt from the end of the temperature quench. Fits were done using Equations 5.12. 145
5.20. Intensity-intensity autocorrelation functions for 25 $wt\%$ samples at $\Delta t = 70\ s$ at different times q values. Fits were performed using Equations 5.12. 145
5.21. Mean decay rate Γ_1 as a function of q for (a) 25 and (b) 35 $wt\%$ 3MP at different Δt. Data were fitted with Equation 5.12. Data for 25% and $\Delta t = 70$ were not fitted and are shown as an example. 146
5.22. Mean decay rate Γ as a function of q for (a) 25 and (b) 35 $wt\%$ 3MP at different Δt. Empty and full symbols represent horizontal (H) and vertical (V) directions respectively. Data show a isotropic dynamics except for an intermediate time range, where the decays related to vertical and horizontal motions do not overlap. 147
5.23. Parameters for (a) effective diffusion coefficient, D_{eff}, (b) velocity fluctuations, Δv, and (c) concentration ratio, $\frac{n}{n_0}$, as a function of time delay Δt from the end of the temperature quench for 25 and 35 $wt\%$ 3MP, where n_0 is the initial concentration of the colloids at 30 $^\circ C$. Solid and dashed lines in (a) represent the diffusion coefficient of the Janus colloids prior to the temperature quench and in (c) are guides to the eye to show the partitioning that occurs during the phase separation. The dashed area in (a) and (b) refers to the missing data. . . . 148
5.24. Curves of the (a) effective diffusion coefficient D_{eff}, (b) velocity fluctuations Δv and (c) concentration ratio $\frac{n}{n_0}$ as a function of time delay Δt from the end of the temperature quench for 35 $wt\%$ 3MP, using samples at different ageing stages. (A) and (F) refer for aged and fresh samples. Solid and dashed lines in (a) represent the diffusion coefficient of the Janus colloids prior to the temperature quench and in (c) are guides to the eye to show the partitioning that occurs during the phase separation. 150
5.25. Curves of the (a) effective diffusion coefficient D_{eff}, (b) velocity fluctuations Δv and (c) concentration ratio $\frac{n}{n_0}$ as a function of time delay Δt from the end of the temperature quench for 35 $wt\%$ 3MP with two different final temperatures, 50 and 55 $^\circ C$. The solid line in (a) represents the diffusion coefficient of the Janus colloids prior to the temperature quench and in (c) are guides to the eye to show the partitioning that occurs during the phase separation. 151

5.26. Sketch of the mechanism inducing phoretic motion of Janus colloids in the phase separating system. Stage (0) represent the 1-phase system before quenching. During the phase separation, stage (1), isotropic phoretic motions are induced by the binodal decomposition of the mixture, where Janus colloids are forced to move toward the interfaces (25%) or the water-rich (W) areas (35%). When the two phase regions are defined, (2), clusters are visible and the phoretic motions start relaxing towards an equilibrium state, stage (3). A dimer is always drawn to remind the ageing effect. 152

A.1. Simulated scattering form factors of a polydisperse cylinder (Gaussian PDF) with $\langle R \rangle = 250\ nm$, $H = 1000\ nm$ and standard deviation $\sigma_R = 12.5\ nm$. Curves are compared to the asymptotic trend of the Porod law $\propto q^{-4}$. The values 30, 90 and 3000× are the numbers of numerical integration steps (Simpson's rule) used during the orientation average (see Eq. 3.2). 167

B.1. a) Two possible paths of the LMA minimisation of $\chi^2(\mathbf{u})$ as a function of the P-dimensional vector $\mathbf{u}$, where the one on the left is trapped in a local minimum. b) Possible path of the SAA minimisation of $\chi^2(\mathbf{u})$ as a function of the P-dimensional vector $\mathbf{u}$. Here the path can explore the χ^2 landscape to find the global minimum. 172

List of Tables

1.1. Technical names of colloidal systems in various combinations of dispersed phase and medium [17]. 15

2.1. List of the scattering length b expressed in Fermi (10^{-13} cm) for common elements. 39

3.1. Results from the fit in Figure 3.3. σ_R is the standard deviation of a normal PDF for R. 52

3.2. Values of cell radius for *E. coli* suspensions. Bacteria were harvested from the culture at $OD_{600} \simeq 1.4$, during the late-exponential growth phase. Due to background subtraction issues, the estimation of the errors on these values is 5 nm. 58

3.3. Estimations of volume ratios with respect the whole cell body. 58

3.4. Typical values for the X-ray and neutron scattering length density of the main components need to describe the system. Water and heavy water values refer to room temperature ($25°C$). 60

3.5. Equivalent D_2O $wt\%$ in buffer composition required to attain contrast matching condition. As an approximation, NSLD linearly increases as a function of D_2O $wt\%$ 63

3.6. List of the 20 parameters involved in the bacterial model. They are classed in Global (10), Local (7) and Fixed (3) parameters. C_{IM} value represents the distance between the IM centre of mass and the centre of the elliptical core along the minor radius. 67

3.7. Set of results from five fits on SANS curves at 11, 42, 65 and 100 D_2O $wt\%$ and the USAXS/SAXS curve at 0 D_2O wt% in buffer composition. Shared columns refer to global parameters. 69

3.8. Summary of the parameters describing the partial SANS curve at 0 D_2O $wt\%$. SLD values were recovered from a linear extrapolation. Values of n, B_{SAW} and Con were obtained by fitting the SANS curve (global and extrapolated parameters were fixed). 70

3.9. Estimation of the water content (x_w) or protein content (x_p) for each layer. The error is calculated as half or the discrepancy between the two values from the XSLD and NSLD profiles. Raws are ranked by the relative error δ_r. 79
3.10. Summary of the parameters describing the partial SANS curve at 0 D_2O *wt%*. SLD values were recovered from a linear extrapolation. 85

4.1. ζ-potential measurements on silica colloids suspensions with different buffer compositions. σ_ζ values is the standard deviation of a Gaussian profile representing the precision limit of the instruments, whilst the effective error in ζ is around 1%. 93
4.2. Crowding conditions of the medium in which bacteria swim. n_s, $\sqrt[3]{1/n_s}$ and $\langle d_s \rangle$ are, respectively, the concentration, the centre-to-centre distance and the average distance between the surfaces of silica colloids of diameter $\langle \sigma \rangle = 478\ nm$. n_s/n_b values represent the number of passive colloids per single bacterium in a system with cell concentration $OD_{600} = 3$. 95
4.3. Results from the global fitting of $I^s(q)$. $\langle R \rangle$ and PDI values were obtained from the fit in Figure 4.1. 99
4.4. Results about the local parameters W and N_r. 100
4.5. Fit results for plots in Figures 4.14 and 4.15. 106

5.1. Fit results from Figure 5.4. σq values refer to the instrumental smearing related to two sample-detector (SD) distances. $^*\rho$ values were used as fixed parameters. 124
5.2. Results from fits in Figure 5.6. $\langle R \rangle$ and PDI values refer to the form factor analysis. ϕ_{eff} is the effective packing fraction of colloids in the aggregates, $\langle \sigma_{HS} \rangle$, ε and $\Delta\sigma$ define the SW potential quantities and R_g is the radius of gyration of the aggregates. 127
5.3. Fit results from Figure 5.17, where P, I and W respectively refer to the curves in 3MP-rich phase, interface and water-rich regions. ϕ_{eff}, $\langle \sigma_{HS} \rangle$, ε and $\Delta\sigma$ are the effective volume fraction, the hard-sphere diameter, the depth and the width of the SW potential, respectively. R_g and p are the radius of gyration and the exponent of the cluster term I_{OZ}. The fractal dimension is linked to either surface, d_f^s, or mass, d_f^m, fractals. (*) The value $d_f^s = 2$ is equivalent to a spatial dimension $d_s = 2$, describing a smooth surface. 141

Bibliography

[1] T. Vicsek, A. Czirók, E. Ben-Jacob, I. Cohen, and O. Shochet. Novel Type of Phase Transition in a System of Self-Driven Particles. *Physical Review Letters*, 75(6):1226(4), 1995.

[2] I. Theurkauff, C. Cottin-Bizonne, J. Palacci, C. Ybert, and L. Bocquet. Dynamic Clustering in Active Colloidal Suspensions with Chemical Signaling. *Physical Review Letters*, 108(26):268303(5), 2012.

[3] D. Beysens and D. Estève. Adsorption Phenomena at the Surface of Silica Spheres in a Binary Liquid Mixture. *Physical Review Letters*, 54(19):2123–2126, 1985.

[4] W. B. Russell, D. A. Saville, and W. R. Schowalter. *Colloidal Dispersions*. Cambridge University Press, Cambridge, 1989.

[5] D. F. Evans and H. Wennerström. *The Colloidal Domain: Where Physics, Chemistry, Biology, and Technology Meet*. Wiley, New York, 2nd edition, 1999.

[6] J. N. Israelachvili. *Intermolecular and Surface Forces*. Academic Press, 3rd edition, 2011.

[7] G. Popkin. The Physics of Life. *Nature*, 529(7584):16–18, 2016.

[8] J. Toner, Y. Tu, and S. Ramaswamy. Hydrodynamics and phases of flocks. *Annals of Physics*, 318(1):170–244, 2005.

[9] A. Ramaswamy and H. Stark. The mechanics and statistics of active matter. *arXiv*, preprint arXiv:1004.1933, 2010.

[10] T. Vicsek and A. Zafeiris. Collective motion. *Physics Reports*, 517(3):71–140, 2012.

[11] M. C. Marchetti, J. F. Joanny, S. Ramaswamy, T. B. Liverpool, J. Prost, M. Rao, and R. A. Simha. Hydrodynamics of soft active matter. *Reviews of Modern Physics*, 85(3):1143–1189, 2013.

[12] C. Bechinger, R. Di Leonardo, H. Löwen, C. Reichhardt, G. Volpe, and Giov. Volpe. Active Brownian particles in complex and crowded environments. *arXiv*, preprint arXiv:1602.00081, 2016.

[13] A. Zöttl and H. Stark. Emergent behavior in active colloids. *Journal of Physics: Condensed Matter*, 28(25):253001, 2016.

[14] H. C. Berg and D. A. Brown. Chemotaxis in *Escherichia coli* analysed by three-dimensional tracking. *Nature*, 239(5374):500–504, 1972.

[15] P. G. de Gennes. Soft Matter. *Reviews of Modern Physics*, 64(3):645–648, 1992.

[16] P. Van Vaerenbergh, J. Léonardon, M. Sztucki, P. Boesecke, J. Gorini, L. Claustre, F. Sever, J. Morse, and T. Narayanan. An Upgrade Beamline for Combined Wide, Small and Ultra Small-Angle X-ray Scattering at the ESRF. In *AIP Conference Proceedings*, volume 1741, page 030034(4). AIP Publishing, 2016.

[17] C. N. Likos. Effective Interactions in Soft Condensed Matter Physics. *Physics reports*, 348(4–5):267–439, 2001.

[18] X. Bian, C. Kim, and G. E. Karniadakis. 111 years of Brownian motion. *Soft Matter*, 12(30):6331–6346, 2016.

[19] L. E. Reichl. *A Modern Course in Statistical Physics*. Wiley, New York, 1998.

[20] B. J. Berne and R. Pecora. *Dynamic Light Scattering with applications to Chemistry, Biology and Physics*. Wiley, New York, 1976.

[21] A. Einstein. Über die von der molekularkinetischen Theorie der Wärme geforderte Bewegung von in ruhenden Flüssigkeiten suspendierten Teilchen. *Annalen der Physik*, 322(8):549–560, 1905.

[22] L. Belloni. Colloidal interactions. *Journal of Physics: Condensed Matter*, 12(46):R549–R587, 2000.

[23] W. Stöber, A. Fink, and E. Bohn. Controlled Growth of Monodisperse Silica Spheres in the Micron Size Range. *Journal of Colloid and Interface Science*, 26(1):62–69, 1968.

[24] G. Frens. Controlled Nucleation for the Regulation of the Particle Size in Monodisperse Gold Suspensions. *Nature Physical Science*, 241(105):20–22, 1973.

[25] T. Narayanan, M. Sztucki, G. Belina, and F. Pignon. Microstructure and Rheology near an Attractive Colloidal Glass Transition. *Physical Review Letters*, 96(25):258301(4), 2006.

[26] H. N. W. Lekkerkerker and Remco Tuinier. *Colloids and the Depletion Interaction*. Springer Science & Business Media, 2011.

[27] S. Asakura and F. Oosawa. On Interaction between Two Bodies Immersed in a Solution of Macromolecules. *Journal of Chemical Physics*, 22(7):1255–1256, 1954.

[28] J. Adler and M. M. Dahl. A Method for Measuring the Motility of Bacteria and for Comparing Random and Non-random Motility. *Journal of General Microbiology*, 46(2):161–173, 1967.

[29] J. Adler and B. Templeton. The Effect of Environmental Conditions on the Motility of *Escherichia coli*. *Journal of General Microbiology*, 46(2):175–184, 1967.

[30] J. Saragosti, P. Silberzan, and A. Buguin. Modeling *E. coli* Tumbles by Rotational Diffusion. Implications for Chemotaxis. *PLoS ONE*, 7(4):e35412, 2012.

[31] H. Salman, A. Zilman, C. Loverdo, M. Jeffroy, and A. Libchaber. Solitary Modes of Bacterial Culture in a Temperature Gradient. *Physical Review Letters*, 97(11):118101(4), 2006.

[32] W. F. Paxton, K. C. Kistler, C. C. Olmeda, A. Sen, S. K. St. Angelo, Y. Cao, T. E. Mallouk, P. E. Lammert, and V. H. Crespi. Catalytic nanomotors: Autonomous movement of striped nanorods. *Journal of the American Chemical Society*, 126(41):13424–13431, 2004.

[33] R. Golestanian, T. B. Liverpool, and A. Ajdari. Propulsion of a Molecular Machine by Asymmetric Distribution of Reaction Products. *Physical Review Letters*, 94(22):220801(4), 2005.

[34] W. F. Paxton, A. Sen, and T. E. Mallouk. Motility of Catalytic Nanoparticles through Self-Generated Forces. *Chemistry - A European Journal*, 11(22):6462–6470, 2005.

[35] J. R. Howse, R. A. L. Jones, A. J. Ryan, T. Gough, R. Vafabakhsh, and R. Golestanian. Self-Motile Colloidal Particles: From Directed Propulsion to Random Walk. *Physical Review Letters*, 99(4):048102(4), 2007.

[36] X. Ma, A. Jannasch, U. Albrecht, K. Hahn, A. Miguel-López, E. Schäffer, and S. Sánchez. Enzyme-Powered Hollow Mesoporous Janus Nanomotors. *Nano Letters*, 15(10):7043–7050, 2015.

[37] I. Buttinoni, G. Volpe, F. Kümmel, G. Volpe, and C. Bechinger. Active Brownian motion tunable by light. *Journal of Physics: Condensed Matter*, 24(28):284129(6), 2012.

[38] A. Würger. Self-Diffusiophoresis of Janus Particles in Near-Critical Mixtures. *Physical Review Letters*, 115(18):188304(5), 2015.

[39] S. Samin and R. van Roij. Self-Propulsion Mechanism of Active Janus Particles in Near-Critical Binary Mixtures. *Physical Review Letters*, 115(18):188305(5), 2015.

[40] T. Narayanan and A. Kumar. Reentrant phase transitions in multicomponent liquid mixtures. *Physics Reports*, 249(3):135–218, 1994.

[41] A. Perro, S. Reculusa, S. Ravaine, E. Bourgeat-Lami, and E. Duguet. Design and synthesis of Janus micro- and nanoparticles. *Journal of Materials Chemistry*, 15(35-36):3745–3760, 2005.

[42] T. Chen, G. Chen, S. Xing, T. Wu, and H. Chen. Scalable Routes to Janus Au-SiO_2 and Ternary Ag-Au-SiO_2 Nanoparticles. *Chemistry of Materials*, 22(13):3826–3828, 2010.

[43] A. Walther and A. H. E. Müller. Janus Particles: Synthesis, Self-Assembly, Physical Properties and Applications. *Chemical Reviews*, 113(7):5194–5261, 2013.

[44] R. Golestanian. Anomalous diffusion of symmetric and asymmetric active colloids. *Physical Review Letters*, 102(18):188305(4), 2009.

[45] X. Zheng, B. Ten Hagen, A. Kaiser, M. Wu, H. Cui, Z. Silber-Li, and H. Löwen. Non-Gaussian statistics for the motion of self-propelled Janus particles: Experiment versus theory. *Physical Review E*, 88(3):032304(11), 2013.

[46] J. G. Gibbs and Y.-P. Zhao. Autonomously motile catalytic nanomotors by bubble propulsion. *Applied Physics Letters*, 94(16):163104(3), 2009.

[47] A. Brown and W. Poon. Ionic effects in self-propelled Pt-coated Janus swimmers. *Soft matter*, 10(22):4016–4027, 2014.

[48] S. Ebbens, D. A. Gregory, G. Dunderdale, J. R. Howse, Y. Ibrahim, T. B. Liverpool, and R. Golestanian. Electrokinetic effects in catalytic platinum-insulator Janus swimmers. *EPL (Europhysics Letters)*, 106(5):58003(6), 2014.

[49] A. L. Thorneywork, R. E. Rozas, R. P. A. Dullens, and J. Horbach. Effect of Hydrodynamic Interactions on Self-Diffusion of Quasi-Two-Dimensional Colloidal Hard Spheres. *Physical Review Letters*, 115(26):268301(5), 2015.

[50] C. Dombrowski, L. H. Cisneros, S. Chatkaew, R. E. Goldstein, and J. O. Kessler. Self-Concentration and Large-Scale Coherence in Bacterial Dynamics. *Physical Review Letters*, 93(9):098103(4), 2004.

[51] A. Sokolov, I. S. Aranson, J. O. Kessler, and R. E. Goldstein. Concentration Dependence of the Collective Dynamics of Swimming Bacteria. *Physical Review Letters*, 98(15):158102(4), 2007.

[52] A. Sokolov and I. S. Aranson. Physical Properties of Collective Motion in Suspensions of Bacteria. *Physical Review Letters*, 109(24):248109(5), 2012.

[53] F. Peruani, J. Starruß, V. Jakovljevic, L. Søgaard-Andersen, A. Deutsch, and M. Bär. Collective Motion and Nonequilibrium Cluster Formation in Colonies of Gliding Bacteria. *Physical Review Letters*, 108(9):098102(5), 2012.

[54] J. Bialké, T. Speck, and H. Löwen. Active colloidal suspensions: Clustering and phase behavior. *Journal of Non-Crystalline Solids*, 407:367–375, 2015.

[55] O. Pohl and H. Stark. Dynamic Clustering and Chemotactic Collapse of Self-Phoretic Active Particles. *Physical Review Letters*, 112(23):238303(5), 2014.

[56] M. E. Cates and J. Tailleur. When are active Brownian particles and run-and-tumble particles equivalent? Consequences for motility-induced phase separation. *EPL (Europhysics Letters)*, 101(2):20010, 2013.

[57] J. Stenhammar, D. Marenduzzo, R. J. Allen, and M. E. Cates. Phase behaviour of active Brownian particles: the role of dimensionality. *Soft Matter*, 10(10):1489–1499, 2014.

[58] A. P. Solon, J. Stenhammar, M. E. Cates, Y. Kafri, and J. Tailleur. Generalized Thermodynamics of Phase Equilibria in Scalar Active Matter. *arXiv*, preprint arXiv:1609.03483, 2016.

[59] R. Soto and R. Golestanian. Self-assembly of Catalytically Active Colloidal Molecules: Tailoring Activity Through Surface Chemistry. *Physical Review Letters*, 112(6):068301(5), 2014.

[60] G. S. Redner, A. Baskaran, and M. F. Hagan. Reentrant phase behavior in active colloids with attraction. *Physical Review E*, 88(1):012305(5), 2013.

[61] R. M. Navarro and S. M. Fielding. Clustering and phase behaviour of attractive active particles with hydrodynamics. *Soft Matter*, 11(38):7525–7246, 2015.

[62] L. Angelani. Collective Predation and Escape Strategies. *Physical Review Letters*, 109(11):118104(5), 2012.

[63] X.-L. Wu and A. Libchaber. Particle Diffusion in a Quasi-Two-Dimensional Bacterial Bath. *Physical Review Letters*, 84(13):3017(4), 2000.

[64] J. P. Hernandez-Ortiz, C. G. Stoltz, and M. D. Graham. Transport and Collective Dynamics in Suspensions of Confined Swimming Particles. *Physical Review Letters*, 95(20):204501(4), 2005.

[65] A. Jepson, V. A. Martinez, J. Schwarz-Linek, A. Morozov, and W. C. K. Poon. Enhanced diffusion of nonswimmers in a three-dimensional bath of motile bacteria. *Physical Review E*, 88(4):041002(5), 2013.

[66] N. Koumakis, A. Lepore, C. Maggi, and R. Di Leonardo. Targeted delivery of colloids by swimming bacteria. *Nature communications*, 4:2588, 2013.

[67] K. Drescher, J. Dunkel, L. H. Cisneros, S. Ganguly, and R. E. Goldstein. Fluid dynamics and noise in bacterial cell-cell and cell-surface scattering. *Proceedings of the National Academy of Sciences*, 108(27):10940–10945, 2011.

[68] J. Hu, M. Yang, G. Gompper, and R. G. Winkler. Modelling the mechanics and hydrodynamics of swimming *E. coli*. *Soft Matter*, 11(40):7867–7876, 2015.

[69] D. Loi, S. Mossa, and L. F. Cugliandolo. Effective temperature of active matter. *Physical Review E*, 77(5):051111(4), 2008.

[70] D. Loi, S. Mossa, and L. F. Cugliandolo. Effective temperature of active complex matter. *Soft Matter*, 7(8):3726–3729, 2011.

[71] J. Palacci, C. Cottin-Bizonne, C. Ybert, and L. Bocquet. Sedimentation and Effective Temperature of Active Colloidal Suspensions. *Physical Review Letters*, 105(8):088304(4), 2010.

[72] F. Ginot, I. Theurkauff, D. Levis, C. Ybert, L. Bocquet, L. Berthier, and C. Cottin-Bizonne. Nonequilibrium Equation of State in Suspensions of Active Colloids. *Physical Review X*, 5(1):011004(8), 2015.

[73] R. Ni, M. A. Cohen Stuart, M. Dijkstra, and P. G. Bolhuis. Crystallizing hard-sphere glasses by doping with active particles. *Soft Matter*, 10(35):6609–6613, 2014.

[74] M. Lieb, J. J. Weigle, and E. Kellenberger. A study of hybrids between two strains of *Escherichia coli*. *Journal of Bacteriology*, 69(4):468–471, 1955.

[75] P. Latimer. Light scattering vs. microscopy for measuring average cell size and shape. *Biophysical Journal*, 27(1):117–126, 1979.

[76] N. E. Lonergan, L. D. Britt, and C. J. Sullivan. Immobilizing live *Escherichia coli* for AFM studies of surface dynamics. *Ultramicroscopy*, 137:30–39, 2014.

[77] J. A. Hobot, E. Carlemalm, W. Villiger, and E. Kellenberger. Periplasmic Gel: New Concept Resulting from the Reinvestigation of Bacterial Cell Envelope Ultrastructure by New Methods. *Journal of Bacteriology*, 160(1):143–152, 1984.

[78] L. L. Graham, T. J. Beveridge, and N. Nanninga. Periplasmic space and the concept of the periplasm. *Trends in Biochemical Sciences*, 16(9):328–329, 1991.

[79] T. J. Beveridge. Structure of Gram-Negative Cell Walls and Their Derived Mebrane Vesicles. *Journal of Bacteriology*, 181(16):4725–4733, 1999.

[80] V. R. F. Matias, A. Al-amoudi, J. Dubochet, and T. J. Beveridge. Cryo-Transmission Electron Microscopy of Frozen-Hydrated Sections of *Escherichia coli* and *Pseudomonas aeruginosa*. *Journal of Bacteriology*, 185(20):6112–6118, 2003.

[81] L. Angelani, C. Maggi, M. L. Bernardini, A. Rizzo, and R. Di Leonardo. Effective Interactions between Colloidal Particles Suspended in a Bath of Swimming Cells. *Physical Review Letters*, 107(13):138302(4), 2011.

[82] T. Narayanan. Synchrotron Small-Angle Scattering. In R. Borsali and R. Pecora, editors, *Soft-Matter Characterization*, chapter 17. Springer-Verlag, Berlin Heidelberg, 2008.

[83] T. Narayanan, H. Wacklin, O. Konovalov, and R. Lund. Recent applications of synchrotron radiation and neutrons in the study of soft matter. *Crystallography Reviews*, 23:160–226, 2017.

[84] O. Glatter and O. Kratky, editors. *Small-Angle X-ray Scattering*. Accademic Press, London, 1982.

[85] L. A. Feigin and D. I. Svergun. *Structural Analysis by Small-Angle X-ray and Neutron Scattering*. Plenum Press, New York, 1987.

[86] P. Lindner and T. Zemb, editors. *Neutrons, X-rays and Light: Scattering Methods Applied to Soft Condensed Matter*. North-Holland Delta Series, Elsevier, Amsterdam, 2002.

[87] M. S. Longair. *High energy astrophysics. Volume 1: Particles, photons and their detection. 2nd edition*. Cambridge University Press, Cambridge, 1992.

[88] J. Schelten and W. Schmatz. Multiple-Scattering Treatment for Small-Angle Scattering Problems. *Journal of Applied Crystallography*, 13(4):385–390, 1980.

[89] M. A. Kiselev, P. Lesieur, A. M. Kisselev, D. Lombardo, and V. L. Aksenov. Model of separated form factors for unilamellar vesicles. *Applied Physics A*, 74(Suppl.):1654–1656, 2002.

[90] N. Kučerka, S. Tristram-Nagle, and J. F. Nagle. Structure of Fully Hydrated Fluid Phase Lipid Bilayers with Monounsaturated Chains. *Journal of Membrane Biology*, 208(3):193–202, 2006.

[91] N. Kučerka, M.-P. Nieh, and J. Katsaras. Small-Angle Scattering from Homogenous and Heterogeneous Lipid Bilayers. In A. Iglic, editor, *Advances in planar lipid bilayers and liposomes*, volume 12, chapter 8. Elsevier, Amsterdam, 2010.

[92] G. Pabst, N. Kučerka, M.-P. Nieh, M. C. Rheinstädter, and J. Katsaras. Applications of neutron and X-ray scattering to the study of biologically relevant model membranes. *Chemistry and Physics of Lipids*, 163(6):460–479, 2010.

[93] N. Kučerka, B. W. Holland, C. G. Gray, B. Tomberli, and J. Katsaras. Scattering Density Profile Model of POPG Bilayers As Determined by Molecular Dynamics Simulations and Small-Angle Neutron and X-ray Scattering Experiments. *The Journal of Physical Chemistry B*, 116(1):232–239, 2012.

[94] D. Marquardt, F. A. Heberle, J. D. Nickels, G. Pabst, and J. Katsaras. On scattered waves and lipid domains: detecting membrane rafts with X-rays and neutrons. *Soft Matter*, 11(47):9055–9072, 2015.

[95] S. J. Singer and G. L. Nicolson. The Fluid Mosaic Model of the Structure of Cell Membranes. *Science*, 175(4023):720–731, 1972.

[96] G. L. Nicolson. The Fluid–Mosaic Model of Membrane Structure: Still relevant to understanding the structure, function and dynamics of biological membranes after more than 40 years. *Biochimica et Biophysica Acta (BBA)-Biomembranes*, 1838(6):1451–1466, 2014.

[97] J. Pencer, S. Krueger, C. P. Adams, and J. Katsaras. Method of separated form factors for polydisperse vesicles. *Journal of Applied Crystallography*, 39(3):293–303, 2006.

[98] T. Foster. Universal analytical scattering form factor for shell-, core-shell, or homogeneous particles with continuously variable density profile shape. *Journal of Physical Chemistry B*, 115(34):10207–10217, 2011.

[99] C. L. P. Oliveira, B. B. Gerbelli, E. R. T. Silva, F. Nallet, L. Navailles, E. A. Oliveira, and J. S. Pedersen. Gaussian deconvolution: A useful method for a form-free modeling of scattering data from mono-and multilayered planar systems. *Journal of Applied Crystallography*, 45(6):1278–1286, 2012.

[100] P. Heftberger, B. Kollmitzer, F. A. Heberle, J. Pan, M. Rappolt, H. Amenitsch, N. Kučerka, J. Katsaras, and G. Pabst. Global small-angle X-ray scattering data analysis for multilamellar vesicles: the evolution of the scattering density profile model. *Journal of Applied Crystallography*, 47(1):173–180, 2014.

[101] A. Guinier and G. Fournet. *Small-Angle Scattering of X-rays*. Wiley, New York, 1955.

[102] C. M. Sorensen. Light Scattering by Fractal Aggregates: A Review. *Aerosol Science and Technology*, 35(2):648–687, 2001.

[103] P. Debye and A. M. Bueche. Scattering by an inhomogeneous solid. *Journal of Applied Physics*, 20(6):518–525, 1949.

[104] R. Klein and B. D'Aguanno. Static Scattering Properties of Colloidal Suspensions. In W. Brown, editor, *Light Scattering: Principles and Development*, chapter 2. Clarendon Press, Oxford, 1996.

[105] M. S. Wertheim. Exact Solution of the Percus-Yevick Integral Equation for Hard-Spheres. *Physical review letters*, 10(8):321–323, 1963.

[106] E. Thiele. Equation of State for Hard Spheres. *The Journal of Chemical Physics*, 39(2):474–479, 1963.

[107] M. S. Wertheim. Analytic Solution of the Percus-Yevick Equation. *Journal of Mathematical Physics*, 5(5):643–651, 1964.

[108] R. V. Sharma and K. C. Sharma. The structure factor and the transport properties of dense fluids having molecules with square well potential, a possible generalization. *Physica*, 89A(1):213–218, 1977.

[109] W.-R. Chen, S.-H. Chen, and F. Mallamace. Small-angle neutron scattering study of the temperature-dependent attractive interaction in dense L64 copolymer micellar solutions and its relation to kinetic glass transition. *Physical Review E*, 66(2):021403(12), 2002.

[110] R. J. Baxter. Pescus-Yevick Equation for Hard Spheres with Surface Adhesion. *Journal of Chemical Physics*, 49(6):2770–2774, 1968.

[111] Y. Liu, W.-R. Chen, and S.-H. Chen. Cluster formation in two-Yukawa fluids. *Journal of Chemical Physics*, 122(4):044507(13), 2005.

[112] J. P. Hansen and J. B. Hayter. A rescaled MSA structure factor for dilute charged colloidal dispersions. *Molecular Physics*, 46(3):651–656, 1982.

[113] F. J. Rogers and D. A. Young. New, thermodynamically consistent, integral equation for simple fluids. *Physical Review A*, 30(2):999, 1984.

[114] A. Lopez-Rubio and E. P. Gilbert. Neutron scattering: a natural tool for food science and technology research. *Trend in Food Science & Technology*, 20(11-12):576–586, 2009.

[115] B. Jacrot. The study of biological structures by neutron scattering from solution. *Reports on Progress in Physics*, 39(10):911–953, 1976.

[116] G. Zaccai. Small-angle neutron scattering. In E. Fanchon, E. Geissler, J. L. Hodeau, J. R. Regnard, and P. A. Timmins, editors, *Structure and Dynamics of Biomolecules*, chapter 12. Oxford University Press, 2002.

[117] G. Grübel, A. Madsen, and A. Robert. X-Ray Photon Correlation Spectroscopy (XPCS). In R. Borsali and R. Pecora, editors, *Soft-Matter Characterization*, chapter 18. Springer-Verlag, Berlin Heidelberg, 2008.

[118] R. L. Leheny. XPCS: Nanoscale motion and rheology. *Current Opinion in Colloid and Interface Science*, 17(1):3–12, 2012.

[119] J. Möller, Y. Chushkin, S. Prevost, and T. Narayanan. Multi-speckle X-ray photon correlation spectroscopy in the ultra-small-angle X-ray scattering range. *Journal of Synchrotron Radiation*, 23(4):929–936, 2016.

[120] M. Sutton. A review of X-ray intensity fluctuation spectroscopy. *Comptes Rendus Physique*, 9(5–6):657–667, 2008.

[121] M. S. Longair. *High energy astrophysics. Volume 2: Particles, photons and their detection. 2nd edition*. Cambridge University Press, Cambridge, 1992.

[122] P. J. Duke. *Synchrotron Radiation: Production and Properties*. Oxford University Press, Oxford, 2000.

[123] M. Sztucki and T. Narayanan. Development of an ultra-small-angle X-ray scattering instrument for probing the microstructure and the dynamics of soft matter. *Journal of Applied Crystallography*, 40(s1):s459–s462, 2007.

[124] A. R. von Gundlach, V. M. Garamus, T. M. Willey, J. Ilavsky, K. Hilpert, and A. Rosenhahn. Use of small-angle X-ray scattering to resolve intracellular structure changes of *Escherichia coli* cells induced by antibiotic treatment. *Journal of Applied Crystallography*, 49(6):2210–2216, 2016.

[125] S. B. Zimmerman and S. O. Trach. Estimation of Macromolecule Concentrations and Excluded Volume Effects for the Cytoplasm of *Escherichia coli*. *Journal of Molecular Biology*, 222(3):599–620, 1991.

[126] T. Kaneshiro and A. G. Marr. Cis-9,10-Methylene the Phospholipids Hexadecanoic Acid from of *Escherichia coli*. *The Journal of Biological Chemistry*, 236(10):2615–2619, 1961.

[127] J. E. Cronan JR. Phospholipid Alterations During Growth of *Escherichia coli*. *Journal of Bacteriology*, 95(6):2054–2061, 1968.

[128] A. J. De Siervo. Alterations in the Phospholipid Composition of *Escherichia coli* B During Growth at Different Temperatures. *Journal of Bacteriology*, 100(3):1342–1349, 1969.

[129] D. Oursel, C. Loutelier-Bourhis, N. Orange, S. Chevalier, V. Norris, and C. M. Lange. Lipid composition of membranes of *Escherichia coli* by liquid chromatography/tandem mass spectrometry using negative electrospray ionization. *Rapid Communications in Mass Spectrometry*, 21(11):1721–1728, 2007.

[130] T. J. Silhavy, D. Kahne, and S. Walker. The bacterial Cell Envelope. *Cold Spring Harbor Perspectives in Biology*, 2(5):a000414, 2010.

[131] A. Zaritsky and C. E. Helmstetter. Rate Maintenance of Cell Division in *Escherichia coli* B/r: Analysis of a Simple Nutritional Shift-Down. *Journal of Bacteriology*, 174(24):8152–8155, 1992.

[132] D. Pink, J. Moeller, B. Quinn, M. Jericho, and T. Beveridge. On the Architecture of the Gram-Negative Bacterial Murein Sacculus. *Journal of Bacteriology*, 182(20):5925–5930, 2000.

[133] L. Gan, S. Chen, and G. J. Jensen. Molecular organization of Gram-negative peptidoglycan. *Proceedings of the National Academy of Sciences*, 105(48):18953–18957, 2008.

[134] W. Shu, J. Liu, H. Ji, and M. Lu. Core structure of the outer membrane lipoprotein from *Escherichia coli* at 1.9 Å resolution. *Journal of Molecular Biology*, 299(4):1101–1112, 2000.

[135] S. Asakura, G. Eguchi, and T. Iino. Reconstitution of Bacterial Flagella in Vitro. *Journal of Molecular Biology*, 10(1):42–56, 1964.

[136] I. Yamashita, K. Hasegawa, H. Suzuki, F. Vonderviszt, Y. Mimori-Kiyosue, and K. Namba. Structure and switching of bacterial flagellar filaments studied by X-ray fiber diffraction. *Nature Structural Biology*, 5(2):125–132, 1998.

[137] N. C. Darnton, L. Turner, S. Rojevsky, and H. C. Berg. On Torque and Tumbling in Swimming *Escherichia coli*. *Journal of Bacteriology*, 189(5):1756–1764, 2007.

[138] L. Turner, R. Zhang, N. C. Darnton, and H. C. Berg. Visualization of Flagella during Bacterial Swarming. *Journal of Bacteriology*, 192(13):3259–3267, 2010.

[139] H. Kaya and N.-R. de Souza. Scattering from cylinders with globular end-caps. *Journal of Applied Crystallography*, 37(2):223–230, 2004.

[140] C. R. Calladine. Change of Waveform in Bacterial Flagella: The Role of Mechanics at the Molecular Level. *Journal of Molecular Biology*, 118(4):457–479, 1978.

[141] A.-C. Chien, N. S. Hill, and P. A. Levin. Cell Size Control in Bacteria. *Current Biology*, 22(9):R340–R349, 2012.

[142] F. I. Maclean and R. J. Munson. Some Environmental Factors Affecting the Length of *Escherichia coli* Organisms in Continuous Cultures. *Journal of general Microbiology*, 25(1):17–27, 1961.

[143] F. J. Trueba and C. L. Woldringh. Changes in Cell Diameter During the Division Cycle of *Escherichia coli*. *Journal of Bacteriology*, 142(3):869–878, 1980.

[144] H. E. Kubitschek. Cell Volume Increase in *Escherichia coli* after shiters to richer media. *Journal of Bacteriology*, 172(1):94–101, 1990.

[145] R. B. Weart, A. H. Lee, A.-C. Chien, D. P. Haeusser, N. S. Hill, and P. A. Levin. A Metabolic Sensor Governing Cell Size in Bacteria. *Cell*, 130(2):335–347, 2007.

[146] H. C. Benoît and J. S. Higgins. *Polymers and Neutron Scattering*. Oxford Series on Neutron Scattering in Condensed Matter, Clarendon Press, Oxford, 1994.

[147] P. Schurtenberger. Static Properties of Polymers. In P. Lindner and T. Zemb, editors, *Neutrons, X-rays and Light: Scattering Methods Applied to Soft Condensed Matter*, chapter 11. North-Holland Delta Series, Elsevier, Amsterdam, 2002.

[148] P. J. Flory. *Statistical Mechanics of Chain Molecules*. Wiley, New York, 1969.

[149] F. Dyson. A meeting with Enrico Fermi. *Nature*, 427(6972):297, 2004.

[150] J. Mayer, K. Khairy, and J. Howard. Drawing an elephant with four complex parameters. *American Journal of Physics*, 78(6):648–649, 2010.

[151] C. W. Mullineaux, A. Nenninger, N. Ray, and C. Robinson. Diffusion of Green Fluorescent Protein in Three Cell Environments in *Escherichia coli*. *Journal of Bacteriology*, 188(10):3442–3448, 2006.

[152] A. Zaritsky, C. L. Woldringh, and D. Mirelman. Constant Peptidoglycan Density in the Sacculus of *Escherichia coli* B/r Growing at Different Rates. *Federation of European Biochemical Societies Letters*, 98(1):29–32, 1979.

[153] D. Svergun, C. Barberato, and M. H. J. Koch. CRYSOL - a Program to Evaluate X-ray Solution Scattering of Biological Macromolecules from Atomic Coordinates. *Journal of Applied Crystallography*, 28(6):768–773, 1995.

[154] B. P. Klaholz, T. Pape, A. V. Zavialov, A. G. Myasnikov, E. V. Orlova, B. Vestergaard, M. Ehrenberg, and M. van Heel. Structure of the *Escherichia coli* ribosomal termination complex with release factor 2. *Nature*, 421(6918):90–94, 2003.

[155] A. R. von Gundlach, V. M. Garamus, T. Gorniak, H. A. Davies, M. Reischl, R. Mikut, K. Hilpert, and A. Rosenhahn. Small angle X-ray scattering as a high-throughput method to classify antimicrobial modes of action. *Biochimica et Biophysica Acta (BBA)-Biomembranes*, 1858(5):918–925, 2015.

[156] J. Möller and T. Narayanan. Velocity fluctuations in sedimenting Browninan particles. *(Submitted)*, 2017.

[157] J. Schwarz-Linek, J. Arlt, A. Jepson, A. Dawson, T. Vissers, D. Miroli, T. Pilizota, V. A. Martinez, and W. C. K. Poon. *Escherichia coli* as a model active colloid: a practical introduction. *Colloids and Surfaces B: Biointerfaces*, 137:2–16, 2015.

[158] H. M. López, J. Gachelin, C. Douarche, H. Auradou, and E. Clement. Turning Bacteria Suspensions into Superfluid. *Physical Review Letters*, 115(2):028301(5), 2015.

[159] F. Sciortino and P. Tartaglia. Glassy colloidal systems. *Advances in Physics*, 54(6–7):471–524, 2005.

[160] E. Zaccarelli and W. C. K. Poon. Colloidal glasses and gels: The interplay of bonding and caging. *Proceedings of the National Academy of Sciences*, 106(36):15203–15208, 2009.

[161] A. H. Elcock. Models of macromolecular crowding effects and the need for quantitative comparisons with experiment. *Current Opinion in Structural Biology*, 20(2):196–206, 2010.

[162] I. M. Sokolov. Models of anomalous diffusion in crowded environments. *Soft Matter*, 8(35):9043–9052, 2012.

[163] E. F. Semeraro, J. Möller, and T. Narayanan. Analysis of multiple-scattering in static and dynamic USAXS. *(In preparation)*, 2017.

[164] J. Schwarz-Linek, C. Valeriani, A. Cacciuto, M. E. Cates, D. Marenduzzo, A. N. Morozov, and W. C. K. Poon. Phase separation and rotor self-assembly in active particle suspensions. *Proceedings of the National Academy of Sciences*, 109(11):4052–4057, 2012.

[165] J. C. Love, B. D. Gates, D. B. Wolfe, K. E. Paul, and G. M. Whitesides. Fabrication and Wetting Properties of Metallic Half-Shells with Submicron Diameters. *Nano Letters*, 2(8):891–894, 2002.

[166] D. Beysens and T. Narayanan. Wetting-Induced Aggregation of Colloids. *Journal of Statistical Physics*, 95(5-6):997–1008, 1999.

[167] B. M. Law, J.-M. Petit, and D. Beysens. Adsorption-induced reversible colloidal aggregation. *Physical Review E*, 57(5):5782(13), 1998.

[168] H. Guo, T. Narayanan, M. Sztucki, P. Schall, and G. H. Wegdam. Reversible Phase Transition of Colloids in a Binary Liquid Solvent. *Physical Review Letters*, 100(18):188303(4), 2008.

[169] R. Okamoto and A. Onuki. Attractive interaction and bridging transition between neutral colloidal particles due to preferential adsorption in a near-critical binary mixture. *Physical Review E*, 88(2):022309(15), 2013.

[170] V. D. Nguyen, S. Faber, Z. Hu, G. H. Wegdam, and P. Schall. Controlling colloidal phase transitions with critical Casimir forces. *Nature Communications*, 4:1584, 2013.

[171] D. Pontoni, T. Narayanan, J.-M. Petit, G. Grübel, and D. Beysens. Microstructure and Dynamics near an Attractive Colloidal Glass Transition. *Physical Review Letters*, 90(18):188301(4), 2003.

[172] C. Gögelein, M. Brinkmann, M. Schröter, and S. Herminghaus. Controlling the Formation of Capillary Bridges in Binary Liquid Mixtures. *Langmuir*, 26(22):17184–17189, 2010.

[173] C. E. Bertrand, P. D. Godfrin, and Y. Liu. Direct observation of critical adsorption on colloidal particles. *Journal of Chemical Physics*, 143(8):084704(5), 2015.

[174] G. D. J. Phillies. Interpretation of Light-Scattering Spectra in Terms of Particles Displacements. *Journal of Chemical Physics*, 122(22), 2005.

[175] H. K. Pak, W. I. Goldburg, and A. Sirivat. An Experimental Study of Weak Turbolence. *Fluid Dynamics Research*, 8(1-4), 1991.

[176] L.-C. Wang, H.-S. Xu, J.-H. Zhao, C.-Y. Song, and F.-A. Wang. Density and Viscosity of (3-picoline + water) Binary Mixtures from T=(293.15 to 343.15) K. *Journal of Chemical Thermodynamics*, 37(5):477–483, 2005.

[177] F. Sciortino, A. Giacometti, and G. Pastore. Phase Diagram of Janus Particles. *Physical Review Letters*, 103(23):237801(4), 2009.

[178] L. Bergström. Hamaker Constants in Inorganic Materials. *Advances in Colloid and Interface Science*, 70:125–169, 1997.

[179] R. M. Epand and H. J. Vogel. Diversity of antimicrobial peptides and their mechanisms of action. *Biochimica et Biophysica Acta (BBA)-Biomembranes*, 1462(1):11–28, 1999.

[180] Y. Shai. Mechanism of the binding, insertion and destabilization of phospholipid bilayer membranes by α-helical antimicrobial and cell non-selective membrane-lytic peptides. *Biochimica et Biophysica Acta (BBA)-Biomembranes*, 1462(1):55–70, 1999.

[181] E. M. Purcell. The efficiency of propulsion by a rotating flagellum. *Proceedings of the National Academy of Sciences*, 94(21):11307–11311, 1997.

[182] S. Chattopadhyay, R. Moldovan, C. Yeung, and X. L. Wu. Swimming efficiency of bacterium *Escherichia coli*. *Proceedings of the National Academy of Sciences*, 103(37):13712–13717, 2006.

[183] V. A. Martinez, J. Schwarz-Linek, M. Reufer, L. G. Wilson, A. N. Morozov, and W. C. K. Poon. Flagellated bacterial motility in polymer solutions. *Proceedings of the National Academy of Sciences*, 111(50):17771–17776, 2014.

[184] P. Boesecke. Reduction of two-dimensional small- and wide-angle X-ray scattering data. *Journal of Applied Crystallography*, 40(s1):s423–s427, 2007.

[185] *Numerical Recipes: The Art of Scientific Computing, 3rd Edition*. Cambridge University Press, Cambridge, 2007.